Mariana de Jesus Paiva Proença

Magnetism at the Nanoscale: Nanoparticles, Nanowires, Nanotubes and their Ordered Arrays



Department of Physics and Astronomy
Faculty of Sciences of the University of Porto
December 2012

Mariana de Jesus Paiva Proença

Magnetism at the Nanoscale: Nanoparticles, Nanowires, Nanotubes and their Ordered Arrays



Supervisor: *Dr. João Pedro Esteves de Araújo*
co-Supervisor: *Dr. Manuel Vázquez Villalabeitia*
co-Supervisor: *Dr. João Oliveira Ventura*

Thesis submitted to the Faculty of Sciences of the University of Porto in partial fulfillment of the requirements for the degree of Doctor in Physics

Department of Physics and Astronomy
Faculty of Sciences of the University of Porto
December 2012

Institutions were the work was performed:









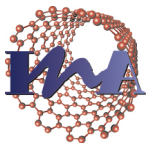


Institutions that collaborated in this work:











Funding:



To my parents,
my brother
and José.

Acknowledgments

The work presented in this thesis results from a collaboration between the research group of *Multifunctional Magnetic Materials and Nanostructures* (MMMN) from the *Instituto de Física dos Materiais da Universidade do Porto* (IFIMUP and IN – Institute of Nanoscience and Nanotechnology), and the research *Group of Nanomagnetism and Magnetization Processes* (GNMP) from the *Instituto de Ciencia de Materiales de Madrid* (ICMM) of the *Consejo Superior de Investigaciones Científicas* (CSIC). As a research work it thus results from the collaboration between several people to whom I am deeply thankful.

First and foremost I would like to thank my supervisor, Professor João Pedro Araújo from IFIMUP-IN, for all his support, guidance and friendship. Throughout this thesis he helped me to look deeper into my results and analyze each detail with a critical point of view. I have learned a lot from his past experience, and I am deeply thankful for the trust, understanding and constant motivation that he has always shown towards me.

To my co-supervisor, Professor Manuel Vázquez from ICMM-CSIC, for giving me the opportunity to work in his group at Madrid, and to receive me so welcomely. I want to thank for all his support and help on my magnetic doubts, for the trust he had in me during all the experimental months that I was spending in the laboratory, and for all the social group lunches of our "magnetic family" tasting nice wine and having some spanish *tapas*.

I want to give a very special thanks to João Ventura, my co-supervisor from IFIMUP-IN. I don't think all the work presented in this thesis would have been possible without his precious help and constant patience, every time I entered his office (and there were many!) asking for a little more help in a small (big) detail with my data. It was a great pleasure for me to work under his co-supervision, and I am looking forward to continue my research career with him in a future post-doc.

I would also like to thank Professor João Bessa Sousa, for all his support and help correcting this thesis. He was the one who introduced me to the MMMN IFIMUP-IN research group, and motivated me to work with nanoporous alumina templates in the first place.

I want to give another special thanks to Célia Sousa, who was always there to help me when I needed the most. She always had a lot of patience to answer my doubts and questions. For that and all the trust and friendship, I thank her deeply.

I want to thank the president of the jury, Prof. José Luís Santos, and the members of the jury, Dr. Victor Manuel De La Prida, Dr. Kristiaan Temst and Dr. Bernardo Almeida, for taking the time to read this thesis, and for the valuable corrections and suggestions.

I also want to thank all the members and former members of IFIMUP-IN for all their help, friendship and support. In particular, I want to thank Arlete Apolinário (you are one of the most kind and honest people I have ever met, and I thank you from my heart for your precious friendship), Diana Leitão (for all your help when I went to Madrid), João Azevedo, Diogo Costa, André Pereira,

Zé Miguel, Maria Paz, Sara Pinto, Alberto, João Horta, Marcelo, Gonçalo (for all the help in the XRD interpretations), João Amaral (for all the help in the computational problems and friendship), Isabel, Luis Miguel Custódio, Luis Guerra, Daniel Silva, Lino Pereira, Dina, Francisco Silva, Rui Rocha (for all the fun at the SEM), Francisco Carpinteiro, Sr. Carlos Torres, Dr. Gleb (for the FMR measurements), Dra. Elina and Isabel Alves (for all the help in the bureaucracy problems), Dra. Maria Armanda Sá (for the VSM measurements and all the recent help in the bureaucracy processes), Prof. Yuriy, Prof. David Schmool, Prof. Moreira, Maria Armanda, Florbela and Dona Rosalina (for all the help in the library, searching for new books).

I also want to thank my friends João Nuno, Marta Matos, Jorge Leitão, Zé Fonseca, Miguel Zilhão, Carlos Guedes, Olga and Marco, for all the friendship and help relaxing and disconnecting from all the work.

I want to give a special thanks also to my best friend João Coelho. I know that you are always there for me. I am really thankful to have your friendship and to share with you some of the best moments of my life. I thank you a lot for all your support throughout this thesis.

I also want to thank all the people I have met during my stay in Madrid. From our magnetic family, I want to thank in particular to Laura (always with a smile in her face and ready to help), Nacho (my best *compañero de despacho* ever!), Oscar (for the late research discoveries, talks and parties, for the great friendship), Sonia (to help me handle Nacho), Karla (for all the pic-nic organizations), Wagner (Vavá, for all the good mood, help around the lab, and party weekends in Madrid), Alfredo (for your tremendous help in the lab, fixing every little problem I had), German, Miriam, Paco, Agustina, David Navas, Ruy Sanz, Jacob, Kleber, Cristina (you also know what it takes to handle Nacho), David, Rhimou, Juana, Rafa (for all the help in the VSM), Giovanni, Alejandro, Oksana and Manuel Hernandez-Veléz. I want to thank the lunch group of ICMM, in particular Tere, Iñigo and Álvaro who helped me a lot improving my spanish (*albondrigas*) and cheered up my day during the lunch time. From the ICMM and related friends, I also want to thank Bernd, Francisco (thank you for your friendship and precious help when I first came to ICMM), Marga, Alex, Andres, Stefania, Leticia, Gladys, Maria, Inma, Marco Leonetti and André Espinha.

I also want to thank my roomies and friends from Tres Cantos, in particular Rui Fermento, Chon, Jonathan, Nuno Sousa, Mayra and Elias, for all the good and relaxed times I spend in that special party-house of the microelectronics group.

I want to thank the Grass Group Members for all the friendship and great moments spent during all the grass group meetings since ESONN09: Leonardo (President), Roberto (Ministry of transportation), Raffaella, Deniao, Bergoi, Laura, Ester, Mirko and João Tutticolori (such a transparent guy).

To my *afilhadinho* Núne and *netinho* Miguel Mota for all the hugs you gave me when I needed them the most.

For my two-month stay in Milan, I first want to thank Dr. Luca Magagnin and Dr. Paula Cojocaru

for receiving me at their group in the *Politecnico di Milano* and for helping me to better understand the electrochemical oxidation processes. To all the members of the group, in particular Massimo Fumagalli (for his precious help in the lab and happy friendship), Andrea Turolla, Yvette (someone to talk in spanish with), Valerio Spreafico, Reza, Anahit, Davide Sacco, Alice, Fabio and Andrea Leserri. And for the nice times at the Vitruvio Residence, I want to thank in particular to Max (the best friend I had there), Egle, Mariusz and Caroline.

I also want to thank Chema (from Hamburg University, Germany) for the discussions on electrodeposition, atomic layer deposition and membrane preparation using phosphoric acid; Fanny (from the State University of Campinas, Brazil) for all the help in the FORC measurements; Javi (from the University of Oviedo, Spain) for his fruitful discussions on the potentiostatic electrodepositions; Juan Escrig (from the University of Santiago de Chile, Chile) for his tremendous help in the analytical calculations; Prof. Pedro Tavares (from the *Universidade de Trás-os-Montes e Alto Douro*, Portugal) for all his help on the TEM and XRD measurements; and Prof. José Maria de Teresa, Dr. César Magen and Dr. Jasiek (from the *Instituto de Ciencia de Materiales de Aragón* in Zaragoza, Spain) for their support in the nanolithographic contacts deposited on a single nanowire/nanotube.

For all of those that I have met during conferences, workshops and seminars, I also want to thank all your contributions to improve my knowledge, all your help during my PhD, and your friendship.

I would also like to acknowledge IFIMUP-IN, ICMM-CSIC and the Physics and Astronomy Department of the Faculty of Sciences of the University of Porto for the support they gave me. I would like to thank FCT (*Fundação para a Ciência e a Tecnologia*) for their funding of my doctoral years (SFRH/BD/43440/2008) and of research projects and conference attendances. The group is also thankful to *Fundação Gulbenkian* for its financial support within the *Programa Gulbenkian de Estímulo à Investigação Científica* and acknowledge funding from FCT through the Associated Laboratory - IN.

Finally, I want to thank my family, specially my mum and dad, my brother Zé, my aunt São, my uncles Paulo and Luis, my cousins Ric, Pedro and Rita, and my granny Teresinha, for all their support, help and friendship. For being there when I needed the most. For their enthusiasm when I accomplished something. For their understanding and guidance when things were tough and more difficult. For their unconditional love.

And to José, the best thing that has ever happened to me. Thanks from the heart for all your love and support. Thank you for your patience and help in the late working nights, and during all the experiments I had to do on weekends... you could have stayed home, waiting for me, but you were always accompanying me to the lab for late measurements. Thank you for being by my side and for making my life infinite times better.

Resumo

Nanomateriais magnéticos têm vindo a atrair um interesse considerável nos últimos anos devido às suas propriedades únicas e potenciais aplicações, desde dispositivos de armazenamento e gravação magnética, sensores e *chips* biomédicos, ou como transportadores de medicamentos e agentes de aumento de contraste em imagiologia. São vários os desafios associados à fabricação de matrizes de grandes áreas altamente organizadas de nanoestruturas magnéticas e à exata compreensão do seu comportamento magnético. A técnica de preenchimento de um molde nanoporoso tem despertado grande interesse e mostrado muitas potencialidades, uma vez que permite uma produção de baixo custo e alto rendimento, de matrizes altamente organizadas de nanomateriais magnéticos. Além disso, a combinação de diferentes técnicas de enchimento, tais como os métodos de sol-gel e electrodeposição, aumenta a diversidade de nanoestruturas que podem ser produzidas [nanofios (NFs) e nanotubos (NTs) homogéneos, concêntricos ou heteroestruturados em multissegmentos], abrindo a possibilidade de ajustar uma maior variedade de respostas magnéticas.

Nesta tese, descrevemos a síntese e caracterização de nanopartículas (NPs), NFs, NTs e respectivas matrizes hexagonais ordenadas, pelo processo de sol-gel e técnicas de eletrodeposição potenciostáticas, usando membranas de alumina nanoporosas (MANs). Em primeiro lugar, estudamos em detalhe as condições ótimas para a eletrodeposição potenciostática de NFs de Ni dentro das MANs, com diâmetros de poro de 50 nm, controlando o valor do potencial aplicado. Desta forma somos capazes de aumentar a taxa de deposição para cerca de 10 μm min^{-1}, que é cerca de dez vezes maior do que os valores geralmente reportados na literatura. Apresentamos também um estudo sistemático e comparativo sobre a fabricação de matrizes de NFs e NTs de Ni com diâmetros pequenos ($\sim$ 50 nm), monitorizando a densidade de corrente de deposição durante o processo de electrodeposição potenciostático nas MANs. Um novo passo de fabricação é introduzido no processo de preparação das membranas, antes da eletrodeposição dos NTs, permitindo-nos produzir matrizes de NTs com diâmetros pequenos ($\sim$ 30 nm).

As propriedades magnéticas de matrizes hexagonais altamente organizadas de NFs e NTs de Ni e Co são também apresentadas. Em particular, descrevemos um estudo sistemático comparativo sobre os processos de reversão da magnetização em matrizes organizadas de NFs e NTs com diferentes diâmetros (30$-$65 nm). Para este estudo foram realizados cálculos analíticos e medições experimentais da dependência angular da coercividade. Do bom acordo encontrado, podemos estimar os modos de reversão em matrizes de NFs e NTs. A reversão da magnetização das matrizes de NTs (com diâmetros $<$ 50 nm) e de NFs de Ni e Co, é feita pela nucleação e propagação de uma parede de domínio do tipo transverso. Por outro lado, para matrizes de NTs de Ni e Co, ocorre um comportamento não-monótono acima de um diâmetro de $\sim$ 50 nm, revelando uma transição entre os modos de inversão do tipo vórtice e transverso.

As interacções magnéticas entre NFs e NTs fabricados dentro das MANs, foram medidas usando curvas de reversão de primeira ordem (CRPOs). Este método tem vindo a ser bastante usado para o estudo das interacções entre nanoelementos individuais de uma matriz, tais como NPs ou NFs. Nesta

tese utilizamos o método CRPO para caracterizar as interações magnéticas presentes numa matriz ordenada de NFs e NTs de Co. O diâmetro dos NFs/NTs foi variado entre 40 e 65 nm, e a rede hexagonal mantida com um parâmetro de rede de 105 nm. Em ambas as matrizes de NFs e NTs, as interações magnéticas aumentam com o diâmetro dos NFs/NTs, exibindo valores mais elevados para as matrizes de NFs.

Nesta tese apresentamos também a evidência experimental do acoplamento de troca do tipo *exchange-bias* (EB) em estruturas nanotubulares núcleo-casca, ao longo das direcções paralela e perpendicular do campo magnético aplicado. Matrizes organizadas de NTs de Co, com diâmetros externos de $\sim$ 40 nm, foram deixados ao ar para a oxidação natural das suas paredes internas, formando NTs concêntricos com uma casca externa ferromagnética (FM) de Co e uma casca interna antiferromagnética (AFM) de CoO. Apresentamos também a dependência térmica e do campo de arrefecimento do efeito de EB, juntamente com o efeito de treino a 6 K. Uma temperatura máxima de bloqueio (T_B) de $\sim$ 220 K, foi encontrada para os NTs de Co/CoO, que é cerca de 70 K abaixo da temperatura de Néel do CoO (293 K). O efeito de treino é ajustado através de uma fórmula recursiva proposta por Binek, dando valores pequenos para a taxa característica de diminuição do efeito de treino, o que pode ser interpretado, ao comparar com interfaces planas, como a existência de um forte acoplamento de troca entre as camadas AFM/FM, quando moldada sob a forma de uma estrutura núcleo-casca nanotubular. Encontramos também uma distribuição bimodal de T_B ao longo das direções paralela e perpendicular. O pico de baixa temperatura pode ser atribuído a fases de *spin-glass* interfaciais, enquanto que o pico de alta temperatura é geralmente atribuído à inversão térmica dos grãos AFM.

Descrevemos também a síntese de nanopartículas de NiO com tamanhos controlados, entre 12 e 70 nm, utilizando um método de sol-gel. A caracterização magnética efectuada mostra um aumento de T_B com o diâmetro das NPs e um aumento da anisotropia magnética eficaz (K_{ef}) com a diminuição do tamanho das NPs. O número de spins não compensados por NP é também estimado, permitindo-nos inferir que a sua maioria se encontra aleatoriamente distribuída na superfície da NP. Para pequenos diâmetros ($<$ 30 nm) foi calculada a constante de anisotropia de superfície através de um modelo que descreve a evolução de K_{ef} com o tamanho da partícula. O aumento da coercividade e os efeitos de *exchange-bias* e de treino, foram também observados para as NPs mais pequenas, após a aplicação de um campo de arrefecimento de 300 a 6 K. Estes resultados demonstram a existência de spins descompensados com correlações FM na superfície da NP, acoplados ao núcleo AFM, exibindo portanto um comportamento EB semelhante ao observado em bicamadas FM/AFM.

No final da tese apresentamos também alguns resultados preliminares sobre (i) o uso de ressonância ferromagnética para estudar a qualidade dos NFs e NTs de Ni e Co electrodepositados; (ii) a fabricação de matrizes de NFs de NiO pelo processo de enchimento dos poros por sol-gel; e (iii) o uso de dois métodos diferentes para aceder electricamente a um único NT, quer utilizando nano-litografia sobre um NT disperso em cima de um substrato, ou através da deposição de uma camada de Au adicional no topo da MAN e controlo da corrente de deposição até que o primeiro NT/NF atinja o topo. Estes métodos vão permitir estudar as propriedades resistivas e magneto-resistivas dos NTs fabricados.

Abstract

Magnetic nanomaterials are attracting considerable interest due to their unique properties and potential applications, ranging from magnetic storage and recording devices, sensors and biomedical chips, to contrast agents in ressonance imaging and drug carriers. There are various challenges associated with the fabrication of highly ordered large area magnetic nanostructures and the accurate understanding of their magnetic behavior. The use of a template assisted method has arouse great interest and shown many potentialities, as it allows the low-cost and high-yield growth of highly ordered nanomagnet arrays. Additionally, the combination of different filling techniques, such as sol-gel and electrodeposition methods, increases the diversity of nanostructures that can be produced [homogeneous, concentric or multisegmented heterostructured nanowires (NWs) and nanotubes (NTs)], opening the possibility to tune a larger variety of magnetic responses.

In this thesis we describe the synthesis and characterization of nanoparticles (NPs), NWs, NTs and their hexagonally ordered arrays, by sol-gel and potentiostatic electrodeposition techniques, using nanoporous alumina templates (NpATs). First, we study in detail the optimized conditions for the potentiostatic electrodeposition of Ni NWs inside NpATs with pore diameters of 50 nm, by tuning the applied potential. In this way we are able to enhance the deposition rate to $\sim 10\mu$m min^{-1}, which is ten times larger than usually reported values. We also present a systematic comparative study on the fabrication of Ni NW and NT arrays with small diameters (~ 50 nm), by monitoring the deposition current density transients during potentiostatic electrodeposition in NpATs. A new fabrication step is introduced in the membranes' preparation procedure, prior to the NTs' electrodeposition process, allowing us to produce small diameter NT arrays (~ 30 nm).

The magnetic properties of highly ordered hexagonal arrays of Ni and Co NWs and NTs are also presented. In particular, we describe a systematic comparative study on the magnetization reversal processes in ordered NW and NT arrays with different diameters ($30 - 65$ nm). For this study we performed analytical calculations and experimental measurements of the angular dependence of the coercivity. From the good agreement between the two, we can determine the reversal modes in NW and NT arrays. The magnetization of Ni and Co NW and small NT (< 50 nm) arrays is found to reverse by the nucleation and propagation of a transverse domain wall. On the other hand, for Ni and Co NT arrays, a non-monotonic behavior occurs above a diameter of ~ 50 nm, revealing a transition between vortex and transverse reversal modes.

The magnetic interactions between the NWs and NTs grown in the NpAT were measured using first-order reversal curves (FORCs). This method is being currently employed for the study of interactions between individual nanoelements of an array, such as NPs or NWs. In this thesis, we used the FORC method to characterize the magnetic interactions present in Co NW and NT arrays. The diameter of the NWs/NTs was varied between $40 - 65$ nm, while the center-to-center distance was kept constant at 105 nm. In both NW and NT arrays, the magnetic interactions were found to increase with the diameter of the NWs/NTs, exhibiting higher values for NW arrays.

In this thesis we also present experimental evidence of exchange-bias (EB) coupling in core-shell nanotubular structures, along both the parallel and perpendicular directions of applied magnetic field. Ordered arrays of Co NTs with outer diameters of $\sim$ 40 nm were left in air for natural oxidation of their inner walls, forming concentric NTs with a ferromagnetic (FM) Co outer shell and an antiferromagnetic (AFM) CoO inner shell. Temperature and field-cooling dependence of the EB effect is here presented, along with the training effect of EB at 6 K. The Co/CoO NTs are found to have a maximum blocking temperature (T_B) at $\sim$ 220 K, which is $\sim$ 70 K below the Néel temperature of bulk CoO (293 K). The training effect is fitted using a recursive formula proposed by Binek, giving small values for the characteristic decay rate of the training behavior, which can be interpreted as the existence of a stronger coupling between the AFM/FM layers that are shaped into a core-shell nanotubular structure, when compared with flat interfaces. Bimodal T_B-distributions are also obtained, along both parallel and perpendicular directions, while the low-temperature peak is ascribed to interfacial spin-glass phases, the high-temperature peak is attributed to the thermally activated reversal of the AFM grains.

Finally, we describe the synthesis of NiO nanoparticles with tuned sizes, ranging from 12 to 70 nm, using a sol-gel method. The magnetic characterization shows an increase in T_B with the diameter of the NPs and an increase in the effective magnetic anisotropy (K_{eff}) with decreasing particle size. The number of uncompensated spins per NP is estimated, allowing us to infer that their majority is randomly distributed on the NP surface. For small diameters ($<$ 30 nm) we calculated the surface anisotropy constant using a model that describes the evolution of K_{eff} with particle size. Coercivity enhancement, exchange-bias effect and training of EB, is also observed for the smaller NPs, after field-cooling from 300 to 6 K. These results demonstrate the existence of uncompensated spins with FM correlations at the surface of the NP coupled to the AFM core, therefore exhibiting an EB behavior similar to the one observed in FM/AFM bilayers.

At the end of the thesis, we also present several ongoing research works, including (i) the use of ferromagnetic resonance to probe the quality of the Ni and Co NW and NT arrays electrodeposited; (ii) the fabrication and characterization of NiO NW arrays by template filling sol-gel method; and (iii) the use of two different methods to electrically access a single NT, either by nanolithography on a dispersed NT on top of a substrate, or by depositing an extra Au layer on top of the NpAT and monitoring the deposition current until the first NT/NW reaches the top. The methods presented in (iii) will allow the study of the resistive and magneto-resistive properties of the fabricated NTs.

Resumen

Los nanomateriales magnéticos son objeto de un considerable interés por sus propiedades únicas y sus potenciales aplicaciones, que van desde dispositivos magnéticos de almacenamiento/grabación de información, sensores y *chips* biomédicos, hasta agentes de contraste en imágenes por resonancia y portadores de fármacos. Existen aún diversos retos científicos asociados con la fabricación de grandes áreas de nanoestructuras magnéticas altamente ordenadas y la comprensión exacta de su comportamiento magnético. El uso de un método de fabricación mediante una plantilla nanoporosa, ha despertado un gran interés y muestra mucho potencial, ya que permite el crecimiento de las matrices de nanoimán altamente ordenadas con un grande rendimiento y un bajo coste. Además, la combinación de diferentes técnicas de llenado, como sol-gel y métodos de electrodeposición, aumenta la diversidad de nanoestructuras que se pueden producir [nanohilos (NHs) y nanotubos (NTs) homogéneos, concéntricos o multisegmentados], dando la posibilidad de generar una mayor variedad de respuestas magnéticas.

En esta tesis se describe la síntesis y caracterización de nanopartículas (NP), NHs, NTs y sus matrices hexagonales ordenadas, por técnicas de sol-gel y de electrodeposición potenciostática, usando plantillas de alúmina nanoporosa (PANs). En primer lugar, se han estudiado en detalle las condiciones óptimas para la electrodeposición potenciostática de NHs de Ni en el interior de las PANs con diámetros de poro de 50 nm, mediante la regulación del potencial aplicado. De esta manera somos capaces de mejorar la tasa de deposición llegando a conseguir tasas de cerca de 10 μm min^{-1}, que son diez veces mayores que los valores reportados generalmente. Se presenta también un estudio comparativo sistemático en la fabricación de matrices de NHs y NTs de Ni con diámetros pequeños ($\sim$ 50 nm), mediante la monitorización de la densidad de corriente de deposición durante la electrodeposición potenciostática en las PANs. Se ha introducido una nueva etapa de fabricación en la preparación de las membranas, antes del proceso de electrodeposición de los NTs, permitiéndonos producir matrices ordenadas de NTs con pequeño diámetro ($\sim$ 30 nm).

Se han analizado las propiedades magnéticas de las matrices hexagonales altamente ordenadas de NHs y NTs de Ni y Co. En particular, se describe un estudio comparativo sistemático de los procesos de reversión de la magnetización en matrices de NHs y NTs con diferentes diámetros (30$-$65 nm). Para este estudio se han realizado cálculos analíticos y mediciones experimentales de la dependencia angular de la coercividad. Teniendo en cuenta la alta concordancia entre los datos teóricos y experimentales, podemos estimar los modos de inversión en las matrices de NHs y NTs. La imanación de las matrices de NTs (con diámetros $<$ 50 nm) y NHs de Ni y Co, se invierte por la nucleación y propagación de una pared de dominio del tipo transversal. Por otro lado, para las matrices de NTs de Ni y Co, se produce un comportamiento no-monotónico por encima de un diámetro de $\sim$ 50 nm, revelando una transición entre los modos de reversión del tipo vórtice y transversal.

Las interacciones magnéticas entre los NHs y NTs, fabricados en las PANs, se han medido utilizando las curvas de reversión de primer orden (CRPOs). Este método está siendo altamente utilizado para el estudio de las interacciones entre nanoelementos individuales de una matriz, tales como NPs o

NHs. En esta tesis, se ha utilizado el método CRPO para caracterizar las interacciones magnéticas presentes en las matrices de NHs y NTs de Co. El diámetro de los NHs/NTs varió entre $40 - 65$ nm, manteniendo una distancia entre sus centros de 105 nm. En ambas matrices de NHs y NTs, las interacciones magnéticas aumentan con el diámetro de los NHs/NTs, mostrando valores más altos para las matrices de NHs.

En esta tesis se presenta también la evidencia experimental del efecto de *exchange-bias* (EB) en estructuras núcleo-corteza nanotubulares, a lo largo de las direcciones paralela y perpendicular del campo magnético aplicado. Matrices ordenadas de NTs de Co con diámetros externos de ~ 40 nm se han expuesto al aire para la oxidación natural de sus paredes interiores, formando NTs concéntricos con una corteza exterior ferromagnética (FM) de Co y una corteza interior antiferromagnética (AFM) de CoO. Apreciamos la variación del efecto de EB con la temperatura y el campo de enfriamiento, junto con el efecto de *training* del EB a 6 K. Los NTs de Co/CoO estudiados, presentan una temperatura máxima de bloqueo ($T_B \sim 220$ K), que es cerca de 70 K más baja que la temperatura de Néel del CoO (293 K). El efecto de *training* se ha ajustado utilizando una fórmula recursiva propuesta por Binek, dando como resultado valores pequeños para la tasa característica de disminución del efecto de *training*, que puede interpretarse como la existencia de un acoplamiento más fuerte entre las capas AFM/FM cuando están conformadas en una estructura de núcleo-corteza nanotubular. Hemos obtenido también una distribución bimodal de T_B a lo largo de las dos direcciones paralela y perpendicular. El pico de baja temperatura puede ser atribuido a fases de *spin-glass* interfaciales, mientras que el pico de alta temperatura se atribuye generalmente a la reversión térmica de los granos AFM.

Finalmente, se describe la síntesis de nanopartículas de NiO con tamaños de 12 a 70 nm, utilizando un método de sol-gel. La caracterización magnética muestra un aumento de T_B con el diámetro de las NPs y un aumento de la anisotropía magnética efectiva (K_{ef}) con la disminución del tamaño de partícula. Hemos estimado el número de espines descompensados por NP, lo que nos ha permitido inferir que la mayoría de estos se distribuyen aleatoriamente en la superficie de la NP. Para diámetros pequeños (< 30 nm), se ha calculado la constante de anisotropía de superficie, utilizando un modelo reciente que describe la evolución de los K_{ef} con el tamaño de partícula. Se observa también un aumento en la coercividad, un efecto de *exchange-bias* y de *training* en las NPs más pequeñas, después de aplicar campo de enfriamiento desde 300 hasta 6 K. Estos resultados demuestran la existencia de espines descompensados con correlaciones FM en la superficie de la NP acoplados al núcleo AFM, mostrando un comportamiento EB similar al observado en bicapas FM/AFM.

Al final de la tesis presentamos algunos resultados preliminares sobre (i) el uso de la técnica de resonancia ferromagnética para estudiar la calidad de los NHs y NTs de Ni y Co electrodepositados; (ii) la fabricación de matrices de NHs de NiO en PANs, con el método sol-gel; y (iii) el uso de dos diferentes técnicas para acceder a un solo NT, ya sea mediante nanolitografía de contactos sobre un NT disperso en un sustrato, o depositando una capa adicional de Au en la parte superior de la PAN y monitorizando la corriente de deposición hasta que el primero NT/NH alcance la parte superior. Estos métodos permitirán estudiar las propiedades resistivas y magneto-resistivas de los NTs fabricados.

Contents

Abstract **xiii**

Thesis Outline **5**

1 Introduction **9**
1.1 Nanotechnology . . . 9
1.2 Magnetism at the Nanoscale . . . 11
1.2.1 2D Nanomaterials: Thin Films . . . 14
1.2.2 1D Nanomaterials: Nanowires and Nanotubes . . . 15
1.2.3 0D Nanomaterials: Nanoparticles . . . 23
1.3 Nanofabrication . . . 24
1.3.1 Nanoparticles . . . 25
1.3.2 Nanowires and Nanotubes . . . 27
Bibliography . . . 36

2 Growth of Ni Nanowires and Nanotubes in Nanoporous Alumina Templates **47**
2.1 Article I – Ni Growth inside Ordered Arrays of Alumina Nanopores: Enhancing the Deposition Rate . . . 48
2.1.1 Introduction . . . 48
2.1.2 Experimental . . . 50
2.1.3 Results and Discussion . . . 51
2.1.3.1 Linear Sweep Voltammetry . . . 51
2.1.3.2 Electrodepositions at Different Potentials . . . 53
2.1.3.3 Structural and Morphological Properties . . . 55
2.1.3.4 Magnetic Properties . . . 56
2.1.4 Conclusions . . . 59
Bibliography . . . 59
2.2 Article II – Distinguishing Nanowires and Nanotubes Formation by the Deposition Current Transients . . . 65
2.2.1 Background . . . 65
2.2.2 Methods . . . 66
2.2.3 Results and Discussion . . . 68
2.2.3.1 Structural and Morphological Properties . . . 68
2.2.3.2 Current Transients during Deposition . . . 70
2.2.3.3 Magnetic Properties . . . 73
2.2.4 Conclusions . . . 74
Bibliography . . . 75

3 Magnetization Reversal in Ordered Arrays of Nanowires and Nanotubes 81
3.1 Article III – Crossover Between Magnetic Reversal Modes in Ordered Ni and Co Nanotube Arrays . . . 82
3.1.1 Introduction . . . 82
3.1.2 Experimental Details . . . 83
3.1.3 Results and Discussion . . . 84
3.1.4 Conclusions . . . 88
Bibliography . . . 88
3.2 Article IV – Magnetization Reversal in Electrodeposited Co Nanowire and Nanotube Arrays with Different Diameters . . . 92
3.2.1 Introduction . . . 92
3.2.2 Experimental Details . . . 94
3.2.3 Results and Discussion . . . 95
3.2.4 First Order Reversal Curves . . . 95
3.2.4.1 Magnetization Reversal . . . 99
3.2.5 Conclusions . . . 102
Bibliography . . . 102

4 Exchange Bias in Ordered Arrays of Co/CoO Nanotubes 107
4.1 Article V – Exchange Bias, Training Effect and Bimodal Distribution of Blocking Temperatures in Electrodeposited Core-Shell Nanotubes . . . 108
4.1.1 Introduction . . . 108
4.1.2 Experimental Details . . . 109
4.1.3 Results and Discussion . . . 110
4.1.3.1 Exchange-bias Coupling in Co/CoO NTs . . . 110
4.1.3.2 Training Effect of Exchange Bias . . . 114
4.1.3.3 Bimodal Distribution of Blocking Temperatures . . . 116
4.1.4 Conclusions . . . 117
Bibliography . . . 118

5 Superparamagnetic Nanoparticles 123
5.1 Article VI – Size and Surface Effects on the Magnetic Properties of NiO Nanoparticles 124
5.1.1 Introduction . . . 124
5.1.2 Experimental . . . 125
5.1.3 Results and Discussion . . . 126
5.1.4 Conclusions . . . 133
Bibliography . . . 133

6 Work in Progress 139
6.1 Comparative Study on Arrays of Magnetic Nanowires and Nanotubes by Ferromagnetic Resonance . . . 139
6.1.1 Ni Samples . . . 141
6.1.2 Co Samples . . . 143
6.2 NiO Nanowires by Sol-gel Template Filling . . . 144
6.3 Accessing a Single Nanotube . . . 147
6.3.1 Nanocontacts by Focused Ion- and Electron-beam Lithography . . . 148
6.3.2 Monitoring the Electrodeposition Current . . . 149
Bibliography . . . 150

7 Conclusions and Perspectives **155**

List of Publications **159**

List of Abbreviations **161**

List of Tables **163**

List of Figures **165**

Thesis Outline

The advances in nanotechnology and the miniaturization of devices demand a continuous search for new materials and an improved understanding of the interesting physical phenomena that emerge at reduced scales. Recent discoveries of unique magnetic properties exhibited when a materials' size is reduced to the nanoscale, have prompt the scientific and engineering communities to develop novel applications in various fields, such as magnetic sensors, storage devices, resonance imaging and biomedical chips.

The major aim of this thesis is to enlarge the understanding of the magnetic properties of nanomaterials, namely nanoparticles (NPs), nanowires (NWs) and nanotubes (NTs), searching for new phenomena at the nanoscale. In particular, one way to improve magnetic information recording and storage is to increase bit density, usually described as an array of nanomagnets. Therefore, in this thesis we also study the magnetic properties of ordered NW and NT arrays, aiming a better understanding of the influence of interwire coupling in the overall magnetic properties.

Nanoparticles (NPs) are characterized by their small sizes, typically in the order of $1-100$ nm. Magnetic NPs are highly attractive for biomedical applications, ranging from magnetic assisted drug delivery methods to magnetic resonance imaging techniques as contrast agents. Very small magnetic NPs ($\sim$ 10 nm) can behave as single-domain nanomagnets exhibiting superparamagnetic behavior, where thermal fluctuations are able to switch their magnetization state. Additionally, due to the increased surface-to-volume ratio present in a NP, surface spins will highly affect its magnetic properties. In particular, antiferromagnetic materials, which have a zero net magnetization at the macroscale, can exhibit weak ferromagnetism when reduced to the nanoscale, due to the presence of uncompensated spins at their surface.

Nanowires (NWs) or high aspect ratio NPs, have an increased shape anisotropy, allowing an additional parameter to be tuned when controlling their magnetic response. High aspect ratio NWs have proved to be potential candidates for applications in magnetic storage devices, as they exhibit high remanence and coercivity along their long axis and much smaller ones when applying the external magnetic field in the perpendicular direction. The recent ability to control the motion of magnetic domain walls along a NW has been revolutionizing the research and technology developments on magnetic storage devices. This new concept, called racetrack memory, consists in the use of magnetic domains in NWs as the memory elements, and to move these elements along the NW by applying

pulsed currents. Intense research in this field is ongoing, as its accurate understanding is of extreme importance for the implementation of actual devices.

Nanotubes (NTs) have an additional degree of freedom given by their empty core. The tubular structure provides also different magnetic responses, in particular with the angle of the applied external magnetic field. Due to the inexistence of a magnetic core in their center, magnetization reversal will take place differently than in NWs. Magnetic NTs show other important advantages over NWs, as their hollow inner core can be coated, functionalized, oxidized or filled with different materials, increasing the potential applicability of such nanostructures and respective magnetic properties.

Ordered Arrays of NWs and NTs are highly interesting systems due to their potential applicability in areas such as magnetic storage, sensors, renewable energy systems and filtration devices. For the fabrication of ordered NW/NT arrays, the use of nanoporous alumina membranes as templates for subsequent filling has proved to be a high yield and low cost attractive technique. An important characteristic feature of nanoporous alumina templates (NpATs) is the ability to easily tune the pore sizes (length and diameter) and the interpore distances, by the Al anodization conditions. Additionally, the possibility to use many different methods of pore filling inside the nanopores, such as atomic layer deposition, sol-gel and electrodeposition techniques, allows one to control the crystallographic structures, chemical compositions and shapes of the nanomaterials deposited, enabling a wide diversity of nanoelement arrays to be produced.

This thesis reports the work made on the synthesis and characterization of NiO antiferromagnetic NPs by sol-gel methods, and ordered arrays of Ni, NiO, Co and Co/CoO NWs and NTs using template sol-gel and potentiostatic electrodeposition filling methods in NpATs. The work has been performed in collaboration between the research group of *Multifunctional Magnetic Materials and Nanostructures* (MMMN) from the *Instituto de Física dos Materiais da Universidade do Porto* (IFIMUP-IN – Institute of Nanoscience and Nanotechnology) led by Prof. João Pedro Araújo, and the research *Group of Nanomagnetism and Magnetization Processes* (GNMP) from the *Instituto de Ciencia de Materiales de Madrid* (ICMM) of the *Consejo Superior de Investigaciones Científicas* (CSIC) led by Prof. Manuel Vázquez Villalabeitia. Nevertheless, we should also emphasize the number and intensity of collaborations with other groups, namely, the team at *Departamento de Química* from the *Universidade de Trás-os-Montes e Alto Douro* in Vila Real (led by Prof. Pedro Tavares) who performed the transmission electron microscopy images; the team at *Dipartimento di Chimica, Materiali ed Ingegneria Chimica "G. Natta"* from *Politecnico di Milano* (Prof. Luca Magagnin and Dr. Paula Cojocaru) who helped in understanding electrochemical deposition and oxidation processes; the team at the *Instituto de Ciencia de Materiales de Aragón* in Zaragoza (Prof. José Maria de Teresa and Dr. César Magen) who supported the final study on individual NTs; the team at the University of Santiago de Chile (Prof. Juan Escrig) who performed the analytical calculations and modeling; and the team at the University of Aveiro (Prof. Nikolai Sobolev and Dr. Andrey Timopheev) who carried out the ferromagnetic resonance measurements.

The work developed in this thesis was only possible after the implementation and development of several new experimental techniques for the synthesis of NPs, NWs and NTs. In particular, NPs were produced for the first time, both at the research laboratories of MMMN (at IFIMUP-IN) and GMNP (at ICMM-CSIC), using optimized sol-gel methods. A new approach to the fabrication of ordered arrays of magnetic NTs was also implemented for the first time, in the two host research groups, using an optimized potentiostatic electrodeposition method to fill the nanoporous alumina templates. Most of the techniques found in the literature on the fabrication of magnetic NTs using nanopores' filling by electrodeposition methods only allow the growth of large diameter NTs (> 200 nm). In this thesis, we implemented a new step in the membrane preparation, prior to the electrodeposition method, that allowed us to fabricate NT arrays with diameters as small as ~ 30 nm.

The thesis is structured in seven Chapters, and comprises an introduction, four Chapters with the main results and discussions organized as a compilation of research works, a Chapter presenting several ongoing works and the final conclusions and future perspectives, as follows:

- The first Chapter introduces the field of nanotechnology, focusing on the magnetic properties of nanomaterials, namely thin films (two-dimensional; 2D), nanowires and nanotubes (one-dimensional; 1D), and nanoparticles (zero-dimensional; 0D). In this Chapter we also present a brief description on the bottom-up nanofabrication techniques used, in particular, the template filling sol-gel and electrodeposition methods, in nanoporous alumina membranes.

- Chapter 2 describes the optimization methods developed for the potentiostatic electrodeposition of Ni NW and NT arrays in NpATs. The results are separated in two recent publications: Article I, on the control of the deposition rate of NWs by the applied electrodeposition potential; and Article II, on the comparative study of the potentiostatic deposition of NWs and NTs analyzing the deposition current transients.

- In Chapter 3, we present a systematic comparative study on the magnetic properties of Ni and Co NW and NT arrays with different diameters. This Chapter is composed of Article III, where the magnetization reversal processes in NW and NT arrays are studied by angular dependent coercivity measurements; and Article IV, where we analyze the magnetic interactions in NW and NT arrays with different diameters using the first-order reversal curve method.

- In Chapter 4 we present for the first time exchange bias effects in Co/CoO NT arrays. In this Chapter, a systematic study on the temperature and field cooling dependence of exchange bias, training effect and bimodal distribution of blocking temperatures is described, and the results presented as Article V.

- In Chapter 5, composed of Article VI, NiO nanoparticles are prepared by the sol-gel method and the corresponding magnetic properties studied as a function of their size. These were found to exhibit superparamagnetic behavior at room temperature, when smaller than 30 nm, and exchange bias effects at 6 K, due to the coupling between the antiferromagnetic core and uncompensated spins with ferromagnetic correlations at the surface.

- Finally, Chapter 6 gives a brief presentation of the several research works currently being developed, namely, the use of ferromagnetic resonance measurements to probe the quality of the NWs and NTs grown inside the NpATs; the fabrication of NiO NW arrays by sol-gel template filling; and the implementation of two different techniques to access a single NT, either by lithography of nanocontacts on dispersed NTs, or by using an extra gold contact on top of the NpAT enabling us to stop the NT growth when the first NT reaches the top, by just monitoring the electrodeposition current.
- The main conclusions and perspectives are summarized in Chapter 7.

This thesis is based on the following publications:

Article I – *Ni Growth inside Ordered Arrays of Alumina Nanopores: Enhancing the Deposition Rate*, M. P. Proenca, C. T. Sousa, J. Ventura, M. Vazquez, and J. P. Araujo, Electrochimica Acta 72 (2012) 215-221;

Article II – *Distinguishing Nanowires and Nanotubes Formation by the Deposition Current Transients*, M. P. Proenca, C. T. Sousa, J. Ventura, M. Vazquez, and J. P. Araujo, Nanoscale Research Letters 7 (2012) 280;

Article III – *Crossover Between Magnetic Reversal Modes in Ordered Ni and Co Nanotube Arrays*, M. P. Proenca, C. T. Sousa, J. Ventura, J. P. Araujo, J. Escrig, and M. Vazquez, SPIN, accepted, DOI: 10.1142/S2010324712500142;

Article IV – *Magnetic Interactions and Reversal Mechanisms in Co Nanowire and Nanotube Arrays*, M. P. Proenca, C. T. Sousa, J. Escrig, J. Ventura, M. Vazquez, and J. P. Araujo, submitted to Journal of Applied Physics;

Article V – *Exchange Bias, Training Effect and Bimodal Distribution of Blocking Temperatures in Electrodeposited Core-Shell Nanotubes*, M. P. Proenca, J. Ventura, C. T. Sousa, M. Vazquez, and J. P. Araujo, submitted to Physical Review B;

Article VI – *Size and Surface Effects on the Magnetic Properties of NiO Nanoparticles*, M. P. Proenca, C. T. Sousa, A. M. Pereira, P. B. Tavares, J. Ventura, M. Vazquez, and J. P. Araujo, Physical Chemistry Chemical Physics 13 (2011) 9561–9567.

Chapter 1

Introduction

This Chapter starts with a brief introduction to nanotechnology, presenting a summary of the most important works that boosted its development. We then evidence the importance of studying materials at the nanoscale, as new properties emerge when their size is reduced, surface atoms become increasingly important, and quantum and proximity effects gain particular relevance. In particular, we focus on the interesting magnetic properties of nanoscaled materials. Such nanomaterials may be divided in three different categories depending on their dimensionality reduction: 2D (thin films), 1D [nanowires (NWs) and nanotubes (NTs)] and 0D [nanoparticles (NPs)]. As a major part of the work presented in this thesis is related to specific magnetic behaviors found in NPs, NWs, NTs and their arrays, in this Chapter we present a more detailed explanation of some of the magnetic properties that will be discussed throughout the thesis. In particular, we give a short description of magnetization reversal modes (here studied by analytical calculations), and magnetostatic interactions (studied by first-order reversal curves), in NWs, NTs and their ordered arrays. The Chapter ends with a description of several nanofabrication techniques, emphasizing the use of chemical bottom-up methods to fabricate NPs, NWs, NTs and their ordered arrays inside nanoporous templates.

1.1 Nanotechnology

Nanotechnology is commonly defined as the controlled synthesis, manipulation, modeling and characterization of materials, devices and systems at the nanoscale [1]. Driven by the desire to explore and understand the unique properties that emerge when the size is reduced, together with the investigation of potential applications of nanosized materials and devices, nanotechnology has gained increased attention during the last years [2, 3].

Nanotechnology requires the optimization of fabrication techniques to prepare nanomaterials, and of measuring techniques that allow the discovery of new effects in nanoscience. One of the first impulses for the research of materials at the nanoscale appeared in the 1930's with the invention of the field emission microscope, allowing the visualization of near-atomic resolution images of

materials [4]. Ten years latter, the first semiconductor transistor was built, greatly expanding the scientific knowledge of semiconductor interfaces, and propelling the design and fabrication of electronic devices [Fig. 1.1(a)]. In the 1950's, the first atoms were successfully imaged using a field ion microscope [5]. With the invention of the scanning tunneling and atomic force microscopies in the 1980's, the manipulation of materials down to a fraction of a nanometer in size became possible. So in 1989, IBM researchers were able to manipulate for the first time 35 individual atoms of Xenon, writing the logo of IBM using a scanning tunneling microscope [Fig. 1.1(b)] [6]. In the late 1990's, the 'dip-pen' nanolithography was invented, improving the fabrication and reproduction techniques of electronic circuits as well as pattering of biomaterials for cell biology research [Fig. 1.1(c)] [7]. At the beginning of this millennium, many consumer products that appeared in the market were already making use of nanotechnology, such as scratch-resistant glass coatings, faster-recharging batteries, improved displays for televisions, cell phones and digital cameras, nano-silver antibacterial socks, deep-penetrating therapeutic cosmetics and stain-resistant clothing [4]. In 2006, the first nanoscale car was built, with four spherical C60 fullerene (buckyball) wheels that would turn in response to increases in temperature, making the nanocar move on a gold surface [Fig. 1.1(d)] [8]. In February 2012, the first single-atom transistor was demonstrated using a combination of scanning tunneling microscopy and hydrogen-resist lithography [9].

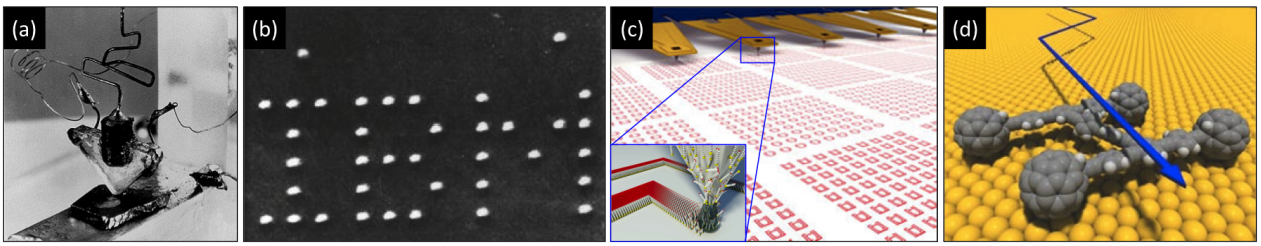


Figure 1.1: (a) The first transistor, developed in 1947, which is a point-contact device roughly one centimeter across [10]. (b) IBM logo written using 35 Xenon atoms arranged in a Ni surface by a scanning tunneling microscope [6]. Schematic representations of (c) 'dip-pen' nanolithography [7] and (d) nanocar with turning buckyball wheels [11].

The fast growing need for the miniaturization of devices has been driving the development of nanotechnology to reach the precise synthesis, characterization and manipulation of materials at the atomic scale. Additionally, nanotechnology has a multidisciplinary nature, requiring the understanding of distinctive scientific areas and propelling research advances in many different fields.

When the size of a material is reduced, the surface-to-volume ratio becomes increasingly important. In Fig. 1.2, a representative scheme illustrates the great importance played by surface area at the nanoscale. Considering a 1 x 1 x 1 cm cube, its volume is equal to 1 cm^3 and the corresponding surface area is 6 cm^2. However, if we consider 10^7 individual nanocubes with 1 x 1 x 1 nm in size, the total volume is still 1 cm^3 but the surface area is now increased to 6 x 10^7 cm^2. The same amount of material, divided into nanosized objects, has now a surface area more than a million times higher. This characteristic of nanomaterials is very important for applications, as the increase in surface area will increase the amount of material that can come into contact with the surrounding elements, thus

affecting their reactivity. In nanoengineered batteries, fuel cells and catalysts, the enhanced reactivity at the nanoscale can be potentially used to fabricate cleaner, safer and more efficient devices for energy storage and production [12, 13]. Nanostructured membranes and materials with large surface areas are also potential candidates for water treatment [14, 15], and for surface functionalization for applications in drug delivery and bioimaging techniques [16, 17].

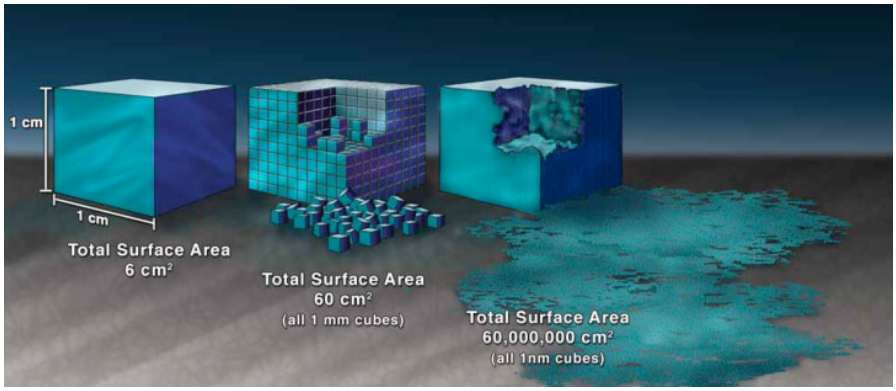


Figure 1.2: Schematic representation of the increased surface area in nanoscaled materials [12].

Nanomaterials

There are three main dimension classes of nanomaterials depending on the number (one, two or three) of dimensions reduced to the nanoscale (Fig. 1.3) [18, 19]. For example, a thin film is a nanomaterial where only one of its three dimensions has been reduced to the nanoscale (2D nanostructures in Fig. 1.3). Magnetic thin films and stacks of magnetic and nonmagnetic layers are considered the heart of many modern magnetic devices, such as spin valves and magnetic tunnel junctions [20]. When two dimensions of a material are reduced to the nanoscale, we fabricate nanowires, nanotubes, nanorods or nanofibers (1D nanostructures in Fig. 1.3). Due to their high shape anisotropy, magnetic nanowires are potential candidates for magnetic storage devices (see Section 1.2). Finally, when we reduce the three dimensions of a material to the nanoscale, we obtain molecular clusters or nanoparticles (0D nanostructures in Fig. 1.3). Magnetic nanoparticles are very attractive for biomedical applications, ranging from magnetic assisted drug delivery methods to forefront imaging techniques [21].

1.2 Magnetism at the Nanoscale

A vast branch of nanotechnology is related to the unique magnetic properties that emerge when the materials' size is reduced to the nanoscale. In modern biology and medicine, magnetic nanomaterials have been widely used for magnetic resonance imaging as contrast agents [21, 23, 24], localized radio-frequency heating [25], cell-manipulation [26, 27] and drug delivery [28, 29]. Favored by the natural nanoscale of biology, the use of magnetic nanomaterials as precise tools for localized treatment, detection and diagnosis of diseases, leading to fewer adverse side-effects, has been highly attractive.

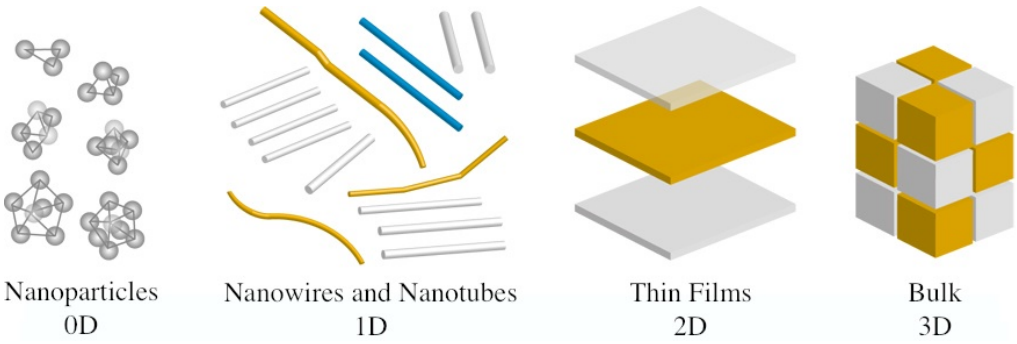


Figure 1.3: Illustrations of the various types of materials by size of their structural elements: 0D (zero-dimensional) nanoparticles; 1D nanowires/nanotubes; 2D thin films; 3D polycrystals. Adapted from [22].

Additionally, since the fundamental discovery of the giant magnetoresistance [30] many spintronic devices have been developed and implemented in our daily life, such as biomedical diagnostic devices (lab-on-a-chip magnetoresistive-based platforms) [31], magnetic sensors [32], read heads of modern hard drives [33, 34], and racetrack memory devices [35, 36]. The latter have been giving special attention in the last years, due to their capability to revolutionize the magnetic storage and read-write technology, creating cheaper storage devices with much higher information densities [35, 37].

Characteristic Length Scales

A fundamental aspect to take into account when reducing the dimension of a material, is the size of critical length scales (Fig. 1.4). When a material is reduced to a size of typically $1 - 100$ nm, its dimensions become comparable to critical length scales of physical phenomena, below which new properties may emerge [20, 38]. One of the elemental magnetic length scales is the exchange length, defined as $L_{ex} = \sqrt{\frac{2A}{\mu_0 M_{Sat}^2}}$, where A is the magnetic stiffness constant, $\mu_0 = 4\pi$ x 10^{-7} N A^{-2} is the vacuum magnetic permeability and M_{Sat} is the saturation magnetization of the magnetic material [20, 39]. The exchange length characterizes the competition between exchange and dipolar energies in a material. It is in the $2 - 10$ nm range for most ferromagnetic materials, and represents the shortest scale on which the magnetization can be twisted in order to minimize the dipolar interaction. Other important length scales include the magnetic domain wall width (transition region between two different magnetic domains, $\delta_w \sim 20 - 130$ nm); the coherence radius (maximum size of a uniformly magnetized particle where magnetization reversal takes place by coherent rotation; $R_{Coh} \sim 10 - 25$ nm); the superparamagnetic blocking radius (below which particles undergo spontaneous thermal fluctuations of the magnetization direction; $R_b \sim 5 - 20$ nm) [20]; and the Imry-Ma domain size (below which the system is in a correlated spin-glass regime) [40]. For transport measurements it is also important to take into account length scales such as the mean free path of the electron, the inelastic scattering length and the spin-diffusion length. These are all in the $1 - 100$ nm range, and represent the mean distances travelled by an electron before it experiences a scattering event that modifies its momentum, energy or spin state, respectively [20].

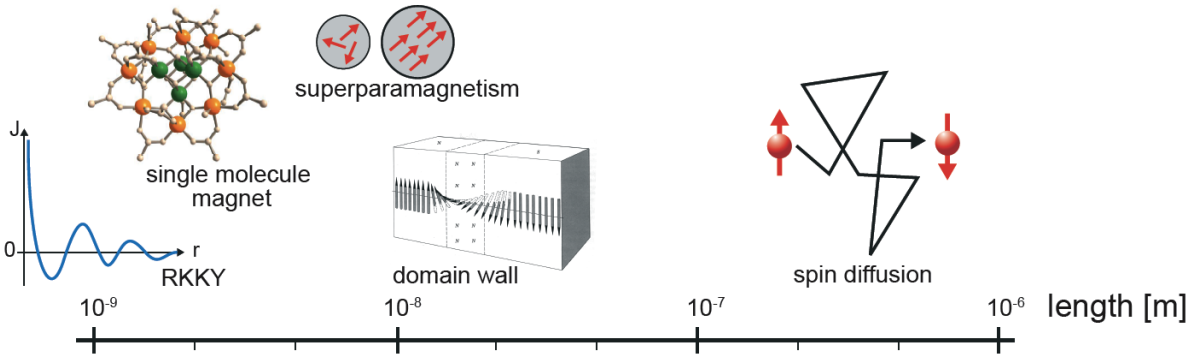


Figure 1.4: Characteristic length scales in magnetism (adapted from [41]).

The combination of the high surface area and the unique properties exhibited by materials reduced to the nanoscale, are of great interest to scientists and engineers making research in nanotechnology. These nanostructures, presenting different properties from conventional materials, can give rise to innovative principles of operation for devices and instruments. Research in this field also stimulates the understanding of the physics of new phenomena and processes at the nanoscale, impelling the development of new modeling and experimental tools, generating new device principles and manufacturing methods [20, 42, 43].

Magnetic Anisotropies

In the study of magnetic materials, one should also take into consideration that most of them have a preferential direction for their magnetic moments to align. This corresponds to the energetically more favorable direction of the spontaneous magnetization and is usually called the easy axis of magnetization. The dependence of the magnetic properties of a material on the direction is determined by the magnetic anisotropies of such material. When considering nanoscaled materials, the importance of these anisotropies in the understanding of the corresponding magnetic properties, is highly increased [20, 38, 44].

The primary sources of magnetic anisotropy are the shape, magnetocrystalline, magnetoelastic and exchange anisotropies. The first one is related to the shape of the material. For non-spherical materials, the demagnetizing field will not be equal in all directions, creating one or more easy axis of magnetization. The magnetocrystalline anisotropy results mostly from the spin-orbit coupling in a material. The crystallographic structure of a material will influence its magnetic response, as some crystallographic directions are preferential for the magnetization alignment. When applying pressure to a material, it may change its magnetization behavior due to stress-induced anisotropy, also called magnetoelastic anisotropy. As for the exchange anisotropy, it is related to the interface interactions between two magnetically ordered systems, thus changing the magnetic properties of the material. For example, when an antiferromagnetic (AFM) material is coupled to a ferromagnetic (FM) material, we have an exchange bias anisotropy (Fig. 1.5). Another case is when coupling a soft magnet to a hard magnet, therefore encountering the exchange spring effect. Some of these anisotropic effects will

be explained in more detail in the next sections, when considering the particular examples of 2D, 1D and 0D nanomaterials [20, 38, 44–46].

1.2.1 2D Nanomaterials: Thin Films

When reducing one of the 3D materials' dimensions to the nanoscale we obtain thin films, in which the critical dimension is defined as the film thickness (δ_{film}). In very thin films, surface anisotropies play a crucial role on the effective magnetic anisotropy of the nanomaterial. The effective magnetic constant of a thin film can be defined as $K_{eff} = K_V + K_S/\delta_{film}$, where K_V and K_S are the volume and surface anisotropies, respectively [20]. An accurate understanding of the nanomaterial's surface contribution is of crucial importance, as it will highly influence the magnetic response of very thin films.

The coupling effect between the surfaces of different materials is also increased at the nanoscale. When we have a multilayer of a FM and an AFM layer, the magnetic response of the system is highly influenced by the exchange bias (EB) coupling between the two different magnetic layers (Fig. 1.5). The EB effect can also be found in 1D and 0D nanomaterials, as will be shown in Chapters 4 and 5, although it is in the 2D nanomaterials that this effect has been mostly studied and reported.

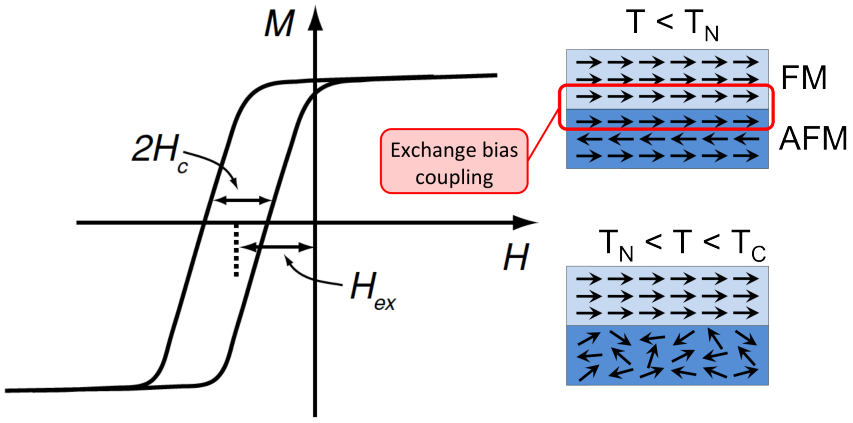


Figure 1.5: Exchange bias effect on the magnetic hysteresis loop of a FM layer coupled to an AFM layer, where H_c, H_{ex}, T_N and T_C, are the coercive and exchange bias fields, and the Néel and Curie temperatures, respectively (adapted from [20]).

Magnetic films and multilayers are intensively used in magnetic recording devices as read and write heads. The interesting coupling behavior found between FM layers separated by a non-magnetic or an AFM spacer, with a few nanometers in thickness, have propelled the development of new devices used in magnetic data storage, sensors and biomedical industries [20, 38]. Figure 1.6 on the left, illustrates the use of a magnetic tunnel junction as a read-head in a hard disk drive. It basically consists of a free magnetic layer, whose magnetization can rotate freely in response to the medium signal field, and a fixed FM layer, whose magnetic moment is "fixed" through an exchange coupling with an AFM layer, and that will act as a reference to the free layer magnetization orientation [34].

For the magnetic storage of data, it is also common to use multilayers of magnetic/non-magnetic materials (Fig. 1.6 on the right), as they allow to retain information even when there is no electric power.

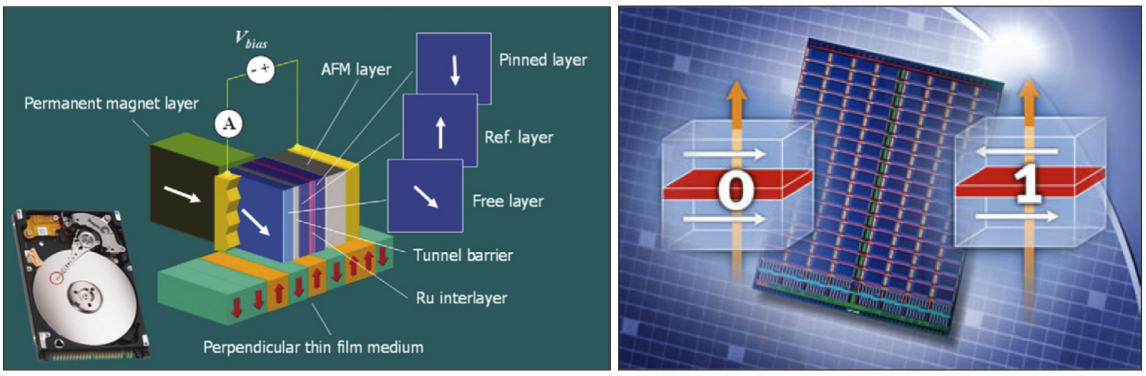


Figure 1.6: (*Left*) Schematic representation of a magnetic tunnel junction read-head in a hard disk drive [34]. (*Right*) Illustration of a conventional memory element design, where the relative orientation of the two magnetic layers will define two different states [47].

1.2.2 1D Nanomaterials: Nanowires and Nanotubes

With the growing need for the miniaturization of devices, the use of nanowires (NWs) for magnetic recording media has gained increased attention in the last years. As previously mentioned, the racetrack memories are revolutionizing the research and technology developments on magnetic storage devices [35]. The racetrack memory is a ferromagnetic NW where the information is stored along the wire, as a sequence of magnetic domains [Fig. 1.7(a)]. Applying short pulses of spin-polarized current, the information patterned can be moved along the NW, reaching the read and write heads [Fig. 1.7(b) and (c)]. The precise control of the movement of magnetic domain walls (DW) along a NW is still under intense investigation, as its accurate understanding is of extreme importance for the implementation of these racetrack memories in new devices [48].

Nanowires and nanotubes (NTs) are potential candidates for applications in magnetic storage devices, sensors, biomedical chips and magnetically assisted drug carriers [25, 28, 29, 51–53]. Their high aspect ratio and large surface areas potentially increase the shape and surface anisotropies of such nanomaterials, providing the discovery and manipulation of unique physical properties that propel future applications. High aspect ratio NWs exhibit high remanence and coercivity values along their long axis. Therefore, they become promising materials for magnetic storage devices, as ordered arrays of NWs could be seen as arrays of bits (0,1), where spins pointing up would be measured as bits 1 and spins facing the opposite direction would be seen as bits 0 (Fig. 1.8).

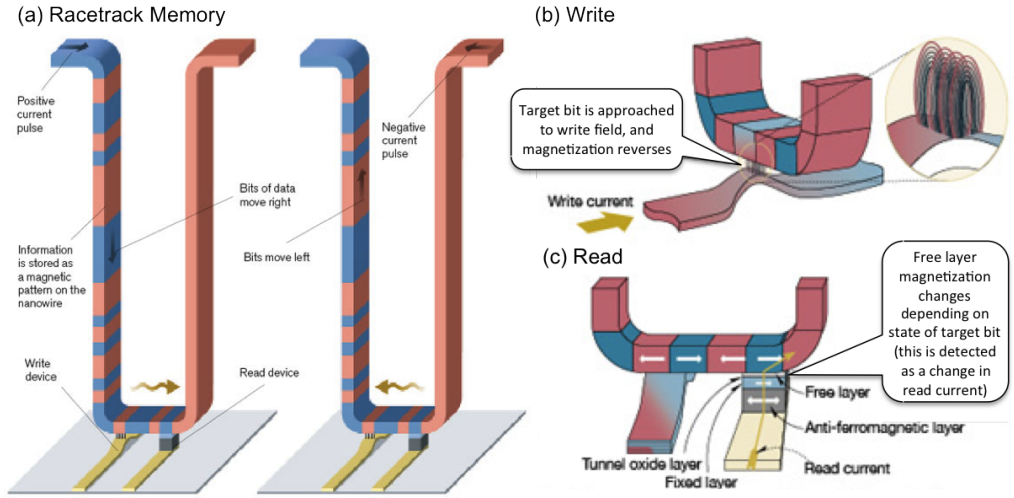


Figure 1.7: Representative diagram of a racetrack memory, evidencing the operating principles of (a) selecting, (b) writing and (c) reading a memory bit. By applying a positive (negative) current pulse to the NW, the magnetic domain walls move to the right (left) in the diagram, controlling in this way the access to the data stored along the wire (adapted from [49, 50]).

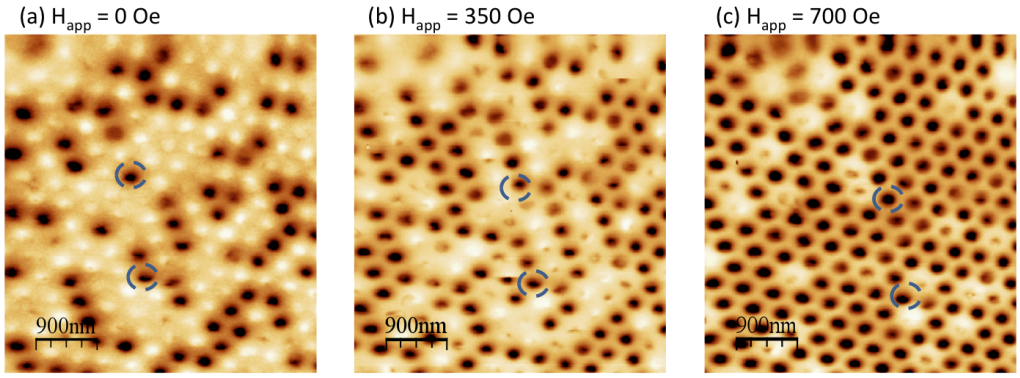


Figure 1.8: Magnetic force microscopy images of an hexagonal ordered array of Ni NWs ($d \sim$ 180 nm) inside a nanoporous alumina template. The white (black) contrast corresponds to NWs with magnetization oriented opposite (equal) to the tip field direction. In (b) and (c) a magnetic field of 350 and 700 Oe, respectively, was applied along the axial direction of the NWs. The increment of the number of black NWs from image (a) to (c) evidences the magnetization reversal of individual NWs by the applied external magnetic field. (Adapted from [54]).

Magnetization Reversal Modes

The major applications of magnetic nanomaterials require a thorough understanding of the magnetization reversal mechanisms. The accurate control of the NWs/NTs geometries, eases the tuning of the magnetization reversal mode by external parameters, such as the direction of the applied magnetic field. For example, Ni NW arrays with diameters of $\sim$ 100 and 50 nm, and lengths of 6 μm, were found to have higher coercivity values when applying the magnetic field perpendicular and parallel to the long axis, respectively [55]. In Chapter 3 we will also show that Ni and Co NT

arrays with diameters of $\sim$ 60 nm exhibit higher coercivity values for a particular angle of applied magnetic field, different from the parallel or perpendicular directions. This behavior is related to the different magnetization reversal processes that can occur in a NT or NW array.

Three main magnetization reversal modes in a cylindrical geometry have been proposed: coherent mode (C), where all magnetic moments rotate coherently and simultaneously; transverse mode (T), where spins rotate progressively by the nucleation and propagation of a transverse domain wall (DW) of width w_T; and vortex mode (V), where a vortex DW of width w_V nucleates and propagates (Fig. 1.9) [56, 57].

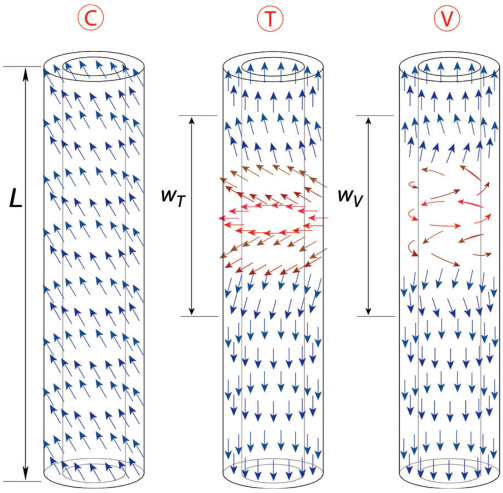


Figure 1.9: Magnetization reversal modes: coherent (C), transverse (T) and vortex (V) modes [57]. w_V and w_T represent the domain wall widths of a vortex and a transverse DW, respectively.

For a better understanding of the magnetization reversal processes in a NW/NT geometry, analytical calculations of the angular dependence of coercivity have been previously developed [56, 57]. Stoner and Wohlfarth [58] have reported the angular dependence of the nucleation field for a coherent magnetization reversal:

$$H_n^C = -\frac{2[K_{sh}(L) + K_{mc}]}{\mu_0 M_{Sat}} \frac{\sqrt{1-\alpha^2+\alpha^4}}{1+\alpha^2}, \tag{1.1}$$

where $\alpha = \tan^{\frac{1}{3}}(\theta)$, θ being the angle between the applied magnetic field and the NW/NT axis [see Fig. 1.10(c)], K_{mc} is the magnetocrystalline anisotropy constant, and $K_{sh}(L) = \frac{1}{4}\mu_0 M_{Sat}^2[1-3N_z(L)]$ is the shape anisotropy constant with $N_z(L)$ the demagnetizing factor along the z axis of a NW/NT of length L. For high aspect ratio NTs, the demagnetizing factor was previously obtained by Escrig *et al.* [59] and is given by:

$$N_z(L) = \frac{d}{L(1-\beta^2)} \int_0^\infty \frac{1-e^{-2yL/d}}{y^2}[J_1(y) - \beta J_1(\beta y)]^2, \tag{1.2}$$

where J_1 is the Bessel function of the first kind and order one, and $\beta = {}^{d_i}/_{d}$, where d_i and d are the inner and outer tube diameters, respectively. According to the Stoner-Wohlfarth model [58], the

angular dependence of the coercivity can then be estimated from the nucleation field, by [56]:

$$H_c^C(\theta) = \begin{cases} |H_n^C(\theta)| & 0 \leqslant \theta < \pi/4 \\ 2|H_n^C(\theta = \pi/4)| - |H_n^C(\theta)| & \pi/4 \leqslant \theta \leqslant \pi/2 \end{cases}. \tag{1.3}$$

A coherent magnetization reversal is only expected to occur for very short tubes ($L \approx w_T$), where the creation of a DW would be energetically unfavorable, considering the exchange and dipolar contributions [60]. For high aspect ratio NWs and NTs, the magnetization reversal is made by the nucleation and propagation of a DW, where the spins can rotate by a vortex or a transverse mode. Typical domain wall widths vary from $\sim$ 40 to 100 nm depending on the geometry of the NW/NT [56, 60].

For the T mode, the angular dependence of coercivity was estimated by an adapted Stoner-Wohlfarth model proposed by Escrig *et al.* [61]. This approximation assumes that when we have two high aspect ratio systems, one of them where the magnetization reverses by a transverse DW, and the other one with an effective volume that reverses by coherent rotation, they will both have an equivalent nucleation field. In this way, the nucleation field for the T mode of reversal can be approximated by:

$$H_n^T = -\frac{2[K_{sh}(w_T) + K_{mc}]}{\mu_0 M_{Sat}} \frac{\sqrt{1-\alpha^2+\alpha^4}}{1+\alpha^2}, \tag{1.4}$$

where w_T was used as the length of the region undergoing coherent rotation. The angular dependence of the coercivity can again be estimated by Eq. (1.3).

The nucleation field for the V mode in a finite prolate spheroid was first obtained by Aharoni [62]. Recently, an adapted expression of the angular dependence of the nucleation field for the V mode in tubular structures, has been reported [57, 63], obtaining a system of equations with variables H_n^V and ϕ (angle where the nucleation starts with respect to the tube axis):

$$\begin{cases} H_n^V(\theta)\cos(\theta-\phi) = \big(N_x(L)\sin^2(\phi) + N_z(L)\cos^2(\phi) - \zeta - \xi[3\cos^2(\phi)-1]\big)M_{Sat} \\ H_n^V(\theta)\sin(\theta-\phi) = \left([N_x(L) - N_z(L) + \xi]\frac{\sin(2\phi)}{2}\right)M_{Sat} \end{cases}, \tag{1.5}$$

where $\zeta = \dfrac{4q^2L_{ex}^2}{d^2}$, $\xi = \dfrac{K_{mc}}{\mu_0 M_{Sat}^2}$, and q satisfies [64]:

$$\frac{qJ_0(q) - J_1(q)}{qY_0(q) - Y_1(q)} = \frac{\beta q J_0(\beta q) - J_1(\beta q)}{\beta q Y_0(\beta q) - Y_1(\beta q)}, \tag{1.6}$$

where J_p and Y_p correspond to the Bessel functions of the first and second kind, respectively, and order p. Considering the wire/tube symmetry, one has $N_x = N_y = \frac{(1-N_z)}{2}$. As previously reported [39, 56, 57], in the V mode, the coercivity is very close to the absolute value of the nucleation field, and we can therefore use the approximation $H_c^V = -H_n^V$, for the estimation of the angular dependence of the coercivity.

Figure 1.10 shows the angular dependence of coercivity of Ni NWs and NTs with different diameters, calculated from the previous equations. As illustrated in Fig. 1.10(a), the coercivity obtained from the Stoner-Wohlfarth model [coherent rotation; Eqs. (1.1) and (1.3)] is much higher than the one obtained assuming a transverse DW]Eqs. (1.4) and (1.3)]. The magnetization reversal occurs by the mode that exhibits the lowest values of the coercivity. Therefore, we can estimate that in a Ni NW with $d \sim 50$ nm the magnetization will reverse by the nucleation and propagation of a transverse DW [Fig. 1.10(a)]. However, when increasing the diameter up to ~ 100 nm it is expected to follow a non-monotonic behavior, where two different magnetization reversal processes occur (vortex mode for lower angles of applied field, and transverse or coherent mode at high angles) [Fig. 1.10(b)].

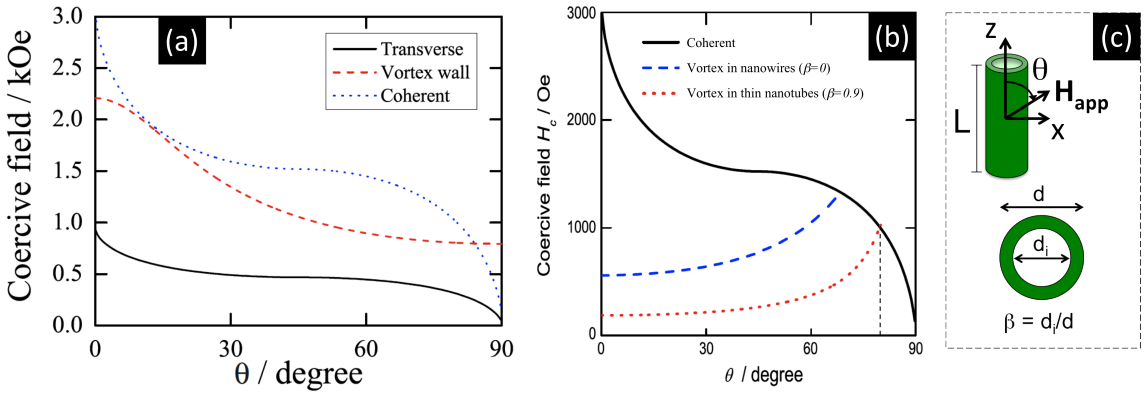


Figure 1.10: Results of the analytical calculations of the angular dependence of coercivity considering a coherent, transverse and vortex mode of magnetization reversal. The calculations were performed for (a) Ni NWs with $d = 50$ nm and $L = 12$ μm; and (b) infinite Ni NWs and NTs with $d = 100$ nm. (c) Geometrical parameters of a nanotube. [(a) and (b) were adapted from [65] and [39], respectively].

First Order Reversal Curves

In the study of an array of nanomagnets it is also important to understand the magnetostatic interactions between individual elements, as they will significantly affect the magnetic properties of the array [66–68]. A simple method for the analysis of the magnetostatic properties of a system (coercivity, remanence, interactions, etc.) is to measure major magnetic hysteresis loops. However, these only provide information regarding the global (average) behavior of the magnetic system. In order to obtain the local magnetostatic properties, using the same experimental set-up for simplicity, Mayergoyz proposed the analysis of multiple minor hysteresis loops, called first-order reversal curves (FORCs) [69]. This technique has proved to be particularly efficient and powerful in the study of highly interacting systems, such as magnetic nanoparticles [70–73] and ferromagnetic NW arrays [66, 74–76].

The FORC method was initially based on the classical Preisach model [77], in which hysteresis was described as a set of elementary processes called "mathematical hysterons" and characterized by a coercive H_c and bias H_u field (Fig. 1.11). Most FORC analysis include several different approaches, either based on physical hypothesis (e.g., the physical analysis model [76]) or on mathematical

distributions (e.g., the moving Preisach model [78]).

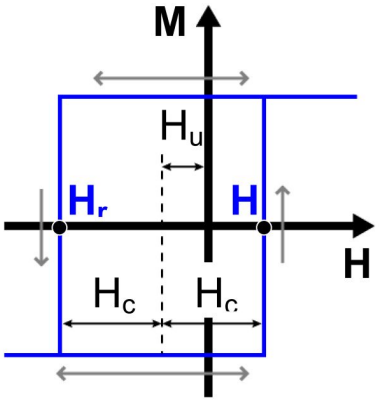


Figure 1.11: Representation of the mathematical hysteron from the classical Preisach model [79].

To perform a FORC measurement one first has to saturate the sample by applying a high positive magnetic saturation field H_{sat}. Then one decreases the applied field H, until it reaches a specific lower field, called reversal field H_r, allowing to switch the magnetization of some hysterons of the system, depending on their H_c and H_u parameters. The magnetization $M(H,H_r)$ is then measured by increasing H from H_r up to a maximum applied field H_{max}, obtaining in this way information on the reversal of a specific amount of hysterons. The minor hysteresis loop measured from H_r to H_{max} is what is known as a first-order reversal curve (FORC). To complete the characterization of the system, H_r is ramped from a minimum applied field H_{min} up to H_{max}, and a set of FORCs are measured starting at each H_r value (Fig. 1.12).

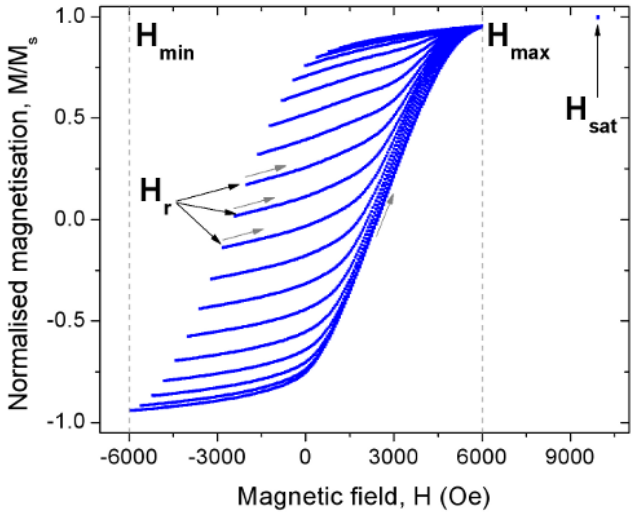


Figure 1.12: Set of first-order reversal curves measured for an array of CoFe NWs with the applied field parallel to the wires' axis [79].

The FORC distribution ρ_{FORC}, which gives information about all the hysterons in the system, is

then obtained by calculating the second-order mixed derivative of $M(H,H_r)$ [79]:

$$\rho(H, H_r) = -\frac{1}{2}\frac{\partial^2 M(H, H_r)}{\partial H \partial H_r} \quad (H > H_r). \tag{1.7}$$

A graphical representation of ρ_{FORC}, called FORC diagram, is illustrated in Figs. 1.13 and 1.14. It consists in a contour plot of ρ_{FORC}, with a scale going from blue (minimum ρ_{FORC}) to red (maximum ρ_{FORC}), indicating the statistical distribution of the mathematical hysterons [79].

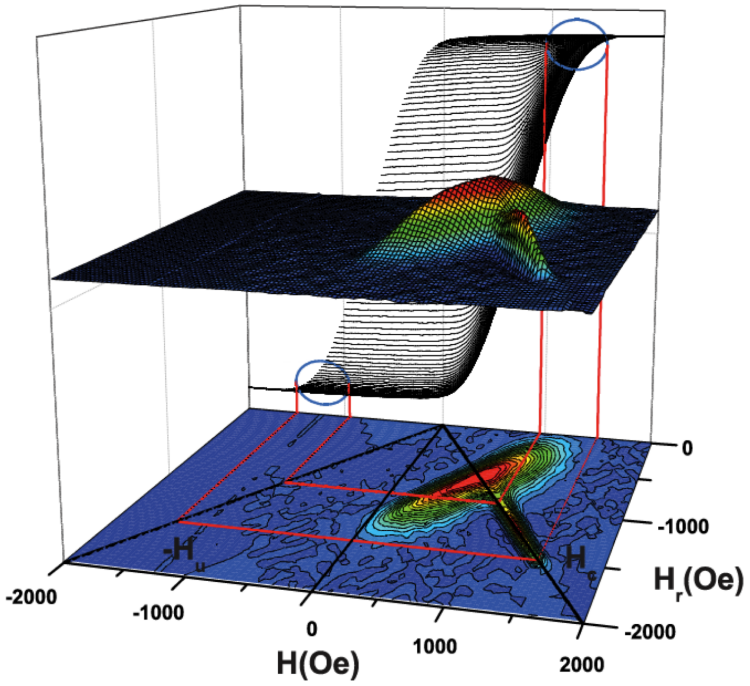


Figure 1.13: Set of FORCs, corresponding FORC 3D distribution (top horizontal panel), and FORC diagram (bottom horizontal panel), measured for an array of Ni NWs with the applied field parallel to the wires' axis [66].

To simplify the analysis of a FORC diagram, it is convenient to perform a change of coordinates, defining a coercive field (H_c) and an interaction field (H_u) axis, by:

$$H_c = \frac{H - H_r}{2}, \quad H_u = -\frac{H + H_r}{2}. \tag{1.8}$$

From a quantitative point of view, one can extract from the FORC diagram the average individual coercivity of easy hysterons (H_c^{FORC}) as the maximum value of ρ_{FORC} at the H_c axis, and the interaction field at saturation (ΔH_u) as the half-width of the FORC distribution elongation parallel to the H_u axis (Fig. 1.14). Using the moving Preisach model [70, 77], that takes into consideration the interactions between the individual magnetic elements, one can approximate the interaction field at saturation as:

$$H_{int,sat} = 2\sigma_{int} - k, \tag{1.9}$$

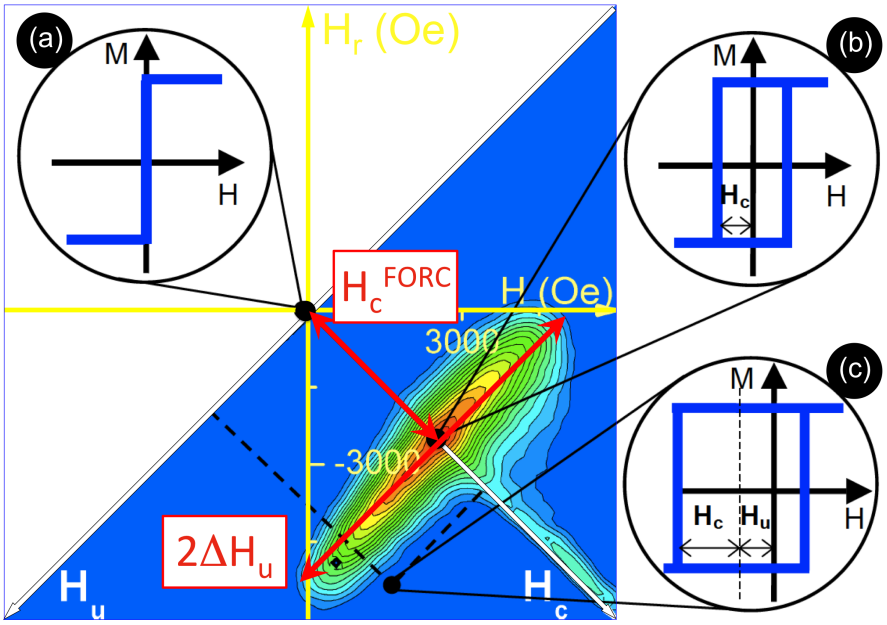


Figure 1.14: FORC diagram illustrating the extraction of H_c^{FORC} and ΔH_u. (a), (b) and (c) are three representations of mathematical hysterons: (a) fundamental hysteron (vertical reversible), (b) and (c) easy hysteron (vertical irreversible). (Adapted from [75]).

where σ_{int} and k are the local and mean interaction fields, respectively [80]. A positive (negative) value of k would correspond to a mean interaction field parallel (antiparallel) to M. For example, an array of high aspect ratio NWs is known to have an antiparallel interaction field (opposite to the magnetization) between each element, due to the strong demagnetizing field produced by the array. This effect can be seen in the FORC diagram as a large elongation of the FORC distribution along the H_u axis [Fig. 1.15(c)].

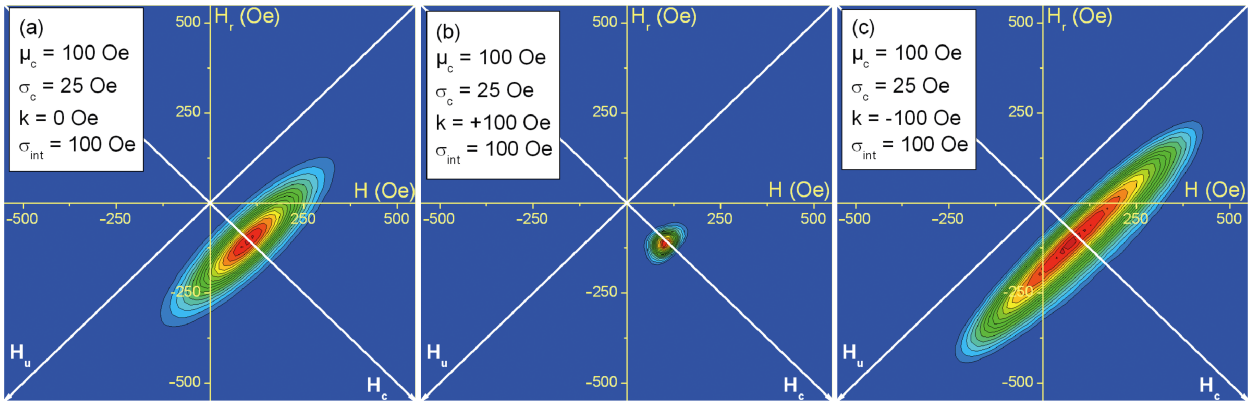


Figure 1.15: Theoretical FORC diagram made with the moving Preisach model, illustrating the effects of the k value for $\sigma_{int} = 100$ Oe: (a) $k = +100$, (b) $k = 0$, (c) $k = -100$ Oe. μ_c and σ_c correspond to theoretical parameter values assumed for the center and width of the coercivity normal distribution, respectively. (Adapted from [80]).

1.2.3 0D Nanomaterials: Nanoparticles

When reducing all three dimensions of an object to the nanoscale we obtain nanoparticles (NPs), also referred to as zero-dimensional nanomaterials. Nanoparticles are characterized by their small sizes, typically in the order of $1 - 100$ nm. As all the dimensions of the material are now reduced, new interesting properties emerge that differ significantly from those observed in bulk materials.

Nanoparticle research is currently an area of intense scientific interest due to a wide variety of potential applications in biomedical, optical and electronic fields [21, 81–83]. For example, gold at the macroscale has the property to reflect light, but when reduced to the nanoscale it can be made to absorb light and turn it into heat. This behavior is explored in nanomedicine by using nanosctructures of gold as miniature thermal machines to kill unwanted cells in the body, such as cancer cells [84]. Additionally, the shape and diameter of the gold NPs determines the wavelengths of the light absorbed, as schematically shown in Fig. 1.16 on the left, so one can tune their sizes and shapes to control the wavelength at which the particles will absorb energy. Another example, shown in Fig. 1.16 on the right, are colloidal suspensions of CdSe NPs. Changing their diameters the suspensions will exhibit different optical properties when illuminated with ultraviolet or visible lights.

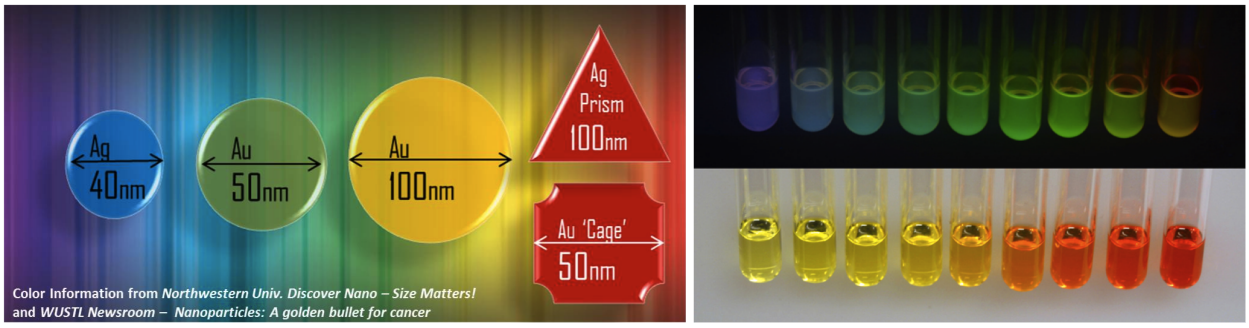


Figure 1.16: (*Left*) Illustration of the influence of nanoparticles' size and shape on the optical properties of the respective suspensions [85]. Colloidal suspensions of CdSe nanoparticles with increasing sizes from left to right, exposed to ultraviolet (top) and ambient (bottom) illumination [86].

When reducing a magnetic material's size to ~ 10 nm, it becomes a single-domain nanomagnet, which can exhibit superparamagnetic (SPM) behavior when the energy barrier Δ for magnetization reversal becomes comparable to the thermal energy $k_B T$ (where $k_B = 1.38066 \times 10^{-23}$ J K^{-1} is the Boltzmann constant, and T is the temperature) [20, 87]. In very small NPs, the characteristic time for the spins to randomly flip, known as the Néel relaxation time τ_N, is given by:

$$\tau_N = \tau_0 \exp\left(\frac{\Delta}{k_B T}\right), \tag{1.10}$$

where τ_0 is the SPM relaxation time ($10^{-9} - 10^{-10}$ s). τ_N is usually much lower than the typical measurement times ($\tau_m \sim 10$ s for SQUID measurements), so when measuring SPM NPs at room

temperature these will exhibit an average zero magnetization value. However, at temperatures low enough so that k_BT is no longer sufficient to influence the spins in a SPM NP, τ_N becomes comparable to τ_m, and the spins become "blocked" along a particular direction. The temperature for which $\tau_N = \tau_m$ is called the blocking temperature T_B:

$$T_B = \frac{K_{eff}V_{NP}}{k_B \ln(\tau_m/\tau_0)}, \tag{1.11}$$

where K_{eff} is the effective magnetic anisotropy constant and V_{NP} is the volume of the NP. The blocking temperature is thus dependent on the measurement method.

At the beginning of this Chapter, we introduced the importance of surface area when the size is reduced to the nanoscale. In very small magnetic NPs, surface spins where found to highly affect the corresponding magnetic properties. In particular, AFM materials, known to have zero magnetization (M) values at the macroscale, were found to exhibit weak ferromagnetism ($M \neq 0$) when reduced to the nanoscale [88, 89]. This behavior could be attributed to the presence of uncompensated spins at the surface that would create a net magnetic moment different from zero. This topic will be presented in more detail in Chapter 5.

To summarize this Section, Fig. 1.17 shows a schematic representation of some of the most important magnetic effects that can occur in magnetic nanomaterials. In particular, it illustrates the magnetic moments in a SPM material and respective magnetization curve [Fig. 1.17(d)]; the EB coupling at the interface between a FM and an AFM layer and respective magnetization curve evidencing a shift along the field axis [Fig. 1.17(e)]; and a magnetization curve of an AFM NP, showing the effect of net magnetization arising from uncompensated surface spins [Fig. 1.17(f)].

1.3 Nanofabrication

The fabrication of nanomaterials is usually categorized by the use of two different approaches: top-down and bottom-up (Fig. 1.18). In the first, one starts with a bulk material and then divide it into smaller pieces until the desired nanosize is reached. The second approach is to use the atoms or molecules as building blocks that will constitute the final material, enabling a better precision in the nanomaterial's fabrication.

The top-down approach is commonly based on nano-lithographic techniques such as e-beam, X-ray and focused ion beam lithographies. These are still very expensive and have a low throughput, thus hindering large scale inexpensive production of nanodevices. Bottom-up approaches for nanofabrication have thus gained increased attention in the last years, as these are generally based on self-assembly techniques, which allow higher production efficiencies at lower costs [90–92]. In this thesis we will focus on nanofabrication methods using the bottom-up approach, namely by self-assembly processes and template-based synthesis.

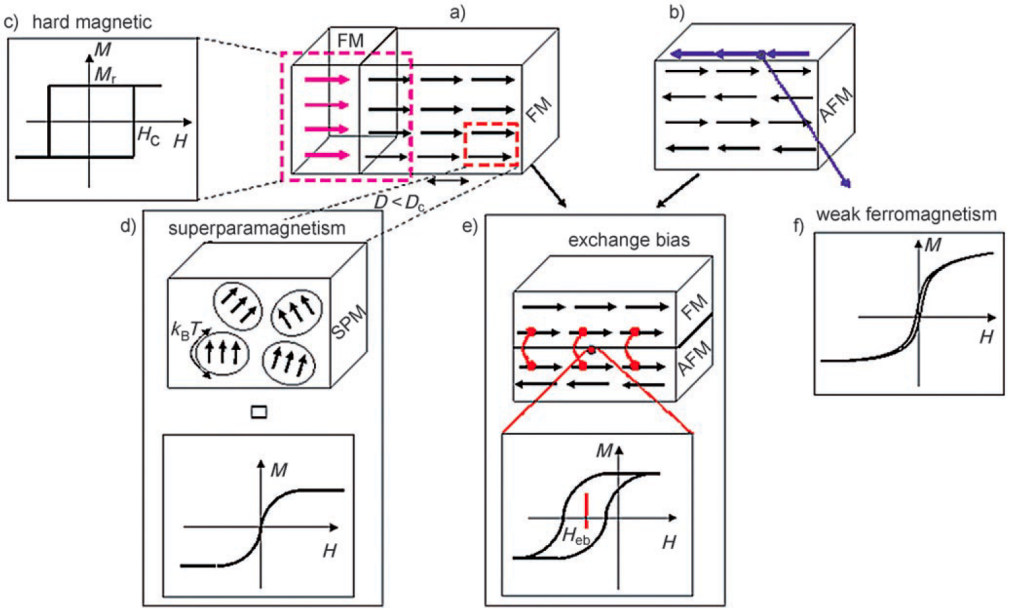


Figure 1.17: Schematic representation of the different magnetic effects occurring in magnetic nanomaterials, where (a) and (b) illustrate the spin arrangements in a ferromagnetic (FM) and an antiferromagnetic (AFM) material, respectively [87].

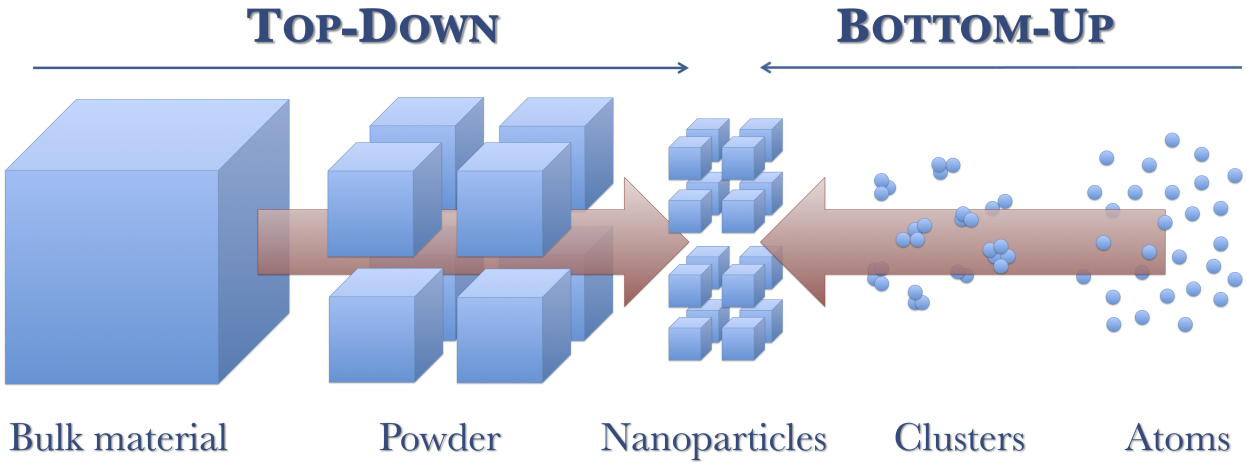


Figure 1.18: Scheme of top-down and bottom-up nanofabrication approaches.

1.3.1 Nanoparticles

There are several methods for the fabrication of nanoparticles (NPs), ranging from top-down approaches, such as ball milling and nano-lithography, to bottom-up routes, like thermal decomposition, microemulsion, co-precipitation, chemical vapor condensation and sol-gel [21, 93, 94]. In this thesis we focused on the fabrication of NPs by a sol-gel route as it is one of the simplest and most commonly used method for the fabrication of metal oxide nanostructures [95–97].

Sol-gel Process

A *sol* is a colloidal suspension of solid particles in a liquid. In a colloid the dispersed particles are so small ($1 - 1000$ nm) that gravitational forces are negligible and interactions are dominated by short-range forces, as van der Waals attraction and surface charges. This type of colloid can be used to generate polymers or particles from which ceramic (non-metallic and inorganic) materials can be made (e.g. metal oxides, nitrides and carbides, both crystalline and non-crystalline). In the sol-gel process, the precursors (starting compounds) for preparation of a colloid consist of a metal or metalloid element surrounded by various ligands (appendages not including another metal or metalloid atom).

The sol-gel route for the fabrication of metal oxide nanomaterials follows various distinct steps. The first one is called hydrolysis, where the metallic precursors react with water, and hydroxyl ions become attached to the metal atoms, forming hydrolyzed molecules. These can link together in a condensation reaction. This type of reaction can continue to build larger and larger molecules by the process of polymerization. A polymer is a huge molecule (also called a macromolecule) formed from hundreds or thousands of units (monomers). If one molecule reaches macroscopic dimensions, so that it extends throughout the solution, the substance is said to be a *gel*. The *gel point* is the time (or degree of reaction) at which the last bond is formed that completes this giant molecule. Thus a *gel* is a substance that contains a continuous solid skeleton enclosing a continuous liquid phase.

The formation of gels, by the so called gelation process, can be produced by rapid evaporation of the solvent, as occurs during preparation of films or fibers [98]. Alternatively, gelation can occur after a *sol* is cast into a template, allowing the fabrication of objects of a desired shape, as will be seen in the next section.

After the gelation process, some segments of the *gel* network can still move close enough together to allow further condensation or other bond-forming processes. Moreover, there is still a *sol* within the *gel* network and those smaller polymers or particles continue to attach themselves to the network. So the bond formation does not stop at the *gel point*, and a following aging process is required. Aging may involve further condensation, dissolution and reprecipitation of monomers, or phase transformation within the solid or liquid phases.

In the end, the *gel* undertakes a final process called drying. This can be performed by solvent evaporation under normal or supercritical conditions, or by sublimation of frozen solvent. These are useful in the preparation of dense ceramics by heating. Although most gels are amorphous (non-crystalline), even after drying, many crystallize when heated to sufficiently high temperatures.

In this thesis, nickel oxide NPs were prepared by the sol-gel method using a citrate route, where nickel nitrate and citric acid were used as precursors. The details on the fabrication and magnetic properties of NiO NPs with different sizes will be presented in Chapter 5.

1.3.2 Nanowires and Nanotubes

Nanowires (NWs) and nanotubes (NTs) can be fabricated by a wide range of different methods, such as nano-lithographic techniques for the deposition of nanowire stripes on top of a substrate [99–101], hydrothermal growth starting from a seed [102], chemical vapor deposition (widely used for the fabrication of carbon nanotubes) [103], molecular self-assembly [104, 105], and template filling by sol-gel [106, 107], atomic layer deposition [61, 108] or electrodeposition [109, 110] techniques. However, for the growth of NW/NT arrays, the use of template-assisted methods has proved to be a highly efficient and low cost fabrication procedure.

The templates most commonly used for the fabrication of NWs and NTs are track-etched polycarbonate and porous anodic alumina membranes. The first ones are made by bombarding a polymeric foil with nuclear fission fragments to create damage tracks in the material, and then chemically etch these tracks into pores [111, 112]. However, due to the random nature of the pore fabrication process, the pore distribution in this type of membranes has no organization, with some pores appearing tilted with respect to the surface normal and many also intersecting each other inside the membrane, thus affecting their use as pore filling templates. On the other hand, porous anodic alumina membranes are fabricated by the commonly reported anodization processes of an Al foil, which basically consists in an electrochemical oxidation of its metallic surface. The self-organized growth of these templates using a two-step anodization method [113] allows one to easily obtain closed-packed arrays of hexagonally arranged pore cells, as schematically represented in Fig. 1.19. Besides their regular hexagonal pore structures and high pore density ($\sim 10^{11}$ pores/cm^2), nanoporous alumina templates also exhibit high thermal and chemical stability, making them attractive for a wide range of template-assisted growth methods and biomedical applications.

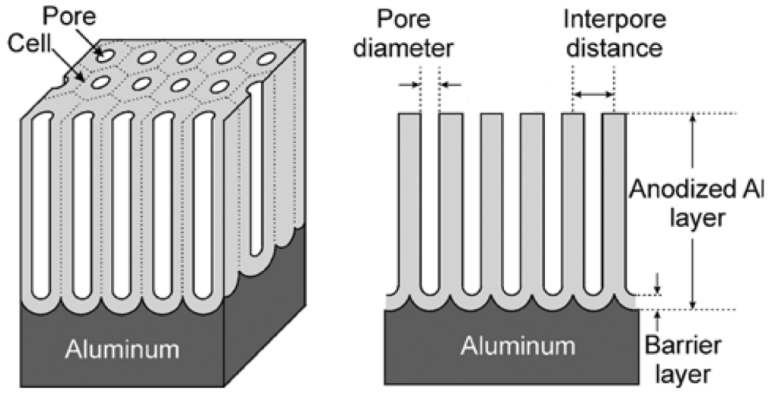


Figure 1.19: Schematic representations of (*left*) an hexagonal closed-pack array of pore cells in an anodic alumina membrane and (*right*) respective cross-sectional view [91].

In the study of arrays of magnetic nanoelements, the order parameter of the array distribution is highly important as it influences the magnetic properties of the array [114]. Therefore, in the magnetic study of NW and NT arrays presented in this thesis, we used optimized home-made hexagonally ordered nanoporous alumina membranes with controlled pore dimensions, as templates

for the subsequent growth of NWs/NTs.

Nanoporous Alumina Templates

The fabrication of nanoporous alumina templates (NpATs) follows a two-step anodizatioan process of an Al foil. Prior to anodization the Al substrate is degreased in acetone and ethanol using an ultrasonic bath for 5 min. For a complete smoothness of the Al surface it is then electropolished in a 75% ethanol and 25% perchloric acid solution, by applying 20 V between the Al foil (anode) and a Pt mesh (cathode) for 2 min, and maintaining the solution below room temperature [115]. The anodization process is then performed in an acidic electrolyte by applying a constant potential between the Al foil (anode) and a Pt mesh (cathode) in an electrochemical cell, as schematically shown in Fig. 1.20.



Figure 1.20: (*Left*) Representation of an electrochemical set-up with two electrodes. (*Right*) Electrochemical cell and experimental set-up used for the anodization process.

For the past three decades, the optimization and control of the nanopores' growth using electrochemical methods has been thoroughly studied [113, 116–121]. Their ordered self-assembling depends on the electrolyte type, concentration, temperature and applied anodization potential. A balanced combination of these parameters can accurately control the sizes and shapes of the nanopores [116].

When a potential is applied between the two electrodes, an oxide layer is formed at the surface of the Al [Fig. 1.21(a)], and the presence of H^+ and OH^- ions in the solution is increased. At the oxide/electrolyte (o/e) interface the water-splitting reaction

$$H_2O(l) \rightarrow 2H^+(aq) + O^{2-}(oxide), \tag{1.12}$$

occurs and is rate-determining, according to Li *et al.* [122]. At the metal/oxide (m/o) interface, the

Al is oxidized,

$$Al(s) \rightarrow Al^{3+}(oxide) + 3e^{-}, \tag{1.13}$$

reacting with the O^{2-}/OH^{-} ions that have migrated across the oxide layer due to the generated electric field

$$2Al^{3+} + 3OH^{-} \rightarrow Al_2O_3 + 3H^{+}, \tag{1.14}$$

$$2Al^{3+} + 3O^{2-} \rightarrow Al_2O_3. \tag{1.15}$$

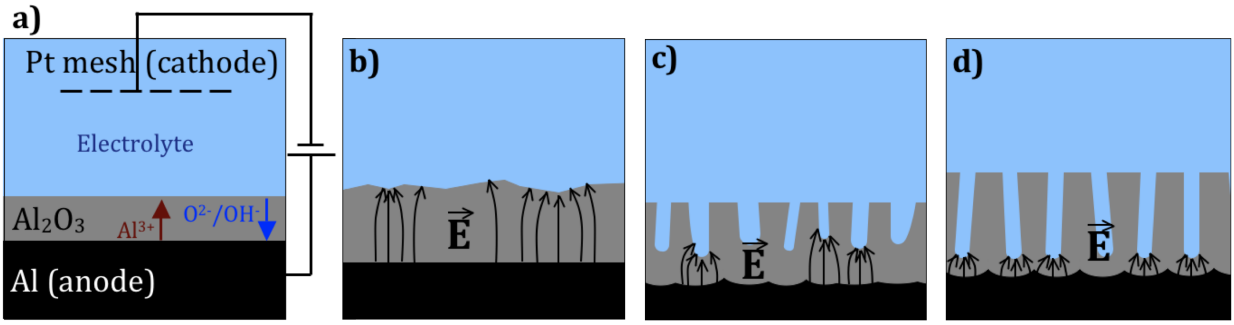


Figure 1.21: Illustration of the four major stages of pore formation in a nanoporous alumina membrane: a) an oxide barrier layer is formed; b) small irregularities are formed at the *o/e* interface due to mechanical stress; c) pores start to nucleate and begin to grow; d) continuous growth of a porous-type alumina film.

Some of the Al^{3+} ions also migrate across the oxide to react with the O^{2-}/OH^{-} ions at the *o/e* interface according to the same reactions [122–124]. Meanwhile, the H^{+} ions migrate to the cathode where they are reduced

$$2H^{+}(aq) + 2e^{-} \rightarrow H_2(g), \tag{1.16}$$

releasing H_2 bubbles. When the Al is anodized to alumina, there is a significant volume expansion ($\varepsilon = V_{Alox}/V_{Al}$), which leads to mechanical stress in the thin alumina layer. For barrier-type layers, the stress is maximal ($\varepsilon_{max} \sim 2$) and it will decrease with porosity [117]. As shown by Jessensky *et al.* [125], if $\varepsilon < 1.2$, i.e. , the initial porosity is large, the force promoting ordering is too small and the pore array remains disordered. If $\varepsilon \sim 1.2$, there is a small force promoting ordered pore growth. If $1.3 < \varepsilon < \varepsilon_{max}$, the interaction between the neighboring pores is reduced, leading to irregular pore growth.

The volume expansion during oxide formation leads to mechanical stress in the thin alumina layer, forming small irregularities at the *o/e* interface [Fig. 1.21(b)]. At the pits of these irregularities (regions where the oxide layer is thinner) an electric field concentration occurs. This phenomenon rises the local temperature which interferes with the pH of the solution.

A suitable combination of the applied potential and the electrolyte type, concentration and temperature is very important for pore formation in the alumina. All contribute to the pH of the solution (pH = $\log[H^{+}]$, where $[H^{+}]$ is the H^{+} ions concentration). The smaller the pH, the larger

the H^+ ions concentration. If the $[H^+]$ is sufficiently large (corresponding to a pH < 1.77) a field-enhanced oxide dissolution of the alumina occurs at the pits of the *o/e* interface according to the chemical reaction:

$$Al_2O_3(s) + 6H^+ \rightarrow 2Al^{3+}(aq) + 3H_2O(l). \tag{1.17}$$

releasing Al^{3+} ions into the electrolyte. A good choice of the anodization conditions allows this dissolution process to keep occurring at the pits while the alumina is being formed at the *m/o* interface [Fig. 1.21(c)]. These pits are the nucleation sites of the alumina pores. As the Al oxide is being formed, pores' walls grow upwards, but their bottoms reach a dynamical equilibrium were the rate of oxide formation equals the rate of its dissolution, maintaining the same oxide barrier layer thickness (δ_b). After this stage a "pore competition" begins where small pores are "eaten" by larger neighbors, improving their organization. Finally, the mechanical stress generated between the pores make them grow straight downwards at a constant rate and hexagonal ordered arrays are formed at the bottom through a self-assembling process [Fig. 1.21(d)].

The porosity of an hexagonal structure is given by:

$$P = \frac{2\pi}{\sqrt{3}} \left(\frac{r}{D_{int}} \right)^2, \tag{1.18}$$

where r is the pore radii and D_{int} the interpore distance. This last one is related to r and δ_b by:

$$D_{int} = 2\delta_b + 2r. \tag{1.19}$$

Nielsch *et al.* [117] found that an optimal porosity value of around 10% is needed for a well-defined self-ordered porous alumina to be formed, which is in good agreement with the volume expansion values ($\varepsilon \sim 1.2$) of Jessensky *et al.* [125]. Fixing the porosity value, then

$$D_{int} \propto r \Rightarrow D_{int} \propto \delta_b. \tag{1.20}$$

Under optimum conditions and small pore diameters, the interpore distance is $D_{int} \approx 2\delta_b$ [117], so that:

$$D_{int} = \kappa V_{app}, \tag{1.21}$$

where κ is a proportionality constant of ~ 2.5 nm V^{-1}, and V_{app} is the applied potential. Studies carried out using several inorganic (sulfuric, phosphoric) and organic acids (oxalic, tartaric, malonic, citric) confirmed this linear dependence between the interpore distance and the applied potential [121]. This distribution indicates that each acid allows the formation of a certain range of self-organized structures, depending on the extension of the acid ionization.

To improve the nanopores' organization, Masuda *et al.* developed the two-step anodization method [113]. At the beginning of the first anodization process, the pores nucleate randomly at the Al surface (step 3 in Fig. 1.22). Then, after a certain anodization time the pores start to self-assemble due

to mechanical stress induced by neighboring pores, as previously described. Long first anodizations allow the formation of large organized domains of nanopores (although always limited by the Al grain dimensions). The porous alumina membrane formed at the Al surface during the first anodization process is subsequently etched away by chemical dissolution (step 4 in Fig. 1.22). The resulting Al foil exhibits ordered hexagonal arrays of pits at its surface due to the self-organized pore formation during the former anodization process. Afterwards, the anodization process is repeated using the same conditions as the first anodization but with the Al surface already hexagonally patterned (step 5 in Fig. 1.22). Since the pore nucleation sites are already defined and ordered, the pores grow with a better alignment and organization during this second anodization process. Partial chemical etching of the porous alumina membrane can also be performed after the two-step anodization process, in order to widen the pore's diameter to its desired value (step 6 in Fig. 1.22). Figure 1.22 shows a schematic representation of the two-step anodization process of an Al foil.

Highly-ordered hexagonal lattices with pore diameters in the $2-900$ nm range (with pore widening) and interpore distances of $35-980$ nm have been successfully prepared by a two-step anodization process under potentials of $8-450$ V [113, 121, 126]. The most commonly reported parameters (summarized in table 1.1) result from the use of sulfuric (H_2SO_4, 0.3 M), oxalic ($C_2O_4H_2$, 0.3 M) and phosphoric (H_3PO_4, 0.1 M) acids, by applying 25, 40 and 195 V, respectively [127]. These allow the fabrication of NpATs with corresponding pore diameters of 20, 35 and 200 nm, and respective interpore distances of 65, 105 and 500 nm. Different pore patterns can also be obtained, by nanoimprint lithography pre-patterning of the Al surface prior to the anodization process, allowing the fabrication of a wide variety of templates [120, 128]. Moreover, the combination of different electrochemical processes allows the modulation of the pore diameters throughout the alumina membrane, giving a more accurate tailoring of these templates to our needs [108, 116, 129].

Table 1.1: Anodization parameters and pore characteristics.

Electrolyte	Concentration (M)	Potential (V)	Temperature (°C)	Diameter (nm)	D_{int} (nm)	Anodization Rate (μm h^{-1})
H_2SO_4	0.3	25	$2-6$	20	65	2
$C_2O_4H_2$	0.3	40	$4-8$	35	105	2.5
H_3PO_4	0.1	195	$0-1$	200	500	2

Template Filling by Electrodeposition Techniques

Electrochemical deposition is one of the most commonly used template filling process for the growth of metallic NWs or NTs. The electrodeposition method basically consists in the growth of a metallic material on top of a conducting substrate, by the electrochemical reduction of metal ions present in an electrolyte solution [130]. The electrolyte is an ionic conductor, where chemical species containing the metal of interest are dissolved into a suitable solvent. The electrodeposition process is then carried out in the electrolyte bath using two (or three) electrodes, as schematically represented in Figs. 1.20 and 1.25. During the deposition process the conducting substrate where the metal will be deposited

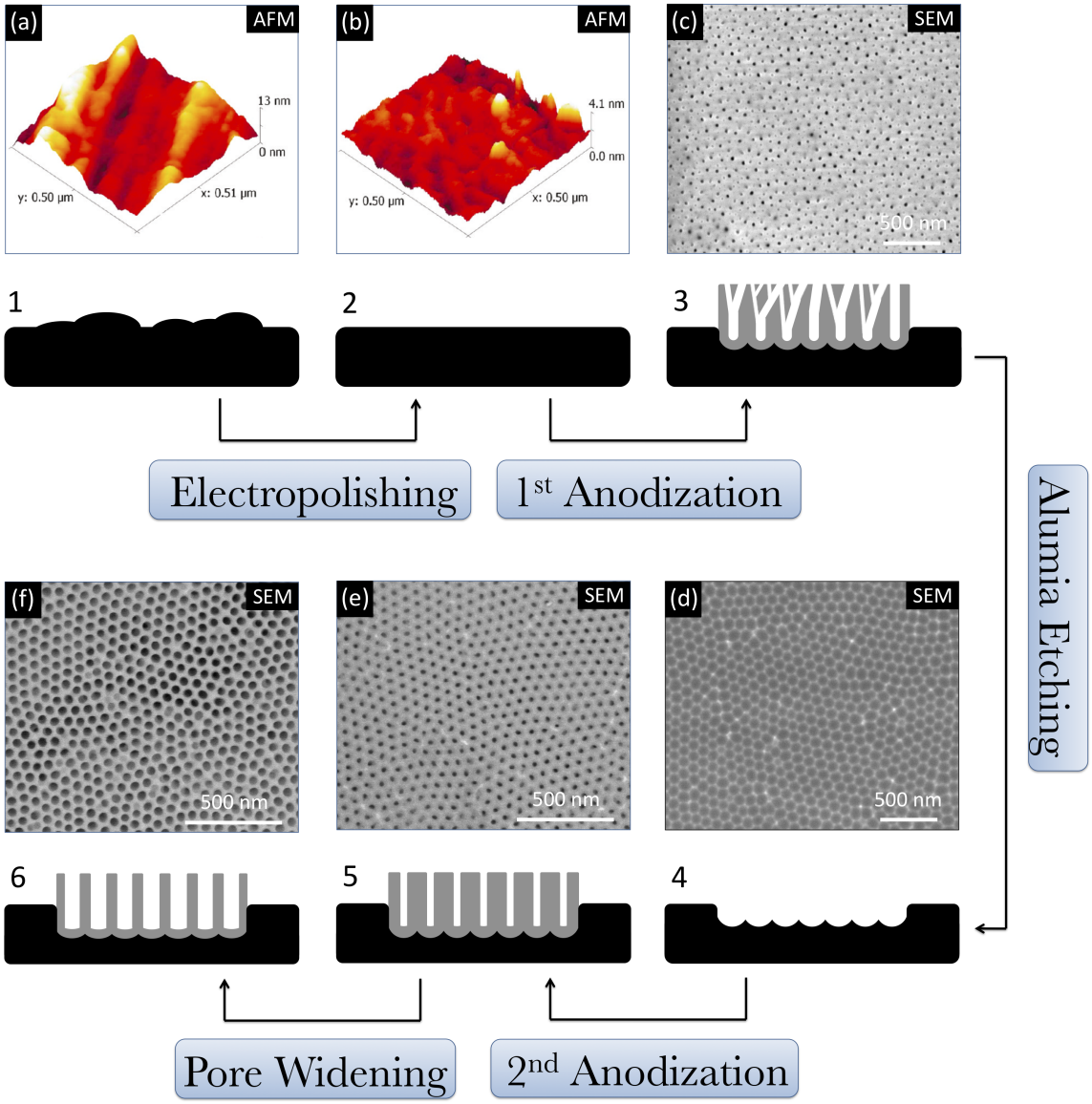


Figure 1.22: Illustration of the fabrication process of a nanoporous alumina template by anodization of an Al foil. For each step of the fabrication process, atomic force microscopy {(a) and (b), taken from [115]} and scanning electron microscopy [(c), (d), (e) and (f)] images of the corresponding top surfaces are shown.

is the cathode, also known as the working electrode, and the anode, or counter electrode, is a Pt mesh (a third electrode can also be used as reference). The general reaction for the process of metal reduction can be written as:

$$(\mathrm{M_xW_y})^z + nx\ \mathrm{e} \rightarrow x\mathrm{M}^0 + y\mathrm{L}, \tag{1.22}$$

where W represents a molecule, ion or radical (e.g. H_2O or SO_4^{2-}) tightly bounded to the metal ion M and thus forming a complex species $(\mathrm{M}_x\mathrm{W}_y)^z$ which takes part in the charge transfer process. This intermediate compound is usually named the *electroactive species* [130]. The amount of electrons that take place in the reaction are represented by n, and z is the electric charge of the electroactive

species. For the deposition of one metal atom, one therefore needs n electrons, i.e. a charge of ne Coulombs. Measuring the current (I) that passes through the circuit during the deposition process and the duration of the deposition, one can estimate the net charge ($Q = \int Idt$) used for the metal reduction process. Then, using the Faraday's law of electrolysis:

$$m = \frac{QA}{nF}, \tag{1.23}$$

we can estimate the deposited metal mass (m, in grams), where A is the atomic weight of the metal and F is the Faraday constant (96485 C mol^{-1}). This equation is extremely important and widely used to estimate the amount of metal deposited during the process, allowing one to tune the thickness or amount of material deposited by controlling the duration of the electrodeposition process.

For the electrodeposition of NW arrays inside nanoporous templates three different methods have been developed aiming its uniform growth: direct current (DC; potentiostatic mode) [110], alternating current (AC) [131, 132] or a hybrid constant potential and constant current in pulses (pulsed electrodeposition; PED) [109, 133]. PED usually consists on the consecutive application of cycles with three different pulses: a deposition pulse at a constant current for a few milliseconds, a shorter pulse with opposite polarity and constant potential to discharge the insulator barrier layer capacitance, and a longer rest pulse ($V = 0$) to allow the repositioning of the ions at the deposition interface. AC deposition is characterized by the application of an alternating current deposition voltage with a given deposition frequency. It is important to note that the anodization of Al leads to an insulating barrier layer at the bottom of the pores that prevents direct contact between the electrodepositing electrolyte and the conducting cathode (Fig. 1.19). Therefore, for the AC and PED processes, the alumina barrier layer must first be thinned to less than 10 nm, for which hollow dendrites are created at the bottom of the pores (Fig. 1.23). Since the pore diameter and consequently the barrier layer thickness (δ_b) depend on the applied potential (V_{app}) [Eqs. (1.19)–(1.21)], the thinning method consists in decreasing V_{app} in successive steps [133]. The electrodeposition process then takes place through such thin insulating barrier layer [131, 133].

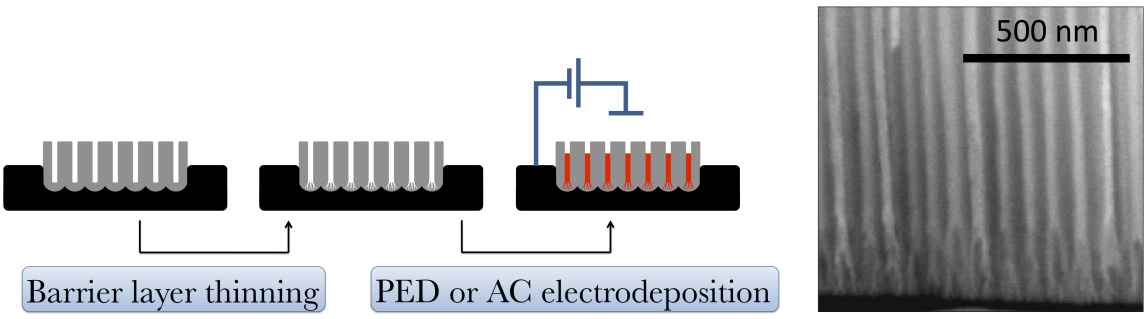


Figure 1.23: Scheme of the barrier thinning process in a NpAT, and subsequent pore filling by the PED or AC deposition methods. SEM cross-sectional image of a NpAT filled with Ni NWs by the PED method, evidencing the filling of the hollow dendrites previously formed at the pores' bottom [134].

In DC deposition, a constant potential is applied, so the current transient monitored allows one to

control the deposition charge involved in the metal reduction reaction. Prior to NW/NT deposition, the NpAT is detached from the Al substrate by a selective chemical dissolution process, the barrier alumina layer is etched by chemical or ion-milling methods and a metallic contact is sputtered on one side of the free-standing membrane, as schematically shown in Fig. 1.24. One of the biggest advantages of the DC method is that, besides the growth of NWs, it also allows the deposition of tubular structures with controlled wall dimensions, by tuning the thickness of the sputtered metallic contact, as illustrated in step 4b of Fig. 1.24. PED and AC methods only allow the deposition of NWs, so for the comparative study on the electrodeposited magnetic NW and NT arrays presented in this thesis, we have chosen to use the DC method for the preparation of both type of nanostructures.

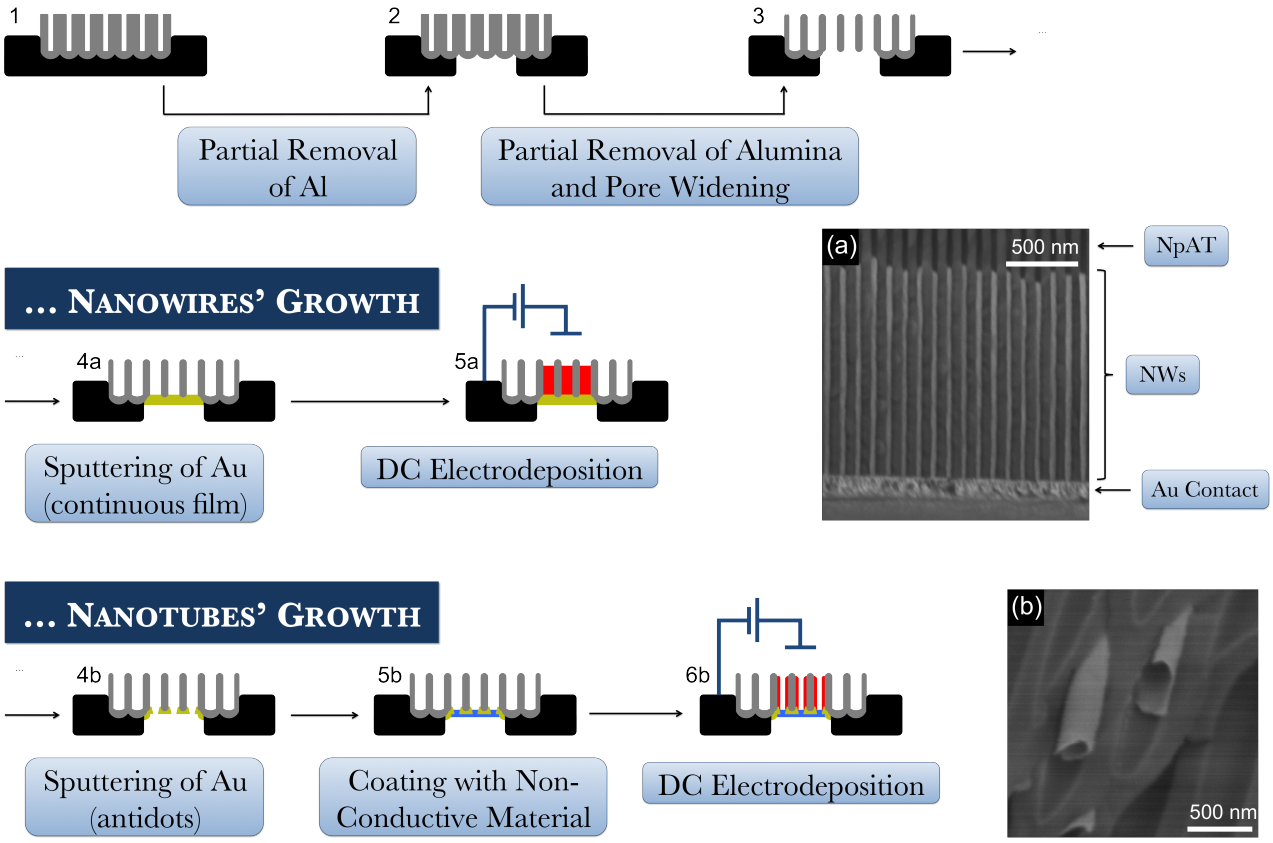


Figure 1.24: Scheme of the template preparation for NW and NT growth by DC electrodeposition. SEM cross-sectional images of Ni (a) NWs with $d \sim 50$ nm and (b) NTs with $d \sim 300$ nm, fabricated by the DC electrodeposition method.

We have fabricated Ni and Co NW and NT arrays inside nanoporous alumina templates by the DC deposition method using a three-electrode cell, as shown in Fig. 1.25. In this set-up, a constant potential is applied between the working and the reference electrodes, and the current transient measured between the working and counter electrodes as schematically represented in Fig. 1.25(b).

For the growth of NW/NT arrays, the electrodeposition process takes place inside the nanopores of a template, where the working electrode is a metallic contact sputtered at one of the pores' open ends. During the deposition process some additional reactions may take place, such as hydrogen reduction

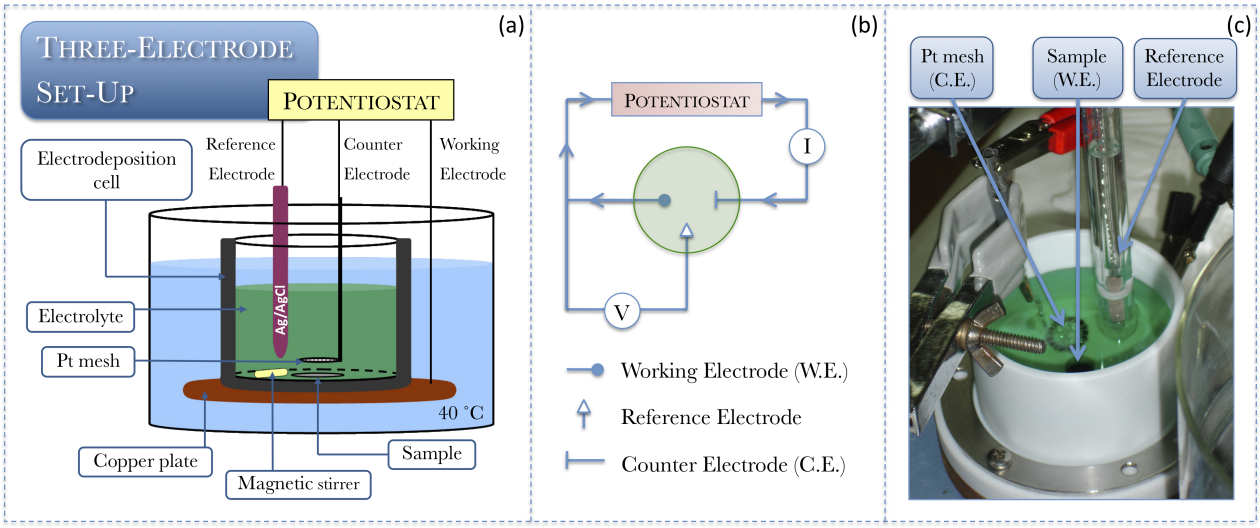


Figure 1.25: Illustration of the DC electrodeposition set-up using a three-electrode cell.

and metal hydroxide formation, that can influence the crystal structure and chemical composition of the metal deposited [135–137]. For example, some of the reactions that may take place at the cathode during Ni deposition include:

$$Ni^{2+} + 2e \rightarrow Ni \quad \text{(Ni deposition)} \tag{1.24}$$

$$2H^{+} + 2e \rightarrow H_2 \quad \text{(Hydrogen evolution)} \tag{1.25}$$

$$2H_2O + 2e \rightarrow H_2 + 2OH^{-} \quad \text{(Water decomposition)} \tag{1.26}$$

$$Ni^{2+} + H_2O \rightarrow Ni(OH)^{+} + H^{+} \quad \text{(Hydrolysis of } Ni^{2+}\text{)} \tag{1.27}$$

$$Ni(OH)^{+} + H_2O \rightarrow Ni(OH)_2 + H^{+} \quad \text{(Hydroxide precipitation)} \tag{1.28}$$

Since in the DC deposition method a constant potential is applied, an adequate control of the overpotential allows one to enhance the metal deposition rate. However, previous reports have shown that the application of high cathodic potentials (-1.3 to -1.8 V vs. Ag/AgCl) for Ni electrodeposition onto flat surfaces could lead to hydrogen evolution reaction (1.25) and water reduction (1.26), rising the pH near the cathode [138]. Above a certain pH value, the hydrolysis of Ni^{2+} (1.27) and its subsequent precipitation (1.28) may occur, generating H^{+} ions and thus decreasing the pH value (buffering effect). The creation of Ni hydroxides contaminates the Ni deposits, reducing its saturation magnetization (M_{Sat}) and changing the corresponding crystallographic structure [139]. The addition of boric acid and the use of vigorous agitation were shown to improve the quality of the deposited material by avoiding hydroxides precipitation [138]. Therefore, a complete understanding and control of the deposition conditions is a crucial step for the accurate electrodeposition of the desired material. A systematic study of some of the deposition conditions in the electrodeposition of Ni NW and NT arrays will be presented in more detail in Chapter 2.

Template Filling by the Sol-gel Process

In the fabrication of metal oxide NW and NT arrays one of the most commonly reported techniques is the template-assisted sol-gel method [106, 140–142]. As previously referred for the fabrication of NPs by the sol-gel route, the use of a template during the gelation process allows one to control the shape of the final nanostructures, as the sol-gel solution will be molded by the pore structure to its desired final shape. This method was implemented at IFIMUP at 2008 [52, 143], resulting in the fabrication of silica NTs for drug delivery [107] and perovskite manganite NTs for the study of magnetic confinement effects [106]. In this thesis we used the sol-gel template filling for the growth of nickel oxide NWs, aiming the fabrication of concentric NW arrays with an antiferromagnetic core of NiO (NW) made by the sol-gel filling method and a ferromagnetic shell of Ni (NT) made by electrodeposition, as schematically illustrated in Fig. 1.26. This is an ongoing investigation that will be presented in Chapter 6.

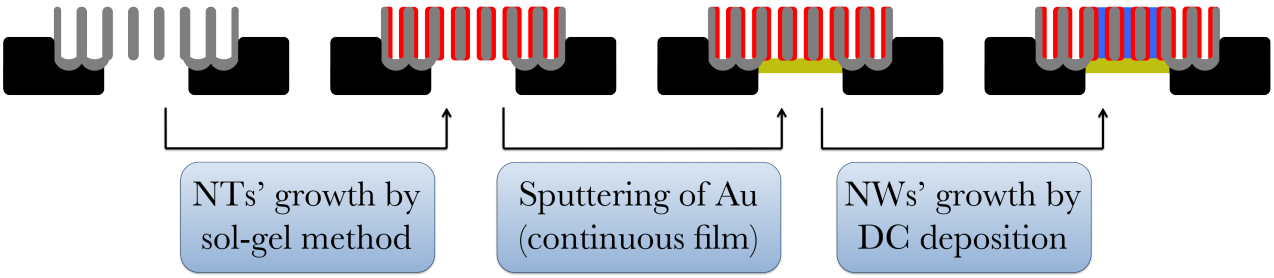


Figure 1.26: Scheme of the fabrication of concentric NW arrays by combining the template-assisted sol-gel and DC electrodeposition methods.

Bibliography

[1] J. Ramsden, *Essentials of nanotechnology*, Jeremy Ramsden & Ventus Publishing ApS, bookboon.com, 2009.

[2] W. Chen, "Reviews in nanoscience and nanotechnology", vol. 1, no. 1, pp. 1–2, 2012.

[3] J. Shi, A. R. Votruba, O. C. Farokhzad, and R. Langer, "Nanotechnology in drug delivery and tissue engineering: From discovery to applications", *Nano Lett.*, vol. 10, pp. 3223–3230, 2010.

[4] "http://www.nano.gov/timeline", May 28^{th}, 2012.

[5] E. W. Muller and T. T Tsong, *Field ion microscopy: Principles and applications*, Elsevier, New York, 1969.

[6] D. M. Eigler and E. K. Schwiezer, "Positioning single atoms with a scanning tunnelling microscope", *Nature*, vol. 344, pp. 524–526, 1990.

[7] R. D. Piner, J. Zhu, F. Xu, S. Hong, and C. A. Mirkin, ""Dip-pen" nanolithography", *Science*, vol. 283, no. 5402, pp. 661–663, 1999.

[8] Y. Shirai, A. J. Osgood, Y. Zhao, Y. Yao, L. Saudan, H. Yang, C. Yu-Hung, L. B. Alemany, T. Sasaki, J.-F. Morin, J. M. Guerrero, K. F. Kelly, and J. M. Tour, "Surface-rolling molecules", *J. Am. Chem. Soc.*, vol. 128, no. 14, pp. 4854–4864, 2006.

[9] M. Fuechsle, J. A. Miwa, S. Mahapatra, H. Ryu, S. Lee, O. Warschkow, L. C. L. Hollenberg, G. Klimeck, and M. Y. Simmons, "A single-atom transistor", *Nature Nanotechnology*, vol. 7, pp. 242–246, 2012.

[10] National Research Council, *The Physics of materials: How science improves our lives*, The National Academies Press, Washington, DC, 1997.

[11] "http://www.rsc.org/chemistryworld/News/2006/March/29030603.asp", May 29^{th}, 2012.

[12] "http://www.nano.gov/nanotech-101/special", May 28^{th}, 2012.

[13] T. Song, H. Cheng, H. Choi, J.-H. Lee, H. Han, D. H. Lee, D. S. Yoo, M.-S. Kwon, J.-M. Choi, S. G. Doo, H. Chang, and J. Xiao, "Si/Ge double-layered nanotube array as a lithium ion battery anode", *ACS Nano*, vol. 6, pp. 303–309, 2012.

[14] J. Brillet, M. Gratzel, and K. Sivula, "Decoupling feature size and functionality in solution-processed, porous hematite electrodes for solar water splitting", *Nano Lett.*, vol. 10, pp. 4155–4160, 2010.

[15] M. Yu, Y.-Z. Long, B. Sun, and Z. Fan, "Recent advances in solar cells based on one-dimensional nanostructure arrays", *Nanoscale*, vol. 4, no. 9, pp. 2783–2796, 2012.

[16] S. J. Son, X. Bai, and S. B. Lee, "Inorganic hollow nanoparticles and nanotubes in nanomedicine Part 1. Drug/gene delivery applications", *Drug Discov. Today*, vol. 12, no. 15-16, pp. 650–656, 2007.

[17] R. Bardhan, S. Lal, A. Joshi, and N. J. Halas, "Theranostic nanoshells: From probe design to imaging and treatment of cancer", *Acc. Chem. Res.*, vol. 44, no. 10, pp. 936–946, 2011.

[18] J. A. Garcia-Calzon and M. E. Diaz-Garcia, "Synthesis and analytical potential of silica nanotubes", *Trends Anal. Chem.*, vol. 35, pp. 27–38, 2012.

[19] P. R. Sajanlal, T. S. Sreeprasad, A. K. Samal, and T. Pradeep, "Anisotropic nanomaterials: Structure, growth, assembly, and functions", *Nano Rev.*, vol. 2, pp. 5883, 2011.

[20] J. M. D. Coey, *Magnetism and magnetic materials*, Cambridge University Press, New York, 2009.

[21] M. Colombo, S. Carregal-Romero, M. F. Casula, L. Gutierrez, M. P. Morales, I. B. Bohm, J. T. Heverhagen, D. Prosperi, and W. J. Parak, "Biological applications of magnetic nanoparticles", *Chem. Soc. Rev.*, vol. 41, pp. 4306–4334, 2012.

[22] "http://eng.thesaurus.rusnano.com/wiki/article1371", May 29^{th}, 2012.

[23] Y. Liu and N. Zhang, "Gadolinium loaded nanoparticles in theranostic magnetic resonance imaging", *Biomaterials*, vol. 33, no. 21, pp. 5363–5375, 2012.

[24] D. Ho, X. Sun, and S. Sun, "Monodisperse magnetic nanoparticles for theranostic applications", *Acc. Chem. Res.*, vol. 44, no. 10, pp. 875–882, 2011.

[25] A. Prina-Mello, Z. Diao, and J. M. D. Coey, "Internalization of ferromagnetic nanowires by different living cells", *J. Nanobiotechnol.*, vol. 4, no. 9, pp. 9–14, 2006.

[26] M. Safi, M. Yan, M.-A. Guedeau-Boudeville, H. Conjeaud, V. Garnier-Thibaud, N. Boggetto, A. Baeza-Squiban, F. Niedergang, D. Averbeck, and J.-F. Berret, "Interactions between magnetic nanowires and living cells: Uptake, toxicity, and degradation", *ACS Nano*, vol. 5, no. 7, pp. 5354–5364, 2011.

[27] A. O. Fung, V. Kapadia, and E. Pierstorff, "Induction of cell death by magnetic actuation of nickel nanowires internalized by fibroblasts", *J. Phys. Chem. C*, vol. 112, no. 39, pp. 15085–15088, 2008.

[28] L. Zhang, T. Petit, K. E. Peyer, and B. J. Nelson, "Targeted cargo delivery using a rotating nickel nanowire", *Nanomedicine: Nanotech. Biol. Med.*, vol. 8, no. 7, pp. 1074–1080, 2012.

[29] S. J. Son, X. Bai, A. Nan, H. Ghandehari, and S. B. Lee, "Template synthesis of multifunctional nanotubes for controlled release", *J. Control. Release*, vol. 114, no. 2, pp. 143–152, 2006.

[30] M. N. Baibich, J. M. Broto, A. Fert, E. Nguyen Van Dau, F. Petroff, P. Etienne, G. Creuzet, A. Friederich, and J. Chazelas, "Giant magnetoresistance of (001)Fe/(001)Cr magnetic superlattices", *Phys. Rev. Lett.*, vol. 61, no. 21, pp. 2472–2475, 1988.

[31] P. P. Freitas, F. A. Cardoso, V. C. Martins, S. A. M. Martins, J. Loureiro, J. Amaral, R. C. Chaves, S. Cardoso, L. P. Fonseca, A. M. Sebastiao, M. Pannetier-Lecoeur, and C. Fermon, "Spintronic platforms for biomedical applications", *Lab Chip*, vol. 12, no. 3, pp. 546–557, 2012.

[32] M. Diaz-Michelena, "Small magnetic sensors for space applications", *Sensors*, vol. 9, no. 4, pp. 2271–2288, 2009.

[33] R. Sbiaa, H. Meng, and S. N. Piramanayagam, "Materials with perpendicular magnetic anisotropy for magnetic random access memory", *Phys. Status Solidi Rapid Res. Lett.*, vol. 5, no. 12, pp. 413–419, 2011.

[34] J. G. Zhu and C. Park, "Magnetic tunnel junctions", *Mater. Today*, vol. 9, no. 11, pp. 36–45, 2006.

[35] S. S. P. Parkin, M. Hayashi, and L. Thomas, "Magnetic domain-wall racetrack memory", *Science*, vol. 320, pp. 190–194, 2008.

[36] G. Catalan, J. Seidel, R. Ramesh, and J. F. Scott, "Domain wall nanoelectronics", *Rev. Mod. Phys.*, vol. 81, no. 1, pp. 119–138, 2012.

[37] G. Hrkac, J. Dean, and D. A. Allwood, "Nanowire spintronics for storage class memories and logic", *Philos. T. Roy. Soc. A*, vol. 369, pp. 3214–3228, 2011.

[38] A. P. Guimaraes, *Principles of nanomagnetism*, Springer-Verlag, Berlin Heidelberg, 2009.

[39] J. Escrig, M. Daub, P. Landeros, K. Nielsch, and D. Altbir, "Angular dependence of coercivity in magnetic nanotubes", *Nanotechnology*, vol. 18, no. 44, pp. 445706, 2007.

[40] Y. Imry and S.-K. Ma, "Random-field instability of the ordered state of continuous symmetry", *Phys. Rev. Lett.*, vol. 35, no. 21, pp. 1399–1401, 1975.

[41] B. D. Patterson, "Ultrafast phenomena at the nanoscale: Science opportunities at the SwissFEL X-ray Laser", in *Nanotechnology*. Paul Scherrer Institut, Switzerland, 2009.

[42] "http://www.sigmaaldrich.com/materials-science/nanomaterials/tutorial.html", June 2^{nd}, 2012.

[43] "http://www.wtec.org/loyola/nano/us_r_n_d/02_01.htm", June 2^{nd}, 2012.

[44] "http://en.wikipedia.org/wiki/Magnetic_anisotropy", June 3^{rd}, 2012.

[45] "http://en.wikipedia.org/wiki/Magnetocrystalline_anisotropy", June 3^{rd}, 2012.

[46] "http://en.wikipedia.org/wiki/Exchange_Bias", June 3^{rd}, 2012.

[47] "http://www.lbl.gov/Science-Articles/Archive/sabl/2006/Jan/02-spin-drag.html", June 3^{rd}, 2012.

[48] "http://physicsworld.com/cws/article/news/2011/jan/10/racetrack-memory-nears-the-finish-line", June 4^{th}, 2012.

[49] "http://techon.nikkeibp.co.jp/article/HONSHI/20061117/123942/", June 4^{th}, 2012.

[50] "http://www.technologyreview.com/computing/22115/", June 4^{th}, 2012.

[51] X. Kou, X. Fan, R. K. Dumas, Q. Lu, Y. Zhang, H. Zhu, X. Zhang, K. Liu, and J. Q. Xiao, "Memory effect in magnetic nanowire arrays", *Adv. Mater.*, vol. 23, no. 11, pp. 1393–1397, 2011.

[52] C. T. Sousa, *Development of nanoporous alumina templates for biotechnological applications*, PhD thesis, University of Porto, 2011.

[53] D. C. Leitao, *Micro and nano patterned magnetic structures*, PhD thesis, University of Porto, 2010.

[54] J. Escrig, D. Altbir, M. Jaafar, D. Navas, A. Asenjo, and M. Vazquez, "Remanence of Ni nanowire arrays: Influence of size and labyrinth magnetic structure", *Phys. Rev. B*, vol. 75, no. 18, pp. 184429, 2007.

[55] A. Ghaddar, F. Gloaguen, J. Gieraltowski, and C. Tannous, "Magnetic crossover effect in nickel nanowire arrays", *Physica B*, vol. 406, no. 10, pp. 2046–2053, 2011.

[56] S. Allende, J. Escrig, D. Altbir, E. Salcedo, and M. Bahiana, "Angular dependence of the transverse and vortex modes in magnetic nanotubes", *Eur. Phys. J. B*, vol. 66, no. 1, pp. 37–40, 2008.

[57] O. Albrecht, R. Zierold, S. Allende, J. Escrig, C. Patzig, B. Rauschenbach, K. Nielsch, and D. Gorlitz, "Experimental evidence for an angular dependent transition of magnetization reversal modes in magnetic nanotubes", *J. Appl. Phys.*, vol. 109, no. 9, pp. 093910, 2011.

[58] E. C. Stoner and E. P. Wohlfarth, "A mechanism of magnetic hysteresis in heterogeneous alloys", *IEEE Trans. Magn.*, vol. 27, no. 4, pp. 3475–3518, 1991.

[59] J. Escrig, P. Landeros, D. Altbir, E. Vogel, and P. Vargas, "Phase diagrams of magnetic nanotubes", *J. Magn. Magn. Mater.*, vol. 308, no. 2, pp. 233–237, 2007.

[60] P. Landeros, S. Allende, J. Escrig, E. Salcedo, D. Altbir, and E. E. Vogel, "Reversal modes in magnetic nanotubes", *Appl. Phys. Lett.*, vol. 90, no. 10, pp. 102501, 2007.

[61] J. Escrig, J. Bachmann, J. Jing, M. Daub, D. Altbir, and K. Nielsch, "Crossover between two different magnetization reversal modes in arrays of iron oxide nanotubes", *Phys. Rev. B*, vol. 77, no. 21, pp. 214421, 2008.

[62] A. Aharoni, "Angular dependence of nucleation by curling in a prolate spheroid", *J. Appl. Phys.*, vol. 82, no. 3, pp. 1281, 1997.

[63] L. G. Vivas, M. Vazquez, J. Escrig, S. Allende, D. Altbir, D. C. Leitao, and J. P. Araujo, "Magnetic anisotropy in CoNi nanowire arrays: Analytical calculations and experiments", *Phys. Rev. B*, vol. 85, no. 3, pp. 035439, 2012.

[64] C. R. Chang, C. M. Lee, and J. S. Yang, "Magnetization curling reversal for an infinite hollow cylinder", *Phys. Rev. B*, vol. 50, no. 9, pp. 6461, 1994.

[65] R. Lavin, J. C. Denardin, J. Escrig, D. Altbir, A. Cortes, and H. Gomez, "Angular dependence of magnetic properties in Ni nanowire arrays", *J. Appl. Phys.*, vol. 106, no. 10, pp. 103903, 2009.

[66] A. Rotaru, J.-H. Lim, D. Lenormand, A. Diaconu, J. B. Wiley, P. Postolache, A. Stancu, and L. Spinu, "Interactions and reversal-field memory in complex magnetic nanowire arrays", *Phys. Rev. B*, vol. 84, no. 13, pp. 134431, 2011.

[67] J. De La Torre Medina, L. Piraux, J. M. Olais Govea, and A. Encinas, "Double ferromagnetic resonance and configuration-dependent dipolar coupling in unsaturated arrays of bistable magnetic nanowires", *Phys. Rev. B*, vol. 81, pp. 144411, 2010.

[68] J. Topp, D. Heitmann, and D. Grundler, "Interaction effects on microwave-assisted switching of $Ni_{80}Fe_{20}$ nanowires in densely packed arrays", *Phys. Rev. B*, vol. 80, pp. 174421, 2009.

[69] I. D. Mayergoyz, "Hysteresis models from the mathematical and control theory points of view", *J. Appl. Phys.*, vol. 57, no. 8, pp. 3803, 1985.

[70] C. R. Pike, A. P. Roberts, and K. L. Verosub, "Characterizing interactions in fine magnetic particle systems using first order reversal curves", *J. Appl. Phys.*, vol. 85, no. 9, pp. 6660, 1999.

[71] F. Brem, L. Tiefenauer, A. Fink, J. Dobson, and A. Hirt, "A mixture of ferritin and magnetite nanoparticles mimics the magnetic properties of human brain tissue", *Phys. Rev. B*, vol. 73, pp. 224427, 2006.

[72] R. Lavin, C. Farias, and J.C. Denardin, "FORC analysis of $Ni(SiO_2)$ nanogranular film in the blocked regime", *J. Magn. Magn. Mater.*, vol. 324, pp. 1800–1803, 2012.

[73] I. Ursachi, A. Vasile, H. Chiriac, P. Postolache, and A. Stancu, "Magnetic properties of magnetite nanoparticles coated with mesoporous silica by sonochemical method", *Mater. Res. Bull.*, vol. 46, pp. 2468–2473, 2011.

[74] L. Spinu, A. Stancu, C. Radu, F. Li, and J. B. Wiley, "Method for magnetic characterization of nanowire structures", *IEEE Trans. Magn.*, vol. 40, no. 4, pp. 2116–2118, 2004.

[75] F. Beron, *Proprietes magnetostatiques de reseaux de nanofils via les courbes de renversement du premier ordre*, PhD thesis, Ecole Polytechnique de Montreal, 2008.

[76] F. Beron, D. Menard, and A. Yelon, "First-order reversal curve diagrams of magnetic entities with mean interaction field: A physical analysis perspective", *J. Appl. Phys.*, vol. 103, no. 7, pp. 07D908, 2008.

[77] I. D. Mayergoyz, *Mathematical models of hysteresis and their applications*, vol. 103, Elsevier, Amsterdam, 2003.

[78] E. Della Torre, "Effect of interaction on the magnetization of single domain particles", *IEEE Trans. Audio Electroacoust.*, vol. AU-14, no. 2, pp. 86–92, 1966.

[79] F. Beron, L.-P. Carignan, D. Menard, and A. Yelon, "Extracting individual properties from global behaviour: First-order reversal curve method applied to magnetic nanowire arrays", in *Electrodeposited nanowires and their applications*, N. Lupu, Ed. INTECH, Croatia, 2010.

[80] F. Beron, L. Clime, M. Ciureanu, D. Menard, R. W. Cochrane, and A. Yelon, "Magnetostatic interactions and coercivities of ferromagnetic soft nanowires in uniform length arrays", *J. Nanosci. Nanotechnol.*, vol. 8, no. 6, pp. 2944–2954, 2008.

[81] Y. Pan, X. Du, F. Zhao, and B. Xu, "Magnetic nanoparticles for the manipulation of proteins and cells", *Chem. Soc. Rev.*, vol. 41, no. 7, pp. 2912–2942, 2012.

[82] F. J. G. Abajo, "Plasmons go quantum", *Nature*, vol. 483, pp. 417–418, 2012.

[83] B. B. Yellen, O. Hovorka, and G. Friedman, "Arranging matter by magnetic nanoparticle assemblers", *Proc. Natl. Acad. Sci. U.S.A.*, vol. 102, no. 25, pp. 8860–8864, 2005.

[84] "http://www.stevens.edu/nue/about.html", June 10^{th}, 2012.

[85] "http://blogs.nature.com/from-the-lab-bench/2011/04/15/big-physics-for-small-science", June 10^{th}, 2012.

[86] "http://mrsec.wisc.edu/Edetc/background/quantum-dots/index.html", June 10^{th}, 2012.

[87] A.-H. Lu, E. L. Salabas, and F. Schuth, "Magnetic nanoparticles: Synthesis, protection, functionalization, and application", *Angew. Chem. Int. Ed.*, vol. 46, no. 8, pp. 1222–1244, 2007.

[88] W. J. Schuele and V. D. Deetscreek, "Appearance of a weak ferromagnetism in fine particles of antiferromagnetic materials", *J. Appl. Phys.*, vol. 33, no. 3, pp. 1136–1137, 1962.

[89] H. Bi, S. Li, Y. Zhang, and Y. Du, "Ferromagnetic-like behavior of ultrafine NiO nanocrystallites", *J. Magn. Magn. Mater.*, vol. 277, no. 3, pp. 363–367, 2004.

[90] K. D. Sattler, *Handbook of nanophysics: Principles and methods*, CRC Press, USA, 2011.

[91] A. Eftekhari, *Nanostructured materials in electrochemistry*, WILEY-VCH Verlag GmbH & Co. KGaA, Weinheim, 2008.

[92] A. Biswas, I. S. Bayer, A. S. Biris, T. Wang, E. Dervishi, and F. Faupel, "Advances in top-down and bottom-up surface nanofabrication: Techniques, applications & future prospects", *Adv. Colloid Interface Sci.*, vol. 170, no. 1-2, pp. 2–27, 2012.

[93] Y.-W. Jun, J.-H. Lee, and J. Cheon, "Chemical design of nanoparticle probes for high-performance magnetic resonance imaging", *Angew. Chem. Int. Ed.*, vol. 47, no. 28, pp. 5122–5135, 2008.

[94] S. C. McBain, H. H. P. Yiu, and J. Dobson, "Magnetic nanoparticles for gene and drug delivery", *Int. J. Nanomed.*, vol. 3, no. 2, pp. 169–180, 2008.

[95] Y. Wu, Y. He, T. Wu, W. Weng, and H. Wan, "Effect of synthesis method on the physical and catalytic property of nanosized NiO", *Mater. Lett.*, vol. 61, pp. 2679–2682, 2007.

[96] M. Niederberger, "Nonaqueous sol-gel routes to metal oxide nanoparticles", *Acc. Chem. Res.*, vol. 40, pp. 793–800, 2007.

[97] G. Oskam, "Metal oxide nanoparticles: Synthesis, characterization and application", *J. Sol-Gel Sci. Technol.*, vol. 37, pp. 161–164, 2006.

[98] C. J. Brinker and G. W. Scherer, *Sol-gel science: The physics and chemistry of sol-gel processing*, Academic Press, Inc., USA, 1990.

[99] A. Colli, A. Fasoli, S. Pisana, Y. Fu, and P. Beecher, "Nanowire lithography on silicon", *Nano Lett.*, vol. 8, no. 5, pp. 1358–1362, 2008.

[100] M. Munoz and J. L. Prieto, "Suppression of the intrinsic stochastic pinning of domain walls in magnetic nanostripes", *Nature Commun.*, vol. 2, pp. 562, 2011.

[101] M. Jaafar, L. Serrano-Ramon, O. Iglesias-Freire, A. Fernandez-Pacheco, M. R. Ibarra, J. M. De Teresa, and A. Asenjo, "Hysteresis loops of individual Co nanostripes measured by magnetic force microscopy", *Nanoscale Res. Lett.*, vol. 6, no. 1, pp. 407, 2011.

[102] S. H. Ko, D. Lee, H. W. Kang, K. H. Nam, J. Y. Yeo, S. J. Hong, C. P. Grigoropoulos, and H. J. Sung, "Nanoforest of hydrothermally grown hierarchical ZnO nanowires for a high efficiency dye-sensitized solar cell", *Nano Lett.*, vol. 11, pp. 666–671, 2011.

[103] M. Kumar and Y. Ando, "Chemical vapor deposition of carbon nanotubes: A review on growth mechanism and mass production", *J. Nanosci. Nanotechnol.*, vol. 10, no. 6, pp. 3739–3758, 2010.

[104] F. Chen, Y.-J. Zhu, K.-W. Wang, and K.-L. Zhao, "Surfactant-free solvothermal synthesis of hydroxyapatite nanowire/nanotube ordered arrays with biomimetic structures", *CrystEngComm*, vol. 13, pp. 1858–1863, 2011.

[105] P. Rahe, M. Nimmrich, A. Greuling, J. Schutte, I. G. Stara, J. Rybacek, G. Huerta-Angeles, I. Stary, M. Rohlfing, and A. Kuhnle, "Toward molecular nanowires self-assembled on an insulating substrate: Heptahelicene-2-carboxylic acid on calcite (1014)", *J. Phys. Chem. C*, vol. 114, pp. 1547–1552, 2010.

[106] C. T. Sousa, A. M. L. Lopes, M. P. Proenca, D. C. Leitao, J. G. Correia, and J. P. Araujo, "Rapid synthesis of ordered manganite nanotubes by microwave irradiation in alumina templates", *J. Nanosci. Nanotechnol.*, vol. 9, no. 10, pp. 6084–6088, 2009.

[107] C. T. Sousa, C. Nunes, M. P. Proenca, D. C. Leitao, J. L. F. C. Lima, S. Reis, J. P. Araujo, and M. Lucio, "pH sensitive silica nanotubes as rationally designed vehicles for NSAIDs delivery", *Colloids Surf. B Biointerfaces*, vol. 94, pp. 288–295, 2012.

[108] K. Pitzschel, J. M. Montero Moreno, J. Escrig, O. Albrecht, K. Nielsch, and J. Bachmann, "Controlled introduction of diameter modulations in arrayed magnetic iron oxide nanotubes", *ACS Nano*, vol. 3, no. 11, pp. 3463–3468, 2009.

[109] K. Nielsch, F. Muller, and A.-P. Li, "Uniform Nickel deposition into ordered alumina pores by pulsed electrodeposition", *Adv. Mater.*, vol. 12, no. 8, pp. 582–586, 2000.

[110] T. M. Whitney, P. C. Searson, J. S. Jiang, and C. L. Chien, "Fabrication and magnetic properties of arrays of metallic nanowires", *Science*, vol. 261, no. 5126, pp. 1316–1319, 1993.

[111] J. C. Hulteen and C. R. Martin, "A general template-based method for the preparation of nanomaterials", *J. Mater. Chem.*, vol. 7, no. 7, pp. 1075–1087, 1997.

[112] H. M. Chen and R.-S. Liu, "Architecture of metallic nanostructures: Synthesis strategy and specific applications", *J. Phys. Chem. C*, vol. 115, pp. 3513–3527, 2011.

[113] H. Masuda and K. Fukuda, "Ordered metal nanohole arrays made by a two-step replication of honeycomb structures of anodic alumina", *Science*, vol. 268, pp. 1466–1468, 1995.

[114] M. Vazquez, K. Nielsch, P. Vargas, J. Velazquez, D. Navas, K. Pirota, M. Hernandez-Velez, E. Vogel, J. Cartes, R. B. Wehrspohn, and U. Gosele, "Modelling hysteresis of interacting nanowires arrays", *Physica B*, vol. 343, pp. 395–402, 2004.

[115] D. C. Leitao, A. Apolinario, C. T. Sousa, J. Ventura, J. B. Sousa, M. Vazquez, and J. P. Araujo, "Nanoscale topography: A tool to enhance pore order and pore size distribution in anodic aluminum oxide", *J. Phys. Chem. C*, vol. 115, no. 17, pp. 8567–8572, 2011.

[116] W. Lee, R. Ji, U. Gosele, and K. Nielsch, "Fast fabrication of long-range ordered porous alumina membranes by hard anodization", *Nature Mater.*, vol. 5, no. 9, pp. 741–747, 2006.

[117] K. Nielsch, J. Choi, K. Schwirn, R. B. Wehrspohn, and U. Gosele, "Self-ordering regimes of porous alumina: The 10% porosity rule", *Nano Lett.*, vol. 2, no. 7, pp. 677–680, 2002.

[118] R. Inguanta, M. Butera, C. Sunseri, and S. Piazza, "Fabrication of metal nano-structures using anodic alumina membranes grown in phosphoric acid solution: Tailoring template morphology", *Appl. Surf. Sci.*, vol. 253, pp. 5447–5456, 2007.

[119] A. P. Li, F. Muller, A. Birner, K. Nielsch, and U. Gosele, "Hexagonal pore arrays with 50-420 nm interpore distance formed by self-organization in anodic alumina", *J. Appl. Phys.*, vol. 84, no. 11, pp. 6023–6026, 1998.

[120] H. Masuda, H. Asoh, M. Watanabe, K. Nishio, M. Nakao, and T. Tamamura, "Square and triangular nanohole array architectures in anodic alumina", *Adv. Mater.*, vol. 13, no. 3, pp. 189–192, 2001.

[121] S. Ono, M. Saito, and H. Asoh, "Self-ordering of anodic porous alumina formed in organic acid electrolytes", *Electrochim. Acta*, vol. 51, no. 5, pp. 827–833, 2005.

[122] F. Y. Li, L. Zhang, and R. M. Metzger, "On the growth of highly ordered pores in anodized aluminum oxide", *Chem. Mater.*, vol. 10, no. 9, pp. 2470–2480, 1998.

[123] J. W. Diggle, T. C. Downie, and C. W. Goulding, "Anodic oxide films on Aluminum", *Chem. Rev.*, vol. 69, no. 3, pp. 365, 1969.

[124] S. K. Thamida and H. C. Chang, "Nanoscale pore formation dynamics during aluminum anodization", *Chaos*, vol. 12, no. 1, pp. 240–251, 2002.

[125] O. Jessensky, F. Muller, and U. Gosele, "Self-organized formation of hexagonal pore arrays in anodic alumina", *Appl. Phys. Lett.*, vol. 72, no. 10, pp. 1173–1175, 1998.

[126] S. Z. Chu, K. Wada, S. Inoue, M. Isogai, Y. Katsuta, and A. Yasumori, "Large-scale fabrication of ordered nanoporous alumina films with arbitrary pore intervals by critical-potential anodization", *J. Electrochem. Soc.*, vol. 153, no. 9, pp. B384–B391, 2005.

[127] M. P. Proenca, C. T. Sousa, D. C. Leitao, J. Ventura, J. B. Sousa, and J. P. Araujo, "Nanopore formation and growth in phosphoric acid Al anodization", *J. Non-Cryst. Solids*, vol. 354, pp. 5238–5240, 2008.

[128] J. Choi, *Fabrication of monodomain porous alumina using nanoimprint lithography and its applications*, PhD thesis, Martin Luther University Halle Wittenberg, 2004.

[129] B. He, S. J. Son, and S. B. Lee, "Shape-coded silica nanotubes for biosensing", *Langmuir*, vol. 22, no. 20, pp. 8263–8265, 2006.

[130] Y. D. Gamburg and G. Zangari, *Theory and practice of metal electrodeposition*, Springer, USA, 2011.

[131] G. Sharma, M. V. Pishko, and C. A. Grimes, "Fabrication of metallic nanowire arrays by electrodeposition into nanoporous alumina membranes: Effect of barrier layer", *J. Mater. Sci.*, vol. 42, no. 13, pp. 4738–4744, 2007.

[132] N. J. Gerein and J. A. Haber, "Effect of ac electrodeposition conditions on the growth of high aspect ratio copper nanowires in porous aluminum oxide templates", *J. Phys. Chem. B*, vol. 109, no. 37, pp. 17372–17385, 2005.

[133] C. T. Sousa, D. C. Leitao, M. P. Proenca, A. Apolinario, J. G. Correia, J. Ventura, and J. P. Araujo, "Tunning pore filling of anodic alumina templates by accurate control of the bottom barrier layer thickness", *Nanotechnology*, vol. 22, no. 31, pp. 315602, 2011.

[134] C. T. Sousa, D. C. Leitao, J. Ventura, P. B. Tavares, and J. P. Araujo, "A versatile synthesis method of dendrites-free segmented nanowires with a precise size control", *Nanoscale Res. Lett.*, vol. 7, no. 1, pp. 168, 2012.

[135] R. Orinakova, A. Turonova, D. Kladekova, M. Galova, and R. M. Smith, "Recent developments in the electrodeposition of nickel and some nickel-based alloys", *J. Appl. Electrochem.*, vol. 36, no. 9, pp. 957–972, 2006.

[136] V. Haehnel, S. Fahler, P. Schaaf, M. Miglierini, C. Mickel, L. Schultz, and H. Schlorb, "Towards smooth and pure iron nanowires grown by electrodeposition in self-organized alumina membranes", *Acta Mater.*, vol. 58, no. 7, pp. 2330–2337, 2010.

[137] Y. Fukunaka, M. Motoyama, Y. Konishi, and R. Ishii, "Producing shape-controlled metal nanowires and nanotubes by an electrochemical method", *Electrochem. Solid-State Lett.*, vol. 9, no. 3, pp. C62–C64, 2006.

[138] H. Deligianni and L. T. Romankiw, "In situ surface pH measurement during electrolysis using a rotating pH electrode", *IBM J. Res. Dev.*, vol. 37, no. 2, pp. 85–95, 1993.

[139] J. A. Koza, M. Uhlemann, A. Gebert, and L. Schultz, "The effect of a magnetic field on the pH value in front of the electrode surface during the electrodeposition of Co, Fe and CoFe alloys", *Journal of Electroanal. Chem.*, vol. 617, pp. 194–202, 2008.

[140] N. I. Kovtyukhova, T. E. Mallouk, and T. S. Mayer, "Templated surface sol-gel synthesis of SiO_2 nanotubes and SiO_2-insulated metal nanowires", *Adv. Mater.*, vol. 15, no. 10, pp. 780–785, 2003.

[141] B. B. Lakshmi, C. J. Patrissi, and C. R. Martin, "Sol-gel template synthesis of semiconductor oxide micro- and nanostructures", *Chem. Mater.*, vol. 9, no. 11, pp. 2544–2550, 1997.

[142] K. S. Shankar and A. K. Raychaudhuri, "Growth of an ordered array of oriented manganite nanowires in alumina templates", *Nanotechnology*, vol. 15, no. 9, pp. 1312–1316, 2004.

[143] M. P. Proenca, *Nanoporous alumina membranes: Fabrication process & template growth of ordered nanotubes*, Final year project, University of Porto, 2008.

Chapter 2

Growth of Ni Nanowires and Nanotubes in Nanoporous Alumina Templates

This Chapter is composed of Articles I and II, on the optimization study of potentiostatic electrodeposition of Ni nanowires (NW) and nanotubes (NT) in nanoporous alumina templates (NpATs). In Article I (Section 2.1) a systematic comparative study on the potentiostatic electrodeposition of Ni NWs in NpATs, by tuning the applied potential (E between -0.5 and -4 V vs. Ag/AgCl), is described. To the best of our knowledge, no work was yet reported on the optimization of Ni deposition in NpATs at high negative overpotentials (lower than -2 V vs. Ag/AgCl). The most commonly applied potentials range from -0.7 to -1.3 V (vs. Ag/AgCl), allowing the fabrication of smooth and well-defined Ni NWs, at deposition rates of ~ 1 μm min^{-1}. This paper introduces a new manner to fabricate Ni NWs with similar crystallographic, morphologic and magnetic properties, but with enhanced deposition rates up to ~ 12 μm min^{-1} (for E $\sim$ -3.5 V). At such high E we also studied the influence of the hydrogen evolution reaction on the Ni NWs fabricated.

In Article II (Section 2.2) we report a comparative analysis on the fabrication process of Ni NW and NT arrays with well controlled ordering and their structural and magnetic properties. The studied nanostructures were prepared by potentiostatic electrodeposition of Ni into suitably modified highly ordered nanoporous alumina templates. The final NW/NT diameter was ~ 50 nm, while the NTs wall thickness was ~ 5 nm, and their length corresponded to the membrane thickness (50 μm). The time of deposition was controlled by the overfilling process in which a Ni continuous film was formed on top of the membrane. In this work we found this process to be considerably different when depositing NWs or NTs inside the pores. The monitorization of the current transients during deposition allowed us to distinguish between NW and NT formation, and identify the four main stages of deposition in nanoporous membranes.

2.1 Article I – Ni Growth inside Ordered Arrays of Alumina Nanopores: Enhancing the Deposition Rate

Mariana P. Proenca, Célia T. Sousa, João Ventura, Manuel Vazquez and João P. Araujo, *Electrochimica Acta* 72 (2012) 215–221.

Abstract

High aspect ratio Ni nanowires (NWs) were electrodeposited inside ordered arrays of self-assembled pores ($\sim$ 50 nm in diameter) in anodic alumina templates by a potentiostatic method. A systematic comparative study is here reported on Ni deposition at different applied potentials between -0.5 and -4.0 V (vs. Ag/AgCl). A detailed analysis of the structural, morphological and magnetic properties of the Ni NWs was performed using scanning electron microscopy, X-ray diffraction and vibrating sample magnetometer. Smooth, well-defined and highly-oriented (220) face-centered cubic Ni NWs were obtained for the whole range of applied potentials (E). The Ni deposition rate (η) was observed to strongly depend on E [η (μm min^{-1}) = 4.5 $\times$ | E | -3.5], reaching $\sim$ 12 μm min^{-1} for $E \sim$ -3.5 V. However, at high cathodic potentials ($E \leqslant$ -2.5 V) we found that H_2 gas bubbles are more likely to nucleate inside the nanopores stopping further Ni deposition. Magnetic measurements revealed the high shape anisotropy of the fabricated nanostructures, and allowed us to estimate the native oxide layer thickness ($\sim$1.5 nm) formed around the Ni NWs, inside the alumina template.

2.1.1 Introduction

Although Ni electroplating has been studied for many years, a renewed interest has emerged in recent years owing to its application in the controlled fabrication of a variety of magnetic nanostructures. A review on the numerous theoretical and practical studies on the electrodeposition of Ni can be found in Ref. [1]. In particular, Ni nanowires (NWs) are potential candidates for magnetic storage devices, nanosensors, biomedical applications, and are vital for the study of nanoconfinement effects [2–5]. Among the various methods used to fabricate arrays of nanowires, template synthesis combined with electrodeposition processes is a low cost, high yield and industrially viable technique [6–11]. In particular, nanoporous alumina templates (NpATs) were found to be ideal for the electrodeposition of dense nanowire arrays [12]. They are stable at high temperature and in organic solvents, and their pore channels are parallel and uniform, aligning perpendicular to the membrane surface [13, 14].

Until now, three different electrodeposition methods have been developed aiming uniform and complete pore filling: direct current (DC; potentiostatic mode) [7], alternating current (AC) [15, 16] or a hybrid constant potential and constant current in pulses method (pulsed electrodeposition; PED) [12, 17]. In DC deposition, a constant potential is applied, allowing the enhancement of the deposition rate by an adequate control of the overpotential. Optimizing this process to enhance

the deposition rate would then allow the industrial production of large and organized arrays of high quality nanostructures in an easy and fast manner.

The electrolytes most commonly used for Ni electrodeposition contain nickel sulphates, sulphamates, chlorides and/or boric acid [12, 17–22], with the pH adjusted between 2 and 5. In DC deposition, the most commonly applied potentials (E) range from -0.7 to -1.3 V (vs. Ag/AgCl) [23]. One way to enhance the rate of Ni deposition would be by decreasing E to lower (more negative) values than the ones commonly used. However, a major problem when electrodepositing at high cathodic potentials is the occurrence of additional undesired reactions [24]. For example, the creation of Ni hydroxides contaminates the Ni deposits, reducing its saturation magnetization (M_{Sat}) and changing the corresponding crystallographic structure [25]. The addition of boric acid and the use of vigorous agitation were shown to improve the quality of the deposited material by avoiding hydroxides precipitation [24].

A powerful method to fabricate highly ordered arrays of metallic nanowires is the use of templates with high aspect ratio nanopores (e.g. NpATs with $\sim$ 50 nm in diameter and 50 μm in length). However, when depositing Ni inside pores with nanometer-sized diameters, a more complex process occurs [26–28]. Due to the existence of narrow paths that connect the bulk electrolyte solution (membrane's top) to the cathode surface (membrane's bottom), the electrodeposition process will now be mainly influenced by the concentration polarization of Ni ions inside the pores and H_2 gas evolution. For Ni deposition the current efficiency (σ) can be estimated by:

$$\sigma = \frac{j_{Ni}}{j_{Ni} + j_{HER}}, \tag{2.1}$$

where j_{Ni} and j_{HER} are the partial current densities of the nickel reduction and the hydrogen evolution reaction (HER), respectively [29]. Previous works showed that $j_{HER} \sim 3$ mA cm^{-2} at pH = 3.5 and remains approximately constant when varying the applied potential (between -1.1 and -1.5 V vs. Ag/AgCl) [30]. However, at very low pH values ($\sim$ 1.5), ten times higher j_{HER} values were found. Fukunama *et al.* showed that although H_2 molecules are produced while simultaneously depositing Ni, they are easily dissolved in the electrolyte allowing a uniform Ni deposition inside the nanopores [31]. But they also observed that the concentration of H_2 gas rapidly increases with increasing current, reaching a supersaturation value and nucleating nanosized H_2 gas bubbles at the cathode surface [31]. In fact, increasing the applied cathodic potential during electrodeposition can raise the local deposition temperature by $\sim 20-40$ °C [32], thus decreasing the local pH and consequently increasing j_{HER}. In this work we used an electrolyte with a high concentration of Ni^{2+} ions ($\sim$ 1.3 M), and pH of the solution ranging between 4 and 5. According to Motoyama *et al.* [30], a current efficiency of around 95% is to be expected for these electrodeposition conditions.

Previous reports on the optimization of Fe [33], Cu [34, 35] and Ni [23] deposition in NpATs referred a limited range of applied potentials (from around -0.7 to -1.2 V vs. Ag/AgCl) for the deposition of defect-free NWs. Many authors also studied the influence of agitation [36], applied potential waveform [37], electrolyte type, concentration, temperature and pH [38, 39] on the Ni deposition

in NpATs. However, no work was yet reported on the optimization of Ni deposition in NpATs at continuous high negative overpotentials (lower than -2.0 V vs. Ag/AgCl). The main question that arises is at what potential will the H_2 supersaturation be reached and prevent Ni NWs formation or influence the corresponding structural and magnetic properties. Finding such limit would then allow the fabrication of long and uniform Ni NWs in very short times.

In this work a systematic study of Ni DC deposition at high cathodic potentials (down to -4.0 V vs. Ag/AgCl) in NpATs is presented. The influence of HER on the electrodeposition process is discussed and reproducibility tests were performed to find the limiting potential for the optimization of the Ni NWs growth inside the nanopores. A deposition rate of ~ 12 μm min^{-1} (more than 10 times larger than commonly reported values) for the fabrication of organized arrays of long Ni NWs was obtained using $E \sim$ -3.5 V. Magnetic measurements were also performed illustrating the high shape anisotropy of the fabricated NWs and allowing the determination of an oxide layer thickness value of ~ 1.5 nm around the Ni NWs, inside the alumina template.

2.1.2 Experimental

In this work Ni was electrodeposited on top of an Au substrate and inside self-assembled pores of anodic alumina templates (pore diameter $\sim$ 50 nm; interpore distance $\sim$ 105 nm and thickness $\sim$ 50 μm). The Au substrate was prepared by sputtering a layer of ~ 60 nm in thickness (3 min at 40 mA) on top of a Cu foil tape, using a Q150R S sputter coater. The membranes where fabricated by a two-step anodization process in 0.3 M oxalic acid at 40 V and 5°C [13, 40]. Prior to the first anodization, Al discs (99.999% purity) were degreased with acetone and ethanol, followed by electropolishing in a 75% ethanol and 25% perchloric acid solution for 2 min at 20 V [41]. First anodizations were carried out for 24 h. Alumina removal after the first anodization was performed in an aqueous solution of 0.2 M H_2CrO_4 and 0.4 M H_3PO_4 at 60°C . Second anodizations were then performed for 20 h under the same conditions as the first ones. For potentiostatic deposition inside the NpATs, a circle with 1.1 cm in diameter was opened on the membrane backside by removing the Al substrate in an aqueous solution of 0.2 M $CuCl_2$ and 4.1 M HCl at room temperature. The remaining alumina barrier layer at the bottom of the pores was then chemically etched in 0.5 M H_3PO_4 at 21°C for 2 h. During this process the pores were slightly widen. Finally, a 100 nm thick Au layer was sputtered on the opened bottom side of the porous membrane to serve as the working electrode in a three-electrode cell. A Pt mesh was used as counter electrode and Ag/AgCl (in 4 M KCl) as reference electrode (0.197 V vs. standard hydrogen electrode; SHE). In the following, all potentials are referred to Ag/AgCl. The depositions were performed in the so-called Watts bath [12], consisting in a mixture of 1.14 M $NiSO_4{\cdot}6H_2O$, 0.19 M $NiCl_2{\cdot}6H_2O$ and 0.73 M H_3BO_3. During the electrodeposition, the solution was magnetically stirred at 250 rpm and kept at a constant temperature of 35°C within a pH ranging between 4 and 5.

Cathodic sweep voltammetries were performed prior to the deposition process by applying a potential from 0 to -1.8 V at different sweep rates (ν; from 5 to 40 mV s^{-1}). The electrodepositions

were performed in a potentiostatic mode using a Solartron 1480 MultiStat. The deposited NWs were magnetically characterized using a vibrating sample magnetometer (VSM; LOT-Oriel EV7). Morphological characterization was performed using a field emission scanning electron microscope (FESEM; FEI Nova NanoSEM 230). Structural analysis was performed by X-ray diffraction (XRD; Panalytical X'Pert Pro) using Cu $K_{\alpha 1}$ radiation (λ = 0.15406 nm) and the Bragg-Brentano $\theta/2\theta$ geometry.

2.1.3 Results and Discussion

2.1.3.1 Linear Sweep Voltammetry

Prior to Ni potentiostatic deposition inside the nanopores we used linear sweep voltammetry (LSV) to find the Ni deposition potentials, which are known to depend on the agitation conditions, electrolyte composition, temperature and pH.

For an accurate comparison of the charge-controlled and diffusion limited processes we performed LSVs on an Au substrate and in the NpATs, at 50 and 20 mV s^{-1} (Fig. 2.1). The Ni deposition on the Au substrate (Ni film 01 in Fig. 2.1), performed from 0 to -8.0 V, clearly shows a charge-controlled process, as expected for metal layer deposition [42]. However, Ni deposition inside the nanopores (Ni NWs 01 and 02 in Fig. 2.1), performed from 0 to -5.0 V, illustrates a combination of charge and diffusion controlled processes, together with the nucleation of H_2 gas bubbles at high cathodic potentials. The LSV curves during Ni deposition inside the nanopores follow the same linear trend as the ones obtained during Ni deposition on the Au substrate, indicating the presence of a similar charge controlled process. However, a cathodic and anodic peak corresponding to the deposition and dissolution of Ni, respectively, are also clearly seen in Fig. 2.2. The cathodic peak, that illustrates a diffusion-controlled process, is only present during Ni deposition inside the nanopores. This evidences the existence of a mixed (charge and diffusion) controlled process for Ni deposition inside the nanopores, while only charge-controlled when deposited on a flat substrate. As for the quick drop of current density to almost zero at high cathodic potentials in Fig. 2.1, this most likely results from the nucleation of H_2 gas bubbles inside the nanopores [30, 31, 43]. When applying high cathodic potentials there is a local increase of temperature, resulting in a pH decrease, and therefore higher H_2 evolution. Due to the high NpATs homogeneity, the nucleation of H_2 gas bubbles will occur at approximately the same time inside all pores, uniformly stopping further Ni deposition. Therefore, there is a limiting applied potential for the deposition of Ni NWs due to the existence of a template with nanochannels instead of a flat metallic substrate.

Additionally, we studied the LSV curves obtained during Ni deposition inside the nanopores at different sweep rates (ν; from 5 to 40 mV s^{-1}; Fig. 2.2). In the first scan (at 5 mV s^{-1}) a small cathodic peak occurred with a maximum at $\sim$ -0.7 V. During this scan Ni deposition already took place, so that, when performing the second scan, one also observes an anodic peak at $\sim$ -0.05 V, corresponding to Ni reduction (Fig. 2.2). In the subsequent scans performed at higher voltage sweep

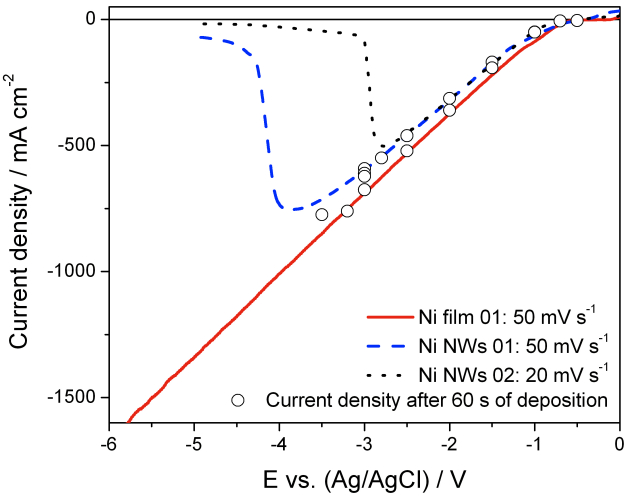


Figure 2.1: Linear potential sweep curves during Ni deposition on an Au substrate (Ni film 01) and in a NpAT (Ni NWs 01 and 02). The scattered points correspond to the current density values after 60 s of Ni potentiostatic deposition.

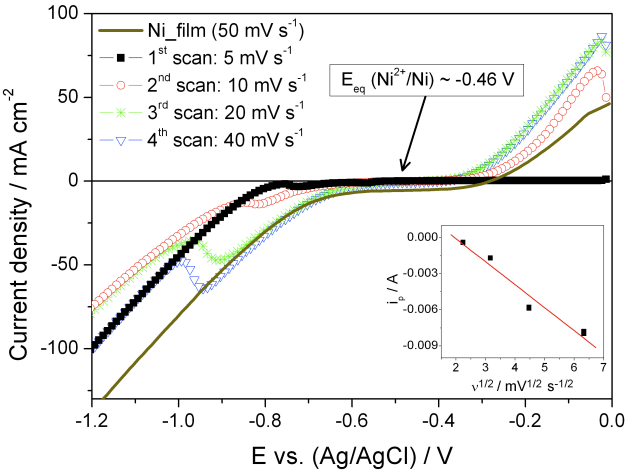


Figure 2.2: Linear potential sweep curves during Ni deposition on an Au substrate (Ni film at 50 mV s^{-1}) and in NpATs at different scan rates (1^{st} to 4^{th} scans). Inset plots the cathodic peak current vs. the square root of sweep rate.

rates (ν = 10, 20 and 40 mV s^{-1}) the cathodic peak is more evident and has its maximum at ~ -0.8, -0.9 and -0.95 V, respectively. The inset of Fig. 2.2 shows that the peak current i_p increases linearly with the square root of the sweep rate $\nu^{1/2}$, following the Randles-Sevcik equation [44]:

$$i_p = 0.4463 \left(\frac{F^3}{RT} \right)^{1/2} n^{3/2} A D^{1/2} c \nu^{1/2}, \tag{2.2}$$

where F is the Faraday constant (96,485 C mol^{-1}), R is the universal gas constant (8.314 J mol^{-1} K^{-1}), T is the absolute temperature (K), n is the number of electrons involved in the electrochemical reaction, A is the surface area of the electrode (cm^2), D is the diffusion coefficient

of the electroactive species (cm^2 s^{-1}) and c is the bulk concentration of electroactive species in the electrolyte solution (mol cm^{-3}). This allowed us to estimate the diffusion coefficient of Ni^{2+} ions in the electrolyte used. The obtained value of $D \sim (1.0 \pm 0.1) \times 10^{-7}$ cm^2 s^{-1} is in good agreement with values reported in the literature [45].

The results in Fig. 2.2 also allowed us to determine the equilibrium potential (E_{eq}) of Ni deposition reaction for the used electrolyte and deposition conditions [$E_{eq}(Ni^{2+}/Ni) \sim$ -0.46 V vs. Ag/AgCl]. In an aqueous solution at 25°C one has $E_{eq} \sim$ -0.257 V vs. SHE, corresponding to $\sim$ -0.454 V vs. Ag/AgCl [24, 44], in good agreement with our results. Ni reduction can thus only occur if a potential lower than -0.46 V is applied. However, one cannot assume that the potential at the maximum cathodic peak corresponds to the optimum potential value for Ni deposition. A systematic study is therefore required to obtain the limiting Ni deposition potential that leads to the growth of smooth and defect-free Ni NWs at a high rate.

2.1.3.2 Electrodepositions at Different Potentials

Ni was electrodeposited in the NpATs at constant potentials (E) between -0.5 and -4.0 V for 1 min. Fig. 2.3 shows selected current transients during the deposition process. After the first few seconds, that correspond to the initial Ni nucleation on the Au contact [34], Ni is deposited at a constant rate for E between -1.0 and -3.5 V. At $E \geqslant$ -0.7 V, no significant amounts of Ni were found inside the pores after 1 min of deposition. On the other hand, the current transient for the deposition at -4.0 V shows a completely different behavior, with a rapid drop to almost zero after the first 10 s. The same drop of the current density to almost zero was also observed during LSV inside the nanopores, occurring at -2.8 and -4.0 V (Fig. 2.1). For a better comparison, the current density values after 1 min of Ni deposition were plotted in Fig. 2.1, showing a good agreement with the linear sweep voltammetry curves.

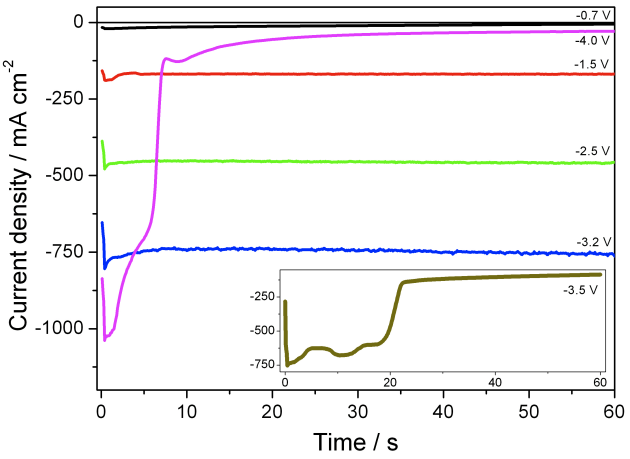


Figure 2.3: Selected current density transients during Ni electrodeposition in NpATs performed at different constant potentials for 1 min. Inset evidences the H_2 gas bubble formation and release during an anomalous Ni deposition at -3.5 V.

Due to the thorough process of template preparation and accurate control of the several experimental parameters of electrodeposition, three reproducibility experiments were performed for each E. The samples where the current density dropped to almost zero after a few seconds are here called anomalous samples, while those where the deposition current density remained approximately constant during the 1 min of deposition are called normal samples. These reproducibility tests were performed at E between -1.0 and -4.0 V. For Ni deposition at $E \geqslant$ -2.0 V all samples presented the expected current density transient during the 1 min experiment, so that one obtained 100% of normal samples. For $E \leqslant$ -2.5 V the percentage of normal samples linearly dropped to 0% at -4.0 V (Fig. 2.4). When increasing the cathodic potential applied we are raising the amount of Ni^{2+} and H^{+} ions at the cathode surface. Therefore j_{Ni} will be higher, but as a result of the local deposition temperature raise and thus local decrease of pH, j_{HER} will also increase [30]. Consequently, there is a higher probability of the nucleation of H_2 gas bubbles to occur at the cathode surface, stopping Ni deposition and leading to the sudden decrease of the current density to almost zero. Nevertheless, one notes that j_{HER} was reported to be around 5% of the total current density during Ni deposition in these experimental conditions [30]. This value is high enough for the local nucleation of H_2 gas bubbles to occur at high cathodic potentials.

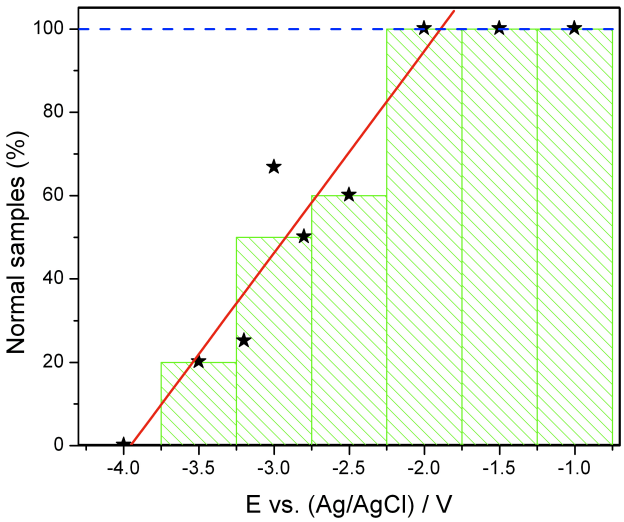


Figure 2.4: Percentage of normal samples obtained at different applied potentials during Ni deposition inside nanopores.

Additionally, note that the use of a two-step anodization process for the preparation of NpATs leads to ordered hexagonal arrays of nanopores with a diameter dispersion of $\sim$ 6% [41], although the boundaries between adjacent ordered domains present pores with larger diameters ($\sim$ 3% of the total number of pores). When increasing the applied cathodic potential one enlarges the probability that small deviations in the nanopore diameters affect the nucleation of H_2 gas bubbles, stopping further Ni deposition, and resulting in an inhomogeneous NWs length distribution. This phenomenon can easily be seen in the fluctuations of the current density transients during Ni deposition (inset of Fig. 2.3), corresponding to the formation and release of H_2 gas bubbles inside a small fraction of nanopores.

At very high cathodic potentials (E = -4 V), Ni deposition will stop in almost all nanopores after a few seconds, keeping Ni deposition only in $\sim$ 3% of the total number of pores (corresponding to the larger pores present at the ordered domain boundaries). This is in good agreement with the decrease of $\sim$ 97% observed in j_{total}, as shown in Fig. 2.3.

2.1.3.3 Structural and Morphological Properties

XRD measurements confirmed the presence of Ni for all depositions at $E \leqslant$ -1.0 V. These samples show similar patterns of face-centered cubic (fcc) Ni strongly textured along the [220] direction (Fig. 2.5), mainly due to the nanopores' geometrical confinement, in good agreement with previous works [46, 47]. This preferential growth can also be attributed to the high overpotentials used that kinetically favor the (220) face formation [39, 48]. The inset of Fig. 2.5 shows a detail of the most intense Ni peak. The grain size of the Ni NWs was estimated using the Scherrer equation [49], with results varying between 80 and 100 nm. We found an overall slight decrease of the NWs grain size with decreasing E down to -3.2 V. In fact, it was previously reported that in Ni thin films the grain size decreases rapidly with increasing current deposition density up to 75 mA cm^{-2}, above which no significant effect is observed [50]. We can thus state that the applied potentials between -1.0 and -4.0 V (combined with the conditions here used) produce fcc Ni NWs with a preferred orientation along [220]. This control of the crystallographic structure of the Ni NWs is very important, since it strongly affects the corresponding magnetic properties.

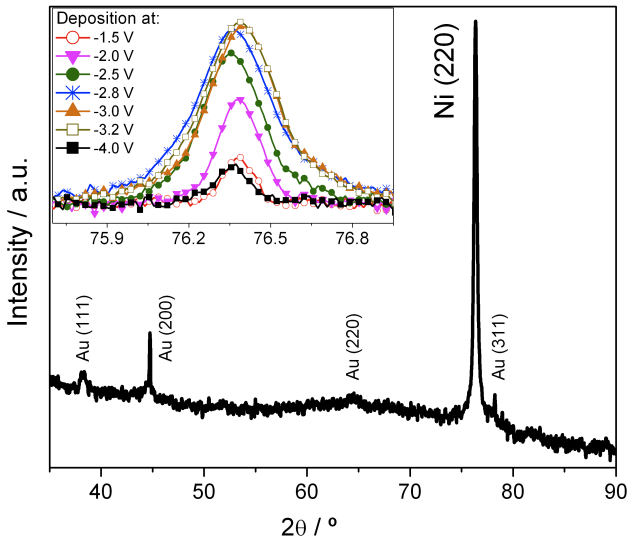


Figure 2.5: XRD pattern of the Ni NWs electrodeposited in a NpAT at -2.5 V. Inset shows a detail of the (220) Ni peak for selected samples.

Ni NWs were also characterized by FESEM cross-sectional views, after breaking the alumina samples. Fig. 2.6a-h shows that a uniform deposition of well-defined and defect-free Ni inside the nanopores can be obtained for all normal samples. Although some fractured NWs can be seen, these likely resulted from the cracking of the alumina templates during FESEM samples preparation. In the

anomalous samples we found some areas where the Ni NWs electrodeposited had an inhomogeneous length distribution (Fig. 2.6i). As previously explained, at higher cathodic potentials, small variations in the nanopores' diameter, local temperature and pH become more relevant. The probability of H_2 gas bubbles to nucleate and stop subsequent Ni deposition increases with the applied cathodic potential. These only affect the NWs length and consequently their size distribution throughout the membrane, and at very high cathodic potentials (E = -4 V) Ni deposition stops in almost all nanopores after a few seconds (Fig. 2.6j).

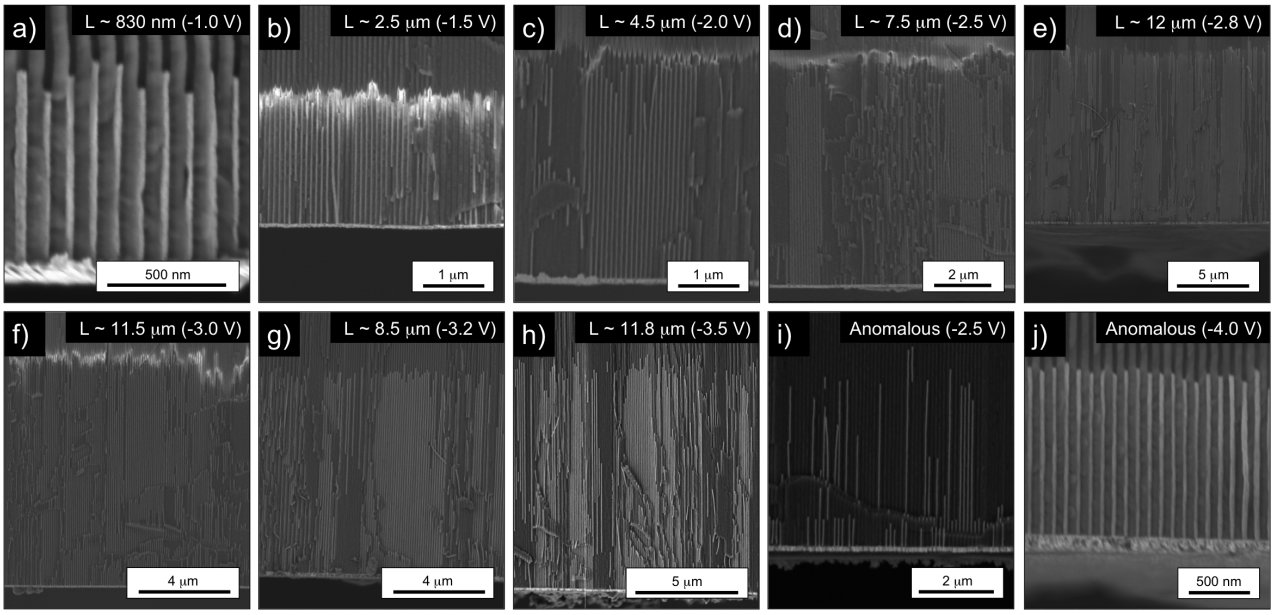


Figure 2.6: FESEM cross-sectional images of Ni NWs deposited in NpATs for 1 min at a constant potential of: (a) -1.0 V ($L \sim 830$ nm); (b) -1.5 V ($L \sim 2.5$ μm); (c) -2.0 V ($L \sim 4.5$ μm); (d) -2.5 V ($L \sim 7.5$ μm); (e) -2.8 V ($L \sim 12$ μm); (f) -3.0 V ($L \sim 11.5$ μm); (g) -3.2 V ($L \sim 8.5$ μm); (h) -3.5 V ($L \sim 11.8$ μm); (i) -2.5 V (anomalous sample); (j) -4.0 V (anomalous sample).

Fig. 2.7 shows the dependence of the deposition rate (η) on the applied potential for Ni deposition, estimated using the normal samples. The average length of the Ni NWs linearly increases with $\mid E \mid$. Our experiments then allowed the estimation of the rate of Ni deposition inside the nanopores for any applied potential: η (μm min^{-1}) = 4.5 $\times$ $\mid E \mid$ – 3.5, reaching $\sim$ 12 μm min^{-1} for $E \sim$ -3.5 V. Most reports on Ni electrodeposition at constant potentials have so far been performed at around -1 V, which corresponds to a deposition rate more than 10 times smaller ($\eta \sim 0.8$ μm min^{-1}).

2.1.3.4 Magnetic Properties

Most of Ni NW array applications exploit the corresponding magnetic properties, particularly the high shape anisotropy [51, 52]. One important step to improve the magnetic properties of Ni NWs is the optimization of their fabrication process. High aspect ratio Ni NWs have sharp magnetization reversal, high coercive field (H_c) and large squareness (S) for an applied magnetic field (H) along the wire long axis ($\parallel$ direction). On the other hand, for H perpendicular to the wire axis ($\perp$ direction),

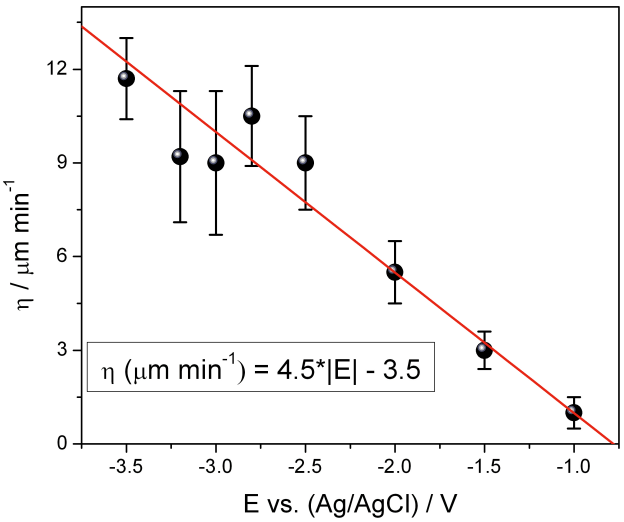


Figure 2.7: Ni deposition rate η after 1 min of deposition at different applied potentials. The error bars were estimated considering several samples fabricated at each potential.

hysteresis is much reduced leading to lower values of H_c and S. The easy axis of magnetization is therefore oriented parallel to the long wire axis as previously reported [51, 53].

Hysteresis loops of the Ni NWs grown in the NpATs were measured using VSM (Fig. 2.8a). Similar magnetic properties were observed for all samples: $H_c^{\parallel} \gg H_c^{\perp}$ and $S^{\parallel} \gg S^{\perp}$. The coercive field measured along the wire axis ($H_c^{\parallel}$) ranged between 800 and 1100 Oe, showing the same overall trend with E for both normal and anomalous samples (Fig. 2.8b). As expected, the values of the coercive field measured perpendicular to the wire axis ($H_c^{\perp}$) were found to be one order of magnitude lower than $H_c^{\parallel}$ (between 100 and 170 Oe), showing however the same overall trend with E for all samples.

The squareness is defined as the ratio between remanent (M_R) and saturation (M_{Sat}) magnetization. Along the wire axis, squareness is close to 1 for all samples, revealing the high magnetic anisotropy in the parallel direction (Fig. 2.8c). Perpendicular to the wire axis, squareness is small (around 0.05 for normal samples and around 0.1 for the anomalous ones).

It is important to note that squareness and coercivity depend on the aspect ratio of the Ni NWs. However, all the results plotted in Fig. 2.8 correspond to Ni NWs with the same diameter and aspect ratios between 16 and 240. For very high aspect ratio values (> 10) only small variations of S are expected [54], so that the coercivity and squareness are not expected to depend much on wire length in our samples, as observed. Magnetic measurements also show no evidence of the presence of impurities or defects in the fabricated Ni NWs. If Ni hydroxides were present, the coercive field and squareness along the long axis would be much smaller [33, 55]. The fact that similar magnetic measurements were obtained for all samples allowed us to infer that no significant amount of impurities is present in the anomalous samples when compared to the normal ones.

The magnetic texture, measured as the ratio between the remanent magnetization perpendicular and parallel to the wire axis ($M_R^{\perp}/M_R^{\parallel}$) [33], is summarized in Fig. 2.8d. The values obtained ranged

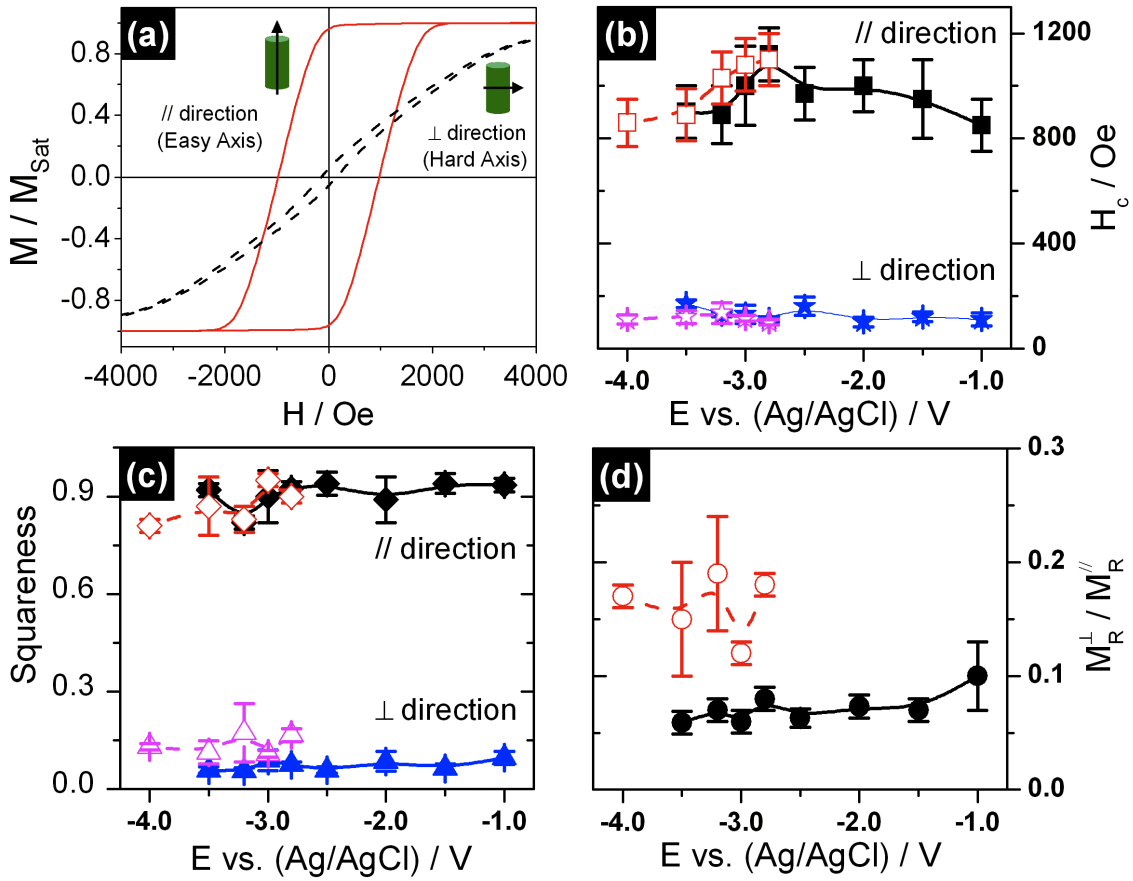


Figure 2.8: (a) Selected hysteretic cycles of Ni NWs measured by VSM, with the magnetic field applied parallel (solid line) and perpendicular (dashed line) to the nanowires axis. Influence of deposition potential on: (b) the coercive field parallel (squares) and perpendicular (triangles) to the wire axis; (c) the squareness parallel (diamonds) and perpendicular (triangles) to the wire axis; and (d) the magnetic texture (circles); for normal (filled symbols) and anomalous (open symbols) samples.

between $0.05-0.1$ for the normal samples and $0.1-0.3$ for the anomalous ones. The smaller magnetic texture corresponds to a better orientation of the magnetization along the wire axis. The higher value observed for the anomalous samples should be related with an inhomogeneous distribution of the NWs length.

The saturation magnetic moment (m_{Sat}) follows the mass distribution of the deposited Ni (Fig. 2.9). The Ni mass electrodeposited was estimated using Faraday's laws of electrochemistry. From the magnetic and structural characterizations already presented we concluded that no impurities were present and pure Ni was electrodeposited. Since the concentration of Ni^{2+} ions in the electrolyte used is very high, and for this electrolyte the current efficiency is 95% (as discussed before), one does not expect a large contribution from HER to the overall electrodeposition current ($j_{HER} \approx 0.05 \times j$). We can thus estimate the charge involved in the Ni deposition reaction as the integral of the current transients, considering a current efficiency of $\sim 95\%$ [Eq. (2.1)]. One should note that, even for the anomalous Ni deposition current transients, where j suddenly drops to almost zero, m_{Sat} follows the

same linear trend with the calculated Ni mass (Fig. 2.9). The expected linear relationship allowed us to extract M_{Sat} for Ni NWs ($\sim$ 49.5 emu g^{-1}), which compares well with other reported values (46 – 50 emu g^{-1}) [17, 56], being slightly lower than M_{Sat} of bulk Ni ($\sim$ 55 emu g^{-1}) [52, 57]. The lower value of M_{Sat} for Ni NWs can be attributed to the presence of a thin nickel oxide layer of $\sim$ 1.5 nm thick at the surface of the nanowires.

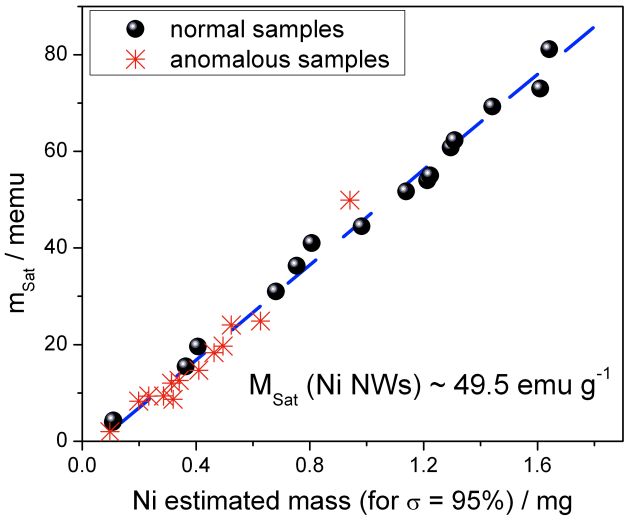


Figure 2.9: Saturation magnetic moment at a field of 15,000 Oe vs. the Ni estimated mass (considering a deposition current efficiency of 95% [30]). The linear fit allows extracting the saturation magnetization value of around 49.5 emu g^{-1} for Ni NWs.

2.1.4 Conclusions

In this work we fabricated in a controlled manner Ni NWs with similar crystallographic, morphologic and magnetic properties by applying different deposition potentials. We then found a wide range of cathodic potentials (from -1 to -3.5 V vs. Ag/AgCl) that allow the electrodeposition of smooth and well-defined Ni NWs in NpATs. The Ni deposition rate was observed to increase with the cathodic applied potential, η (μm min^{-1}) = 4.5 $\times$ | E | – 3.5, reaching $\sim$ 12 μm min^{-1} for $E \sim$ -3.5 V. This rate is approximately 10 times higher than at -1 V (the value usually reported in the literature). Such negative applied potentials allow the faster growth of long Ni NWs. However, it also increases the probability of small deviations in the pore diameter, local temperature and pH to affect the nucleation of H_2 gas bubbles, stopping subsequent Ni deposition, and resulting in an inhomogeneous NW length distribution. For $E \geqslant$ -2.0 V all the samples showed normal current density transients. However, for $E \leqslant$ -2.5 V the probability of H_2 gas bubbles to stop deposition increased linearly, reaching 100% at -4.0 V. Magnetic measurements showed high shape anisotropy for all samples, making them prospective candidates for magnetic memory devices. Moreover, the optimization of the DC deposition here described can improve the industrial production of large and organized arrays of high quality nanostructures making this a much easier and faster process.

Bibliography

[1] R. Orinakova, A. Turonova, D. Kladekova, M. Galova, and R. M. Smith, "Recent developments in the electrodeposition of nickel and some nickel-based alloys", vol. 36, no. 63, pp. 957–972, 2006.

[2] F. Byrne, A. Prina-Mello, A. Whelan, B. M. Mohamed, A. Davies, Y. K. Gunko, J. M. D. Coey, and Y. Volkov, "High content analysis of the biocompatibility of nickel nanowires", *J. Magn. Magn. Mater.*, vol. 321, no. 10, pp. 1341–1345, 2009.

[3] A. A. Stashkevich, Y. Roussigne, P. Djemia, S. M. Cherif, P. R. Evans, A. P. Murphy, W. R. Hendren, R. Atkinson, R. J. Pollard, A. V. Zayats, G. Chaboussant, and F. Ott, "Spin-wave modes in Ni nanorod arrays studied by Brillouin light scattering", *Phys. Rev. B*, vol. 80, no. 14, pp. 144406, 2009.

[4] S.-F. Chen, H. H. Wei, C.-P. Liu, C. Y. Hsu, and J. C. A. Huang, "Microstructural effects on the magnetic and magneto-transport properties of electrodeposited Ni nanowire arrays", *Nanotechnology*, vol. 21, no. 42, pp. 425602, 2010.

[5] A. N. Banerjee, S. Qian, and S. W. Joo, "Large field enhancement at electrochemically grown quasi-1D Ni nanostructures with low-threshold cold-field electron emission", *Nanotechnology*, vol. 22, no. 3, pp. 035702, 2011.

[6] H. M. Chen and R.-S. Liu, "Architecture of metallic nanostructures: Synthesis strategy and specific applications", *J. Phys. Chem. C*, vol. 115, pp. 3513–3527, 2011.

[7] T. M. Whitney, J. S. Jiang, P. C. Searson, and C. L. Chien, "Fabrication and magnetic properties of arrays of metallic nanowires", *Science*, vol. 261, no. 5126, pp. 1316–1319, 1993.

[8] C. R. Martin, "Nanomaterials: A membrane-based synthetic approach", *Science*, vol. 266, no. 5193, pp. 1961–1966, 1994.

[9] T. Thurn-Albrecht, J. Schotter, G. A. Kastle, N. Emley, T. Shibauchi, L. Krusin-Elbaum, K. Guarini, C. T. Black, M. T. Tuominen, and T. P. Russell, "Ultrahigh-density nanowire arrays grown in self-assembled diblock copolymer templates", *Science*, vol. 290, no. 5499, pp. 2126–2129, 2000.

[10] M. Tanase, L. A. Bauer, A. Hultgren, D. M. Silevitch, L. Sun, D. H. Reich, P. C. Searson, and G. J. Meyer, "Magnetic alignment of fluorescent nanowires", *Nano Lett.*, vol. 1, no. 3, pp. 155–158, 2001.

[11] H. M. Chen, C. F. Hsin, P. Y. Chen, R.-S. Liu, S.-F. Hu, C.-Y. Huang, J.-F. Lee, and L.-Y. Jang, "Ferromagnetic $CoPt_3$ nanowires: Structural evolution from fcc to ordered $L1^2$", *J. Am. Chem. Soc.*, vol. 131, no. 43, pp. 15794–15801, 2009.

[12] K. Nielsch, F. Muller, A.-P. Li, and U. Gosele, "Uniform nickel deposition into ordered alumina pores by pulsed electrodeposition", *Adv. Mater.*, vol. 12, no. 8, pp. 582–586, 2000.

[13] H. Masuda and K. Fukuda, "Ordered metal nanohole arrays made by a two-step replication of honeycomb structures of anodic alumina", *Science*, vol. 268, pp. 1466–1468, 1995.

[14] O. Jessensky, F. Muller, and U. Gosele, "Self-organized formation of hexagonal pore arrays in anodic alumina", *Appl. Phys. Lett.*, vol. 72, no. 10, pp. 1173–1175, 1998.

[15] G. Sharma, M. V. Pishko, and C. A. Grimes, "Fabrication of metallic nanowire arrays by electrodeposition into nanoporous alumina membranes: Effect of barrier layer", *J. Mater. Sci.*, vol. 42, no. 13, pp. 4738–4744, 2007.

[16] N. J. Gerein and J. A. Haber, "Effect of ac electrodeposition conditions on the growth of high aspect ratio copper nanowires in porous aluminum oxide templates", *J. Phys. Chem. B*, vol. 109, no. 37, pp. 17372–17385, 2005.

[17] C. T. Sousa, D. C. Leitao, M. P. Proenca, A. Apolinario, J. G. Correia, J. Ventura, and J. P. Araujo, "Tunning pore filling of anodic alumina templates by accurate control of the bottom barrier layer thickness", *Nanotechnology*, vol. 22, no. 31, pp. 315602, 2011.

[18] Y. Rheem, B.-Y. Yoo, W. P. Beyermann, and N. V. Myung, "Magnetotransport studies of a single nickel nanowire", *Nanotechnology*, vol. 18, no. 1, pp. 015202, 2007.

[19] H. Pan, B. Liu, J. Yi, C. Poh, S. Lim, J. Ding, Y. Feng, C. H. A. Huan, and J. Lin, "Growth of single-crystalline Ni and Co nanowires via electrochemical deposition and their magnetic properties", vol. 109, no. 8, pp. 3094–3098, 2005.

[20] D. Navas, K. R. Pirota, P. Mendoza Zelis, D. Velazquez, C. A. Ross, and M. Vazquez, "Effects of the magnetoelastic anisotropy in Ni nanowire arrays", *J. Appl. Phys.*, vol. 103, no. 7, pp. 07D523, 2008.

[21] P. Cojocaru, L. Magagnin, E. Gomez, and E. Valles, "Nanowires of NiCo/barium ferrite magnetic composite by electrodeposition", *Mater. Lett.*, vol. 65, no. 17-18, pp. 2765–2768, 2011.

[22] S. Spanou and E. A. Pavlatou, "Pulse electrodeposition of Ni/nano-TiO_2 composites: Effect of pulse frequency on deposits properties", *J. Appl. Electrochem.*, vol. 40, no. 7, pp. 1325–1336, 2010.

[23] K. S. Napolskii, I. V. Roslyakov, A. A. Eliseev, D. I. Petukhov, A. V. Lukashin, S.-F. Chen, C.-P. Liu, and G. A. Tsirlina, "Tuning the microstructure and functional properties of metal nanowire arrays via deposition potential", *Electrochim. Acta*, vol. 56, no. 5, pp. 2378–2384, 2011.

[24] H. Deligianni and L. T. Romankiw, "In situ surface pH measurement during electrolysis using a rotating pH electrode", *IBM J. Res. Dev.*, vol. 37, no. 2, pp. 85–95, 1993.

[25] J. A. Koza, M. Uhlemann, A. Gebert, and L. Schultz, "The effect of a magnetic field on the pH value in front of the electrode surface during the electrodeposition of Co, Fe and CoFe alloys", *J. Electroanal. Chem.*, vol. 617, pp. 194–202, 2008.

[26] C. Yu, Y. Xie, T. Xu, Y. Chen, X. Li, W. Li, B. Liu, and X. Zhang, "Growth kinetics of nickel crystals in nanopores", *Cryst. Growth Des.*, vol. 9, no. 9, pp. 3840–3843, 2009.

[27] A. Ghahremaninezhad and A. Dolati, "A study on electrochemical growth behavior of the Co-Ni alloy nanowires in anodic aluminum oxide template", *J. Alloys Compd.*, vol. 480, pp. 275–278, 2009.

[28] A. Ghahremaninezhad and A. Dolati, "Diffusion-controlled growth model for electrodeposited cobalt nanowires in highly ordered aluminum oxide membrane", *ECS Trans.*, vol. 28, no. 17, pp. 13–25, 2010.

[29] A. Ispas, *Electrochemical phase formation of Ni and Ni-Fe alloys in a magnetic field*, PhD thesis, Technical University of Dresden, Germany, 2007.

[30] M. Motoyama, Y. Fukunaka, Y. H. Ogata, and F. B. Prinz, "Impact of accompanying hydrogen generation on metal nanotube electrodeposition", *J. Electrochem. Soc.*, vol. 157, no. 6, pp. D357–D369, 2010.

[31] Y. Fukunaka, M. Motoyama, Y. Konishi, and R. Ishii, "Producing shape-controlled metal nanowires and nanotubes by an electrochemical method", *Electrochem. Solid-State Lett.*, vol. 9, no. 3, pp. C62–C64, 2006.

[32] D. C. Leitao, J. Ventura, C. T. Sousa, A. M. Pereira, J. B. Sousa, M. Vazquez, and J. P. Araujo, "Insights into the role of magnetoelastic anisotropy in the magnetization reorientation of magnetic nanowires", *Phys. Rev. B*, vol. 84, no. 1, pp. 014410, 2011.

[33] V. Haehnel, S. Fahler, P. Schaaf, M. Miglierini, C. Mickel, L. Schultz, and H. Schlorb, "Towards smooth and pure iron nanowires grown by electrodeposition in self-organized alumina membranes", *Acta Mater.*, vol. 58, no. 7, pp. 2330–2337, 2010.

[34] R. Inguanta, S. Piazza, and C. Sunseri, "Influence of the electrical parameters on the fabrication of copper nanowires into anodic alumina templates", vol. 255, no. 21, pp. 8816–8823, 2009.

[35] S. Shin, B. S. Kim, K. M. Kim, B. H. Kong, H. K. Cho, and H. H. Cho, "Tuning the morphology of copper nanowires by controlling the growth processes in electrodeposition", *J. Mater. Chem.*, vol. 21, no. 44, pp. 17967, 2011.

[36] F. Tian, J. Zhu, D. Wei, and Y. T. Shen, "Magnetic field assisting DC electrodeposition: General methods for high-performance Ni nanowire array fabrication", *J. Phys. Chem. B*, vol. 109, no. 31, pp. 14852–14854, 2005.

[37] R. Inguanta, S. Piazza, and C. Sunseri, "Influence of electrodeposition techniques on Ni nanostructures", *Electrochim. Acta*, vol. 53, no. 19, pp. 5766–5773, 2008.

[38] K. M. Razeeb, F. M. F. Rhen, and S. Roy, "Magnetic properties of nickel nanowires: Effect of deposition temperature", *J. Appl. Phys.*, vol. 105, no. 8, pp. 083922, 2009.

[39] A. Cortes, G. Riveros, J. L. Palma, J. C. Denardin, R. E. Marotti, E. A. Dalchiele, and H. Gomez, "Single-crystal growth of nickel nanowires: Influence of deposition conditions on structural and magnetic properties", *J. Nanosci. Nanotechnol.*, vol. 9, no. 3, pp. 1992–2000, 2009.

[40] M. P. Proenca, C. T. Sousa, D. C. Leitao, J. Ventura, J. B. Sousa, and J. P. Araujo, "Nanopore formation and growth in phosphoric acid Al anodization", *J. Non-Cryst. Solids*, vol. 354, pp. 5238–5240, 2008.

[41] D. C. Leitao, A. Apolinario, C. T. Sousa, J. Ventura, J. B. Sousa, M. Vazquez, and J. P. Araujo, "Nanoscale topography: A tool to enhance pore order and pore size distribution in anodic aluminum oxide", *J. Phys. Chem. C*, vol. 115, no. 17, pp. 8567–8572, 2011.

[42] S. J. Hearne and J. A. Floro, "Mechanisms inducing compressive stress during electrodeposition of Ni", *J. Appl. Phys.*, vol. 97, no. 1, pp. 014901, 2005.

[43] G. Tong, J. Guan, Z. Xiao, F. Mou, W. Wang, and G. Yan, "In situ generated H_2 bubble-engaged assembly: A one-step approach for shape-controlled growth of Fe nanostructures", *Chem. Mater.*, vol. 20, no. 4, pp. 3535–3539, 2008.

[44] A. J. Bard and L. R. Faulkner, *Electrochemical methods: Fundamentals and applications*, John Wiley & Sons, Inc., USA, 2001.

[45] A. C. F. Ribeiro, J. C. S. Gomes, C. I. A. V. Santos, V. M. M. Lobo, M. A. Esteso, and D. G. Leaist, "Ternary mutual diffusion coefficients of aqueous $NiCl_2$+ NaCl and $NiCl_2$+ HCl solutions at 298.15 K", *J. Chem. Eng. Data*, vol. 56, pp. 4696–4699, 2011.

[46] H. Pan, H. Sun, C. Poh, Y. Feng, and J. Lin, "Single-crystal growth of metallic nanowires with preferred orientation", *Nanotechnology*, vol. 16, no. 9, pp. 1559–1564, 2005.

[47] F. Tian, J. Zhu, and D. Wei, "Phase transition and magnetism of Ni nanowire arrays", *J. Phys. Chem. C*, vol. 111, no. 19, pp. 6994–6997, 2007.

[48] E. Budevski, G. Staikov, and W. J. Lorenz, *Electrochemical phase formation and growth*, VCH Verlagsgesellschaft mbH, Weinheim, 1996.

[49] A. L. Patterson, "The Scherrer formula for X-ray particle size determination", *Phys. Rev.*, vol. 56, pp. 978–982, 1939.

[50] A. M. Rashidi and A. Amadeh, "The effect of current density on the grain size of electrodeposited nanocrystalline nickel coatings", *Surf. Coat. Technol.*, vol. 202, no. 16, pp. 3772–3776, 2008.

[51] K. Nielsch, R. B. Wehrspohn, J. Barthel, J. Kirschner, U. Gosele, S. F. Fischer, and H. Kronmuller, "Hexagonally ordered 100 nm period nickel nanowire arrays", *Appl. Phys. Lett.*, vol. 79, no. 9, pp. 1360–1362, 2001.

[52] K. Pitzschel, J. Bachmann, S. Martens, J. M. Montero-Moreno, J. Kimling, G. Meier, J. Escrig, K. Nielsch, and D. Gorlitz, "Magnetic reversal of cylindrical nickel nanowires with modulated diameters", *J. Appl. Phys.*, vol. 109, no. 3, pp. 033907, 2011.

[53] G. Kartopu, O. Yalcin, K.-L. Choy, R. Topkaya, S. Kazan, and B. Aktas, "Size effects and origin of easy-axis in nickel nanowire arrays", *J. Appl. Phys.*, vol. 109, no. 3, pp. 033909, 2011.

[54] H. Schlorb, V. Haehnel, M. S. Khatri, A. Srivastav, A. Kumar, L. Schultz, and S. Fahler, "Magnetic nanowires by electrodeposition within templates", *Phys. Status Solidi B*, vol. 247, no. 10, pp. 2364–2379, 2010.

[55] D. J. Sellmyer, M. Zheng, and R. Skomski, "Magnetism of Fe, Co and Ni nanowires in self-assembled arrays", *J. Phys.: Condens. Matter*, vol. 13, pp. R433–R460, 2001.

[56] A. O. Fung, V. Kapadia, E. Pierstorff, D. Ho, and Y. Chen, "Induction of cell death by magnetic actuation of nickel nanowires internalized by fibroblasts", *J. Phys. Chem. C*, vol. 112, no. 39, pp. 15085–15088, 2008.

[57] R. Baron and R. W. Hoffman, "Saturation magnetization and perpendicular anisotropy of nickel films", *J. Appl. Phys.*, vol. 41, no. 4, pp. 1623, 1970.

2.2 Article II – Distinguishing Nanowires and Nanotubes Formation by the Deposition Current Transients

Mariana P. Proenca, Célia T. Sousa, João Ventura, Manuel Vazquez and João P. Araujo, *Nanoscale Research Letters* 7 (2012) 280.

Abstract

High aspect ratio Ni nanowires (NWs) and nanotubes (NTs) were electrodeposited inside ordered arrays of self-assembled pores (approximately 50 nm in diameter and approximately 50 μm in length) in anodic alumina templates by a potentiostatic method. The current transients monitored during each process allowed us to distinguish between NW and NT formation. The depositions were long enough for the deposited metal to reach the top of the template and form a continuous Ni film. The overfilling process was found to occur in two steps when depositing NWs and in a single step in the case of NTs. A comparative study of the morphological, structural and magnetic properties of the Ni NWs and NTs was performed using scanning electron microscopy, X-ray diffraction and vibrating sample magnetometry, respectively.

2.2.1 Background

One-dimensional metallic nanostructured materials have attracted extensive attention in recent years because of their technological importance in nanometer-scale devices and information storage systems [1–6]. By combining deposition techniques with nanoporous templates, one can easily tune the growth of these nanostructures and form concentric and multisegmented nanotubes (NTs) and nanowires (NWs) [7–10].

A large number of works have focused on magnetic NWs embedded in ordered arrays of self-assembled pores in alumina membranes [11–17]. However, only a few works have been reported on ordered arrays of magnetic NTs [18–22]. These novel nanostructures have recently attracted much interest due to their inner functionalizable surfaces that can be used for drug delivery [23–25], and also owing to their interesting magnetic behavior [20–22]. In particular, Ni NTs have been prepared in nanoporous membranes by triblock-copolymer-assisted hard-template method [26], electroplating [27], a sequential electrochemical synthetic method inside conducting polypyrrole NTs [8], and using chemically modified templates [28].

In recent reports, the magnetic behavior of arrays of magnetic NTs was investigated [8, 20–22, 26–28]. Nevertheless, there are a number of different parameters that seem to lead to diverse results. For example, Wang *et al.* [22] found higher remanence values for Ni NT arrays with different diameters (25 to 220 nm) when applying the field parallel to the nanotube's axis, evidencing the important role played by shape anisotropy in the magnetic hysteresis loops. However, other works showed that the easy axis of Ni NT arrays with diameters of approximately 200 nm is perpendicular

to the tube axis [21, 26, 28]. Such differences are related to the distinct preparation methods, geometrical characteristics, ordering degree of hexagonal symmetry, or the final crystalline structure of the magnetic elements. Polycrystalline Ni NWs and NTs, with 45 nm diameters, fabricated using a direct-current electrodeposition method also showed similar magnetic hysteresis loops for both NW and NT arrays [27]. In the present work, we used a potentiostatic electrodeposition method to grow Ni NWs and NTs strongly textured along the [110] direction, showing different coercivity values along the parallel direction. One should also note that few reports can be found on the preparation of small-diameter (< 60 nm) Ni NT arrays [22, 27]. Reducing the diameter of these tube-like nanostructures, one expects to increase their coercivity and remanence values along the parallel direction.

The objective of the present work is to address a comparative analysis of careful preparation of Ni NW and NT arrays with well-controlled ordering and their structural and magnetic response. These nanostructures were prepared by potentiostatic electrodeposition of Ni into suitably modified nanoporous alumina templates (NpATs) opened from both top and bottom sides [17]. Long-range ordering of hexagonal symmetry of the alumina membranes with 105 nm interpore distance and 50 nm pore diameter was achieved [29, 30]. The final NW/NT diameter was approximately 50 nm, while the NTs' wall thickness was approximately 5 nm, and their length corresponded to the membrane thickness (50 μm). The time of deposition was controlled by the overfilling process in which a Ni continuous film was formed on top of the membrane. In this work we found this process to be considerably different when depositing NWs or NTs inside the pores. A thorough comparative study of the current transients monitored during the electrodeposition process showed a clear distinction between NW and NT formation. The presence of Ni NWs and NTs inside the nanopores was also confirmed by scanning electron microscopy (SEM).

2.2.2 Methods

Ni was electrodeposited inside self-assembled pores of anodic alumina membranes (approximately 50 nm in pore diameter, approximately 105 nm in interpore distance and approximately 50 μm thick) using a three-electrode cell in a potentiostatic mode. The NpATs were prepared by a two-step anodization process of high purity (99.999%) aluminum disks in 0.3 M oxalic acid at 40 V and 5°C [30]. First and second anodizations were performed during 24 and 20 h, respectively. The Al substrate was then removed on the backside of the membrane by chemical etching in an aqueous solution of 0.2 M $CuCl_2$ and 4.1 M HCl, and the pores widened and opened at the bottom using 0.5 M phosphoric acid at room temperature (Fig. 2.10). Further details on the membranes preparation can be found elsewhere [17].

For the deposition of NWs, a 100 nm thick Au film was sputtered at the opened pores' bottom of the NpAT to serve as the working electrode. In the case of NTs formation, a thinner (approximately 40 nm thick) Au layer was sputtered so as not to completely close the bottom of the pores [31]. To avoid leaking of the electrolyte at the opened membrane bottom, a non-conductive varnish was coated on top of the 40 nm thick Au contact (Fig. 2.10). A Pt mesh was used as the counter electrode

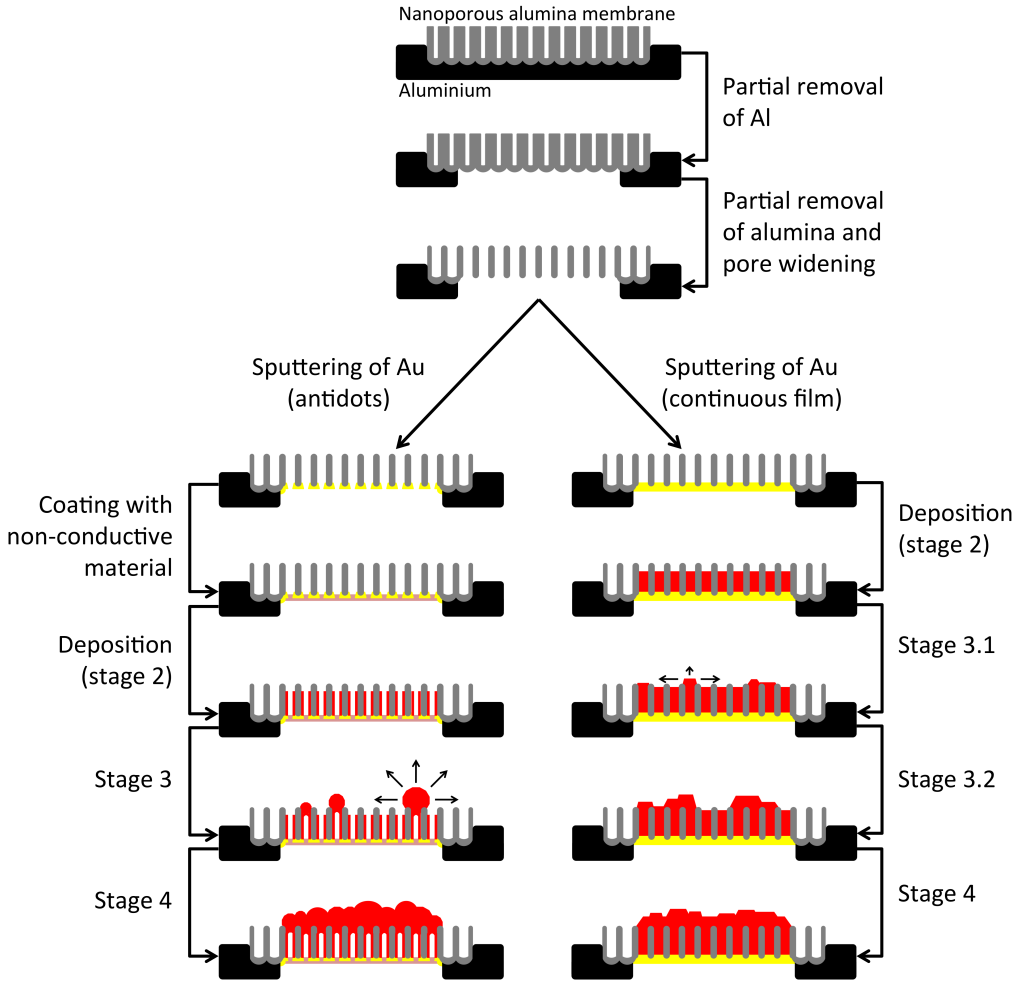


Figure 2.10: Stages in the fabrication of NW and NT arrays in NpATs by potentiostatic deposition.

and Ag/AgCl (in 4 M KCl) as the reference electrode (0.197 V vs. standard hydrogen electrode). The depositions were performed in a Watts bath (1.14 M $NiSO_4 \cdot 6H_2O$, 0.19 M $NiCl_2 \cdot 6H_2O$ and 0.73 M H_3BO_3), at -1.5 V vs. Ag/AgCl, using a Solartron 1480 MultiStat (Solartron Analytical, Farnborough, Hampshire, UK). During the electrodeposition, the electrolyte was magnetically stirred at 250 rpm and kept at a constant temperature of 35°C within a pH range between 3.5 and 4 [32].

To explore the differences between NW and NT formation, the depositions were performed until a continuous Ni film was formed on top of the NpAT. Different stages were then found in the overfilling process, and to better understand them, several experiments were made, stopping the deposition at each stage (Fig. 2.10).

Prior to NW and NT characterization, the Ni film formed on top of the NpAT was removed by mechanical polishing using alumina powder (particle size of 10 μm). The mechanical polishing was only performed on the upper surface of the nanoporous alumina template, in order to remove the Ni caps that overfilled and are present at the membranes' top, without causing any damage to the electrodeposited nanostructures. The remaining Ni caps on top of the NpATs were then completely

etched by ion milling (5 to 10 μm). The milling process was carried out using an ion beam sputter deposition system by Commonwealth Scientific Corporation [15]. Morphological characterization was performed using SEM (FEI Nova NanoSEM 230 and FEI Quanta 400FEG, FEI Co., Eindhoven, The Netherlands). Structural analysis was performed by X-ray diffraction (XRD; PANalytical X'Pert Pro, PANalytical B.V., Almelo, The Netherlands) using Cu $K_{\alpha 1}$ radiation ($\lambda = 0.15406$ nm) and the Bragg-Brentano $\theta/2\theta$ geometry [33]. The deposited NWs and NTs were magnetically characterized using a vibrating sample magnetometer (VSM; LOT-Oriel EV7, LOT-Oriel, Leatherhead, Surrey, UK).

2.2.3 Results and Discussion

2.2.3.1 Structural and Morphological Properties

Smooth and well-defined high aspect ratio (length/diameter approximately 1,000) Ni NWs and NTs were fabricated. For cross-sectional SEM images the filled NpATs were broken and observed in the vertical fractured region (Figs. 2.11a,d). Prior to top and bottom SEM imaging, ion milling was performed to remove the Au contact at the bottom (1 μm) and the Ni caps on top (5 to 10 μm) and smoothen the NpAT surface (Fig. 2.11b,c,e,f). Pore filling percentage is approximately 100% for Ni NWs grown in a NpAT by potentiostatic deposition (Fig. 2.11b,c). The obtained NWs were approximately 50 nm in diameter and approximately 50 μm in length, corresponding to the pores diameter and template thickness, respectively. On the other hand, we observe that the fabrication of Ni NTs leads to only approximately 40% pore filling (Fig. 2.11e), which we attribute to the fact that the nonmetallic coating enters some of the pores and covers the inner Au contact, avoiding subsequent Ni deposition. The optimization of the coating process and material deposition is underway, aiming for 100% NT formation. However, notice that as reported before [15], the obtained percentage of pore filling does not influence the magnetic properties. Additionally, Fig. 2.11d,e,f clearly shows that the NTs outer diameter correspond to the pores diameter (approximately 50 nm), and their wall is smooth and uniform, evidencing a constant thickness value (t_w approximately 5 nm) throughout the whole nanopore. Fig. 2.11f also shows that some NTs do not reach the upper end of the nanopores. This is because the Ni film overgrown on top will cover some of the pores before they can be completely filled with NTs.

XRD measurements illustrate a face-centered cubic (fcc) Ni pattern for the NWs and NTs in NpATs and for the continuous film overgrown on top (Fig. 2.12). The Ni NWs and NTs were found strongly textured along the [110] direction (Fig. 2.12), seemingly due to the nanopores' geometrical confinement [17]. However, the continuous film formed on top exhibits four different peaks that correspond to the (111), (200), (220), and (311) planes of fcc Ni (Fig. 2.12). The Ni crystallite size of the deposited nanostructures was estimated using the Scherrer equation [34], giving 90 $\pm$ 10 nm and 40 $\pm$ 10 nm for the Ni NWs and NTs, respectively. This is consistent with the fact that both nanostructures have the same outer diameter of approximately 50 nm (corresponding to the nanopores' diameter), but the NTs present a core cylindrical hole with an estimated diameter of approximately 40 nm.

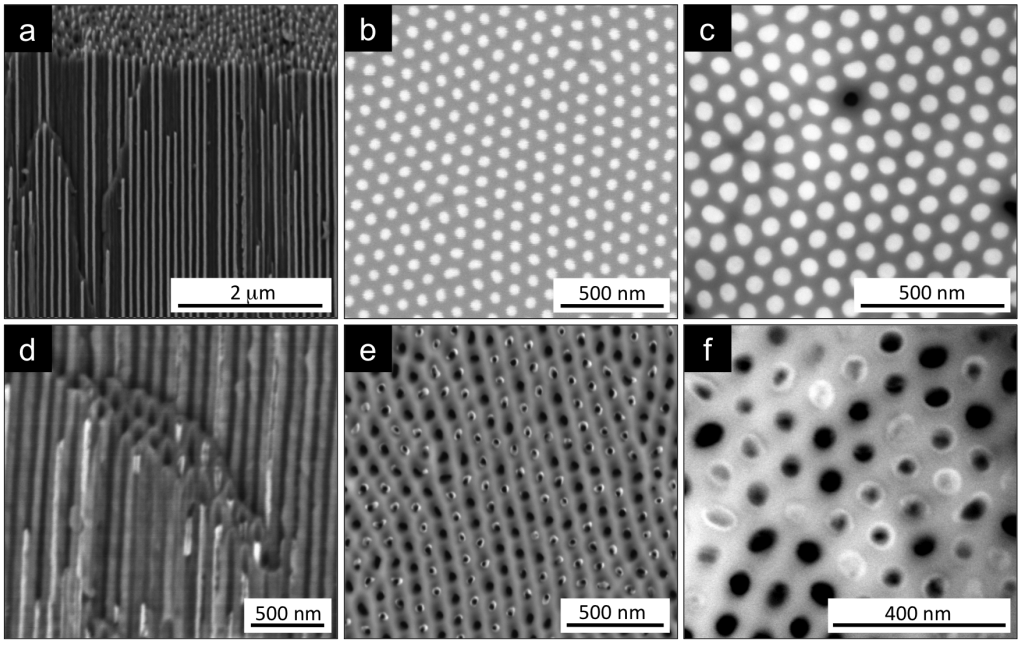


Figure 2.11: SEM images of Ni NWs (a, b, c) and NTs (d, e, f) in NpATs. Cross-sectional (a, d), bottom (b, e, after 1 μm milling), and top (c, f, after 5 μm milling) views.

Therefore, the NTs' crystallite size is much smaller as it corresponds to a thin film of approximately 5 nm wrapped in a cylindrical shape.

The average crystallite sizes of the continuous Ni film overgrown on top of the NpATs were estimated to be of 70 ± 10 nm for the Ni film formed after overgrowth of NWs, and 75 ± 10 nm for the Ni film grown on top of NTs. The grain size of an electrodeposited film is known to strongly depend on the electrodeposition conditions (applied potential, electrolyte composition, temperature, pH, agitation, etc.) and substrate used [35–38]. For both Ni films overgrown on top of NWs or NTs, the deposition conditions were kept the same. However, the substrates on which the films start to grow have different geometries (Fig. 2.13). At the moment when the NWs start overfilling the membrane, their sectional area, which corresponds to approximately 20% of the total membrane's area, has a preferential crystallographic texture along the [110] direction. According to previous works [39, 40], a deposited material will favorably grow epitaxially on oriented grains in the substrate. Therefore, the Ni film overgrown on top of the NWs will continue to exhibit a textured growth orientation along the [110] direction (Fig. 2.12). Nonetheless, since a lateral growth will also start to occur, different grain orientations (along the [111] and [100] directions) can also be found on the Ni film formed.

As for the NTs, their deposition area is approximately 40% of the NWs' area, and their geometry will favor the metal deposition to occur without a preferred orientation (Fig. 2.13). One therefore finds different Ni grain orientations on the film grown on top of the NTs, exhibiting a preferential crystallographic texture along the [100] direction.

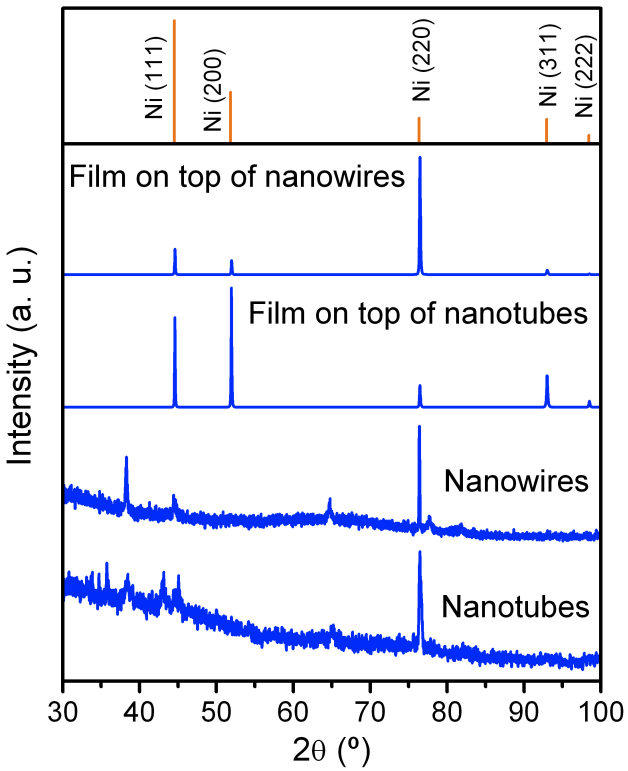


Figure 2.12: XRD patterns of the Ni NWs, NTs and films overgrown on top after electrodeposition in NpAT.

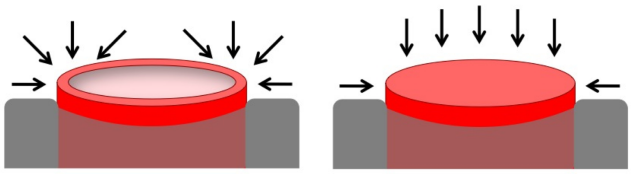


Figure 2.13: Schematic representations of the preferential growth directions of the deposited material. Growth directions on top of a nanotube (left) and nanowire (right).

2.2.3.2 Current Transients during Deposition

The depositions of Ni inside the nanopores were performed until the metal reached the top of the membrane and formed a continuous Ni film. During the complete process of deposition, from the nucleation at the Au contact at the bottom of the pores until the formation of a continuous metallic film on top of the membrane, several stages of metal deposition can be identified. Fig. 2.14a,b illustrates the current transient during Ni NWs and NTs deposition inside the nanopores, respectively, and the overfilling process that leads to the continuous film on top. The nucleation at the Au contact (stage 1) is similar for both nanostructures and has already been described in the literature [41]. During metal growth inside the nanopores (stage 2), the current is approximately constant for the NT formation, corresponding to a constant wall thickness formation throughout the whole tube. However, during NW growth, it slightly increases (by around 4% of its initial value), illustrating the

small enlargement of the pore diameter due to the pore widening process when opening the pores' bottom. In fact, one should note that a small enlargement of approximately 2% in the pore diameter from the lower to the upper part of the membrane results in an approximately 4% raise of the effective deposition area, due to an increase of the membrane's porosity, in good agreement with the current increase seen during deposition.

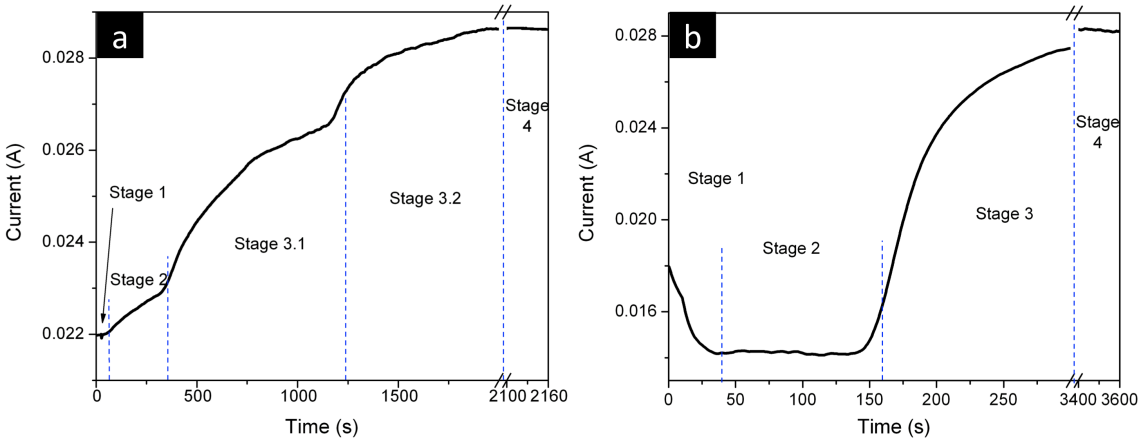


Figure 2.14: Current transients during Ni NW (a) and NT (b) deposition in NpATs.

The main difference found between NW and NT formation occurs when Ni reaches the end of the pores, starting to deposit on top of the membrane. The current transients monitored during this overfilling process allowed us to characterize whether NTs or NWs had grown inside the pores. When NWs are being deposited, the metal overfilling occurs in a two-step process (stages 3.1 and 3.2 in Fig. 2.14a). During the deposition of NWs inside the pores, the electrode area corresponds to the membranes' porosity (approximately 20%). As the first NWs reach the upper end of the pores, they start to form polygonal-shaped caps of Ni on top of the NpAT (Fig. 2.15). These will enlarge the electrode area and therefore increase the deposition current (stage 3.1). When the surface area associated with the deposition of Ni on top of the membrane becomes higher than the area of the remaining opened pores, where NWs are still being formed, a second sudden increase in the deposition current occurs (stage 3.2). At this point, the metallic layer being deposited on top of the NpAT becomes the main cathode surface. Therefore the current will preferentially flow into the metal film being formed on top, increasing the rate of the metallic layer deposition and decreasing the NWs growth rate inside the pores.

On the other hand, once NTs are present inside the pores, their overfill process occurs in a one-step manner (stage 3 in Fig. 2.14b). During the NTs growth inside the pores, the cathode deposition surface is less than 5% of the total NpAT area exposed to the electrolyte. Therefore, as the first NTs emerge and start overfilling, the effective deposition area is drastically enlarged, as confirmed by the sharp increase of the current (stage 3 in Fig. 2.14b). Additionally, the caps formed at the NpAT surface display a spherical shape without well-defined facets (Fig. 2.16). This phenomenon will largely influence the increase in current occurring in only one stage. One should note that as soon as a few spheres are formed on top, the cathode surface area increases to a higher value than

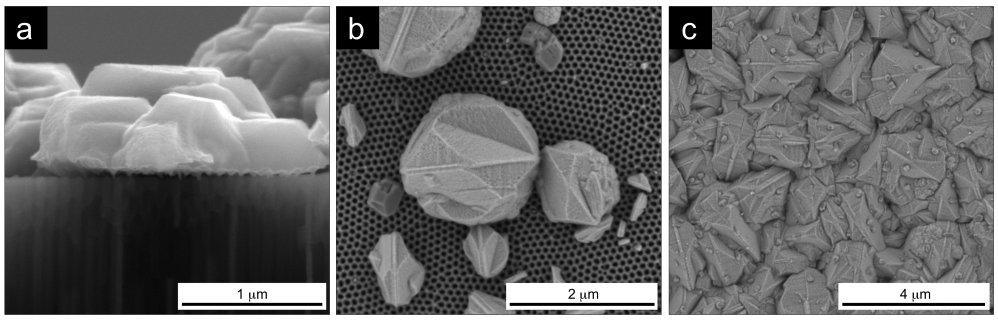


Figure 2.15: Cross-sectional (a) and top (b) SEM images of polygonal caps. These are formed at the NpAT surface when Ni NWs start to overfill, forming a continuous Ni film on top (c).

the effective area of NT deposition inside the nanopores. Stage 3 of NT deposition should therefore be equivalent to stage 3.2 of NW deposition. Since for the NW growth this only occurs after a small amount of Ni film was already formed on top (during stage 3.1), the overfilling process will exhibit two steps during stage 3 (Fig. 2.10).

When considering the current data from Fig. 2.14 together with the XRD data of Fig. 2.12, one can see that the high current increase, observed when the NTs start overfilling, helps promote the growth orientations along the [211] and [100] directions while lowering the [110] texture. However, when the NWs overfill, the current increase is smoother than in the case of the NTs (Fig. 2.14), therefore promoting with less evidence the Ni crystal growth along the [211] and [100] directions (Fig. 2.12).

After complete covering of the nanopores, a continuous Ni film grows at the NpAT surface. This corresponds to stage 4 of deposition (Fig. 2.10), exhibiting a constant current transient, associated with the constant cathode surface area (Fig. 2.14). The deposited films presented different surface morphologies depending on whether NWs or NTs were overfilled. For NWs, it shows smooth facets corresponding to the agglomeration of polygonal caps, typical of crystals with mixed [100] and [110] textures (Fig. 2.15c), while for NTs, it results from the superposition of spherical caps, typical of almost randomly oriented crystals with [100], [110], and [211] textures (Fig. 2.16c). However, in both cases, if a continuous Ni film is formed on top, it then easily detaches from the membrane (Fig. 2.17a). In this way, one can fabricate NpATs with their pores completely filled with NWs or NTs, removing in an easy way all the undesired caps formed on top. The careful observation of the bottom side of the detached Ni film allowed us to visualize the ordered hexagonal pattern printed by the NpAT, and some NWs (Fig. 2.17b) and NTs (Fig. 2.17c) that were broken upon lifting the Ni film. These are, however, very small in length (approximately 100 to 200 nm), corresponding to approximately 0.2% to 0.4% of their total length, and thus will not influence the structural and magnetic properties of the array [15]. The observation of small fractions of NTs at the bottom side of the detached Ni film provides additional evidence that the NTs reach the top of the membrane, maintaining their tubular structure.

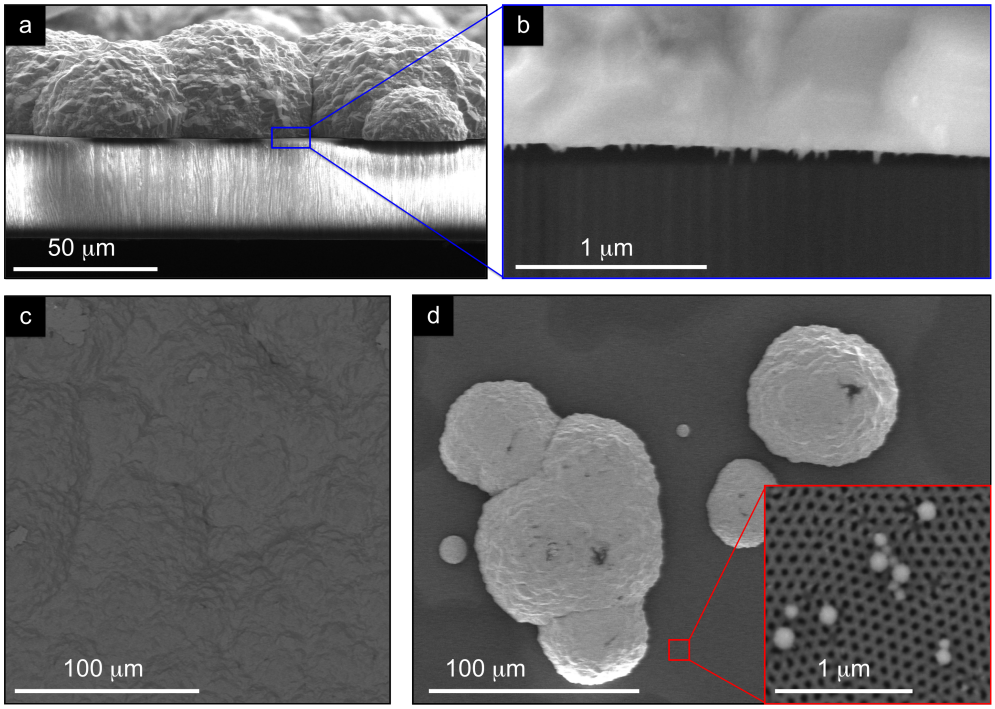


Figure 2.16: Cross-sectional (a, b) and top (c, d) SEM images of spherical polycrystalline caps. These are formed at the NpAT surface when Ni NTs start to overfill (d), creating a continuous Ni film on top (c).

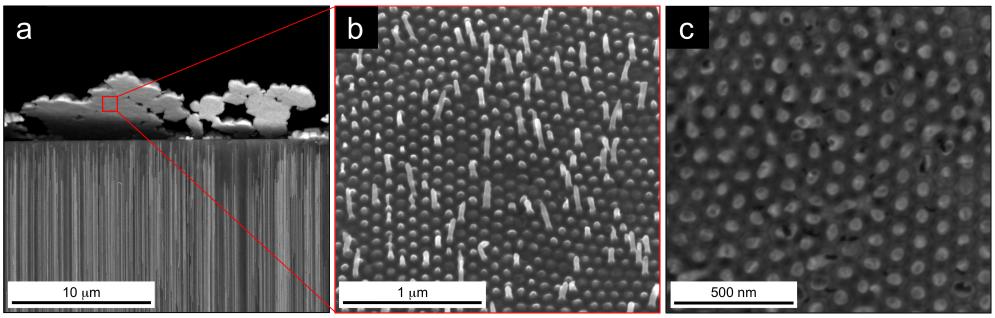


Figure 2.17: SEM images of the Ni film formed on top of the NpAT. Cross-sectional view of respective lift off after NWs deposition (a), and Ni film's bottom view after NWs (b) and NTs (c) deposition.

2.2.3.3 Magnetic Properties

The magnetic behavior of the fabricated samples was studied using a VSM, in two different magnetic field configurations: parallel ($\parallel$, $\varphi = 0°$) and perpendicular ($\perp$, $\varphi = 90°$) modes, according to the angle φ between the applied field and the NW/NT long axis. Magnetic hysteresis loops of Ni NWs and NTs grown in ordered NpATs are presented in Fig. 2.18a,b, respectively. From a straightforward comparison between parallel and perpendicular direction hysteresis loops, we can deduce that the easy magnetization direction is parallel to the NW/NT long axis, and the perpendicular direction is a magnetization hard direction. The easy direction is ascribed to the shape anisotropy of the NWs/NTs [16, 17, 42].

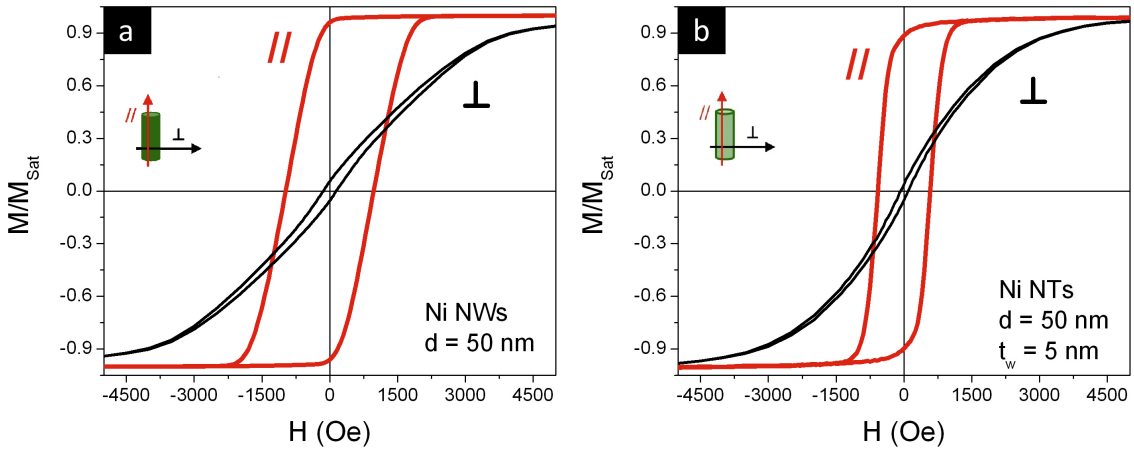


Figure 2.18: Magnetic hysteresis loops of Ni NW (a) and NT (b) arrays in NpATs. The hysteresis loops were measured in the parallel (∥, red) and perpendicular (⊥, black) directions.

The longitudinal anisotropy of the NW/NT arrays is confirmed by the large remanence in the ∥-direction loop that nearly reaches the saturation magnetization (M_{Sat}) value. The coercive field (H_c) is approximately 1,000 Oe for the NW and approximately 600 Oe for the NT arrays, in good agreement with the values reported in previous works [16, 22, 27]. Seemingly, the longitudinal remagnetization involves the presence of domain walls like process. Perpendicular hysteresis loops show reduced coercivity (approximately 100 Oe) and the presence of a magnetization rotation reversal mode. Values of the longitudinal anisotropy field can be derived (from extrapolation of initial susceptibility) to be approximately 3,500 and 2,500 Oe for NWs and NTs, respectively, in agreement with the reduced longitudinal coercivity observed for NTs. One should note that the preparation of NTs with small diameters (< 60 nm) is a laborious process and very difficult to achieve [43], so that most of the reports on magnetic measurements in NT arrays correspond to NTs with outer diameters of approximately 200 nm. For these nanostructures one finds very small coercive fields (< 100 Oe) and remanence (approximately 0.05) along the ∥-direction [8, 20, 21, 26, 28]. However, Wang *et al.* [22, 27] found that coercivity and remanence along the ∥-direction increase with the decrease of the outer diameter, obtaining $H_c^{\parallel}$ of approximately 610 Oe for outer diameters of approximately 45 nm.

2.2.4 Conclusions

In this work we fabricated Ni NW and NT arrays in NpATs by a potentiostatic electrodeposition process using a three-electrode cell. The monitorization of the current transients during deposition allowed us to distinguish between NW and NT formation, and identify the four main stages of deposition in nanoporous membranes. The overfilling of the deposited metal was found to occur in a two-step process for the NWs and only in one step for the NTs. Morphological and structural characterization of the Ni NWs, NTs and film overgrown on top of the membrane was performed by SEM and XRD. Both NWs and NTs exhibit a preferential crystallographic growth textured along the [110] direction. The films overgrown on top illustrated the presence of Ni grains oriented along

the [111], [100] and [110] directions. The Ni NWs overgrow with a preferential orientation along the [110] direction, showing polygonal-shaped caps at the surface of the membrane. On the other hand, the Ni film on top of the NTs exhibits a preferential growth along the [100] direction, and an agglomeration of spherical polycrystalline caps. Magnetic hysteresis loops illustrate a magnetization easy axis parallel to the long axis for both NW and NT arrays, exhibiting stronger anisotropy and higher coercivity values for the NW arrays.

Bibliography

[1] F. Byrne, A. Prina-Mello, A. Whelan, B. M. Mohamed, A. Davies, Y. K. Gunko, J. M. D. Coey, and Y. Volkov, "High content analysis of the biocompatibility of nickel nanowires", *J. Magn. Magn. Mater.*, vol. 321, no. 10, pp. 1341–1345, 2009.

[2] A. A. Stashkevich, Y. Roussigne, P. Djemia, S. M. Cherif, P. R. Evans, A. P. Murphy, W. R. Hendren, R. Atkinson, R. J. Pollard, A. V. Zayats, G. Chaboussant, and F. Ott, "Spin-wave modes in Ni nanorod arrays studied by Brillouin light scattering", *Phys. Rev. B*, vol. 80, no. 14, pp. 144406, 2009.

[3] C. T. Boone, J. A. Katine, J. R. Childress, V. Tiberkevich, A. Slavin, J. Zhu, X. Cheng, and I. N. Krivorotov, "Resonant nonlinear damping of quantized spin waves in ferromagnetic nanowires: A spin torque ferromagnetic resonance study", *Phys. Rev. Lett.*, vol. 103, no. 16, pp. 167601, 2009.

[4] S.-F. Chen, H. H. Wei, C.-P. Liu, C. Y. Hsu, and J. C. A. Huang, "Microstructural effects on the magnetic and magneto-transport properties of electrodeposited Ni nanowire arrays", *Nanotechnology*, vol. 21, no. 42, pp. 425602, 2010.

[5] A. N. Banerjee, S. Qian, and S. W. Joo, "Large field enhancement at electrochemically grown quasi-1D Ni nanostructures with low-threshold cold-field electron emission", *Nanotechnology*, vol. 22, no. 3, pp. 035702, 2011.

[6] X. Kou, X. Fan, R. K. Dumas, Q. Lu, Y. Zhang, H. Zhu, X. Zhang, K. Liu, and J. Q. Xiao, "Memory effect in magnetic nanowire arrays", *Adv. Mater.*, vol. 23, no. 11, pp. 1393–1397, 2011.

[7] H. M. Chen and R.-S. Liu, "Architecture of metallic nanostructures: Synthesis strategy and specific applications", *J. Phys. Chem. C*, vol. 115, pp. 3513–3527, 2011.

[8] D. H. Park, Y. B. Lee, M. Y. Cho, B. H. Kim, S. H. Lee, Y. K. Hong, J. Joo, H. C. Cheong, and S. R. Lee, "Fabrication and magnetic characteristics of hybrid double walled nanotube of ferromagnetic nickel encapsulated conducting polypyrrole", *Appl. Phys. Lett.*, vol. 90, no. 9, pp. 093122, 2007.

[9] W. Lee, R. Scholz, K. Nielsch, and U. Gosele, "A template-based electrochemical method for the synthesis of multisegmented metallic nanotubes", *Angew. Chem. Int. Ed.*, vol. 44, no. 37, pp. 6050–6054, 2005.

[10] S. Karim and K. Maaz, "Magnetic behavior of arrays of nickel nanowires: Effect of microstructure and aspect ratio", *Mater. Chem. Phys.*, vol. 130, no. 3, pp. 1103–1108, 2011.

[11] D. C. Leitao, C. T. Sousa, J. Ventura, J. S. Amaral, F. Carpinteiro, K. R. Pirota, M. Vazquez, J. B. Sousa, and J. P. Araujo, "Characterization of electrodeposited Ni and $Ni_{80}Fe_{20}$ nanowires", *J. Non-Cryst. Solids*, vol. 354, no. 47-51, pp. 5241–5243, 2008.

[12] T. M. Whitney, J. S. Jiang, P. C. Searson, and C. L. Chien, "Fabrication and magnetic properties of arrays of metallic nanowires", *Science*, vol. 261, no. 5126, pp. 1316–1319, 1993.

[13] N. J. Gerein and J. A. Haber, "Effect of ac electrodeposition conditions on the growth of high aspect ratio copper nanowires in porous aluminum oxide templates", *J. Phys. Chem. B*, vol. 109, no. 37, pp. 17372–17385, 2005.

[14] K. Nielsch, F. Muller, A.-P. Li, and U. Gosele, "Uniform nickel deposition into ordered alumina pores by pulsed electrodeposition", *Adv. Mater.*, vol. 12, no. 8, pp. 582–586, 2000.

[15] C. T. Sousa, D. C. Leitao, M. P. Proenca, A. Apolinario, J. G. Correia, J. Ventura, and J. P. Araujo, "Tunning pore filling of anodic alumina templates by accurate control of the bottom barrier layer thickness", *Nanotechnology*, vol. 22, no. 31, pp. 315602, 2011.

[16] K. Nielsch, R. B. Wehrspohn, J. Barthel, J. Kirschner, U. Gosele, S. F. Fischer, and H. Kronmuller, "Hexagonally ordered 100 nm period nickel nanowire arrays", *Appl. Phys. Lett.*, vol. 79, no. 9, pp. 1360–1362, 2001.

[17] M. P. Proenca, C. T. Sousa, J. Ventura, M. Vazquez, and J. P. Araujo, "Ni growth inside ordered arrays of alumina nanopores: Enhancing the deposition rate", *Electrochim. Acta*, vol. 72, pp. 215–221, 2012.

[18] H. Cao, L. Wang, Y. Qiu, Q. Wu, G. Wang, L. Zhang, and X. Liu, "Generation and growth mechanism of metal (Fe, Co, Ni) nanotube arrays", *ChemPhysChem*, vol. 7, no. 7, pp. 1500–1504, 2006.

[19] X. Li, Y. Wang, G. Song, Z. Peng, Y. Yu, X. She, and J. Li, "Synthesis and growth mechanism of Ni nanotubes and nanowires", *Nanoscale Res. Lett.*, vol. 4, pp. 1015–1020, 2009.

[20] D. Li, R. S. Thompson, G. Bergmann, and J. G. Lu, "Template-based synthesis and magnetic properties of cobalt nanotube arrays", *Adv. Mater.*, vol. 20, no. 23, pp. 4575–4578, 2008.

[21] X.-F. Han, S. Shamaila, R. Sharif, J.-Y. Chen, H.-R. Liu, and D.-P. Liu, "Structural and magnetic properties of various ferromagnetic nanotubes", *Adv. Mater.*, vol. 21, no. 45, pp. 4619–4624, 2009.

[22] X. W. Wang, Z. H. Yuan, and B. C. Fang, "Template-based synthesis and magnetic properties of Ni nanotube arrays with different diameters", *Mater. Chem. Phys.*, vol. 125, no. 1-2, pp. 1–4, 2011.

[23] C. T. Sousa, C. Nunes, M. P. Proenca, D. C. Leitao, J. L. F. C. Lima, S. Reis, J. P. Araujo, and M. Lucio, "pH sensitive silica nanotubes as rationally designed vehicles for NSAIDs delivery", *Colloids Surf. B Biointerfaces*, vol. 94, pp. 288–295, 2012.

[24] S. J. Son, X. Bai, and S. B. Lee, "Inorganic hollow nanoparticles and nanotubes in nanomedicine Part 1. Drug/gene delivery applications", *Drug Discov. Today*, vol. 12, no. 15-16, pp. 650–656, 2007.

[25] S. J. Son, J. Reichel, B. He, M. Schuchman, and S. B. Lee, "Magnetic nanotubes for magnetic-field-assisted bioseparation, biointeraction, and drug delivery", *J. Am. Chem. Soc.*, vol. 127, pp. 7316–7317, 2005.

[26] F. Tao, M. Guan, Y. Jiang, J. Zhu, Z. Xu, and Z. Xue, "An easy way to construct an ordered array of nickel nanotubes: The triblock-copolymer-assisted hard-template method", *Adv. Mater.*, vol. 18, no. 16, pp. 2161–2164, 2006.

[27] X. W. Wang, Z. H. Yuan, S. Q. Sun, Y. Q. Duan, and L. J. Bie, "Electrochemically synthesis and magnetic properties of Ni nanotube arrays with small diameter", *Mater. Chem. Phys.*, vol. 112, pp. 329–332, 2008.

[28] J. Bao, C. Tie, Z. Xu, Q. Zhou, D. Shen, and Q. Ma, "Template synthesis of an array of nickel nanotubules and its magnetic behavior", *Adv. Mater.*, vol. 13, no. 21, pp. 1631, 2001.

[29] H. Masuda and K. Fukuda, "Ordered metal nanohole arrays made by a two-step replication of honeycomb structures of anodic alumina", *Science*, vol. 268, pp. 1466–1468, 1995.

[30] M. P. Proenca, C. T. Sousa, D. C. Leitao, J. Ventura, J. B. Sousa, and J. P. Araujo, "Nanopore formation and growth in phosphoric acid Al anodization", *J. Non-Cryst. Solids*, vol. 354, pp. 5238–5240, 2008.

[31] J. Fu, S. Cherevko, and C.-H. Chung, "Electroplating of metal nanotubes and nanowires in a high aspect-ratio nanotemplate", *Electrochem. Commun.*, vol. 10, pp. 514–518, 2008.

[32] J. A. Di Bari, "Electrodeposition of nickel", in *Modern Electroplating*, M. Schlesinger and M. Paunovic, Eds., pp. 79–114. John Wiley and Sons, Inc, New Jersey, 2010.

[33] M. P. Proenca, C. T. Sousa, A. M. Pereira, P. B. Tavares, J. Ventura, M. Vazquez, and J. P. Araujo, "Size and surface effects on the magnetic properties of NiO nanoparticles", *Phys. Chem. Chem. Phys.*, vol. 13, pp. 9561–9567, 2011.

[34] A. L. Patterson, "The Scherrer formula for X-ray particle size determination", *Phys. Rev.*, vol. 56, pp. 978–982, 1939.

[35] I. U. Schuchert, M. E. Toimil Molares, D. Dobrev, J. Vetter, R. Neumann, and M. Martin, "Electrochemical copper deposition in etched ion track membranes: Experimental results and a qualitative kinetic model", *J. Electrochem. Soc.*, vol. 150, no. 4, pp. C189–C194, 2003.

[36] H. Pan, H. Sun, C. Poh, Y. Feng, and J. Lin, "Single-crystal growth of metallic nanowires with preferred orientation", *Nanotechnology*, vol. 16, no. 9, pp. 1559–1564, 2005.

[37] M. E. Toimil Molares, V. Buschmann, D. Dobrev, R. Neumann, R. Scholz, U. Schuchert, I, and J. Vetter, "Single-crystalline copper nanowires produced by electrochemical deposition in polymeric ion track membranes", *Adv. Mater.*, vol. 13, no. 1, pp. 62–65, 2001.

[38] F. Czerwinski and J. A. Szpunar, "Controlling the surface texture of nickel for high temperature oxidation inhibition", *Corr. Sci.*, vol. 41, pp. 729–740, 1999.

[39] S. Psarrou, P. Gyftou, and N. Spyrellis, "Electron microscopy study of nickel and nickel composite electrocoatings", *Mikrochim. Acta*, vol. 136, pp. 159–163, 2001.

[40] J. Amblard, M. Froment, and N. Spyrellis, "Origine des textures dans les depots electrolytiques de nickel", *Surf. Technol.*, vol. 5, pp. 205–234, 1977.

[41] M. Motoyama, Y. Fukunaka, T. Sakka, and Y. H. Ogata, "Initial stages of electrodeposition of metal nanowires in nanoporous templates", *Electrochim. Acta*, vol. 53, no. 1, pp. 205–212, 2007.

[42] G. Kartopu, O. Yalcin, K.-L. Choy, R. Topkaya, S. Kazan, and B. Aktas, "Size effects and origin of easy-axis in nickel nanowire arrays", *J. Appl. Phys.*, vol. 109, no. 3, pp. 033909, 2011.

[43] S. Cherevko, J. Fu, N. Kulyk, S. M. Cho, S. Haam, and C.-H. Chung, "Electrodeposition mechanism of palladium nanotube and nanowire arrays", *J. Nanosci. Nanotechnol.*, vol. 9, no. 5, pp. 3154–3159, 2009.

Chapter 3

Magnetization Reversal in Ordered Arrays of Nanowires and Nanotubes

This Chapter is composed of Articles III and IV, on the magnetization reversal processes in ordered arrays of Co and Ni nanowires (NWs) and nanotubes (NTs), grown inside nanoporous alumina templates. Article III presents the angular dependence of coercivity in ordered arrays of Ni and Co NWs and NTs with outer diameters of ~ 30 and ~ 55 nm. A simple analytical model is used for the study of the corresponding magnetization reversal modes. Comparing the experimental and theoretical data, the magnetization in Ni and Co NW arrays was found to reverse by the nucleation and propagation of a transverse domain wall; while for the NT arrays a critical diameter of ~ 50 nm was found, above which a transition between vortex and transverse reversal modes occurs.

In Article IV, we present a systematic study on magnetization reversal modes and magnetostatic interactions between Co NW and NT arrays with different outer diameters ($30 - 65$ nm). The magnetization processes were studied by the angular dependence of the coercivity and a simple analytical model. Again, a non-monotonic behavior was found for Co NT arrays above a diameter of ~ 50 nm, revealing a transition between the vortex and transverse reversal modes. The magnetic interactions between NWs/NTs with different diameters were studied using first-order reversal curves. The NW arrays exhibited higher magnetic interaction values than the NT arrays, yet for both systems they were found to increase with the diameter of the NWs/NTs.

3.1 Article III – Crossover Between Magnetic Reversal Modes in Ordered Ni and Co Nanotube Arrays

Mariana P. Proenca, Célia T. Sousa, João Ventura, João P. Araujo, Juan Escrig and Manuel Vazquez, *SPIN*, accepted, DOI: 10.1142/S2010324712500142.

Abstract

Ordered arrays of Ni and Co nanowires and nanotubes, with diameters between 30 and 60 nm, were prepared by electrodeposition into nanoporous alumina templates. The study of the corresponding magnetization reversal processes was performed by analyzing the angular dependence of coercivity (H_c) and using a simple analytical model. The agreement between experimental and theoretical data shows that magnetization in nanowire arrays reverses by means of nucleation and propagation of a transverse domain wall, independently of the diameter. However, a critical diameter of ~ 50 nm was found in the case of nanotubes, above which a non-monotonic angular dependent H_c was observed, evidencing a transition between vortex and transverse reversal modes.

3.1.1 Introduction

With the growing interest in nanotechnology, nanomaterials are becoming increasingly important. Spherical nanoparticles have been produced, offering potential applications in a diversified set of fields, ranging from biomedicine [1] to energy storage [2]. However, nanowires (NWs; high aspect ratio nanoparticles) and nanotubes (NTs) exhibit anisotropic (shape-dependent) collective properties (e.g. photoluminescence, conductivity, magnetization) [3, 4], increasing the number of degrees of freedom that can be manipulated. For magnetic applications such as sensors or media, it is important to study both the domain structure and magnetic configuration within the NW/NT arrays, and their dependence on geometry, element size (and shape) and inter-element distance [5–8]. As the size is reduced, the balance between different energies (magnetostatic, magnetocrystalline, exchange, thermal) can be critically altered, drastically affecting domain configuration [9–12]. The detailed physical study of such assemblies can give us the ability to tune competing interactions, searching for novel phenomena induced by nanoscopic confinement or proximity effects.

The major applications of magnetic nanomaterials require a thorough understanding of the magnetization reversal mechanisms. These are in turn directly related to the coercivity [13–15], and depend on geometric parameters such as shape, length, diameter, wall thickness or spatial ordering [16–18]. The accurate control of such parameters, combined with a detail study of the nanomaterial's magnetic properties, provides new information on the application of each nanomagnet array. Additionally, it eases the tuning of the magnetization reversal mode by external parameters, such as the direction of the applied magnetic field.

A limited number of studies have been reported on the angular dependent magnetic properties of NW and NT arrays fabricated inside nanopore templates (polycarbonate track etched membranes [19, 20], inclined Si columns [21]). Even scarcer experimental results on the angular dependence of the coercivity in highly ordered NW/NT arrays have been obtained [16, 21–25]. Additionally, the preparation of NTs with small diameters ($d < 60$ nm) is a difficult and complex task, so that most of the reports on the magnetic properties of NT arrays correspond to outer diameters of $d \sim 200$ nm [26–30]. Interesting changes in the magnetic behavior when reducing the NTs diameter have been theoretically predicted [17], but they remain an open question as the corresponding experimental evidence is still limited. In particular, theoretical calculations predict the existence of a critical diameter ($\sim 10 - 50$ nm) in ferromagnetic NTs, bellow which the magnetization reverses by a transverse mechanism, and above which a vortex mode is expected to occur [17]. However, this critical diameter was not yet found experimentally, as the magnetization reversal modes have only been reported for ferromagnetic NTs with $d > 100$ nm.

In this work, Ni and Co NW and NT arrays with small diameters ($\sim 30 - 60$ nm) were fabricated by controlled potentiostatic deposition into highly ordered nanoporous alumina templates (NpATs). A comparative study of the magnetization reversal processes of NW/NT arrays was performed by measuring the angular dependence of the coercivity for each sample. Experimental evidence of the transition between two magnetization reversal modes was achieved for NTs with $d \sim 50 - 60$ nm and confirmed by analytical calculations, showing that for both Co and Ni there is a critical diameter of ~ 50 nm, bellow which a transverse reversal mode occurs, as theoretically predicted.

3.1.2 Experimental Details

Long range ordering of hexagonal symmetry of precursor alumina membranes was achieved using a two-step anodization process of high purity (99.999%) aluminum disks [31]. Interpore distances of 65 and 105 nm were obtained by anodizing at 25 V and 2°C in 0.3 M sulfuric acid, and at 40 V and 4°C in 0.3 M oxalic acid, respectively. First anodizations were performed for 24 h, while second anodizations lasted for 20 h leading to ~ 50 μm thick membranes.

For subsequent electrodeposition, the nanopores were opened at the bottom by chemical etching of Al in an aqueous solution of 0.2 M $CuCl_2$ and 4.1 M HCl at room temperature, and chemical dissolution of the alumina bottom barrier layer in 0.5 M phosphoric acid [32]. Pore widening using phosphoric acid was also performed in selected samples to obtain pore diameters of $d \sim 50 - 60$ nm. A thin Au layer (~ 120 nm) was then sputtered on the backside of the membrane to serve as the working electrode in a three-electrode cell. For the growth of NTs, a smaller Au layer thickness ($\sim 30 - 60$ nm; depending on the pore diameter) was deposited so as not to completely close the bottom of the pores, followed by the coating of a non-metallic protective film at the bottom of the metallic contact [33]. In this case electrodeposition results in the formation of nanotubes along the internal side of the pores. A Pt mesh and Ag/AgCl (in 4 M KCl) were used as the counter and reference electrodes, respectively.

Ni and Co were electrodeposited inside the nanopores using an aqueous solution of 1.14 M $NiSO_4{\cdot}6H_2O$ + 0.19 M $NiCl_2{\cdot}6H_2O$ + 0.73 M H_3BO_3 at 35°C, and 0.89 M $CoSO_4{\cdot}7H_2O$ + 0.49 M H_3BO_3 at 30°C, respectively. The electrodepositions were performed in potentiostatic mode at -1.5 V for $\sim$ 2 min, using a Solartron 1480 MultiStat. The fabricated NWs and NTs had a final diameter equal to that of the pores of the template [d= (30, 50 and 60) $\pm$ 4 nm], NT wall thicknesses of $t = (8 - 12) \pm 3$ nm, and aspect ratios (length/diameter) higher than 50. Morphological characterization was performed using a scanning and a scanning transmission electron microscopes (SEM and STEM, respectively; FEI Quanta 400FEG). Prior to SEM bottom images, the Au contact at the bottom of the NpATs was etched by ion-milling using an ion beam sputter deposition system by the Commonwealth Scientific Corporation [33]. Sample preparation for STEM imaging was performed by chemically etching the NpAT in 0.2 M H_2CrO_4 + 0.4 M H_3PO_4 at 60°C and subsequently disperse the NTs in ethanol. Figures 3.1(a) and (b) show SEM bottom images (after $\sim$ 200 nm of ion-milling) of the obtained NWs and NTs inside NpATs with pore diameters of $d \sim 50 - 60$ nm and interpore distance of 105 nm. Figure 3.1(c) shows a STEM image of Ni NTs, illustrating the tubular shape with a hollow core and an homogeneous wall thickness along the tube.

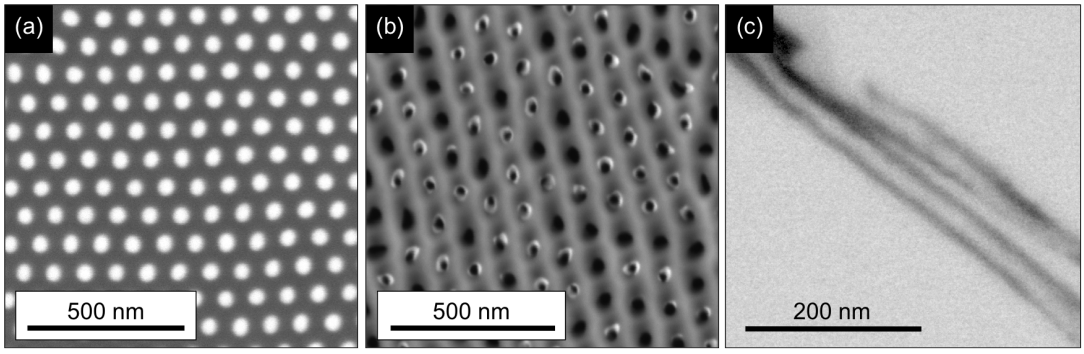


Figure 3.1: SEM bottom (after $\sim$ 200 nm of ion-milling) images of (a) Co NW and (b) Ni NT arrays in NpATs with $d \sim 50$ and 60 nm, respectively. (c) STEM image of Ni NTs.

3.1.3 Results and Discussion

To investigate the magnetization reversal processes of the NW and NT arrays, magnetization hysteresis loops were measured at different angles (θ) of applied external magnetic field (H), using a vibrating sample magnetometer (VSM; LOT-Oriel EV7). Figure 3.2 shows the magnetic hysteresis loops measured for Ni NTs, with diameters $d \sim 60$ nm and wall thickness $t \sim 12$ nm, evidencing an increase in the coercive field (H_c) for $\theta > 0°$, followed by a decreasing trend for $\theta > 70°$.

Three main modes of magnetization reversal have been previously identified depending on the geometry of the system under study: coherent mode (C), where all magnetic moments rotate simultaneously; transverse mode (T), where spins rotate progressively by the nucleation and propagation of a transverse domain wall; and vortex mode (V), where a vortex wall is nucleated and propagates [17]. A simple analytical model has been proposed to account for the angular

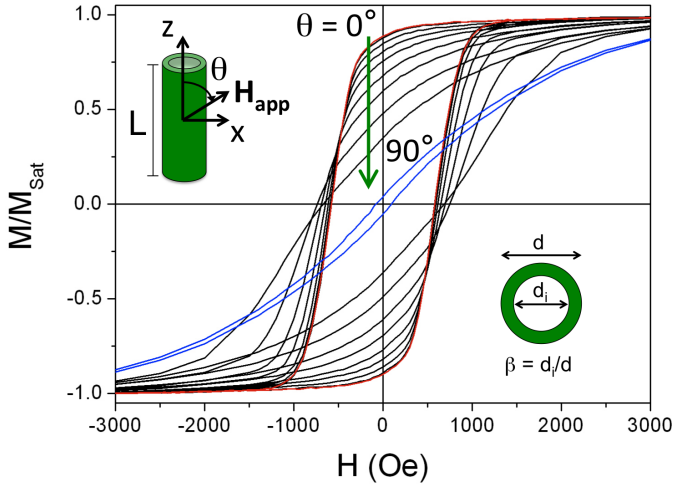


Figure 3.2: Magnetic hysteresis loops of ordered Ni NT arrays with $d \sim 60$ nm and $d_i \sim 36$ nm, measured at different angles of applied magnetic field, with a 10° step.

dependence of the coercive field of each of the above magnetization reversal processes (H_c^i; i = C, T and V) [14, 17, 34]. For the coherent magnetization reversal case one can directly apply the Stoner-Wohlfarth model to estimate the nucleation field [13]:

$$H_n^C = -M_{Sat}\frac{1-3N_z(L)}{2}\frac{\sqrt{1-\alpha^2+\alpha^4}}{1+\alpha^2}, \tag{3.1}$$

where $\alpha = \tan^{\frac{1}{3}}(\theta)$, N_z is the demagnetization factor of a wire/tube along the z (long) axis, and M_{Sat} is the saturation magnetization (= 4.9×10^5 and 1.4×10^6 A m^{-1} for Ni and Co, respectively). Since the Co NWs and NTs fabricated in this work are polycrystalline (not shown), evidencing a mixture of cubic and hexagonal crystalline phases, the magnetocrystalline anisotropy constant is very small and was not included in our calculations.

It was also shown that the coercivity can be written as a function of the nucleation field as [13]:

$$H_c^C(\theta) = \begin{cases} |H_n^C(\theta)| & 0 \leqslant \theta < \pi/4 \\ 2|H_n^C(\theta = \pi/4)| - |H_n^C(\theta)| & \pi/4 \leqslant \theta \leqslant \pi/2 \end{cases}. \tag{3.2}$$

For a generalized description of our geometrical system, it is convenient to define the ratio $\beta = \frac{d_i}{d}$, where d_i and d are the inner and outer tube diameters, respectively (inset of Fig. 3.2). In this work we have $\beta \sim 0.4$ and 0.7 for the fabricated NTs with $d \sim 30$ and $50-60$ nm, respectively. On the other hand $\beta = 0$ for NWs. The dependence of the demagnetization factor on β was calculated by Escrig *et al.*, and is given by [35]:

$$N_z(L) = \frac{d}{L(1-\beta^2)}\int_0^\infty \frac{1-e^{-2yL/d}}{y^2}[J_1(y) - \beta J_1(\beta y)]^2 dy, \tag{3.3}$$

where J_1 is the Bessel function of the first kind and order one.

For the transverse mode an adapted Stoner-Wohlfarth model has been proposed [16]. In this model the nucleation field of a system that reverses its magnetization by means of the nucleation and propagation of a transverse domain wall is assumed to be equivalent to the nucleation field of a system with an effective volume that reverses its magnetization by coherent rotation. The effective volume considers the transverse domain wall width (w_T), which can be estimated depending on geometrical parameters [10, 17]. We can therefore use equations (3.1) – (3.3) to calculate $H_c^T(\theta)$, replacing L with w_T.

Finally, the angular dependence of the nucleation field in the vortex mode can be estimated using [36]:

$$\frac{H_n^V}{M_{Sat}} = \frac{\left(N_z - \zeta^2\right)\left(N_x - \zeta^2\right)}{\sqrt{\left(N_z - \zeta^2\right)^2 \sin^2\theta + \left(N_x - \zeta^2\right)^2 \cos^2\theta}}, \tag{3.4}$$

where $\zeta = \frac{2qL_{ex}}{d}$, $L_{ex} = \sqrt{\frac{2A}{\mu_0 M_{Sat}^2}}$ is the exchange length, A is the magnetic stiffness constant (here considered 0.9×10^{-11} J m^{-1} for Ni and 3.0×10^{-11} J m^{-1} for Co) [10, 37] and q satisfies [38]:

$$\frac{qJ_0(q) - J_1(q)}{qY_0(q) - Y_1(q)} = \frac{\beta qJ_0(\beta q) - J_1(\beta q)}{\beta qY_0(\beta q) - Y_1(\beta q)}, \tag{3.5}$$

where J_p and Y_p correspond to the Bessel functions of the first and second kind, respectively, and order p. Considering the wire/tube symmetry, one has $N_x = N_y = \frac{(1-N_z)}{2}$. In the V mode, the coercivity is very close to the absolute value of the nucleation field, and we thus use $H_c^V = -H_n^V$, as in previous works [14, 21, 37].

Figures 3.3 and 3.4 show the angular dependence of the coercivity for the Co and Ni samples, respectively. In the NW arrays, the coercivity always decreases as θ increases, showing a monotonic behavior. The coercivity estimated using the coherent magnetization reversal mode gives much higher values than those experimentally obtained (Fig. 3.3). As previously reported by Landeros *et al.* [17], coherent magnetization reversal is only present in very short wires/tubes where $L \approx w_T$ or less. For long NWs the reversal of magnetization is achieved through the nucleation and propagation of a transverse domain wall. Our analytical calculations confirm the presence of a transverse magnetization reversal mode for all NW arrays [Figs. 3.3 and 3.4, (a) and (b)].

The same is observed in the case of NT arrays with very small outer diameters (~ 30 nm) [Figs. 3.3 and 3.4, (c)]. However, NT arrays with $d \gtrsim 50$ nm illustrate a non-monotonic behavior, where H_c starts by increasing with θ, reaching a maximum value at $\theta_T \neq 0°$, and then decreases for $\theta > \theta_T$ [Figs. 3.3 and 3.4, (d)]. This inhomogeneous behavior evidences a transition from two different magnetization reversal processes (transverse and vortex modes).

The analytical calculations obtained for the magnetization reversal modes of NT arrays with $d \gtrsim 50$ nm are plotted in Figs. 3.3(d) and 3.4(d), for Co and Ni, respectively. Since the system reverses its magnetization by the mode that offers the lowest coercivity, the analytical calculations allow the identification of the magnetization reversal modes expected for each system. The good agreement found between the analytical calculations and the experimental data of the angular dependence of

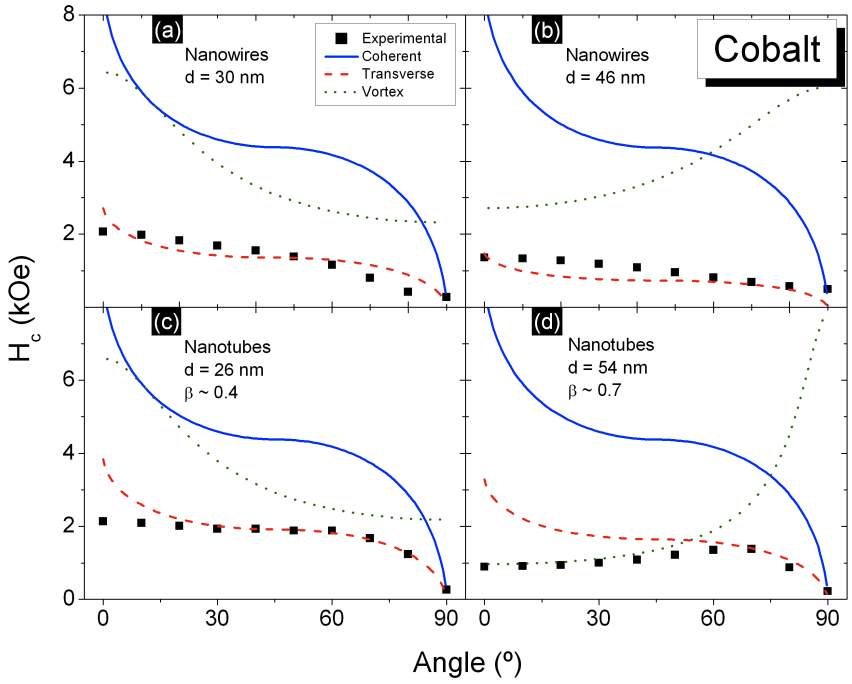


Figure 3.3: Angular dependence of the coercive field measured experimentally (squares) and calculated analytically (C mode: blue solid; T mode: red dashed; and V mode: green dotted) for Co NW [(a) and (b)] and NT [(c) and (d)] arrays in NpATs with different outer diameters.

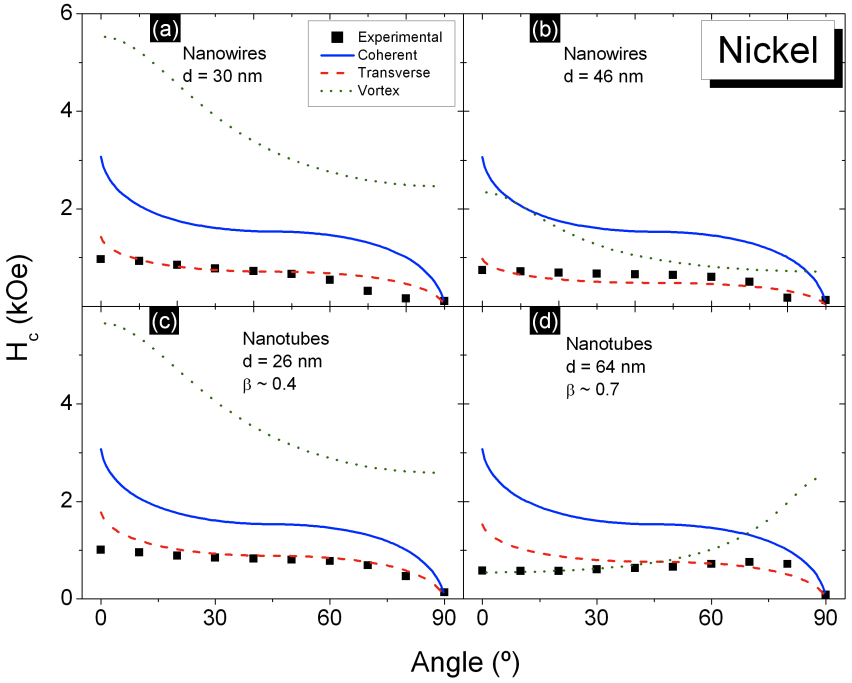


Figure 3.4: Angular dependence of the coercive field measured experimentally (squares) and calculated analytically (C mode: blue solid; T mode: red dashed; and V mode: green dotted) for Ni NW [(a) and (b)] and NT [(c) and (d)] arrays in NpATs with different outer diameters.

coercivity [Figs. 3.3(d) and 3.4(d)] evidences the existence of a crossover between the vortex and the transverse reversal modes, occurring at theoretically predicted angles very close to the experimentally obtained maxima. The small differences between the experimental data and the analytical calculations can be explained by deviations from the NTs cross section from perfect circular shape and dipolar interactions of neighboring NTs [16, 21, 34].

3.1.4 Conclusions

In summary, the angular dependence of the coercivity was measured for Ni and Co NW and NT arrays with small diameters (between 30 and 60 nm). For NTs with $d \gtrsim 50$ nm we reported experimental evidence for an angular dependent transition of magnetization reversal modes, which had been theoretically predicted. Analytical calculations then allowed us to identify a transverse reversal mode for all NW and NT arrays with $d \sim 30$ nm, and a transition between the vortex and transverse reversal modes occurring for NTs with $d \sim 50 - 60$ nm. Due to the additional degree of freedom provided by the hollow core in the NT centre, the here shown fabrication of tubular structures with different inner and outer diameters provides the first step towards the design of a sensor device with NT arrays of different inner/outer diameter ratios, with enhanced sensitivity by providing a broader angle of detection.

Bibliography

[1] R. Bardhan, S. Lal, A. Joshi, and N. J. Halas, "Theranostic nanoshells: From probe design to imaging and treatment of cancer", *Acc. Chem. Res.*, vol. 44, no. 10, pp. 936–946, 2011.

[2] G. Polizos, V. Tomer, E. Manias, and C. A. Randall, "Epoxy-based nanocomposites for electrical energy storage. II: Nanocomposites with nanofillers of reactive montmorillonite covalently-bonded with barium titanate", *J. Appl. Phys.*, vol. 108, no. 7, pp. 074117, 2010.

[3] K. D. Sattler, *Handbook of nanophysics: Nanotubes and nanowires*, CRC Press, USA, 2010.

[4] S. S. P. Parkin, M. Hayashi, and L. Thomas, "Magnetic domain-wall racetrack memory", *Science*, vol. 320, pp. 190–194, 2008.

[5] M. Daub, M. Knez, U. Goesele, and K. Nielsch, "Ferromagnetic nanotubes by atomic layer deposition in anodic alumina membranes", *J. Appl. Phys.*, vol. 101, no. 9, pp. 09J111, 2007.

[6] J. Bachmann, J. Jing, M. Knez, S. Barth, H. Shen, S. Mathur, U. Gosele, and K. Nielsch, "Ordered iron oxide nanotube arrays of controlled geometry and tunable magnetism by atomic layer deposition", *J. Am. Chem. Soc.*, vol. 129, no. 31, pp. 9554–9555, 2007.

[7] J. Son, S. J.and Reichel, B. He, M. Schuchman, and S. B. Lee, "Magnetic nanotubes for magnetic-field-assisted bioseparation, biointeraction, and drug delivery", *J. Am. Chem. Soc.*, vol. 127, no. 20, pp. 7316–7317, 2005.

[8] K. Nielsch, F. J. Castano, S. Matthias, W. Lee, and C. A. Ross, "Synthesis of cobalt/polymer multilayer nanotubes", *Adv. Eng. Mater.*, vol. 7, no. 4, pp. 217–221, 2005.

[9] C. A. Ross, "Patterned magnetic recording media", *Annu. Rev. Mater. Res.*, vol. 31, no. 1, pp. 203–235, 2001.

[10] J. M. D. Coey, *Magnetism and magnetic materials*, Cambridge University Press, New York, 2009.

[11] S. M. Reddy, J. J. Park, S.-M. Na, M. M. Maqableh, A. B. Flatau, and B. J. H. Stadler, "Electrochemical synthesis of magnetostrictive Fe-Ga/Cu multilayered nanowire arrays with tailored magnetic response", *Adv. Funct. Mater.*, vol. 21, no. 24, pp. 4677–4683, 2011.

[12] M. Yan, C. Andreas, A. Kakay, F. Garcia-Sanchez, and R. Hertel, "Fast domain wall dynamics in magnetic nanotubes: Suppression of Walker breakdown and Cherenkov-like spin wave emission", *Appl. Phys. Lett.*, vol. 99, no. 12, pp. 122505, 2011.

[13] E. C. Stoner and E. P. Wohlfarth, "A mechanism of magnetic hysteresis in heterogeneous alloys", *IEEE Trans. Magn.*, vol. 27, no. 4, pp. 3475–3518, 1991.

[14] S. Allende, J. Escrig, D. Altbir, E. Salcedo, and M. Bahiana, "Angular dependence of the transverse and vortex modes in magnetic nanotubes", *Eur. Phys. J. B*, vol. 66, no. 1, pp. 37–40, 2008.

[15] L. G. Vivas, M. Vazquez, J. Escrig, S. Allende, D. Altbir, D. C. Leitao, and J. P. Araujo, "Magnetic anisotropy in CoNi nanowire arrays: Analytical calculations and experiments", *Phys. Rev. B*, vol. 85, no. 3, pp. 035439, 2012.

[16] J. Escrig, J. Bachmann, J. Jing, M. Daub, D. Altbir, and K. Nielsch, "Crossover between two different magnetization reversal modes in arrays of iron oxide nanotubes", *Phys. Rev. B*, vol. 77, no. 21, pp. 214421, 2008.

[17] P. Landeros, S. Allende, J. Escrig, E. Salcedo, D. Altbir, and E. E. Vogel, "Reversal modes in magnetic nanotubes", *Appl. Phys. Lett.*, vol. 90, no. 10, pp. 102501, 2007.

[18] L. G. Vivas, R. Yanes, O. Chubykalo-Fesenko, and M. Vazquez, "Coercivity of ordered arrays of magnetic Co nanowires with controlled variable lengths", *Appl. Phys. Lett.*, vol. 98, no. 23, pp. 232507, 2011.

[19] A. Ghaddar, F. Gloaguen, J. Gieraltowski, and C. Tannous, "Magnetic crossover effect in nickel nanowire arrays", *Physica B*, vol. 406, no. 10, pp. 2046–2053, 2011.

[20] R. Sharif, S. Shamaila, M. Ma, L. D. Yao, R. C. Yu, X. F. Han, and M. Khaleeq-ur Rahman, "Magnetic switching of ferromagnetic nanotubes", *Appl. Phys. Lett.*, vol. 92, no. 3, pp. 032505, 2008.

[21] O. Albrecht, R. Zierold, S. Allende, J. Escrig, C. Patzig, B. Rauschenbach, K. Nielsch, and D. Gorlitz, "Experimental evidence for an angular dependent transition of magnetization reversal modes in magnetic nanotubes", *J. Appl. Phys.*, vol. 109, no. 9, pp. 093910, 2011.

[22] J. Escrig, R. Lavin, J. L. Palma, J. C. Denardin, D. Altbir, A. Cortes, and H. Gomez, "Geometry dependence of coercivity in Ni nanowire arrays", *Nanotechnology*, vol. 19, no. 7, pp. 075713, 2008.

[23] R. Lavin, J. C. Denardin, A. P. Espejo, A. Cortes, and H. Gomez, "Magnetic properties of arrays of nanowires: Anisotropy, interactions, and reversal modes", *J. Appl. Phys.*, vol. 107, no. 9, pp. 09B504, 2010.

[24] L.-P. Carignan, M. Massicotte, C. Caloz, A. Yelon, L. Fellow, and D. Menard, "Magnetization reversal in arrays of Ni nanowires with different diameters", *IEEE Trans. Magn.*, vol. 45, no. 10, pp. 4070–4073, 2009.

[25] N. Ahmad, J. Y. Chen, W. P. Zhou, D. P. Liu, and X. F. Han, "Magnetoelastic anisotropy induced effects on field and temperature dependent magnetization reversal of Ni nanowires and nanotubes", *J. Supercond. Nov. Magn.*, vol. 24, no. 1-2, pp. 785–792, 2010.

[26] D. H. Park, Y. B. Lee, M. Y. Cho, B. H. Kim, S. H. Lee, Y. K. Hong, J. Joo, H. C. Cheong, and S. R. Lee, "Fabrication and magnetic characteristics of hybrid double walled nanotube of ferromagnetic nickel encapsulated conducting polypyrrole", *Appl. Phys. Lett.*, vol. 90, no. 9, pp. 093122, 2007.

[27] D. Li, R. S. Thompson, G. Bergmann, and J. G. Lu, "Template-based synthesis and magnetic properties of cobalt nanotube arrays", *Adv. Mater.*, vol. 20, no. 23, pp. 4575–4578, 2008.

[28] X.-F. Han, S. Shamaila, R. Sharif, J.-Y. Chen, H.-R. Liu, and D.-P. Liu, "Structural and magnetic properties of various ferromagnetic nanotubes", *Adv. Mater.*, vol. 21, no. 45, pp. 4619–4624, 2009.

[29] F. Tao, M. Guan, Y. Jiang, J. Zhu, Z. Xu, and Z. Xue, "An easy way to construct an ordered array of nickel nanotubes: The triblock-copolymer-assisted hard-template method", *Adv. Mater.*, vol. 18, no. 16, pp. 2161–2164, 2006.

[30] J. Bao, C. Tie, Z. Xu, Q. Zhou, D. Shen, and Q. Ma, "Template synthesis of an array of nickel nanotubules and its magnetic behavior", *Adv. Mater.*, vol. 13, no. 21, pp. 1631, 2001.

[31] O. Jessensky, F. Muller, and U. Gosele, "Self-organized formation of hexagonal pore arrays in anodic alumina", *Appl. Phys. Lett.*, vol. 72, no. 10, pp. 1173–1175, 1998.

[32] M. P. Proenca, C. T. Sousa, J. Ventura, M. Vazquez, and J. P. Araujo, "Ni growth inside ordered arrays of alumina nanopores: Enhancing the deposition rate", *Electrochim. Acta*, vol. 72, pp. 215–221, 2012.

[33] M. P. Proenca, C. T. Sousa, J. Ventura, M. Vazquez, and J. P. Araujo, "Distinguishing nanowire and nanotube formation by the deposition current transients", *Nanoscale Res. Lett.*, vol. 7, pp. 280, 2012.

[34] R. Lavin, J. C. Denardin, J. Escrig, D. Altbir, A. Cortes, and H. Gomez, "Angular dependence of magnetic properties in Ni nanowire arrays", *J. Appl. Phys.*, vol. 106, no. 10, pp. 103903, 2009.

[35] J. Escrig, P. Landeros, D. Altbir, E. Vogel, and P. Vargas, "Phase diagrams of magnetic nanotubes", *J. Magn. Magn. Mater.*, vol. 308, no. 2, pp. 233–237, 2007.

[36] A. Aharoni, "Angular dependence of nucleation by curling in a prolate spheroid", *J. Appl. Phys.*, vol. 82, no. 3, pp. 1281, 1997.

[37] J. Escrig, M. Daub, P. Landeros, K. Nielsch, and D. Altbir, "Angular dependence of coercivity in magnetic nanotubes", *Nanotechnology*, vol. 18, no. 44, pp. 445706, 2007.

[38] C. R. Chang, C. M. Lee, and J. S. Yang, "Magnetization curling reversal for an infinite hollow cylinder", *Phys. Rev. B*, vol. 50, no. 9, pp. 6461, 1994.

3.2 Article IV – Magnetization Reversal in Electrodeposited Co Nanowire and Nanotube Arrays with Different Diameters

Mariana P. Proenca, Célia T. Sousa, Juan Escrig, João Ventura, Manuel Vazquez and João P. Araujo,
submitted to *Journal of Applied Physics*.

Abstract

Ordered hexagonal arrays of Co nanowires (NWs) and nanotubes (NTs), with diameters between 40 and 65 nm, were prepared by potentiostatic electrodeposition into suitably modified nanoporous alumina templates. The geometrical parameters of the NW/NT arrays were tuned by the pore etching process and deposition conditions. The magnetic interactions between NWs/NTs with different diameters were studied using first-order reversal curves (FORCs). From a quantitative analysis of the FORC measurements, we are able to obtain the profiles of the magnetic interactions and the coercive field distributions. In both NW and NT arrays, the magnetic interactions were found to increase with the diameter of the NWs/NTs, exhibiting higher values for NW arrays. A comparative study of the magnetization reversal processes was also performed by analyzing the angular dependence of the coercivity and correlating the experimental data with theoretical calculations based on a simple analytical model. The magnetization in the NW arrays is found to reverse by the nucleation and propagation of a transverse-like domain wall; on the other hand, for the NT arrays a non-monotonic behavior occurs above a diameter of ~ 50 nm, revealing a transition between the vortex and transverse reversal modes.

3.2.1 Introduction

With the growing need for the miniaturization of sensors, storage devices and biomedical chips, magnetic nanomaterials have gained much importance in the last years [1–3]. Nanowires (NWs) and nanotubes (NTs) have thus received increased attention, as they exhibit anisotropic (shape-dependent) collective properties, such as photoluminescence, conductivity and magnetization [4]. Most applications use arrays of nanostructures, adding new degrees of freedom as the importance of inter-element coupling increases. The ability to control the NW/NT dimensions (length, inner/outer diameters and wall thickness), the array configuration and interwire distance, allows the tuning of different energies (magnetostatic, magnetocrystalline, exchange) to obtain novel phenomena induced by nanoscopic confinement or proximity effects [5–9].

A thorough understanding of the magnetic properties of NW and NT arrays with tailored geometries is of extreme importance for their implementation in future applications. In particular, new insights on the magnetostatic interactions between nanoelements will highly influence the design of improved devices using magnetic arrays. Interwire interactions are known to affect the magnetic properties of NW and NT arrays, particularly magnetization switching processes. The ability to

quantitatively study these interactions can provide an accurate understanding of magnetic nanoscopic effects. A straightforward way of studying the magnetic properties of a system is the analysis of major hysteresis cycles. However, such information is not sufficient for a complete understanding of magnetic interactions. Using the same experimental set-up, but measuring multiple minor hysteresis loops, the so-called first-order reversal curves (FORCs), one can extract quantitative information on the magnetic interactions of nanoelement arrays [10–12].

Additionally, the ability to tune the magnetization reversal modes of nanoelement arrays by external parameters, such as the applied magnetic field, has also become attractive as it improves the implementation and control of novel devices. Depending on the geometrical specifications of the system under study, three main modes of magnetization reversal have been previously identified: coherent mode (C), where all magnetic moments rotate homogeneously; transverse mode (T), where spins rotate progressively by the nucleation and propagation of a transverse-like domain wall (DW); and vortex mode (V), where a vortex-like DW nucleates and propagates [13]. In recent reports a simple analytical model has been proposed to understand the magnetization reversal processes by predicting the variation of the coercivity with the angle of applied external magnetic field (H) and allowing the understanding of the magnetization reversal processes for NW and NT arrays with different geometrical parameters [13–15].

Nanoporous alumina templates (NpATs) have been extensively used for the growth of NWs and NTs as they offer the possibility to build ordered arrays of aligned nanostructures and the ability to easily control the required dimensions by changing the anodization conditions [16, 17]. Controlling the applied potential and the electrolyte type, concentration and temperature, one can easily obtain ordered hexagonal arrays of nanopores with diameters between 20 and 200 nm and interpore distances in the range of $60 - 500$ nm [18]. The thickness of the NpATs can be tuned from a few nanometers to hundreds of micrometers by varying the anodization time.

Several methods can then be used for the growth of NWs and NTs inside the nanopores of the templates, including sol-gel filling, atomic layer and electrochemical depositions [19–21]. For the fabrication of large arrays of metallic NWs and NTs, potentiostatic electrodeposition in NpATs has proved to be a low cost and high yield technique [22]. Varying the deposition conditions (time, applied potential and electrolyte temperature, pH and concentration) we can also tune the crystallographic structure and metal alloy composition, changing the respective physical response [23, 24]. Additionally, the accurate coating of the metallic contact (cathode) at the bottom of the pores, where the deposition of the nanostructure initiates, allows the controlled formation of NWs or NTs [25].

In this work, ordered hexagonal arrays of Co NWs and NTs, with diameters between 40 and 65 nm, were fabricated by template assisted electrodeposition using NpATs. FORC measurements were performed with H along the wire axis, allowing us to obtain quantitative results on the magnetic interwire interactions in NW and NT arrays. These were found stronger in the NW case, increasing with the diameter for both NW and NT arrays. Magnetization reversal modes were also studied

for both NW and NT arrays measuring the angular dependence of the coercivity and comparing the experimental data with theoretical analytical calculations. We found that the magnetization in NW arrays reverses by the nucleation and propagation of a transverse DW. In the case of NT arrays we find a critical diameter of ~ 50 nm above which magnetization reverses by a vortex DW.

3.2.2 Experimental Details

Nanoporous alumina templates (NpATs) were prepared by a two-step anodization process of high-purity Al (99.999%) disks [16]. Prior to anodization, Al disks were cleaned in acetone and ethanol, and electropolished in a solution of 75% ethanol and 25% perchloric acid by applying 20 V for 2 min [26]. The subsequent anodization processes were performed in 0.3 M oxalic acid at 40 V, maintaining the electrolyte temperature at $\sim$ 4°C. To obtain ordered hexagonal nanopore arrays first anodizations were performed for 24 h. The alumina was then removed by chemical etching and second anodizations were performed using the same conditions as the first ones, but only for ~ 20 h, producing membranes with ~ 50 μm in thickness [22]. The obtained NpATs had pore diameters of $d \sim 35 \pm 4$ nm and interpore distances of $D_{int} \sim 102 \pm 3$ nm.

For the subsequent pore filling of the NpATs using potentiostatic electrodeposition, a circle with ~ 1 cm in diameter was opened on the template backside, by chemically etching the Al substrate in an aqueous solution of 0.2 M $CuCl_2$ and 4.1 M HCl at room temperature. The alumina barrier layer present at the bottom of the nanopores was then removed by a controlled chemical etching using 0.5 M H_3PO_4. Tuning the time and temperature of this last process allowed us to obtain final nanopore diameters of $d \sim$ (40, 50 and 65) $\pm$ 4 nm. Finally an Au metallic contact was sputtered at the opened nanopores side of the NpATs to serve as the working electrode in a three-electrode cell. For the fabrication of NWs, a continuous Au film was sputtered at the nanopores' bottom, to completely close its opened end. For the growth of NTs, a thinner metallic contact was sputtered, as not to completely close the bottom of the pores, allowing the electrochemical growth of a tubular structure throughout the nanopores [25]. A Pt mesh was used as the counter electrode and Ag/AgCl (in 4 M KCl) as the reference electrode (0.197 V vs. standard hydrogen electrode).

The electrodepositions were performed in an aqueous solution of 0.89 M $CoSO_4{\cdot}7H_2O$ and 0.49 M H_3BO_3, at 30°C, and applying a constant potential of -1.5 V vs. Ag/AgCl, using a Solartron 1480 MultiStat. Morphological characterizations were performed using a scanning electron microscope (SEM; FEI Quanta 400FEG). Prior to bottom SEM imaging, ion milling was performed to remove the Au contact (200 nm) and smoothen the NpAT surface. The milling process was carried out using an ion beam sputter deposition system by Commonwealth Scientific Corporation [21]. The angular dependent magnetic hysteresis loops and FORC measurements were performed in a vibrating sample magnetometer (VSM; LOT-Oriel EV7) at room temperature. For all the magnetic measurements, the samples were saturated under a maximum applied magnetic field of 15 kOe.

3.2.3 Results and Discussion

Ordered hexagonal arrays of Co NWs and NTs with diameters of $d \sim$ (40, 50 and 65) $\pm$ 4 nm, NT wall thicknesses of $t \sim 11 \pm 2$ nm, and aspect ratios (length/diameter) higher than 20 were obtained by electrodeposition inside the nanopores. Figure 3.5 shows bottom (after 200 nm ion milling) and cross-sectional SEM images of selected samples of Co NW and NT arrays in NpATs, evidencing the high order of the hexagonal array and the pore filling uniformity. In particular, Figs. 3.5(a) and (b) correspond to two ordered NW arrays with different diameters and equal interpore distances, illustrating the control of the interwire spacing by adjusting the NWs diameter. The cross-sectional SEM image presented in Fig. 3.5(c) evidences the homogeneity of the pore filling and the uniformity of the NWs structure along the pore walls. Finally, Fig. 3.5(d) shows a SEM image of the bottom of a NpAT filled with Co NTs, after ion milling etching, illustrating the NT shape formed inside the nanopores. Note that, when the Co NTs are removed from the NpAT we observed a fast oxidation process that prevented us from obtaining clear transmission electron microscopy (TEM) images. However, when analyzing the TEM images of similarly fabricated Ni NTs [27], a tubular structure with uniform walls can be found throughout the tube, and thus a similar structure is expected to be also produced when electrodepositing Co NTs.

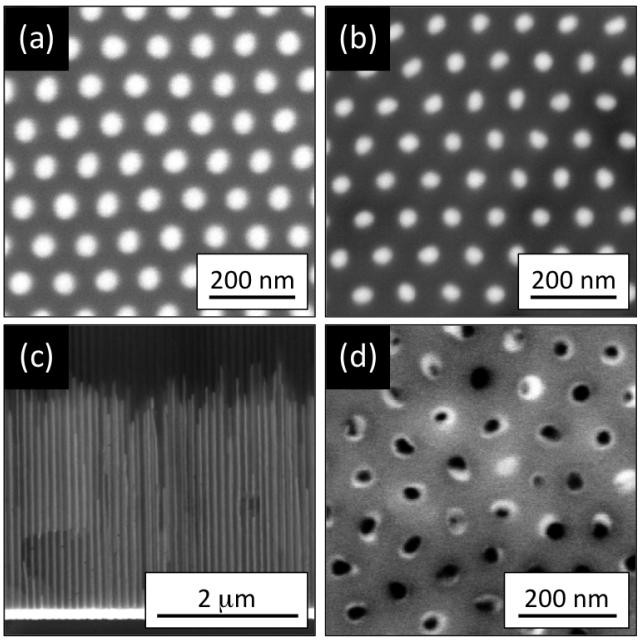


Figure 3.5: SEM [(a), (b) and (d)] bottom (after 200 nm milling) and (c) cross-sectional images of Co [(a), (b) and (c)] NW and (d) NT arrays in NpATs with (a) $d \sim 50$ nm and [(b), (c) and (d)] $d \sim 40$ nm and $D_{int} \sim 102$ nm.

3.2.4 First Order Reversal Curves

Aiming the accurate understanding of the magnetic interactions in Co NW and NT arrays we measured first order reversal curves (FORCs). Although major magnetic hysteresis loops can give

information on the coercivity, remanence and saturation fields of a magnetic system, they will only describe its global (average) behavior. When studying an array of smaller entities (NWs, NTs, nanodots or nanoparticles) it becomes vital to understand the interactions between the individual particles as they affect the behavior of the array. The FORC method has proved to be an effective way to characterize magnetic interactions and magnetization reversal in nanomagnet arrays [28–31].

To obtain FORCs one first has to saturate the sample applying a large positive magnetic field. Then we lower H to the so-called reversal field H_r (not yet sufficient to saturate the sample in the negative direction), and measure the magnetization M as a function of H, varying H from H_r to the positive saturation field value. This procedure is then repeated in increasing steps of H_r, until a complete set of FORCs is obtained (insets of Fig. 3.6). The FORC distribution is then given by the mixed second derivative of $M(H, H_r)$ [10]:

$$\rho(H, H_r) = -\frac{1}{2}\frac{\partial^2 M(H, H_r)}{\partial H \partial H_r} \quad (H > H_r). \tag{3.6}$$

According to the classical Preisach model, the FORC distribution can be seen as a statistical distribution of square hysteresis curves with coercivity H_c and bias field H_u, called *mathematical hysterons* [10]. Various models have been recently developed for the interpretation of FORC results applied to arrays of nanowires [11, 28, 30, 32]. These models then enable one to extract quantitative information on the coercivity distribution of individual nanowires, interaction field at saturation, and obtain insights into the magnetization reversal mechanism. For a better interpretation of the FORC measurements, it is usual to plot the FORC diagram as a contour plot of the FORC distribution (Fig. 3.6), with a color scale from minimum (blue) to maximum (red) [12]. It is also convenient to define a new set of coordinates (H_c, H_u), that will correspond to the coercive field and interaction field axis, respectively, as follows:

$$H_c = \frac{H - H_r}{2}, \quad H_u = -\frac{H + H_r}{2}. \tag{3.7}$$

Figure 3.6 shows the FORC results obtained in NW and NT arrays with different diameters and the same center-to-center wire/tube distances, and H parallel to the long axis. From the overall analysis of the FORC results of all samples, one can observe an increase of the FORC distribution along the H_u axis as the diameter increases. This can be ascribed to the increase of magnetostatic interactions among the NWs/NTs as their diameter increases and the distance between them decreases. The half-width of the FORC distribution along the H_u axis (ΔH_u) can be used as an estimative value of the interaction field between the NWs/NTs at saturation. For most NW array systems, the maximum observed in the FORC diagram can be associated to a good approximation with the average value of the NW coercivity (H_c^{FORC}) [28]. However, for small diameters ($d \sim 40$ nm) we found a high coercivity distribution along the H_c axis. In these cases the maximum value of the FORC diagram cannot be associated with H_c^{FORC} as previously reported [11, 29].

From the quantitative analysis of the FORC measurements, we calculated H_c^{FORC} and the

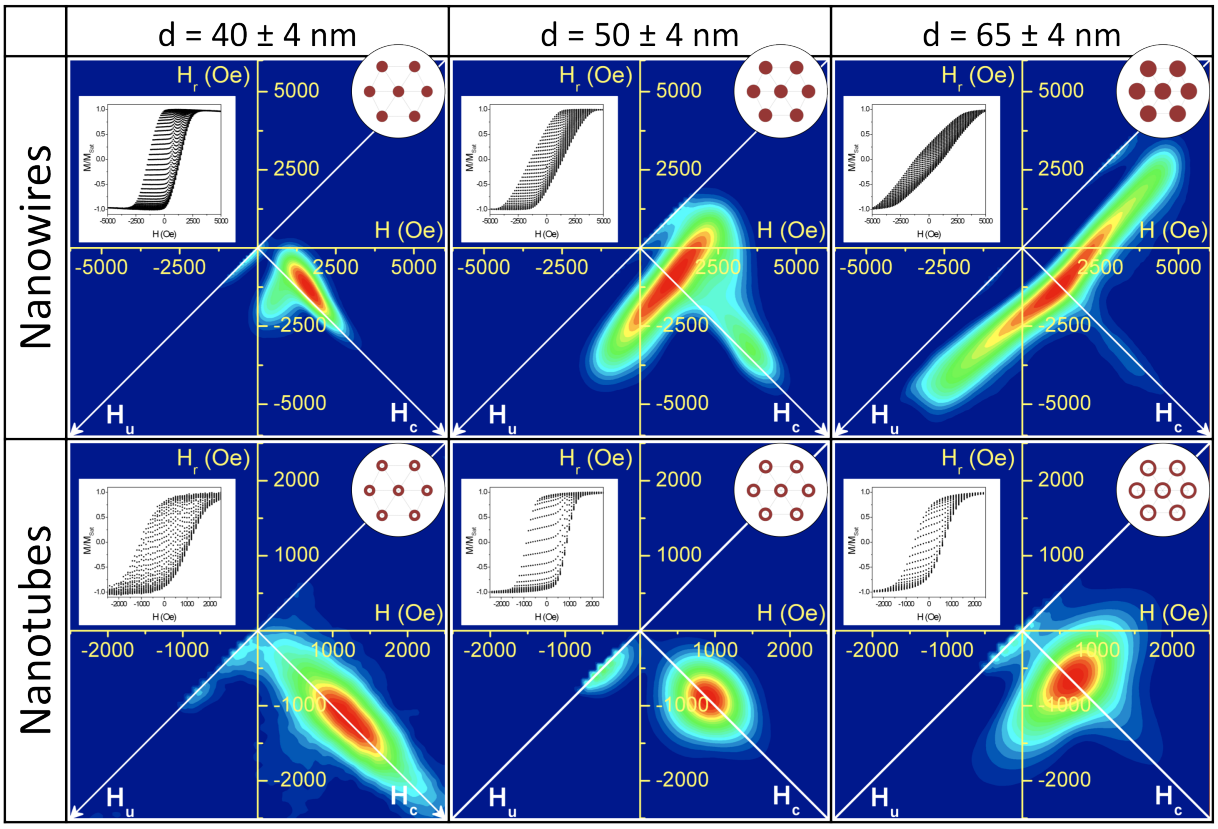


Figure 3.6: FORCs (insets) and FORC diagrams of Co NW and NT ordered hexagonal arrays with different diameters and lattice parameter of $\sim$ 102 nm, when applying the magnetic field parallel to the wire/tube long axis.

magnetic interactions (ΔH_u) between the NWs/NTs. Keeping the distance between the NWs/NTs centers constant, we see that ΔH_u increases with increasing diameter, due to the increased proximity of the neighboring NWs/NTs walls (Fig. 3.7) [30]. Additionally, the magnetic interactions are found much stronger between NWs than between NTs. However, lowering the NW/NT diameter down to $\sim$ 35 nm, while keeping the interwire distance, should already lead to a similar behavior for both NW and NT arrays (Fig. 3.7).

Using the moving Preisach model [28, 33], that also takes into consideration the interactions between the *mathematical hysterons*, the interaction field at saturation can be approximated by [28]:

$$H_{int,sat} = 2\sigma_{int} - k, \tag{3.8}$$

where σ_{int} is the standard deviation of the interaction field distribution (assumed constant at a given particle site but varying randomly from site to site) [34], and k is related with the mean interaction field kM/M_{Sat}, that can be parallel ($k > 0$) or antiparallel ($k < 0$) to M.

Analyzing the theoretical FORC diagrams reported using the moving Preisach model and different combinations of (σ_{int}, k) values [28], and comparing them with our experimental data, we see that

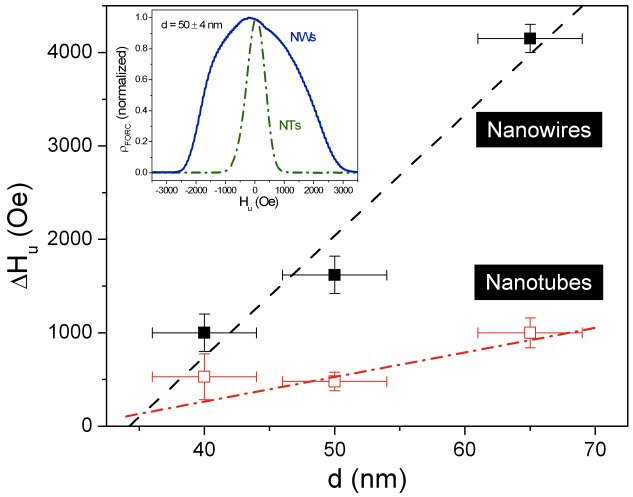


Figure 3.7: Magnetic interactions, extracted from the FORC diagrams in Fig. 3.6, as a function of the wire/tube diameter. Inset shows the cross-section of the FORC diagram along the H_u axis for NW and NT arrays with $d \sim 50$ nm.

our NT arrays behave like systems with $k \sim 0$, while NW arrays are comparable to systems with $|k| \approx |\sigma_{int}|$ and $k < 0$. The NT arrays can therefore be considered as almost non-interacting systems, where the mean interaction field is close to zero and there is only a small local interaction field (Fig. 3.6). The NW arrays present a much broader distribution of the interaction field along the H_u axis, which is attributed to the presence of a mean interaction field antiparallel to M ($k < 0$). As previously reported, the stray field of the NW array will induce an antiferromagnetic-like coupling between NWs creating a macroscopic demagnetizing field [23, 32, 35–37]. The inset of Fig. 3.7 corresponds to the cross-section along the H_u axis for NW and NT arrays with $d \sim 50$ nm. A sharp (broad) distribution can be seen for the NT (NW) arrays. From the theoretical FORC diagrams of Ref. [28], sharp peaks were obtained when considering $\Delta H_u = H_{int,sat}$ with $k \sim 0$ and $\sigma_{int} = 250$ Oe, while broader distributions resulted when using $k = -500$ Oe and $\sigma_{int} = 500$ Oe. In fact, for the NW and NT arrays with $d \sim 50$ nm we estimated $\Delta H_u \approx 1500$ and 500 Oe, respectively. If we consider $|k| = |\sigma_{int}|$ for the NW array and $k = 0$ for the NT array, we obtain $|k| = |\sigma_{int}| = 500$ Oe and $\sigma_{int} = 250$ Oe, respectively. The good agreement found between the experimental cross-sectional plots along the H_u axis (inset of Fig. 3.7) and the theoretical FORC diagrams reported in Ref. [28], reinforces our statement that the mean interaction field for NT arrays is very low, while that of NW arrays is much stronger and antiparallel to M. It has also been reported from theoretical calculations [28] that the distribution top along the H_u axis becomes flatter with increasing $|k|/\sigma_{int}$, indicating an array where all nanomagnets experience similar magnetostatic interactions. In the inset of Fig. 3.7 we can already observe a flatter top in the H_u profile of the NW arrays, revealing a more homogeneous distribution of magnetostatic interactions between NWs than between NTs.

Figure 3.8 shows a comparison between H_c^{FORC} and the coercive field measured from the major hysteresis loops (H_c^{Hyst}), with the applied field parallel to the wire axis, for both NW and NT arrays. The decrease of H_c^{Hyst} and H_c^{FORC} with the increase of NW/NT diameter is confirmed. For the NT

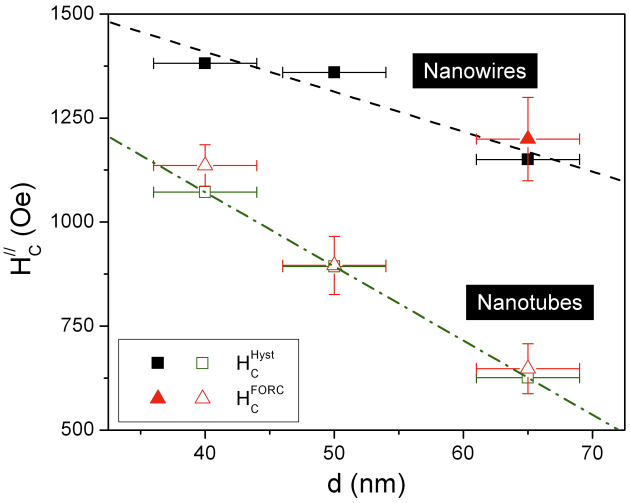


Figure 3.8: Coercive field along the parallel direction, extracted from the maximum value of the FORC diagrams (H_c^{FORC}) in Fig. 3.6, and from the major magnetic hysteresis loops (H_c^{Hyst}), as a function of the NWs/NTs diameter.

arrays we found $H_c^{FORC} \approx H_c^{Hyst}$. Since H_c^{FORC} is assumed to be related with the switching field of single nanoelements, the fact that its value is similar to H_c^{Hyst} is an additional evidence that the mean interaction field can be neglected in NT array systems. For the NW arrays, due to the high coercivity distribution present in the FORC diagrams for $d \sim 40$ and 50 nm, we were not able to extract the correct value of H_c^{FORC}. One should also note that the magnetization reversal mechanisms reported for NWs are much more complicated than the ones expected in NTs, which may explain the sharper and better-defined distribution of coercivities exhibited in the latter case (Fig. 3.6). Additionally, the FORC diagrams presented in Fig. 3.6 illustrate a coercivity distribution along the H_c axis for all NW arrays, and for NT arrays with smaller outer diameters (~ 40 nm). However, for NT arrays with $d \sim 50$ and 65 nm such coercivity distribution is practically inexistent. This may be attributed to different magnetization reversal mechanisms for the NW and NT arrays, specially at larger diameters ($\sim\ 50 - 65$ nm), where the differences in H_c^{FORC} distributions are more pronounced. The FORC analysis thus allows one to extract quantitative knowledge on the interaction field, average individual coercivity and overall array anisotropy, that can help in the interpretation of the magnetization reversal mechanisms. However, for a deeper understanding of the reversal processes occurring in NW or NT arrays, additional information must be retrieved using complementary measurements, such as the angular dependence of the coercivity that will be presented in the next section.

3.2.4.1 Magnetization Reversal

In order to obtain further insights into the magnetic properties of Co NW and NT arrays, magnetic hysteresis loops were measured at different angles (θ) between H and the NW/NT long axis. Figure 3.9 shows the magnetic hysteresis loops measured for Co NW and NT arrays, with $d \sim 50$ nm. A monotonic decrease of the coercive field (H_c), from $\theta = 0°$ to 90° can be seen for the NW arrays,

as expected. However, for NT arrays, a non-monotonic behavior of H_c is present, evidenced by an increase in H_c for $\theta > 0°$, followed by a decreasing trend for $\theta > 60°$.

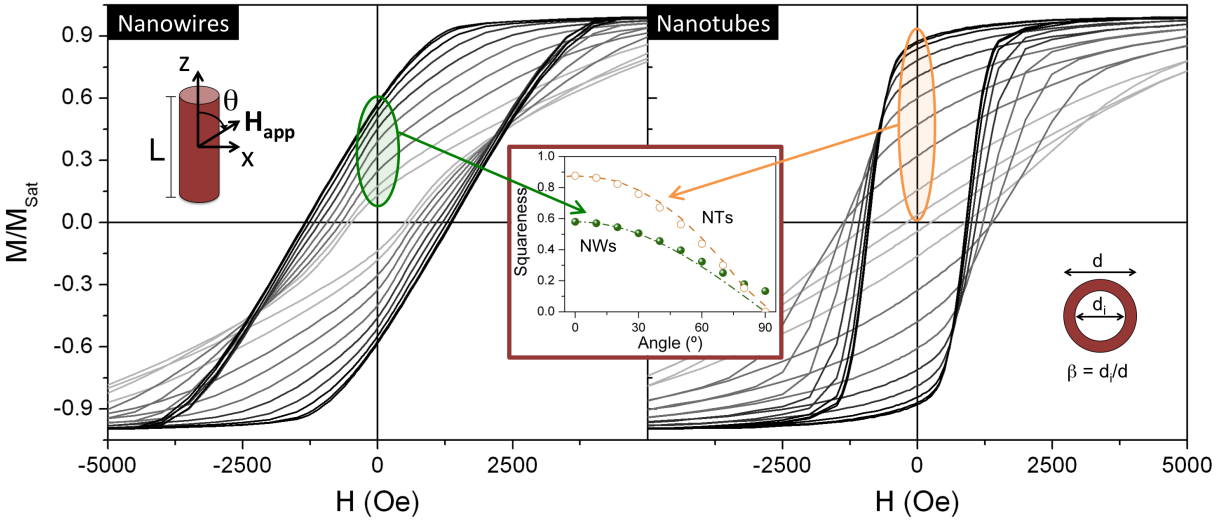


Figure 3.9: Magnetic hysteresis loops of ordered Co NW (left) and NT (right) arrays with $d \sim 50$ nm and $d_i \sim 30$ nm, measured at different angles of H, in 10° steps. Inset shows the angular dependence of squareness (dots - experimental data; line - theoretical calculations).

The squareness (S), defined as the ratio between remanence (M_R) and saturation (M_{Sat}) magnetization, was measured for all samples as a function of θ (inset of Fig. 3.9). A maximum S value was observed when $\theta = 0°$, corresponding to H parallel to the NW/NT axis. Inset of Fig. 3.9 shows a good agreement between the experimental results (dots) and theoretical calculations (line), performed using $S(\theta) = S_0|\cos\theta|$, where $S_0 = S(\theta = 0°)$ [15].

To investigate the magnetization reversal processes of Co NW and NT arrays we analyzed the angular dependence of H_c. Previous works reported analytical calculations of the magnetic reversal modes [coherent (C) magnetization rotation, and transverse (T) and vortex-like (V) domain walls] that are energetically more favorable for high aspect ratio NWs and NTs [8, 13–15, 20, 27, 38–40]. For analytical calculations it is important to define the parameter $\beta = d_i/d$, where d_i and d are the NT inner and outer diameters, respectively (Fig. 3.9).

Figure 3.10 shows the angular dependence of the coercivity for Co NW and NT arrays. From the analytical calculations one expects the magnetization reversal mechanism to correspond to the mode that offers the lowest coercivity values. From the good agreement obtained between our experimental results and the analytical calculations of the angular dependence of coercivity (Fig. 3.10) we can identify the reversal processes that occur in each NW/NT array system. One should note that the model used for the analytical calculations does not take into consideration the magnetic interactions between the NWs/NTs. However, the FORC analysis presented in the previous section allowed us to deduce that the NT arrays behave as almost non-interacting systems, while the NWs exhibit higher values of magnetostatic interactions. This can explain the better agreement found between the analytical calculations and the experimental data for the NT arrays (Fig. 3.10).

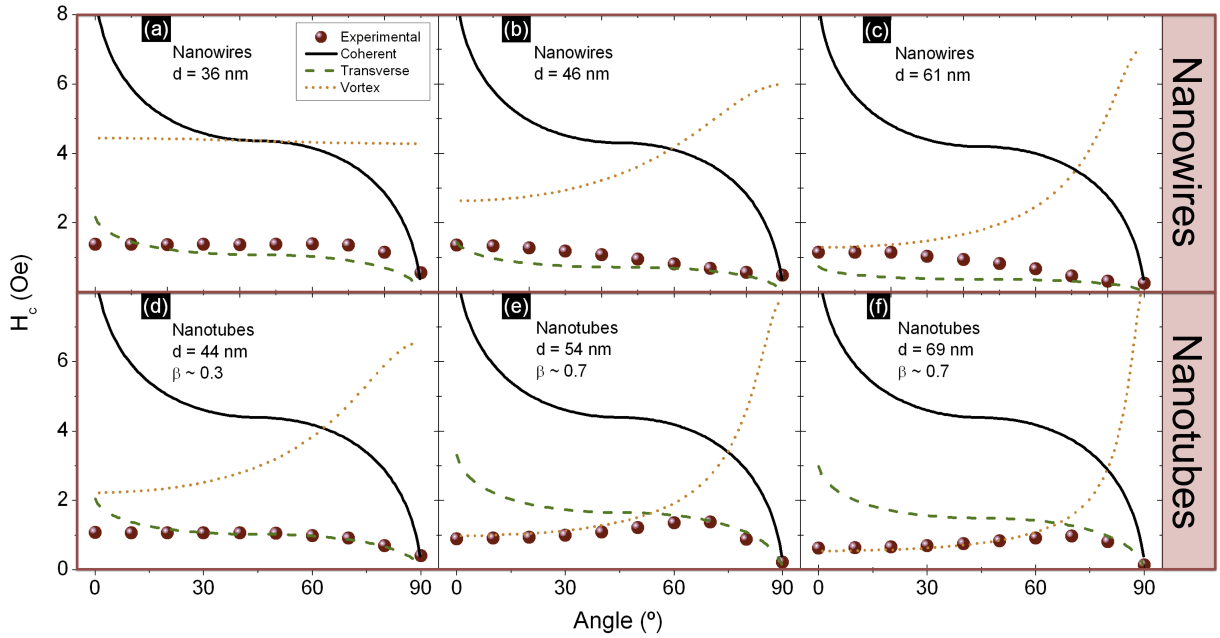


Figure 3.10: Angular dependence of the coercive field measured experimentally (dots) and calculated analytically (C mode: black solid; T mode: green dashed; and V mode: orange dotted) for Co NW and NT arrays in NpATs with different outer diameters.

For all the Co NW arrays studied ($d \sim 40 - 65$ nm) we can deduce that the spins reverse by the nucleation and propagation of a transverse DW [Figs. 3.10(a), (b) and (c)]. As previously reported [13], the magnetization on a NW with a length larger than the domain wall width is expected to reverse by the nucleation and propagation of a DW.

For Co NT arrays with small diameters ($\lesssim 40$ nm) the reversal mode was also found to occur by the nucleation and propagation of a transverse DW [Fig. 3.10(d)]. However, when the NTs outer diameter becomes larger than ~ 50 nm, a transition between two different reversal modes can be identified [Figs. 3.10(e) and (f)]. At small angles of H the nucleation of a vortex wall was found to be energetically favorable. Only for higher angles, where H is almost perpendicular to the NT long axis, is the reversal mechanism given by the propagation of a transverse DW. Comparing NT arrays with $d \sim 50$ and 65 nm [Figs. 3.10(e) and (f), respectively], we can also observe that the critical angle (θ_c) of H at which the transition from a vortex to a transverse DW occurs depends on the NT outer diameter. For $d \sim 50$ nm, we obtained $\theta_c \sim 55°$, while for $d \sim 65$ nm, the critical transition angle reaches $\theta_c \sim 67°$. One should note that the outer and inner diameters of a NT array will highly influence the type of DW that is energetically more favorable to nucleate. Therefore, tuning the outer/inner diameters of the NT arrays allows one to control the magnetization reversal mechanisms for the different angles of applied magnetic field.

3.2.5 Conclusions

The here presented results allowed us to deduce the magnetization reversal mechanisms in both studied systems. While Co NW arrays with $d \sim 40 - 65$ nm and NT arrays with $d \sim 40$ nm reverse their magnetization by the nucleation and propagation of a transverse-like DW, NT arrays with $d \sim 50 - 65$ nm nucleate a vortex-like DW. On the other hand, the FORC diagrams shown in Fig. 3.6 reveal a coercivity distribution along the H_c axis in all NW arrays and NT arrays with $d \sim 40$ nm. However, for the remaining NT arrays such coercivity distribution is practically inexistent. This shows that magnetization reversal by the nucleation and propagation of a transverse wall increases the coercivity distribution along the H_c axis of the FORC diagram, while the nucleation and propagation of a vortex DW does not affect the corresponding coercivity distribution.

Also, the quantitative analysis of FORC measurements allowed us to obtain the profiles of magnetic interaction and coercive field distributions. NW arrays exhibited stronger magnetic interactions than the NT arrays, although in both cases they were found to increase with increasing diameter of the NWs/NTs. The angular dependence of the coercivity of Co NW and NT arrays with different diameters (between 40 and 65 nm) was also measured. For NTs with $d \geqslant 50$ nm we reported experimental evidence for an angular dependent transition of the magnetization reversal modes, which had been theoretically predicted. Analytical calculations allowed us to identify a transverse reversal mode for NW arrays with $d \leqslant 70$ nm and NT arrays with $d < 50$ nm, and a transition between vortex and transverse reversal modes for NTs with $d \geqslant 50$ nm.

Bibliography

[1] P. P. Freitas, F. A. Cardoso, V. C. Martins, S. A. M. Martins, J. Loureiro, J. Amaral, R. C. Chaves, S. Cardoso, L. P. Fonseca, A. M. Sebastiao, M. Pannetier-Lecoeur, and C. Fermon, "Spintronic platforms for biomedical applications", *Lab Chip*, vol. 12, no. 3, pp. 546–57, 2012.

[2] G. Polizos, V. Tomer, E. Manias, and C. A. Randall, "Epoxy-based nanocomposites for electrical energy storage. II: Nanocomposites with nanofillers of reactive montmorillonite covalently-bonded with barium titanate", *J. Appl. Phys.*, vol. 108, no. 7, pp. 074117, 2010.

[3] T. Kawahara, K. Ito, R. Takemura, and H. Ohno, "Spin-transfer torque RAM technology: Review and prospect", *Microelectron. Reliab.*, vol. 52, no. 4, pp. 613–627, 2012.

[4] K. D. Sattler, *Handbook of nanophysics: Nanotubes and nanowires*, CRC Press, USA, 2010.

[5] C. A. Ross, "Patterned magnetic recording media", *Annu. Rev. Mater. Res.*, vol. 31, no. 1, pp. 203–235, 2001.

[6] J. M. D. Coey, *Magnetism and magnetic materials*, Cambridge University Press, New York, 2009.

[7] S. M. Reddy, J. J. Park, S.-M. Na, M. M. Maqableh, A. B. Flatau, and B. J. H. Stadler, "Electrochemical synthesis of magnetostrictive Fe-Ga/Cu multilayered nanowire arrays with tailored magnetic response", *Adv. Funct. Mater.*, vol. 21, no. 24, pp. 4677–4683, 2011.

[8] M. Yan, C. Andreas, A. Kakay, F. Garcia-Sanchez, and R. Hertel, "Fast domain wall dynamics in magnetic nanotubes: Suppression of Walker breakdown and Cherenkov-like spin wave emission", *Appl. Phys. Lett.*, vol. 99, no. 12, pp. 122505, 2011.

[9] D. Serantes, V. Vega, W. O. Rosa, V. M. Prida, B. Hernando, M. Pereiro, and D. Baldomir, "Interplay between magnetic anisotropy and dipolar interaction in one-dimensional nanomagnets: Optimized magnetocaloric effect", *Phys. Rev. B*, vol. 86, no. 10, pp. 104431, 2012.

[10] I. D. Mayergoyz, "Hysteresis models from the mathematical and control theory points of view", *J. Appl. Phys.*, vol. 57, no. 8, pp. 3803, 1985.

[11] F. Beron, *Proprietes magnetostatiques de reseaux de nanofils via les courbes de renversement du premier ordre*, PhD thesis, Ecole Polytechnique de Montreal, 2008.

[12] F. Beron, L.-P. Carignan, D. Menard, and A. Yelon, "Extracting individual properties from global behaviour: First-order reversal curve method applied to magnetic nanowire arrays", in *Electrodeposited nanowires and their applications*, N. Lupu, Ed. INTECH, Croatia, 2010.

[13] P. Landeros, S. Allende, J. Escrig, E. Salcedo, D. Altbir, and E. E. Vogel, "Reversal modes in magnetic nanotubes", *Appl. Phys. Lett.*, vol. 90, no. 10, pp. 102501, 2007.

[14] S. Allende, J. Escrig, D. Altbir, E. Salcedo, and M. Bahiana, "Angular dependence of the transverse and vortex modes in magnetic nanotubes", *Eur. Phys. J. B*, vol. 66, no. 1, pp. 37–40, 2008.

[15] R. Lavin, J. C. Denardin, J. Escrig, D. Altbir, A. Cortes, and H. Gomez, "Angular dependence of magnetic properties in Ni nanowire arrays", *J. Appl. Phys.*, vol. 106, no. 10, pp. 103903, 2009.

[16] H. Masuda and K. Fukuda, "Ordered metal nanohole arrays made by a two-step replication of honeycomb structures of anodic alumina", *Science*, vol. 268, pp. 1466–1468, 1995.

[17] K. Nielsch, F. Muller, and A.-P. Li, "Uniform nickel deposition into ordered alumina pores by pulsed electrodeposition", *Adv. Mater.*, vol. 12, no. 8, pp. 582–586, 2000.

[18] M. P. Proenca, C. T. Sousa, D. C. Leitao, J. Ventura, J. B. Sousa, and J. P. Araujo, "Nanopore formation and growth in phosphoric acid Al anodization", *J. Non-Cryst. Solids*, vol. 354, pp. 5238–5240, 2008.

[19] C. T. Sousa, A. M. L. Lopes, M. P. Proenca, D. C. Leitao, J. G. Correia, and J. P. Araujo, "Rapid synthesis of ordered manganite nanotubes by microwave irradiation in alumina templates", *J. Nanosci. Nanotechnol.*, vol. 9, no. 10, pp. 6084–6088, 2009.

[20] J. Escrig, J. Bachmann, J. Jing, M. Daub, D. Altbir, and K. Nielsch, "Crossover between two different magnetization reversal modes in arrays of iron oxide nanotubes", *Phys. Rev. B*, vol. 77, no. 21, pp. 214421, 2008.

[21] C. T. Sousa, D. C. Leitao, M. P. Proenca, A. Apolinario, J. G. Correia, J. Ventura, and J. P. Araujo, "Tunning pore filling of anodic alumina templates by accurate control of the bottom barrier layer thickness", *Nanotechnology*, vol. 22, no. 31, pp. 315602, 2011.

[22] M. P. Proenca, C. T. Sousa, J. Ventura, M. Vazquez, and J. P. Araujo, "Ni growth inside ordered arrays of alumina nanopores: Enhancing the deposition rate", *Electrochim. Acta*, vol. 72, pp. 215–221, 2012.

[23] L. G. Vivas, M. Vazquez, J. Escrig, S. Allende, D. Altbir, D. C. Leitao, and J. P. Araujo, "Magnetic anisotropy in CoNi nanowire arrays: Analytical calculations and experiments", *Phys. Rev. B*, vol. 85, no. 3, pp. 035439, 2012.

[24] L. G. Vivas, J. Escrig, D. G. Trabada, G. A. Badini-Confalonieri, and M. Vazquez, "Magnetic anisotropy in ordered textured Co nanowires", *Appl. Phys. Lett.*, vol. 100, pp. 252405, 2012.

[25] M. P. Proenca, C. T. Sousa, J. Ventura, M. Vazquez, and J. P. Araujo, "Distinguishing nanowire and nanotube formation by the deposition current transients", *Nanoscale Res. Lett.*, vol. 7, pp. 280, 2012.

[26] D. C. Leitao, A. Apolinario, C. T. Sousa, J. Ventura, J. B. Sousa, M. Vazquez, and J. P. Araujo, "Nanoscale topography: A tool to enhance pore order and pore size distribution in anodic aluminum oxide", *J. Phys. Chem. C*, vol. 115, no. 17, pp. 8567–8572, 2011.

[27] M. P. Proenca, C. T. Sousa, J. Ventura, J. P. Araujo, J. Escrig, and M. Vazquez, "Crossover between magnetic reversal modes in ordered Ni and Co nanotube arrays", *SPIN*, accepted, DOI: 10.1142/S2010324712500142.

[28] F. Beron, L. Clime, M. Ciureanu, D. Menard, R. W. Cochrane, and A. Yelon, "Magnetostatic interactions and coercivities of ferromagnetic soft nanowires in uniform length arrays", *J. Nanosci. Nanotechnol.*, vol. 8, no. 6, pp. 2944–2954, 2008.

[29] C. Pike, C. Ross, R. Scalettar, and G. Zimanyi, "First-order reversal curve diagram analysis of a perpendicular nickel nanopillar array", *Phys. Rev. B*, vol. 71, no. 13, pp. 134407, 2005.

[30] A. Rotaru, J.-H. Lim, D. Lenormand, A. Diaconu, J. B. Wiley, P. Postolache, A. Stancu, and L. Spinu, "Interactions and reversal-field memory in complex magnetic nanowire arrays", *Phys. Rev. B*, vol. 84, no. 13, pp. 134431, 2011.

[31] L. Spinu, A. Stancu, C. Radu, F. Li, and J. B. Wiley, "Method for magnetic characterization of nanowire structures", *IEEE Trans. Magn.*, vol. 40, no. 4, pp. 2116–2118, 2004.

[32] C. Pike, "First-order reversal-curve diagrams and reversible magnetization", *Phys. Rev. B*, vol. 68, no. 10, pp. 104424, 2003.

[33] I. D. Mayergoyz, *Mathematical models of hysteresis and their applications*, vol. 103, Elsevier, Amsterdam, 2003.

[34] C. R. Pike, A. P. Roberts, and K. L. Verosub, "Characterizing interactions in fine magnetic particle systems using first order reversal curves", *J. Appl. Phys.*, vol. 85, no. 9, pp. 6660, 1999.

[35] K. Nielsch, R. B. Wehrspohn, J. Barthel, J. Kirschner, U. Gosele, S. F. Fischer, and H. Kronmuller, "Hexagonally ordered 100 nm period nickel nanowire arrays", *J. Appl. Phys.*, vol. 79, no. 9, pp. 1360, 2001.

[36] R. Ferre, K Ounadjela, J. M. George, L Piraux, and S. Dubois, "Magnetization processes in nickel and cobalt electrodeposited nanowires", *Phys. Rev. B*, vol. 56, no. 21, pp. 66–75, 1997.

[37] F. Beron, D. Menard, and A. Yelon, "First-order reversal curve diagrams of magnetic entities with mean interaction field: A physical analysis perspective", *J. Appl. Phys.*, vol. 103, no. 7, pp. 07D908, 2008.

[38] O. Albrecht, R. Zierold, S. Allende, J. Escrig, C. Patzig, B. Rauschenbach, K. Nielsch, and D. Gorlitz, "Experimental evidence for an angular dependent transition of magnetization reversal modes in magnetic nanotubes", *J. Appl. Phys.*, vol. 109, no. 9, pp. 093910, 2011.

[39] R. Lavin, J. C. Denardin, A. P. Espejo, A. Cortes, and H. Gomez, "Magnetic properties of arrays of nanowires: Anisotropy, interactions, and reversal modes", *J. Appl. Phys.*, vol. 107, no. 9, pp. 09B504, 2010.

[40] J. Escrig, M. Daub, P. Landeros, K. Nielsch, and D. Altbir, "Angular dependence of coercivity in magnetic nanotubes", *Nanotechnology*, vol. 18, no. 44, pp. 445706, 2007.

Chapter 4

Exchange Bias in Ordered Arrays of Co/CoO Nanotubes

This Chapter is composed of Article V, on the magnetic study of the exchange-bias (EB) coupling in core-shell Co/CoO nanotube (NT) arrays. The Co NTs electrodeposited inside the nanoporous alumina templates (NpATs) had outer and inner diameters of $\sim$ 40 and $\sim$ 20 nm, respectively. These were left in air while inside the NpAT for natural oxidation of their inner walls, forming ferromagnetic/antiferromagnetic (FM/AFM) core-shell nanotubular structures. Temperature and field-cooling dependence of the EB effect is here presented, along with the training effect of EB at 6 K. A maximum blocking temperature (T_B) was found at $\sim$ 220 K, close to the bulk Néel temperature of CoO (293 K). The T_B-distribution was also measured, evidencing a bimodal distribution as previously reported in FM/AFM thin films.

4.1 Article V – Exchange Bias, Training Effect and Bimodal Distribution of Blocking Temperatures in Electrodeposited Core-Shell Nanotubes

Mariana P. Proenca, João Ventura, Célia T. Sousa, Manuel Vazquez and João P. Araujo, submitted to *Physical Review B*.

Abstract

Co nanotubes (NTs) were electrodeposited inside nanoporous alumina templates by a potentiostatic method and then left in air for natural oxidation of their inner walls. Temperature dependent magnetic measurements evidenced the existence of exchange-bias (EB) coupling between the Co ferromagnetic (FM) outer wall and the CoO antiferromagnetic (AFM) inner wall of the NTs. The effect of temperature and cooling field on the EB effect between the Co/CoO walls of the NTs is here reported. Training effct of the EB in the Co/CoO NT arrays, measured at 6 K, suggested the existence of a stronger coupling between the AFM and the FM layers when shapped into a core-shell nanotubular structure. A bimodal distribution of blocking temperatures was found when applying the magnetic field parallel and perpendicular to the NTs axis.

4.1.1 Introduction

High aspect ratio magnetic nanoparticles have attracted much interest in the last years due to their potential applications in nanoelectronic devices, catalysis, high-density recording media, and drug delivery [1, 2]. Their shape anisotropy combined with tunable nanosized dimensions give rise to new interesting phenomena, such as enhanced magnetic anisotropy and hence higher coercivity [3]. In particular, magnetic nanotubes (NTs) show great advantages over nanowires (NWs) as they present high surface areas, small wall thicknesses and a hollow inner core that can be coated, oxidized or filled with different materials, increasing the potential applicability of such structures and respective magnetic properties [4, 5].

One of the most interesting phenomena that has prompted intense research spanning several decades is the exchange-bias (EB) coupling between ferromagnetic (FM) and antiferromagnetic (AFM) layers, after field-cooling (FC) the AFM material from above its Néel temperature (T_N) [6–10]. The EB effect is highly important in magnetic applications such as high-density magnetic recording, spin valve and magnetic tunnel junction devices (read heads, sensors), where it is used to stabilize the magnetization of a reference FM layer [6, 8]. EB refers to the shift of the magnetic hysteresis loop along the field axis by an exchange-bias field (H_{ex}) measured from the origin, and usually accompanied by a vertical magnetization shift and a coercive field (H_c) enhancement. In addition, when cycling the FM/AFM bilayer structure through consecutive hysteresis loops, a H_{ex} decrease can be observed. This phenomenon, called training effect (TE), can be explained as arising

from the partial loss of the AFM net magnetization, as its spin structure rearranges with each magnetization reversal of the FM layer [8, 10–12].

The EB effect strongly depends on temperature (T), disappearing above the so-called blocking temperature (T_B). Recent reports have shown the existence of a bimodal distribution of T_B in FM/AFM heterostructures, with distinct high- and low-T contributions [13–15]. The first is related with the thermal stability of the AFM spin structure and the bulk grain size distribution, while the second is ascribed to spin-glass-like interfacial regions present at the FM/AFM interface.

Most of the recent studies on the EB mechanism have been performed on thin-film systems [7, 10, 16–19], or core-shell nanoparticles [9, 20–24]. However, no work was found yet on the study of EB coupling in high aspect ratio nanotubular structures. In this work, Co NT and NW arrays were prepared by electrodeposition inside nanoporous alumina templates (NpATs) with diameters of $\sim$ 40 nm. Nanotubular heterostructures of FM/AFM bilayers were then obtained after natural oxidation of the inner Co NT walls, forming Co/CoO NTs. Temperature and field-cooling dependent magnetic measurements allowed us to study the EB phenomenon, the respective TE and the T_B-distribution exhibited by the arrays of tubular core-shell AFM/FM bilayer nanostructures. Additionally, the EB effect in the fabricated Co/CoO NTs was found to arise at temperatures below $\sim$ 220 K, close to the bulk T_N value of CoO (293 K) [9, 16]. Training of the EB effect was also observed at 6 K and fitted using a recursive formula proposed by Binek [11]. The T_B-distribution revealed a bimodal structure with an average T_B value of $\sim$ 87 K and a maximum $T_B^{max} \sim$ 220 K, for both parallel and perpendicular directions of the applied magnetic field.

4.1.2 Experimental Details

Nanoporous alumina templates (NpATs) were prepared by a two-step anodization process [25] of high-purity Al (99.999%) disks in 0.3 M oxalic acid at 40 V and $\sim$ 4°C [26]. First and second anodizations were performed for 24 h and 20 h, respectively, leading to porous alumina membranes with ordered hexagonal nanopore arrays with diameters $d \sim$ 35 nm, interpore distances of $\sim$ 105 nm and membrane thickness of $\sim$ 50 μm.

For the subsequent nanopores' filling by a potentiostatic electrodeposition method, the Al substrate and the alumina layer present at the pores' bottom were chemically etched, opening the pores from both sides of the membrane [27]. During this process the pore diameter was enlarged to $\sim$ 40 nm. An Au metallic contact was then sputtered at the opened pores' side of the NpAT to serve as the working electrode. The thickness of the sputtered Au layer is a key parameter to control the formation of nanowires ($\sim$ 100 nm, closing the pore bottom) or nanotubes ($\sim$ 40 nm) [27]. A Pt mesh and Ag/AgCl (in 4 M KCl) were used as the counter and reference electrodes, respectively, in a three-electrode deposition cell. Further details on the membranes preparation for subsequent electrodeposition of NW/NT-like structures can be found in Ref. 19.

Cobalt electrodeposition was performed in an aqueous solution of 0.89 M $CoSO_4 \cdot 7H_2O$ and 0.49 M

H_3BO_3, at 30°C, and applying a constant potential of -1.5 V vs. Ag/AgCl for about 2 min, using a Solartron 1480 MultiStat. Morphological characterization was performed using a scanning electron microscope (SEM; FEI Quanta 400FEG). Prior to bottom SEM imaging, ion-milling was performed to remove the Au contact and smooth the NpAT surface. The milling process was carried out using an ion-beam sputter deposition system by Commonwealth Scientific Corporation [28]. The NpATs filled with Co NWs and NTs were then left in air for several months after electrodeposition, to allow natural oxidation of the Co tops/walls to occur. Due to the highly oxidative nature of the cobalt element, exposing the Co layer to ambient atmosphere leads to the formation of an antiferromagnetic polycrystalline CoO layer at the surface, with a thickness of ~ 3 nm, as previously reported [29–33]. Temperature ($6 - 300$ K) and field-cooling (-50 to 50 kOe) dependent magnetic measurements were then performed using a superconducting quantum interference device (SQUID) MPMS magnetometer from Quantum Design, by applying the magnetic field (H) parallel and perpendicular to the tube/wire axis.

4.1.3 Results and Discussion

Ordered hexagonal arrays of Co NWs and NTs with outer diameters of ~ 40 nm, inner NT diameters of ~ 20 nm, intertube distances of ~ 105 nm and aspect ratios (length/diameter) higher than 150, were successfully obtained by electrodeposition inside NpATs. Figure 4.1(a) shows a bottom SEM image of a NpAT after chemical etching of the barrier alumina layer at the pores' bottom and subsequent ion-milling, illustrating the high order degree of the nanoporous array. A bottom SEM view of the electrodeposited Co NT arrays is displayed in Fig. 4.1(b), after ion-milling of the Au working electrode, illustrating the tubular shape grown along the nanopores' wall, and the hollow cores that typically form a NT-like structure. By exposing the NpAT filled with Co NTs to air, natural oxidation of the inner Co NT walls occurs [31, 32]. Figure 4.1(c) gives a schematic representation of the Co/CoO bilayer NTs after natural oxidation of Co. These bilayer tubular nanostructures are thus formed of an outer FM and inner AFM layer, providing a very interesting system to study EB, TE and T_B-distributions. Note that, when the Co NTs are removed from the template their outer walls also start to oxidize, preventing us from obtaining clear transmission electron microscopy (TEM) images. However, when analyzing the TEM images of similarly fabricated Ni NTs [5], a tubular structure with uniform walls can be found throughout the tube, and thus a similar structure is expected to be also produced when electrodepositing Co NTs [34].

4.1.3.1 Exchange-bias Coupling in Co/CoO NTs

Magnetic hysteresis loops [$M(H)$] were performed at 6 K, after field-cooling (FC) in 50 kOe from 320 K (above $T_N^{CoO} \sim 290$ K), by applying the magnetic field parallel ($H^{\parallel}$) and perpendicular ($H^{\perp}$) to the wire/tube axis. For our partially oxidized Co NT arrays, a loop shift was observed in both parallel ($\parallel$) and perpendicular ($\perp$) directions of the applied magnetic field (Fig. 4.2), which is interpreted as arisen from the exchange bias coupling. This evidences the partial oxidation of the Co NTs' walls,

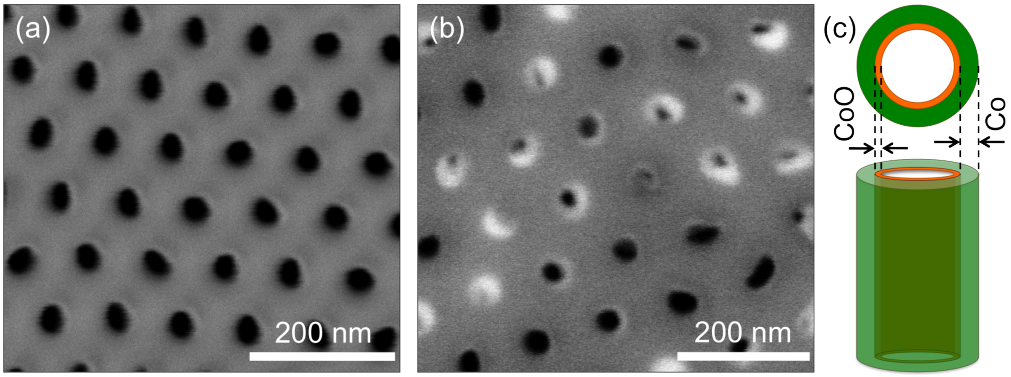


Figure 4.1: SEM bottom image of a NpAT (a) empty and (b) filled with Co NTs, after ∼ 200 nm of etching by ion-milling. (c) Schematic representation of a Co/CoO NT.

forming a FM/AFM bilayer nanostructure. Figure 4.2 also illustrates that, at 6 K, the easy axis of magnetization has a preferential component parallel to the NT axis.

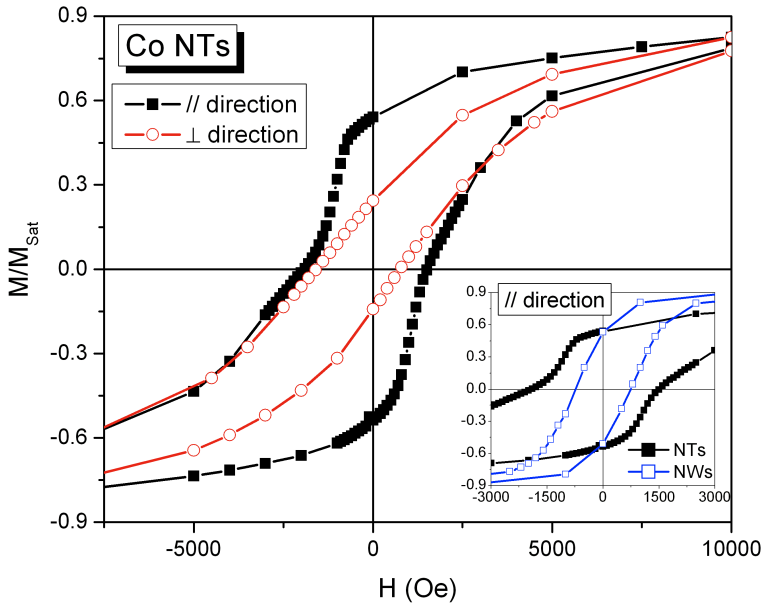


Figure 4.2: Magnetic hysteresis loops of Co/CoO NT arrays measured at 6 K after field cooling in 50 kOe, by applying the magnetic field parallel (filled symbols) and perpendicular (opened symbols) to the NT axis, evidencing the exchange-bias effect (loop shift along the field axis). Inset shows a comparison between the magnetic hysteresis loop of Co/CoO NT (filled symbols) and Co NW (opened symbols) arrays, measured at 6 K after field cooling in 50 kOe, by applying the magnetic field parallel to the wire/tube axis, evidencing the inexistence of loop shift in the NW arrays.

On the other hand, no EB effect is observed in the Co NW arrays (inset of Fig. 4.2). This indicates that the natural oxidation of the NWs does not form a FM/AFM interface, probably due to the protection of the NW walls by the alumina membrane, difficulting the formation of a crystalline oxide layer. This also demonstrates that the Co oxide formed after partial oxidation of the Co NTs is mainly composed of crystalline CoO and grows in their inner walls [as schematically represented

in Fig. 4.1(c)].

To study the temperature dependence of the EB effect in Co/CoO NT arrays, $M(H)$ were measured at T = 6, 50, 150, 250 and 300 K, after FC in 50 kOe from 320 K to T. Figures 4.3(a) and (b) illustrate the $M(H)$ measurements performed by applying the magnetic field parallel and perpendicular to the NTs' axis, respectively. The shift observed in the $M(H)$ loops along the field axis is defined as the exchange bias field $H_{ex} = (H_{cL} + H_{cR})/2$, where H_{cL} and H_{cR} are the left and right coercive fields, respectively. The inset of Fig. 4.3 shows the variation of the exchange-bias field (H_{ex}) with T, allowing the determination of a maximum T_B value of $\sim$ 220 K, which is $\sim$ 70 K below the bulk Néel temperature of CoO (293 K), in close agreement with previous reported works [9, 16]. Additionally, it is remarkable to see (Fig. 4.3) that at low temperatures ($T < T_B$) the magnetization reversal follows two different processes depending on the value of the applied magnetic field. This double-step reversal mechanism seams to be related to the EB process, as it only appears at $T < T_B$.

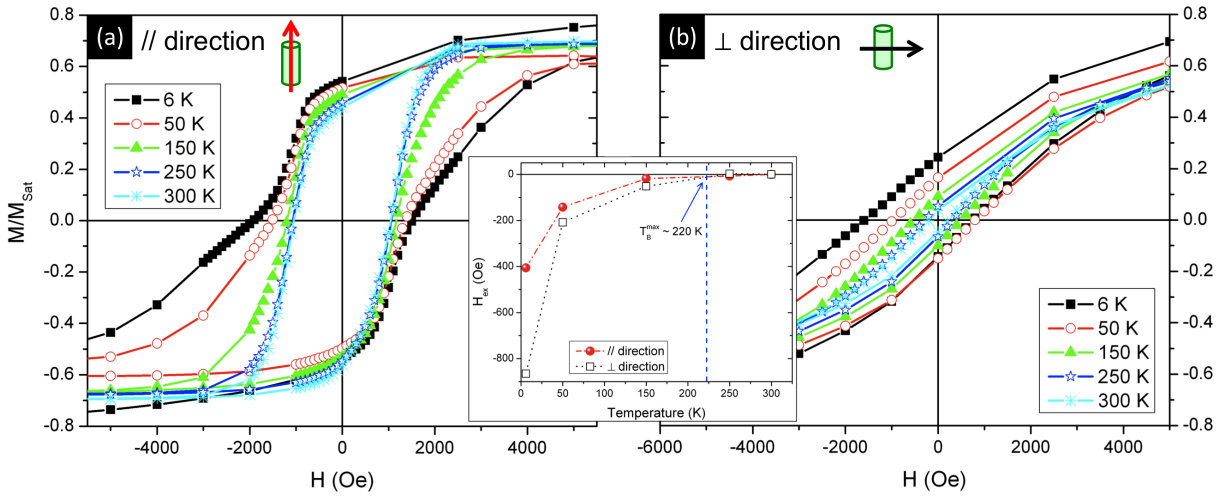


Figure 4.3: Magnetic hysteresis loops of Co/CoO NT arrays measured at different temperatures after field cooling in 50 kOe, by applying the magnetic field (a) parallel and (b) perpendicular to the NT axis. Inset shows the temperature dependence of the exchange-bias field, measured by applying the magnetic field parallel (filled symbols) and perpendicular (opened symbols) to the tube long axis.

It is important to note that the $M(H)$ measurements performed in both parallel and perpendicular directions exhibited an exchange bias effect, that can be quantified by the loop shift along the field axis (Fig. 4.3). Previous works on the study of longitudinal and perpendicular exchange bias in FM/AFM multilayers (Co/Pt/Co+CoO [16]; FeMn/FeNi/FeMn [17]; FePt/FeMn [18]) have also observed in-plane and out-of-plane exchange coupling, with the cooling field applied along the corresponding directions [16–19]. The majority of these multilayered systems exhibit higher $|H_{ex}|$ values when both the cooling and measurement fields are applied along the easy axis of magnetization of the FM layer. On the other hand, in our case, in which the easy axis of magnetization of the Co NTs is in the parallel ($\|$) direction, we obtained $|H_{ex}^{\|}| < |H_{ex}^{\perp}|$ (Fig. 4.3). In particular, at 6 K, we obtained $H_{ex}^{\perp} \sim 2H_{ex}^{\|} \sim -800$ Oe.

Many different parameters are involved in the exchange bias effect, including anisotropy, roughness,

spin configuration and magnetic domains. The complete understanding of EB at the microscopic level is still the focus of intense research [6]. The in-plane/out-of-plane exchange bias ratio was previously reported to be strongly dependent on the AFM crystalline orientation and on the thickness of the FM layer, suggesting that the AFM spin structure at the interface could differ from that of the bulk [18]. Assuming ideal interfaces between the AFM and the FM layers, the exchange bias magnitude can be estimated as:

$$H_{ex} = \frac{J_{INT}}{M_{FM} t_{FM}}, \tag{4.1}$$

where J_{INT} is the interface coupling constant, and M_{FM} and t_{FM} are the saturation magnetization and the thickness of the FM layer, respectively [6]. Using $J_{INT} = 2.5$ erg cm^{-2} [29], $M_{FM} = 1420$ emu cm^{-3} and $t_{FM} \sim 10 \pm 2$ nm for the Co/CoO NTs, we estimated $|H_{ex}| \sim 1.8 \pm 0.4$ Oe, which is, as expected, higher than the experimentally obtained values (Fig. 4.3). The EB effect is highly dependent on the coupling energy between the FM and AFM layers, which is also known to strongly depend on the domain formation in the AFM or FM layer, the grain size distribution, induced thermoremanent magnetization in the AFM layer, non-colliniarity of AFM-FM spins, random anisotropy in the AFM layer, or uncompensated surface spins [6, 35]. The Co NTs electrodeposited in this work have a polycrystalline structure with no preferred orientation (not shown). For the oxidation of the Co NTs' inner walls one thus expects the formation CoO with a polycrystalline structure.

To compare our system with previously reported studies in Co/CoO multilayers [6], we estimated the interface energy per unit area given by:

$$\Delta E = M_{FM} t_{FM} |H_{ex}|. \tag{4.2}$$

Considering $t_{FM} \sim 10$ nm and using $M_{FM} = 1420$ emu cm^{-3} for the Co/CoO NTs, we estimate $\Delta E^{\parallel} \sim 0.57$ erg cm^{-2} and $\Delta E^{\perp} \sim 1.14$ erg cm^{-2}, in good agreement with values reported for a CoO layer obtained from Co oxidation ($0.40 - 3.50$ erg cm^{-2}) [6]. The different energy values found for the two directions were attributed to the microstructure in the distinct crystalline orientations of both the Co NT walls and respective oxidized layer [16, 18]. A report on a systematic study of in-plane and out-of-plane EB in FePt/FeMn multilayers grown with different crystalline orientations, showed a strong dependence of EB on the crystalline orientation of the FePt layer [18]. In particular, when the multilayers were epitaxially grown on a MgO (110) substrate, the H_{ex} value observed along the hard axis of magnetization was almost two times that of the easy axis, as also obtained in this work for the Co/CoO NT arrays.

The dependence of H_{ex} on the cooling field H_{FC} was studied by measuring $M(H)$ at 6 K, after cooling the samples from 320 K at different H_{FC}, applied along the parallel and perpendicular directions (Fig. 4.4). When cooling a FM/AFM system from a temperature T between the FM Curie temperature (T_C) and T_N ($T_C > T > T_N$), the H_{FC} will affect the domain/spin structure of the FM layer, and, due to the high J_{INT}, also the AFM spins [6, 20, 36]. Figure 4.4 shows an increase in $|H_{ex}|$ with increased $|H_{FC}|$. Note that a larger H_{FC} magnitude leads to a higher alignment degree of the

magnetization of the NTs along the applied field. Due to the strong coupling exhibited between the FM and AFM spins, this will then lead to higher $|H_{ex}|$ values. As H_{FC} approaches zero, the strength of the applied magnetic field will no longer be enough to completely saturate the FM magnetization during the cooling procedure, thus decreasing the degree of alignment of the AFM spins. Therefore, at $H_{FC} \sim 0$, the $|H_{ex}|$ values are much lower (Fig. 4.4). Figure 4.4 also shows a lower saturation field along the parallel direction, as the $|H_{ex}^{\parallel}|$ exhibits a constant value ($\sim$ 400 Oe) for both $|H_{FC}^{\parallel}| =$ 3 kOe and 50 kOe, indicating a complete saturation of the FM magnetization already at 3 kOe. As for the perpendicular direction, $|H_{ex}^{\perp}|$ increases from $\sim$ 600 Oe to $\sim$ 800 Oe for $|H_{FC}^{\perp}| =$ 3 kOe and 50 kOe, respectively, showing that at 3 kOe the magnetization of the FM layer is not yet completely saturated.

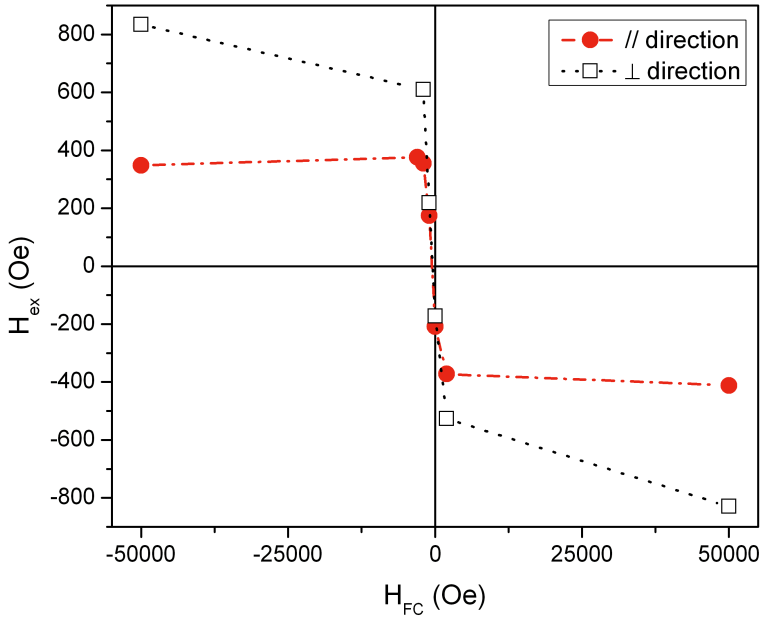


Figure 4.4: Dependence of H_{ex} on the field-cooling field (H_{FC}), measured at 6 K by applying the magnetic field parallel (filled symbols) and perpendicular (opened symbols) to the tube long axis.

4.1.3.2 Training Effect of Exchange Bias

The training of the exchange bias field was studied at 6 K, after field cooling the Co/CoO NT arrays in 50 kOe along both parallel and perpendicular directions. Five consecutive magnetic hysteresis loops were then measured with a maximum applied field of 50 kOe, and the $|H_{ex}|$ values extracted from each $M(H)$. The variation of $|H_{ex}|$ with the number of magnetic cycles (n) is represented in Fig. 4.5. A monotonic decrease of the EB effect when cycling the magnetic field through consecutive loops is seen, corresponding to the traning effect (TE).

In a previous work by C. Binek [11], the training effect was explained within the framework of non-equilibrium thermodynamics of the spin configurational relaxation at the AFM surface. It was argued that this spin relaxation towards equilibrium is driven by the reversal of the FM magnetization during

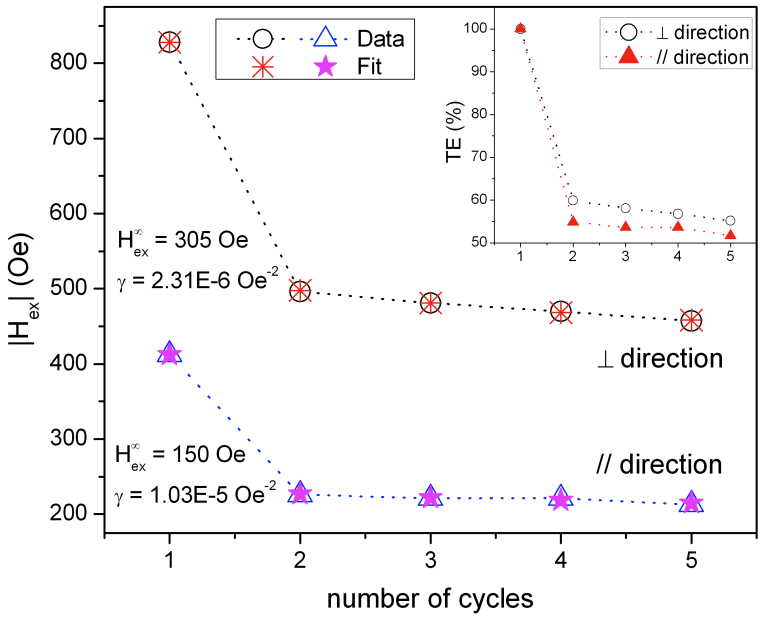


Figure 4.5: Dependence of $|H_{ex}|$ on the number of magnetic hysteresis cycles, measured at 6 K after field cooling in 50 kOe, by applying the magnetic field parallel ($\parallel$) and perpendicular ($\perp$) to the tube axis, and respective fits using Eq. (4.3). Inset illustrates the corresponding training effect (TE).

the consecutive cycling of the external magnetic field. The gradual decrease of $|H_{ex}|$ with increasing n thus reflects the rearrangement of the spin structure of the AFM layer after each reversal of the FM layer magnetization [8, 10, 11, 37]. Based on free energy considerations, the following recursive formula was obtained to describe the TE of H_{ex} [11]:

$$H_{ex}^{n+1} - H_{ex}^{n} = -\gamma (H_{ex}^{n} - H_{ex}^{\infty})^3, \tag{4.3}$$

where H_{ex}^{n} (H_{ex}^{∞}) is the exchange bias field at the n^{th} cycle (in the limit of an infinite number of cycles) and γ describes the characteristic decay rate of the training behavior. The physical parameter γ depends on the leading expansion coefficient b of the free energy, on a factor ζ which is proportional to the coupling constant between the AFM and FM layer, and on a damping constant ξ that can be considered as a typical inverse relaxation time [11]:

$$\gamma = \frac{b}{\zeta^2 \xi}. \tag{4.4}$$

The results presented in Fig. 4.5 were fitted using the recursive relation [Eq. (4.3)], giving $H_{ex}^{\infty,\perp}$ = 305 Oe and $\gamma^{\perp} = 2.31 \times 10^{-6}$ Oe^{-2} along the perpendicular direction, and $H_{ex}^{\infty,\parallel}$ = 150 Oe and $\gamma^{\parallel} = 1.03 \times 10^{-5}$ Oe^{-2} along the parallel direction. In both cases, the γ values obtained are one to two orders of magnitude smaller than previously reported for Co/CoO bilayers ($\gamma = 5 \times 10^{-4}$ Oe^{-2}) [10]. This can be interpreted as the existence of a stronger coupling between the AFM and FM layers when shaped into a core-shell nanotubular structure.

The inset of Fig. 4.5 shows the percentage of TE for both parallel and perpendicular directions, defined as the relative decrease in H_{ex} from the first to the n^{th} cycle [8]:

$$\mathrm{TE}_n(\%) = \left(1 - \frac{H_{ex}^1 - H_{ex}^n}{H_{ex}^1}\right) \times 100(\%). \tag{4.5}$$

A large decrease of the TE of $\sim 50 - 60\%$ from the first to the second cycles is observed, while for the subsequent cycles the TE only drops $\sim 2\%$. This is usually attributed to the difference between the dominant FM layer reversal mechanisms. For $n = 1$ the magnetization of the FM layer reverses by domain wall motion, while for $n \geqslant 2$ the FM layer will mainly reverse by coherent magnetization rotation [8, 30]. Recent studies have also attributed the strong TE of H_{ex} between the first and second cycles to some initial non-equilibrium arrangement or metastable state of the AFM spins [10, 38].

4.1.3.3 Bimodal Distribution of Blocking Temperatures

The EB effect is also known to strongly depend on temperature, disappearing for T above T_B. This coupling behavior is highly complex and was found to result from the combination of several different phenomena. In particular, the AFM layer can be described as an assembly of almost uncoupled grains, having a pinning energy $K_{AFM} \times V$, where K_{AFM} is the AFM anisotropy energy per unit volume, and V is the AFM grain volume [13, 15]. Each AFM grain is then coupled to the adjacent FM layer by an effective interfacial exchange interaction per unit area ΔE, as estimated in Eq. (4.2).

To further extend our study on the EB effect in Co/CoO NT arrays, we measured the T_B-distribution along both the parallel and perpendicular directions, following a specific cooling procedure [13, 14]. First, $M(H)$ is measured at 6 K after field-cooling the sample from 320 K under $H_{FC} = 50$ kOe. Such field saturates the FM magnetization in the positive direction, thus inducing the same direction to the first interfacial atomic layer of the AFM. The temperature is then increased to an intermediate temperature (T_0), field-cooled from T_0 to 6 K, with H_{FC} = -50 kOe, and $M(H)$ is measured again at 6 K. During this second field-cooling procedure, the AFM entities (grains and/or spin-glass regions) whose T_B is in the range of 6 K $< T_B < T_0$ are magnetically ordered in the negative direction. By increasing T_0 from 6 K to 320 K, we are able to obtain the dependence of H_{ex} on T_0. The variation of H_{ex} with T_0 ($\mathrm{d}H_{ex}/\mathrm{d}T_0$), is proportional to the amount of reversed AFM entities, and thus to the T_B-distribution of the AFM layer (Fig. 4.6). It is important to note that all the $M(H)$ measurements were made at a fixed temperature (6 K), thus avoiding the influence of the temperature dependence of relevant physical parameters (like anisotropy constants or interfacial coupling energy).

Figure 4.6 shows the T_B-distribution of our Co/CoO NT arrays as a function of T_0, where two peaks can be identified: one at very low-T; and the other centered at $T \sim 87$ K and extending to higher temperatures. Previous reports have shown that various polycrystalline FM/AFM bilayers exhibit two distinct peaks in the T_B-distribution [13, 14]. The first peak, occurring at low-T, is attributed to the presence of FM/AFM disordered interfacial spins exhibiting a spin-glass-like behavior. Due to

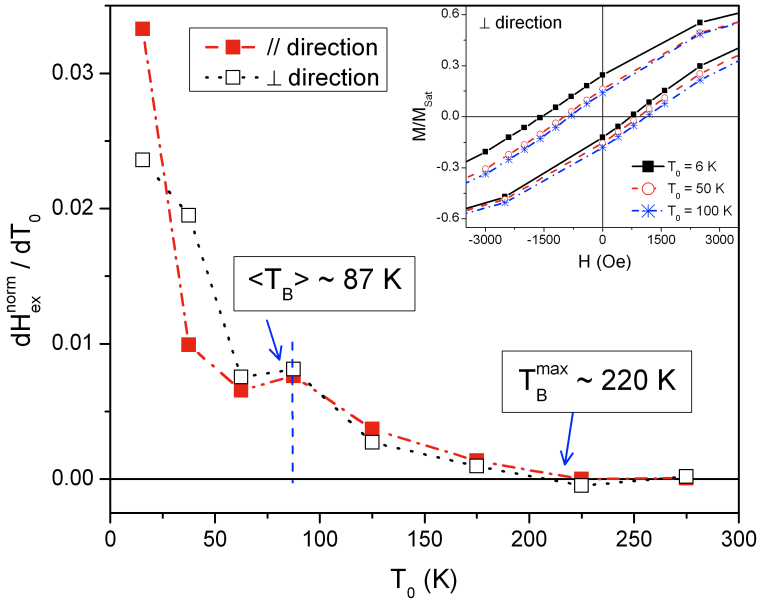


Figure 4.6: Representation of the T_B-distribution of the CoO AFM grains formed at the inner Co NT walls, by illustrating the dependence on T_0 of the derivative of normalized H_{ex}, $\mathrm{d}H_{ex}^{norm}/\mathrm{d}T_0$, along both parallel (filled symbols) and perpendicular (opened symbols) directions. Inset shows the magnetic hysteresis loops measured at 6 K along the perpendicular direction for $T_0 = 6$, 50 and 100 K.

interfacial roughness, random coupling within a grain can occur at the FM/AFM interface, resulting in a high degree of interfacial exchange frustration [13]. When the frustration is particularly high, the interfacial spins behave like a spin-glass below a certain freezing temperature (typically between 4 and 70 K). These interfacial spin reorganizations will induce a strong T-variation of the effective coupling energy, thus affecting the EB field. Therefore, up to the freezing temperature and within each grain, the FM/AFM coupling is enhanced by spin-glass-like interfacial regions.

The second peak, occurring at higher temperatures, is ascribed to the AFM grains themselves, which are submitted to thermally activated magnetic reversal [13]. The T_0 value of the peak's maximum is associated with the average blocking temperature $\langle T_B \rangle$, which in this case is $\sim$ 87 K. From the T_B-distribution plot (Fig. 4.6) we can also estimate the value of T_B^{max}, confirmed to be $\sim$ 220 K.

4.1.4 Conclusions

We demonstrated the existence of exchange bias coupling in Co/CoO NT arrays, along both parallel and perpendicular directions of applied magnetic field. Measurements of the temperature dependence of EB allowed the estimation of a maximum $T_B^{max} \sim 220$ K, which is $\sim$ 70 K below the T_N of bulk CoO (293 K). Training effect along both parallel and perpendicular directions was also observed at 6 K, after field-cooling in 50 kOe. The TE was fitted using the recursive Binek formula, giving small values for the characteristic decay rate of the training behavior (fitting parameter γ), which was interpreted as the existence of a stronger coupling between the FM/AFM layer when shaped into a core-shell

nanotubular structure. Bimodal T_B-distributions were also obtained when measuring along both parallel and perpendicular directions. The low-T peak was ascribed to interfacial spin-glass phases, while the high-T peak was attributed to thermal reversal of AFM grains.

Bibliography

[1] S. S. P. Parkin, M. Hayashi, and L. Thomas, "Magnetic domain-wall racetrack memory", *Science*, vol. 320, pp. 190–194, 2008.

[2] L. Zhang, T. Petit, K. E. Peyer, and B. J. Nelson, "Targeted cargo delivery using a rotating nickel nanowire", *Nanomedicine: Nanotech. Biol. Med.*, vol. 8, no. 7, pp. 1074–1080, 2012.

[3] N. Ahmad, J. Y. Chen, J. Iqbal, W. X. Wang, W. P. Zhou, and X. F. Han, "Temperature dependent magnetic properties of Co nanowires and nanotubes prepared by electrodeposition method", *J. Appl. Phys.*, vol. 109, pp. 07A331, 2011.

[4] S. J. Son, X. Bai, A. Nan, H. Ghandehari, and S. B. Lee, "Template synthesis of multifunctional nanotubes for controlled release", *J. Contr. Rel.*, vol. 114, no. 2, pp. 143–152, 2006.

[5] M. P. Proenca, C. T. Sousa, J. Ventura, J. P. Araujo, J. Escrig, and M. Vazquez, "Crossover between magnetic reversal modes in ordered Ni and Co nanotube arrays", *SPIN*, accepted, DOI: 10.1142/S2010324712500142.

[6] J. Nogues and I. K. Schuller, "Exchange bias", *J. Magn. Magn. Mater.*, vol. 192, no. 2, pp. 203–232, 1999.

[7] S. Brems, D. Buntinx, K. Temst, C. Van Haesendonck, F. Radu, and H. Zabel, "Reversing the training effect in exchange biased CoO/Co bilayers", *Phys. Rev. Lett.*, vol. 95, no. 15, pp. 157202, 2005.

[8] J. Ventura, J. P. Araujo, and J. B. Sousa, "Training effect in specular spin valves", *Phys. Rev. B*, vol. 77, no. 18, pp. 184404, 2008.

[9] T. Maurer, F. Zighem, F. Ott, G. Chaboussant, G. Andre, Y. Soumare, J.-Y. Piquemal, G. Viau, and C. Gatel, "Exchange bias in Co/CoO core-shell nanowires: Role of antiferromagnetic superparamagnetic fluctuations", *Phys. Rev. B*, vol. 80, no. 6, pp. 064427, 2009.

[10] S. R. Ali, M. R. Ghadimi, M. Fecioru-Morariu, B. Beschoten, and G. Guntherodt, "Training effect of the exchange bias in Co/CoO bilayers originates from the irreversible thermoremanent magnetization of the magnetically diluted antiferromagnet", *Phys. Rev. B*, vol. 85, no. 1, pp. 012404, 2012.

[11] C. Binek, "Training of the exchange-bias effect: A simple analytic approach", *Phys. Rev. B*, vol. 70, no. 1, pp. 014421, 2004.

[12] S. Brems, D. Buntinx, K. Temst, and C. Van Haesendonck, "Origin of the training effect and asymmetry of the magnetization in polycrystalline exchange bias systems", *Phys. Rev. Lett.*, vol. 99, no. 06, pp. 067201, 2007.

[13] V. Baltz, B. Rodmacq, A. Zarefy, L. Lechevallier, and B. Dieny, "Bimodal distribution of blocking temperature in exchange-biased ferromagnetic/antiferromagnetic bilayers", *Phys. Rev. B*, vol. 81, no. 5, pp. 052404, 2010.

[14] C. K. Safeer, M. Chamfrault, J. Allibe, C. Carretero, C. Deranlot, E. Jacquet, J.-F. Jacquot, M. Bibes, A. Barthelemy, B. Dieny, H. Bea, and V. Baltz, "Anisotropic bimodal distribution of blocking temperature with multiferroic $BiFeO_3$ epitaxial thin films", *Appl. Phys. Lett.*, vol. 100, no. 7, pp. 072402, 2012.

[15] J. Ventura, J. P. Araujo, J. B. Sousa, A. Veloso, and P. P. Freitas, "Distribution of blocking temperatures in nano-oxide layers of specular spin valves", *J. Appl. Phys.*, vol. 101, no. 11, pp. 113901, 2007.

[16] S. Maat, K. Takano, S. S. P. Parkin, and E. E. Fullerton, "Perpendicular exchange bias of Co/Pt multilayers", *Phys. Rev. Lett.*, vol. 87, no. 8, pp. 087202, 2001.

[17] L. Sun, S. M. Zhou, P. C. Searson, and C. L. Chien, "Longitudinal and perpendicular exchange bias in FeMn/$(FeNi/FeMn)_n$ multilayers", *J. Appl. Phys.*, vol. 93, no. 10, pp. 6841–6843, 2003.

[18] N. N. Phuoc and T. Suzuki, "In-plane and out-of-plane exchange biases in epitaxial FePt-FeMn multilayers with different crystalline orientations", *IEEE Trans. Magn.*, vol. 44, no. 11, pp. 2828–2831, 2008.

[19] E. Shipton, K. Chan, T. Hauet, O. Hellwig, and E. E. Fullerton, "Suppression of the perpendicular anisotropy at the CoO Neel temperature in exchange-biased CoO/[Co/Pt] multilayers", *Appl. Phys. Lett.*, vol. 95, no. 13, pp. 132509, 2009.

[20] E. L. Salabas, A. Rumplecker, F. Kleitz, F. Radu, and F. Schuth, "Exchange anisotropy in nanocasted Co_3O_4 nanowires", *Nano Lett.*, vol. 6, no. 12, pp. 2977–2981, 2006.

[21] V. Skumryev, S. Stoyanov, Y. Zhang, G. Hadjipanayis, D. Givord, and J. Nogues, "Beating the superparamagnetic limit with exchange bias", *Nature*, vol. 423, pp. 850–853, 2003.

[22] M. P. Proenca, C. T. Sousa, A. M. Pereira, P. B. Tavares, J. Ventura, M. Vazquez, and J. P. Araujo, "Size and surface effects on the magnetic properties of NiO nanoparticles", *Phys. Chem. Chem. Phys.*, vol. 13, pp. 9561–9567, 2011.

[23] M. Feygenson, Y. Yiu, A. Kou, K.-S. Kim, and M. C. Aronson, "Controlling the exchange bias field in Co core/CoO shell nanoparticles", *Phys. Rev. B*, vol. 81, no. 19, pp. 195445, 2010.

[24] M. P. Fernandez-Garcia, P. Gorria, M. Sevilla, A. B. Fuertes, R. Boada, J. Chaboy, G. Aquilantid, and J. A. Blanco, "Co nanoparticles inserted into a porous carbon amorphous matrix: The role of cooling field and temperature on the exchange bias effect", *Phys. Chem. Chem. Phys.*, vol. 13, pp. 927–932, 2011.

[25] H. Masuda and K. Fukuda, "Ordered metal nanohole arrays made by a two-step replication of honeycomb structures of anodic alumina", *Science*, vol. 268, pp. 1466–1468, 1995.

[26] M. P. Proenca, C. T. Sousa, J. Ventura, M. Vazquez, and J. P. Araujo, "Ni growth inside ordered arrays of alumina nanopores: Enhancing the deposition rate", *Electrochim. Acta*, vol. 72, pp. 215–221, 2012.

[27] M. P. Proenca, C. T. Sousa, J. Ventura, M. Vazquez, and J. P. Araujo, "Distinguishing nanowire and nanotube formation by the deposition current transients", *Nanoscale Res. Lett.*, vol. 7, pp. 280, 2012.

[28] D. C. Leitao, J. Ventura, C. T. Sousa, J. M. Teixeira, J. B. Sousa, M. Jaafar, A. Asenjo, M. Vazquez, J. M. De Teresa, and J. P. Araujo, "Tailoring the physical properties of thin nanohole arrays grown on flat anodic aluminum oxide templates", *Nanotechnology*, vol. 23, pp. 425701, 2012.

[29] B. H. Miller and E. Dan Dahlberg, "Use of the anisotropic magnetoresistance to measure exchange anisotropy in Co/CoO bilayers", *Appl. Phys. Lett.*, vol. 69, no. 25, pp. 3932–3934, 1996.

[30] F. Radu, M. Etzkorn, T. Schmitte, R. Siebrecht, A. Schreyer, K. Westerholt, and H. Zabel, "Asymmetric magnetization reversal on exchange biased CoO/Co bilayers", *J. Magn. Magn. Mater.*, vol. 240, pp. 251–253, 2002.

[31] S. Sahoo, S. Polisetty, Y. Wang, T. Mukherjee, X. He, S. S. Jaswal, and C. Binek, "Asymmetric magnetoresistance in an exchange bias Co/CoO bilayer", *J. Phys.: Condens. Matter*, vol. 24, pp. 096002, 2012.

[32] L. Smardz, U. Kbbler, and W. Zinn, "Beating the superparamagnetic limit with exchange bias", *J. Appl. Phys.*, vol. 71, no. 10, pp. 5199–5204, 1992.

[33] M. Verelst, T. O. Ely, C. Amiens, E. Snoeck, P. Lecante, A. Mosset, M. Respaud, J. M. Broto, and B. Chaudret, "Synthesis and characterization of CoO, Co_3O_4, and mixed Co/CoO nanoparticules", *Chem. Mater.*, vol. 11, pp. 2701–2708, 1999.

[34] M. P. Proenca, J. Ventura, C. T. Sousa, M. Vazquez, and J. P. Araujo, "Magnetization reversal in electrodeposited Co nanowire and nanotube arrays with different diameters", submitted.

[35] A. E. Berkowitz and K. Takano, "Exchange anisotropy - a review", *J. Magn. Magn. Mater.*, vol. 200, pp. 552–570, 1999.

[36] B. Kagerer, Ch. Binek, and W. Kleemann, "Freezing field dependence of the exchange bias in uniaxial FeF_2-CoPt heterosystems with perpendicular anisotropy", *J. Magn. Magn. Mater.*, vol. 217, pp. 139–146, 2000.

[37] Z. M. Tian, J. T. Chen, S. L. Yuan, Y. S. Zhang, Z. Z. Ma, H. N. Duan, and C. L. Lu, "Cooling field and temperature dependence on training effect in $NiFe_2O_4$-NiO nanogranular system", *J. Appl. Phys.*, vol. 110, no. 10, pp. 103902, 2011.

[38] A. G. Biternas, R. W. Chantrell, and U. Nowak, "Behavior of the antiferromagnetic layer during training in exchange-biased bilayers within the domain state model", *Phys. Rev. B*, vol. 82, no. 13, pp. 134426, 2010.

Chapter 5

Superparamagnetic Nanoparticles

This Chapter is composed of Article VI, on the magnetic properties of NiO nanoparticles (NPs) of controlled diameters ($d \sim 12 - 70$ nm) prepared by a sol-gel method. The smaller NPs (< 30 nm) exhibit a superparamagnetic behavior at room temperature. An increase in the blocking temperature with d was also observed, as expected. Nevertheless, our study of a wide range of NP sizes allowed us to determine the relation between the number of uncompensated spins (q) and the total number of spins (n_S) in a NP. The proportionality factor between q and n_S allows one to infer the location of the uncompensated spins in the NP, which is still a subject under intense debate. Our results show that the uncompensated spins are located at the surface of the NP, with q proportional to $n_S^{1/3}$. We were then also able to estimate the surface effective magnetic anisotropy constant (K_S) for NiO NPs, assuming the existence of a shell of uncompensated surface spins, and to separate the contributions of the ferromagnetic (FM) shell and antiferromagnetic (AFM) core to the total effective anisotropy. We show that the values obtained for K_S of NiO NPs are in good agreement with the ones reported for NiO thin films. Furthermore, we estimated the critical diameter above which NiO NPs start to exhibit bulk-like behavior. Magnetic hysteresis loops measured at 6 K after field-cooling illustrated an enhancement in the coercive field, a loop shift and training effect (higher and more evident for the smaller NPs). Our results thus demonstrate the existence of uncompensated spins with FM correlations at the surface of the NP coupled to the AFM core, exhibiting an exchange bias-like behavior, similar to the one observed in FM/AFM bilayers.

5.1 Article VI – Size and Surface Effects on the Magnetic Properties of NiO Nanoparticles

Mariana P. Proenca, Célia T. Sousa, André M. Pereira, Pedro B. Tavares, João Ventura, Manuel Vazquez and João P. Araujo, *Physical Chemistry Chemical Physics* 13 (2011) 9561–9567.

Abstract

NiO nanoparticles (NPs) were prepared by a sol-gel process using the citrate route. The sol-gel parameters were tuned to obtain samples with different average particle sizes, ranging from 12 to 70 nm. Magnetic characterization revealed an increase in the blocking temperature with the diameter of the NPs and an increase in the effective magnetic anisotropy (K_{eff}) with decreasing particle size. The magnetic moment per particle was calculated for all samples using the susceptibility value at $T = 300$ K. The number of uncompensated spins per NP was found to be proportional to $n_S^{1/3}$ (n_S = total number of spins), indicating that they are randomly distributed on the NP surface. For small diameters (< 30 nm) the surface anisotropy constant was estimated, using, for NiO NPs, a recent model describing the evolution of K_{eff} with particle size. Hysteretic loops performed at low temperatures after field cooling displayed loop shifts (~ 6.5 kOe in the field axis and ~ 0.18 emu g^{-1} vertically), coercive field enhancement ($H_c \approx 4.8$ kOe) and training effects for the smaller NPs. The sample with NPs of larger diameters presented magnetic properties close to those of bulk NiO.

5.1.1 Introduction

Nickel oxide (NiO) is a promising material, extensively used in catalysis, battery cathodes, gas sensors and electrochromic films [1–5]. Furthermore, bulk NiO is an antiferromagnetic (AFM) material with a Néel temperature of 523 K and can thus be used in a variety of magnetic applications, particularly as a pinning layer in spin valves and magnetic tunnel junctions [6]. Nanostructured AFM oxides have therefore recently gained increased attention [7, 8]. When the dimensions of AFM oxides are decreased to the nanoscale, they start to exhibit a variety of new physical phenomena, such as weak ferromagnetism (FM) arising from the surface and finite size effects or a net magnetic moment coming from uncompensated spins. This surface effect was first studied by L. Néel in 1961, when he inferred that small particles of an AFM material should exhibit superparamagnetism (SPM) and weak FM, and attributed the permanent magnetic moment to uncompensated spins in the two sublattices [9]. However, the 2-sublattice model was not able to fully explain the observed large magnetic moments, enhanced coercivity and hysteretic loop shifts found in AFM nanoparticles (NPs) at low temperatures. These results were then explained considering that the uncompensated spins are in a multi-sublattice spin configuration [10]. It was found that the number of sublattices needed to accurately model the net magnetic moment of a particle increases with decreasing NP size. This model, besides being able to account for the high net magnetic moment experimentally observed, also allowed the occurrence of

a variety of magnetization reversal paths when cycling the applied magnetic field (H), thus explaining coercivity enhancement and loop shift [11]. These two latter phenomena are a consequence of the so-called exchange bias effect that appears when a FM or a spin-glass (SG) like surface shell is exchange coupled to an AFM core [12, 13]. There have been recent discussions on whether NiO NPs should exhibit SPM or SG behaviours, since their magnetization cannot be well described by the modified Langevin function [14]. Detailed studies on the magnetic and time dependent properties of NiO NPs concluded that they indeed show SG behaviour, originating from the freezing of the NPs surface spins [15–17]. In addition, Néel also found that the number of uncompensated spins (q) depends on the crystal structure and particle morphology, and considered three different models [18, 19]. If the uncompensated spins are randomly distributed in the particle, one expects $q \propto n_S^{1/2}$ (where n_S is the total number of spins). If they are arranged parallel to each other in an odd number of layers stacked in a cube, then $q \propto n_S^{2/3}$. Finally, if the core of the particles has no defects, and the uncompensated moments are randomly distributed at the surface, then one has $q \propto n_S^{1/3}$. The nature of the anomalous effects observed in the NiO NPs is still under discussion but it was already confirmed that the magnetic behaviour largely depends on their method of preparation, whether they are coated or not, and the nature of the coating [16, 17, 20–22].

In this work we synthesised NiO NPs with controlled diameters using a sol-gel procedure [23, 24]. Crystalline NiO NPs were obtained, as confirmed by both transmission electron microscopy (TEM) and X-ray diffraction (XRD). The smaller nanoparticles ($12 - 18$ nm in size) were found to have an approximate spherical shape and could be well dispersed, while the larger ones ($40 - 100$ nm) had irregular shapes and tended to agglomerate. Magnetization measurements of the obtained NiO NPs both as a function of temperature $M(T)$ (from 5 to 370 K) and applied magnetic field $M(H)$ (at 300 and 6 K), after zero-field (ZFC) and field-cooling (FC), were performed. The smaller NPs showed a temperature below which the ZFC and FC magnetization split, due to the freezing of uncompensated spins. A peak in the ZFC $M(T)$ curve was also verified, associated with the blocking temperature (T_B) of the NPs. Such temperature was found to increase with NP diameter. From the magnetic susceptibility and particle size measurements, we found $q \propto n_S^{1/3}$, indicating that the uncompensated spins are randomly distributed at the surface of the NP. We also extracted the effective magnetic anisotropy (K_{eff}) of the NPs and confirmed the presence of strong contributions from the surface [25, 26]. Finally, enhanced coercivity, hysteretic loop shifts and training effects [27–31], associated with the exchange bias effect, were found for the smaller NPs at low temperatures, denoting the presence of a FM shell/AFM core exchange coupling.

5.1.2 Experimental

NiO NPs were synthesized by a sol-gel method using $Ni(NO_3)_2{\cdot}6H_2O$ as a precursor and citric acid as a ligand [23]. A first solution was prepared by dissolving measurable $Ni(NO_3)_2{\cdot}6H_2O$ in deionised water and a second solution by dissolving citric acid in deionised water. The latter was then added dropwise to the first at room temperature and under magnetic stirring. The molar ratio of citric acid to nickel nitrate (c : n) was 1 : 4 (samples S1 and S3) and 1 : 1 (sample S2). The pH value was

adjusted only in sample S3 by adding NH_4OH. The final solution was stirred and heated at 343 K overnight for the aging of the gel. Finally, the solution was dried at 373 K for 24 h and calcined at 673 K (sample S1) and 773 K (samples S2 and S3) for 4 h. Table 5.1 summarizes the preparation parameters used for each sample.

Table 5.1: Preparation conditions used for each sample during a sol-gel process and respective particle size and lattice strain estimated by XRD and TEM

			Calcination process				
Sample	pH	Molar ratio (c : n)	Temperature (K)	Heating rate (K min^{-1})	Particle size by XRD (nm)	Particle size by TEM (nm)	Strain by XRD (10^4)
S1	2.0	1 : 4	673	1	12.8 ± 0.6	13.6 ± 1.0	9.25
S2	2.0	1 : 1	773	1	18.4 ± 0.3	19.5 ± 1.0	7.62
S3	6.8	1 : 4	773	10	60.3 ± 2.2	70 ± 30	11.8

The morphologies and distributions of the NiO NPs were observed by TEM (LEO 906E), using an accelerating voltage of 100 kV. Structural analysis was performed by XRD (PW 3040/60 X'Pert Pro Rontgen diffractometer) using Cu K_α radiation (λ = 0.15418 nm) and the Bragg-Brentano $\theta/2\theta$ geometry. The system includes an ultra-fast X'Celerator detector PW3015/20 and a secondary monochromator. Magnetic measurements were preformed on a superconducting quantum interference device (SQUID) magnetometer from Quantum Design, both as a function of temperature [$M(T)$; from 5 to 370 K] and applied magnetic field [$M(H)$; at 300 and 6 K], after ZFC and FC at 10 kOe. The powder samples were mounted inside a gelatin capsule. Cotton was used to completely fill the capsule and ensure that the powder would not move during measurement. The capsule was placed inside a plastic straw that was directly mounted on the SQUID magnetometer. The diamagnetic contribution of the sample holder for the used fields is estimated to be lower than the SQUID magnetic sensibility.

5.1.3 Results and Discussion

Structural Characterization

The size and shape of the produced nanoparticles were obtained using TEM. Dispersed NiO NPs with an approximate spherical shape were observed for samples S1 and S2 [Fig. 5.1(a) and (b)]. The average diameter of such nanoparticles (D_{TEM}) was estimated using *ImageJ* [32] to obtain the histogram of the size distribution. This histogram was then fitted to a log-normal distribution [lower inset of Fig. 5.1(a)], allowing us to obtain for S1 and S2, $D_{TEM} \approx$ 13.6 and 19.5 nm, respectively (Table 5.1). In sample S3 the particles were agglomerated and exhibited a more irregular shape with larger dimensions [Fig. 5.1(c)], making it harder to determine their sizes, although an average value of 70 ± 30 nm could be estimated. Upper insets of Fig. 5.1 correspond to electron diffraction (SAED) patterns of the NiO NPs, where rings can be observed, confirming the presence of polycrystalline NiO.

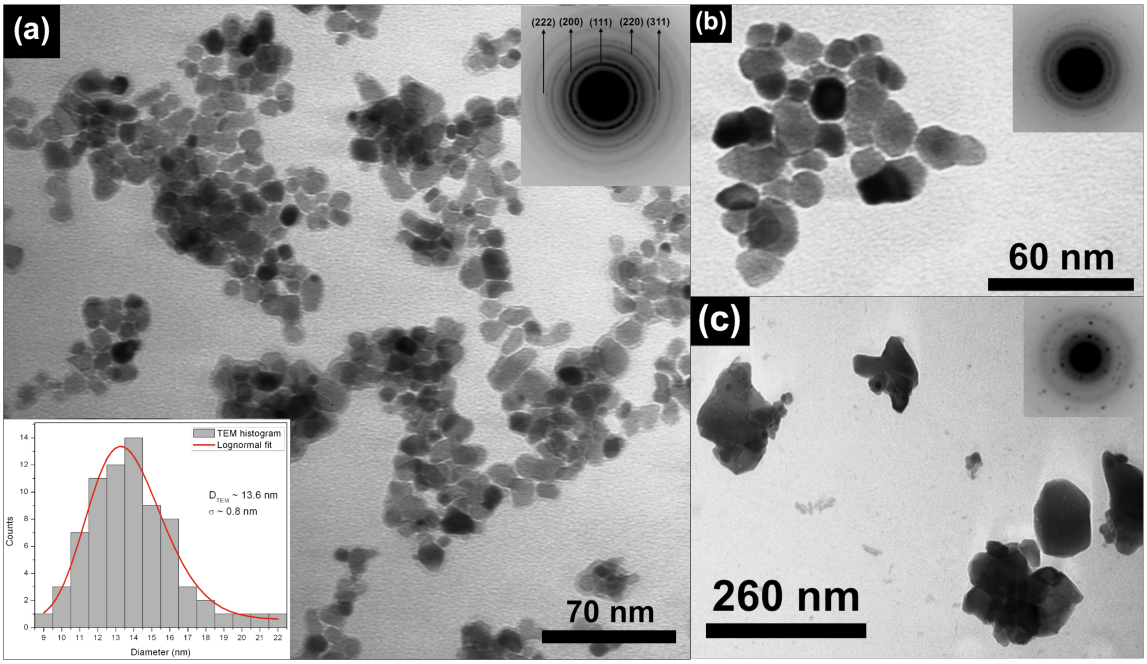


Figure 5.1: TEM images of samples S1 (a), S2 (b) and S3 (c). Lower inset on (a) shows the respective histogram of the particles' size distribution and a log-normal fit. Upper insets on all images show the corresponding SAED where the usual rings of polycrystalline NiO can be identified.

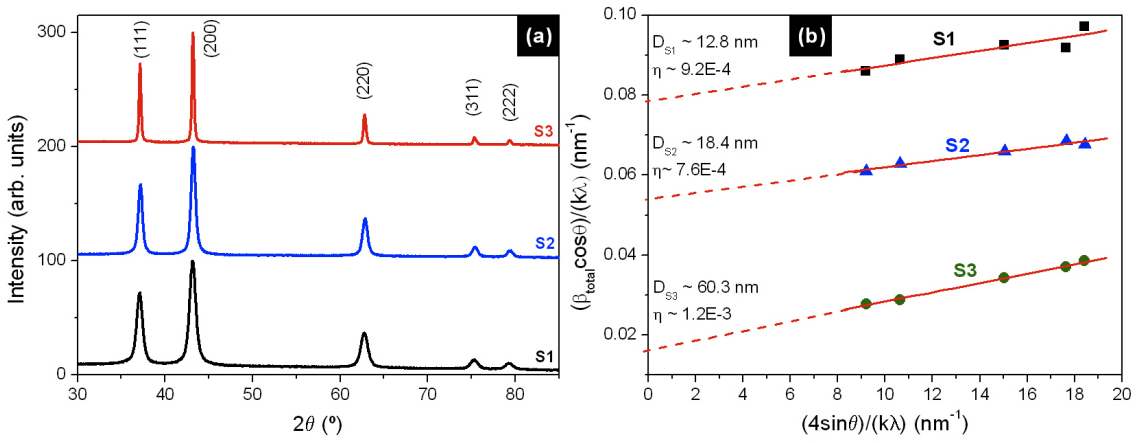


Figure 5.2: (a) XRD pattern of the NiO NPs synthesized and (b) linear fit using the Williamson-Hall correlation (the different slopes represent different mean strains and the line interception gives the inverse particle size).

Structural studies performed in all samples using XRD confirmed the formation of face-centred cubic (*fcc*) NiO with space group $Fm\bar{3}m$, and lattice parameter $a_0 \approx 0.4188$ nm, in close agreement with the reported value for bulk NiO (~ 0.4178 nm) [33]. Figure 5.2(a) shows the diffraction patterns obtained for the different synthesized samples, presenting the reflections characteristic of NiO and evidencing the high quality of the samples. The average crystallite size of the particles (D_{XRD}) was

calculated using the Williamson-Hall relationship [34]:

$$\beta_{total} = \beta_{size} + \beta_{strain} = \frac{k\lambda}{D_{XRD}\cos\theta} + 4\eta\tan\theta, \tag{5.1}$$

where β_{total} is the full width at half-maximum of the XRD peak, k the Scherrer constant for spherical NPs (~ 0.94), λ the incident X-ray wavelength, θ the diffraction angle and η the microstrain parameter. Figure 5.2(b) shows a plot of $\frac{\beta_{total}\cos\theta}{k\lambda}$ vs. $\frac{4\sin\theta}{k\lambda}$ for all samples, allowing the estimation of D_{XRD} and η (Table 5.1). The values obtained for D_{XRD} are in good agreement with the ones measured by TEM. Internal strain is also present for all samples, however it can be considered negligible [η (%) $< 0.2\%$] and therefore does not play a significant role in the main physical properties of these nanomaterials [35].

Magnetic Characterization

Temperature dependent magnetization $M(T)$ measurements were performed for all samples under zero-field- and field-cooling conditions, from 370 to 5 K. Fig. 5.3(a)-(c) show the $M(T)$ curves obtained for samples S1, S2 and S3, respectively.

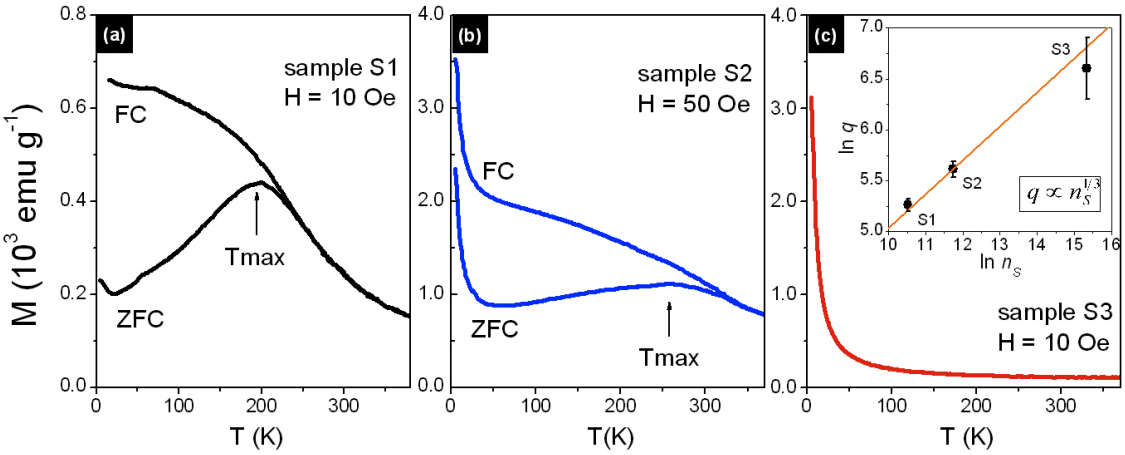


Figure 5.3: ZFC and FC magnetization measurements of samples S1 (a), S2 (b) and S3 (c). Inset shows the relation between the number of uncompensated spins q and the total number of spins n_S in a small particle, showing that $q \propto n_S^{1/3}$.

For samples S1 and S2 the ZFC magnetization curves show a peak, together with a bifurcation between FC and ZFC data below a certain temperature. This behaviour is typically present in an assembly of ferromagnetic-like nanoparticles exhibiting superparamagnetism above a certain temperature. The peak in the ZFC curve is usually associated with the mean blocking temperature (T_B), that decreases with the size of the NPs [$T_B \approx 270$ K for 18 nm (sample S2), ≈ 200 K for 13 nm (S1) and ≈ 50 K for 7 nm (according to Ref. [36])]. The joining of the ZFC and FC curves at the so-called irreversible temperature (T_{IRR}), above which all spins are unblocked, usually marks the highest blocking temperature of the ensemble, i.e. the largest nanoparticle present. We also

registered a decrease of T_{IRR} with decreasing NP size [$T_{IRR} \approx 330$ K for 18 nm (sample S2), ≈ 250 K for 13 nm (S1) and ≈ 200 K for 7 nm (according to Ref. [36])].

For sample S3 (larger average NP diameter), no bifurcation was found in the FC and ZFC magnetizations in the measured temperature range [Fig. 5.3(c)]. In fact, a paramagnetic (PM) behaviour is found in the whole temperature range, as typically observed in bulk NiO samples [13]. This PM behaviour can be attributed to the incomplete compensation of the AFM sublattices at the surface [37]. Notice that a similar PM behaviour can also be seen in the low temperature regime of the $M(T)$ curves of samples S1 and S2 [Fig. 5.3(a) and (b)], as revealed by the sharp M-increase with decreasing T. This low temperature behaviour can be associated with the presence of uncorrelated PM spins at the surface that undergo a magnetic transition to a collective spin state at low temperatures, plus suggesting that the large magnetization values measured are related with broken exchange bonds and reduced coordination at the surface.

Figure 5.4 shows the susceptibility obtained directly by $\chi = M/H$ [since the $M(T)$ measurements were performed under a low applied magnetic field ($H < 50$ Oe)], showing that the NPs with smaller diameters present higher susceptibilities. This can be further inferred from the inset of Fig. 5.4, where the magnetic susceptibility is seen to decrease with the inverse of the NPs average size, with a slope of 2.28×10^4 emu g^{-1} Oe^{-1} nm^{-1}. This result is in good agreement with that of Richardson *et al.* [38], where a slope of 2.38×10^4 emu g^{-1} Oe^{-1} nm^{-1} was obtained.

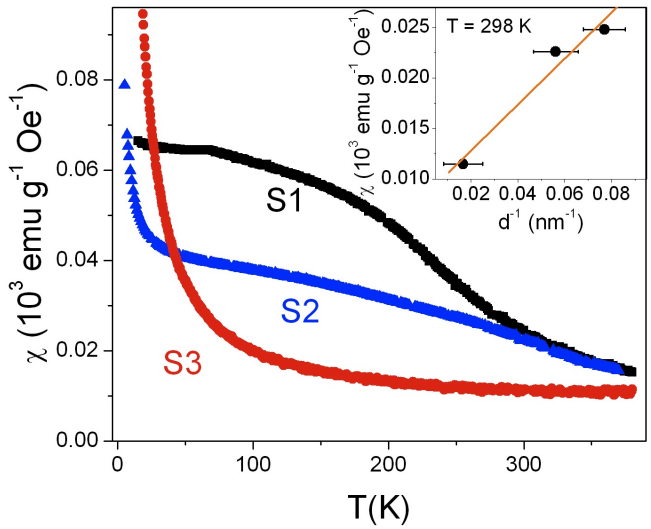


Figure 5.4: Variation of magnetic susceptibility with temperature for all samples. Inset shows the linear variation of magnetic susceptibility with the inverse of the NPs' size at 298 K.

To extract information on the uncompensated surface contribution, we can consider that (as a first approximation) the susceptibility is given by [18]:

$$\chi_{total} = \frac{n\mu_0}{3k_BT}\langle\mu_{NP}^2\rangle + \chi_{bulk}, \tag{5.2}$$

where n is the number of nanoparticles per gram, μ_0 the permeability of free space, k_B the

Boltzmann constant, μ_{NP} the magnetic moment per particle and χ_{bulk} the susceptibility of bulk NiO ($\sim$ 9.7 $\times$ 10^{-6} emu g^{-1} Oe^{-1} at 295 K) [39]. Considering the 295 K susceptibility for the 3 samples and using eqn (5.2), we estimate a magnetic moment per particle of $\sim 390\mu_B$, $550\mu_B$ and $1470\mu_B$ for S1, S2 and S3, respectively (where μ_B is the Bohr magneton). Taking into account $\mu = 2\mu_B$ per Ni^{2+} ions, we calculate the number of uncompensated Ni^{2+} ions per NP, resulting in $\sim$ 195, 275 and 735 for S1, S2 and S3 samples, respectively. The total number of Ni^{2+} ions per particle was also estimated considering *fcc* NiO with a lattice parameter $a_0 \approx 0.4188$ nm and spherical NPs of diameter D_{XRD}, allowing us to plot $\ln(q)$ vs. $\ln(n_S)$ and the corresponding fit with slope 1/3 [inset of Fig. 5.3(c)]. Considering the Néel relation on the nature of the uncompensated spins [18, 19], the good fit obtained indicates that the uncompensated spins occur randomly on the surface of the NP ($q \propto n_S^{1/3}$).

Therefore, we can conclude that the bifurcation in the ZFC and FC curves for S1 and S2 samples also comes from surface effects, mainly due to the presence of uncompensated surface spins (USS).

The magnetic properties of SPM NPs are very sensitive to interparticle interactions [40]. However, in the case of our AFM NPs, the magnetic moments were found to be too small for dipolar interactions to significantly affect the obtained results [41]. In fact, the energy of the dipolar interactions can be estimated using [42]:

$$U_{int} = \frac{\mu_0 \mu_{NP}^2}{4\pi d_p^3} \cos 45^\circ, \tag{5.3}$$

where d_p is the distance between the particles. Using the magnetic moment calculated from eqn (5.2) and considering $d_p \approx D_{XRD}$, we estimate $U_{int} \approx (0.4 - 3.3) \times 10^{-6}$ eV. This corresponds to a negligible critical temperature between 0.004 K (S1) and 0.04 K (S3). The dipolar interactions in our samples can thus be ignored, making them unique for the study of exchange coupling within magnetic particles.

Considering isolated SPM particles, we can define the blocking temperature as [43]:

$$T_B = \frac{K_{eff}\ V_{NP}}{k_B\ \ln(\tau_m/\tau_0)}, \tag{5.4}$$

where K_{eff} is the effective magnetic anisotropy constant, V_{NP} the volume of the NP, τ_m the characteristic measurement time ($\sim$ 10 s for SQUID measurements) and τ_0 the characteristic SPM relaxation time ($\sim 10^{-10}$ s). Using the values of T_B for S1 and S2 we estimated $K_{eff} \approx 6.00 \times 10^5$ and 3.05×10^5 erg cm^{-3}, respectively. These show the expected tendency to increase as the particle size decreases [25, 44]. According to Tobia *et al.* the effective magnetic anisotropy can be expressed as the sum of the core and surface contribution as follows [26]:

$$K_{eff} = K_{bulk}\left(\frac{V_{mo}}{V_{NP}}\right) + \frac{K_S}{t_{shell}}\left(\frac{V_{shell}}{V_{NP}}\right), \tag{5.5}$$

where K_{bulk} and K_S are the bulk and surface anisotropy constants, respectively, V_{mo} is the internal magnetic ordered volume, and V_{shell} and t_{shell} are the volume and thickness of the uncompensated

spins' shell, respectively. Since the surface-to-volume ratio is higher for smaller NPs, surface effects start to govern the magnetic properties when their size is reduced. Considering that the uncompensated spins are located at the surface of the NP (inset scheme of Fig. 5.5), we can approximate eqn (5.5) to:

$$K_{eff} \propto \frac{K_S}{t_{shell}} \left(\frac{V_{shell}}{V_{NP}} \right), \tag{5.6}$$

below a certain NP diameter (d_c) [12, 26]. One thus has $K_{eff} \propto K_S/d$ in the limit where the NP diameter (d) is very small. Figure 5.5 shows the evolution of K_{eff} with d^{-1}, where data from Ref. [45] were added for better comparison. Such a simplified model shows the importance of the surface anisotropy contribution, giving a surface anisotropy constant of $K_S \approx 1.1$ erg cm^{-1} and a critical diameter of $d_c \approx 32$ nm, above which bulk behaviour regains importance. However, the value of K_S was found to be higher than the one predicted for NiO [12]. For the same reason, Tobia *et al.* proposed a new model [eqn (5.7)] for AFM Cr_2O_3 NPs that takes into consideration other important changes that the particles undergo when their size is reduced [26]:

$$K_{eff} \propto \frac{K_S}{t_{shell}} \left(\frac{V_{shell}}{V_{NP}} \right)^2. \tag{5.7}$$

They found a good fitting for t_{shell} of the order of the lattice parameter. Considering then $t_{shell} \approx 0.4188$ nm, we obtain $K_S \approx (0.40 \pm 0.04)$ erg cm^{-2}, in close agreement with the values reported elsewhere for NiO thin films [12]. These results further support the fact that the uncompensated spins are indeed located at the surface of the NPs, and therefore largely contribute to the effective magnetic anisotropy constant.

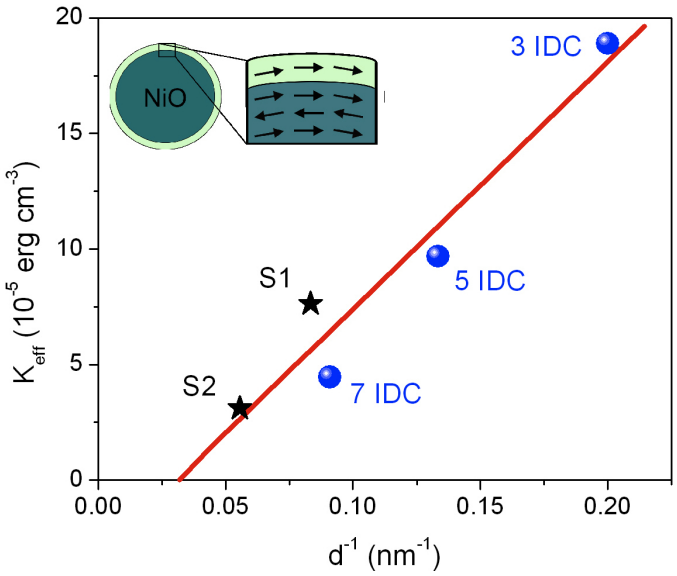


Figure 5.5: Variation of the effective magnetic anisotropy with the inverse diameter of small NiO NPs. Samples 3, 5 and 7 IDC are taken from Ref. [45]. Inset scheme illustrates the NiO NP formed by a shell of uncompensated spins with FM correlations and an AFM core.

Hysteretic loops $M(H)$ were also measured for the smaller NPs (S1 and S2) at 300 K exhibiting a typical SPM behaviour (Fig. 5.6). The magnetization curves, above the blocking temperature, are usually fitted using a Langevin function [40], allowing the estimation of the magnetic moment per particle. For FM and ferrimagnetic NPs, this model gives a good approximation. However, in AFM NPs, where the magnetic moments are relatively small, the anisotropy energy becomes more evident, and the $M(H)$ curves present significant deviations from the Langevin function [25, 46]. In weakly uncompensated AFM particles, the uncompensated magnetic moments must be considered as fluctuating essentially along the AFM axis. However, in the Langevin model, the uncompensated moments are assumed to rotate freely. Therefore, the parameters obtained using the Langevin function for AFM NPs can be incorrect. The other method here used [eqn (5.2)] is thus more appropriate for the estimation of the magnetic moment per NP.

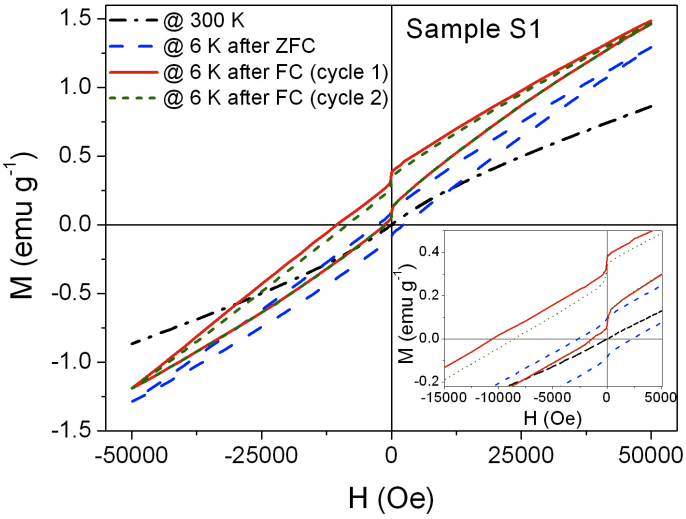


Figure 5.6: Magnetic hysteresis loop of sample S1 at 300 K (dash-dotted line) and at 6 K after ZFC (dashed line) and after FC with an applied field of 10 kOe (continuous line - 1^{st} cycle and dotted line - 2^{nd} cycle). Inset shows a detail of the hysteresis loop around zero field, evidencing the exchange bias and training effect found after FC.

Magnetization curves $M(H)$ were also measured at 6 K after ZFC and FC (Fig. 5.6). The non-saturation behaviour of the curves, also seen at 300 K, is associated with the AFM core behaviour of the NPs. However, an extra contribution coming from the USS can also be detected at low temperatures. The coupling between the AFM core and the USS is evidenced by the remarkable enhancement of the coercive field (H_c) and loop shift observed at 6 K after FC with an applied field of 10 kOe. The loop shift is characterized by an exchange bias field H_{ex}, here defined as $H_{ex} = (H_{c1} + H_{c2})/2$, where H_{c1} and H_{c2} are the left and right coercive fields, respectively, and by a vertical shift, defined as $M_{EB} = (M_{max} + M_{min})/2$, where M_{max} and Mm_{in} are the maximum and minimum magnetization values (obtained at high field), respectively [36]. For sample S1, we obtained $H_c^{FC} \approx 4.8$ kOe, $H_c^{ZFC} \approx 2.5$ kOe, $H_{ex} \approx 6.5$ kOe and $M_{EB} \approx 0.18$ emu g^{-1}, while for sample S2 smaller values of H_c, H_{ex} and M_{EB} were found ($H_c^{FC} \approx 1.0$ kOe, $H_c^{ZFC} \approx 0.2$ kOe, $H_{ex} \approx 2.9$ kOe and $M_{EB} \approx 0.10$ emu g^{-1}). These results demonstrate the increase in importance of the USS when

the NPs size is decreased. In fact, when increasing the surface-to-volume ratio, one expects that the effect of the USS becomes more evident, as experimentally observed. Since T_B of both samples is below room temperature, lowering the temperature from 370 to 5 K with an applied field blocks the USS in one direction. The resulting unidirectional anisotropy (below T_B) between the FM coupled USS and the AFM core provides a pinning force against spin reversal, leading to the shift of the hysteresis loop. The increase of H_c with the decreasing size of the NPs is in accordance with the splitting found in the ZFC and FC $M(T)$ curves, that reflects the remanence of the spin system, and shows the same tendency with the NPs size.

Finally, we also observed the so-called training effect for both samples S1 and S2 (Fig. 5.6). Measuring two consecutive magnetic hysteretic cycles after FC, one observes a drop of H_c^{FC} and H_{ex} from 4550 and 5950 Oe (1^{st} cycle) to 3620 and 4880 Oe (2^{nd} cycle), respectively, in sample S1 and from 990 and 2880 Oe (1^{st} cycle) to 795 and 2665 Oe (2^{nd} cycle) in S2. Such a training effect is often observed in AFM/FM exchange systems and explained as the rearrangement of the (metastable) spin structure of the AFM layer with each reversal of the FM layer magnetization. This leads to a partial loss of its net magnetization and, thus, to a reduction of the exchange bias. Our results then suggest irreversible spin rearrangements with field cycling, likely occurring in the disordered spin surface.

5.1.4 Conclusions

In this paper we have discussed the magnetic properties of NiO nanoparticles with different sizes. Temperature dependent magnetization measurements showed a bifurcation in the ZFC and FC curves for smaller NPs, corresponding to a superparamagnetic behaviour. The blocking temperature increased with the diameter of the NPs, so that, for the samples with larger diameters, no T_B was observed below 370 K. The magnetic moment per particle was estimated for all samples using the susceptibility value at $T = 300$ K. The number of uncompensated spins per NP was proportional to the cubic root of the total number of spins, suggesting that the uncompensated spins occur randomly on the NP surface. The effective anisotropy extracted from the T_B values showed a tendency to increase as the particle size decreases (from $K_{eff} \approx 3 \times 10^5$ to 6×10^5 erg cm^{-3} when the NP size goes from 18 to 13 nm). The surface anisotropy constant ($K_S \approx 0.40$ erg cm^{-2}) was estimated for NiO NPs. Magnetic hysteretic loops measured at 6 K after FC illustrated an enhancement in the coercive field, a loop shift and training effect (higher and more evident for the smaller NPs). Our results demonstrate the existence of uncompensated spins with FM correlations at the surface of the NP coupled to the AFM core, therefore exhibiting an exchange bias behaviour similar to the one observed in FM/AFM bilayers.

Bibliography

[1] R. M. Gabr, A. N. El-Naimi, and M. G. Al-Thani, "Effect of thermal treatment on the kinetics and sintering characteristics of nickel hydroxide as a precursor for the thermal genesis of nickel oxide catalyst", *Thermochim. Acta*, vol. 197, no. 2, pp. 307–318, 1992.

[2] M. Yoshio, Y. Todorov, K. Yamato, H. Noguchi, J.-I. Itoh, M. Okada, and T. Mouri, "Preparation of $Li_yMn_xNi_{1-x}O_2$ as a cathode for lithium-ion batteries", *J. Power Sources*, vol. 74, no. 17, pp. 46–53, 1998.

[3] S. Ikeda, T. Takata, M. Komoda, M. Hara, J. N. Kondo, K. Domen, A. Tanaka, H. Hosono, and H. Kawazoe, "Mechano-catalysis – a novel method for overall water splitting", *Phys. Chem. Chem. Phys.*, vol. 1, pp. 4485–4491, 1999.

[4] H. Steinebach, S. Kannan, L. Rieth, and F. Solzbacher, "H_2 gas sensor performance of NiO at high temperatures in gas mixtures", *Sens. Actu. B: Chem.*, vol. 151, no. 1, pp. 162–168, 2010.

[5] A. C. Sonavane, A. I. Inamdar, P. S. Shinde, H. P. Deshmukh, R. S. Patil, and P. S. Patil, "Efficient electrochromic nickel oxide thin films by electrodeposition", *J. Alloys Compd.*, vol. 489, no. 2, pp. 667–673, 2010.

[6] A. E. Berkowitz and K. Takano, "Exchange anisotropy – a review", *J. Magn. Magn. Mater.*, vol. 200, pp. 552–570, 1999.

[7] V. Skumryev, S. Stoyanov, Y. Zhang, G. Hadjipanayis, D. Givord, and J. Nogues, "Beating the superparamagnetic limit with exchange bias", *Nature*, vol. 423, no. 6942, pp. 850–853, 2003.

[8] J. Nogues, J. Sort, V. Langlais, V. Skumryev, S. Surinach, J. S. Munoz, and M. D. Baro, "Exchange bias in nanostructures", *Phys. Rep.*, vol. 422, no. 3, pp. 65–117, 2005.

[9] L. Neel, *Low Temperature Physics*, Gordon and Beach, New York, 1962.

[10] R. Kodama, S. Makhlouf, and A. Berkowitz, "Finite size effects in antiferromagnetic NiO nanoparticles", *Phys. Rev. Lett.*, vol. 79, no. 7, pp. 1393–1396, 1997.

[11] R. H. Kodama, "Magnetic nanoparticles", *J. Magn. Magn. Mater.*, vol. 200, pp. 359–372, 1999.

[12] J. Nogues and I. K. Schuller, "Exchange bias", *J. Magn. Magn. Mater.*, vol. 192, no. 2, pp. 203–232, 1999.

[13] M. Jagodic, Z. Jaglicic, A. Jelen, J. B. Lee, Y.-M. Kim, H. J. Kim, and J. Dolinsek, "Surface-spin magnetism of antiferromagnetic NiO in nanoparticle and bulk morphology", *J. Phys.: Condens. Matter*, vol. 21, no. 21, pp. 215302, 2009.

[14] S. A. Makhlouf and F. T. Parker, "Magnetic anomalies in NiO nanoparticles", *J. Appl. Phys.*, vol. 81, no. 8, pp. 5561–5563, 1997.

[15] S. Tiwari and K. Rajeev, "Signatures of spin-glass freezing in NiO nanoparticles", *Phys. Rev. B*, vol. 72, no. 10, pp. 104433, 2005.

[16] E. Winkler, R. D. Zysler, M. Vasquez Mansilla, D. Fiorani, D. Rinaldi, M. Vasilakaki, and K. N. Trohidou, "Surface spin-glass freezing in interacting core-shell NiO nanoparticles", *Nanotechnology*, vol. 19, no. 18, pp. 185702, 2008.

[17] V. Bisht and K. P. Rajeev, "Memory and aging effects in NiO nanoparticles", *J. Phys.: Condens. Matter*, vol. 22, no. 1, pp. 016003, 2010.

[18] C. R. H. Bahl, M. F. Hansen, T. Pedersen, S. Saadi, K. H. Nielsen, B. Lebech, and S. Morup, "The magnetic moment of NiO nanoparticles determined by Mossbauer spectroscopy", *J. Phys.: Condens. Matter*, vol. 18, no. 17, pp. 4161–4175, 2006.

[19] L. Neel, *Comptes Rendus*, vol. 252, pp. 4075, 1961.

[20] M. Ghosh, K. Biswas, A. Sundaresan, and C. N. R. Rao, "MnO and NiO nanoparticles: Synthesis and magnetic properties", *J. Mater. Chem.*, vol. 16, no. 1, pp. 106–111, 2006.

[21] M. Feygenson, A. Kou, L. E. Kreno, A. L. Tiano, J. M. Patete, F. Zhang, M. S. Kim, V. Solovyov, S. S. Wong, and M. C. Aronson, "Properties of highly crystalline NiO and Ni nanoparticles prepared by high-temperature oxidation and reduction", *Phys. Rev. B*, vol. 81, no. 1, pp. 014420, 2010.

[22] M. P. Fernandez-Garcia, P. Gorria, M. Sevilla, M. P. Proenca, R. Boada, J. Chaboy, A. Fuertes, and J. Blanco, "Enhanced protection of carbon-encapsulated magnetic nickel nanoparticles through a sucrose-based synthetic strategy", *J. Phys. Chem. C*, vol. 115, pp. 5294–5300, 2011.

[23] Y. Wu, Y. He, T. Wu, T. Chen, W. Weng, and H. Wan, "Influence of some parameters on the synthesis of nanosized NiO material by modified sol-gel method", *Mater. Lett.*, vol. 61, no. 14-15, pp. 3174–3178, 2007.

[24] Q. Yang, J. Sha, X. Ma, and D. Yang, "Synthesis of NiO nanowires by a sol-gel process", *Mater. Lett.*, vol. 59, no. 14-15, pp. 1967–1970, 2005.

[25] C. Gilles, P. Bonville, K. K. W. Wong, and S. Mann, "Non-Langevin behaviour of the uncompensated magnetization in nanoparticles of artificial ferritin", *Eur. Phys. J. B*, vol. 17, pp. 417–427, 2000.

[26] D. Tobia, E. De Biasi, M. Granada, H. E. Troiani, G. Zampieri, E. Winkler, and R. D. Zysler, "Evolution of the magnetic anisotropy with particle size in antiferromagnetic Cr_2O_3 nanoparticles", *J. Appl. Phys.*, vol. 108, no. 10, pp. 104303, 2010.

[27] S. Brems, D. Buntinx, K. Temst, C. Van Haesendonck, F. Radu, and H. Zabel, "Reversing the training effect in exchange biased CoO/Co bilayers", *Phys. Rev. Lett.*, vol. 95, no. 15, pp. 157202, 2005.

[28] F. Radu, M. Etzkorn, R. Siebrecht, T. Schmitte, K. Westerholt, and H. Zabel, "Interfacial domain formation during magnetization reversal in exchange-biased CoO/Co bilayers", *Phys. Rev. B*, vol. 67, no. 13, pp. 134409, 2003.

[29] J. Ventura, J. P. Araujo, and J. B. Sousa, "Training effect in specular spin valves", *Phys. Rev. B*, vol. 77, no. 18, pp. 184404, 2008.

[30] N. J. O. Silva, A. Millan, F. Palacio, M. Martins, T. Trindade, I. Puente-Orench, and J. Campo, "Remanent magnetization in CoO antiferromagnetic nanoparticles", *Phys. Rev. B*, vol. 82, no. 9, pp. 094433, 2010.

[31] M. P. Fernandez-Garcia, P. Gorria, M. Sevilla, A. B. Fuertes, R. Boada, J. Chaboy, G. Aquilanti, and J. A. Blanco, "Co nanoparticles inserted into a porous carbon amorphous matrix: The role of cooling field and temperature on the exchange bias effect", *Phys. Chem. Chem. Phys.*, vol. 13, no. 3, pp. 927–932, 2011.

[32] W. S. Rasband, *ImageJ*, US National Institutes of Health, Bethesda, Maryland, USA, http://rsb.info.nih.gov/ij/, 1997-2009.

[33] S. Sasaki, K. Fujino, and Y. Takeuchi, "X-ray determination of electron-density distributions in oxides, MgO, MnO, CoO, and NiO, and atomic scattering factors of their constituent atoms", *Proc. Jpn. Acad. B Phys. Biol. Sci.*, vol. 55, pp. 43–48, 1979.

[34] H. Bi, S. Li, Y. Zhang, and Y. Du, "Ferromagnetic-like behavior of ultrafine NiO nanocrystallites", *J. Magn. Magn. Mater.*, vol. 277, no. 3, pp. 363–367, 2004.

[35] P. Kameli, H. Salamati, and A. Aezami, "Effect of particle size on the structural and magnetic properties of $La_{0.8}Sr_{0.2}MnO_3$", *J. Appl. Phys.*, vol. 100, no. 5, pp. 053914, 2006.

[36] S. K. Sharma, J. M. Vargas, E. De Biasi, F. Beron, M. Knobel, K. R. Pirota, C. T. Meneses, S. Kumar, C. G. Lee, P. G. Pagliuso, and C. Rettori, "The nature and enhancement of magnetic surface contribution in model NiO nanoparticles", *Nanotechnology*, vol. 21, no. 3, pp. 035602, 2010.

[37] E. Winkler, R. D. Zysler, M. Vazquez Mansilla, and D. Fiorani, "Surface anisotropy effects in NiO nanoparticles", *Phys. Rev. B*, vol. 72, no. 13, pp. 132409, 2005.

[38] J. T. Richardson, D. I. Yiagas, B. Turk, K. Forster, and M. V. Twigg, "Origin of superparamagnetism in nickel oxide", *J. Appl. Phys.*, vol. 70, no. 11, pp. 6977–6982, 1991.

[39] W. J. Schuele and V. D. Deetscreek, "Appearance of a weak ferromagnetism in fine particles of antiferromagnetic materials", *J. Appl. Phys.*, vol. 33, no. 3, pp. 1136–1137, 1962.

[40] S. Morup, D. E. Madsen, and C. Frandsen, "Experimental and theoretical studies of nanoparticles of antiferromagnetic materials", *J. Phys.: Condens. Matter*, vol. 19, no. 21, pp. 213202, 2007.

[41] M. Hansen, C. Koch, and S. Morup, "Magnetic dynamics of weakly and strongly interacting hematite nanoparticles", *Phys. Rev. B*, vol. 62, no. 2, pp. 1124–1135, 2000.

[42] A. M. Pereira, C. Pereira, A. S. Silva, D. S. Schmool, C. Freire, J.-M. Greneche, and J. P. Araujo, "Unravelling the effect of interparticle interactions and surface spin canting in γ-Fe_2O_3@SiO_2 superparamagnetic nanoparticles", *J. Appl. Phys.*, vol. 109, no. 11, pp. 114319, 2011.

[43] G. C. Papaefthymiou, E. Devlin, A. Simopoulos, D. K. Yi, S. N. Riduam, S. S. Lee, and J. Y. Ying, "Interparticle interactions in magnetic core/shell nanoarchitectures", *Phys. Rev. B*, vol. 80, no. 2, pp. 024406, 2009.

[44] J. M. D. Coey, *Magnetism and magnetic materials*, Cambridge University Press, New York, 2009.

[45] N. M. Carneiro, W. C. Nunes, R. P. Borges, M. Godinho, L. E. Fernandez-Outon, W. A. A. Macedo, and I. O. Mazali, "NiO nanoparticles dispersed in mesoporous silica glass", *J. Phys. Chem. C*, vol. 114, no. 44, pp. 18773–18778, 2010.

[46] N. J. O. Silva, V. S. Amaral, and L. D. Carlos, "Relevance of magnetic moment distribution and scaling law methods to study the magnetic behavior of antiferromagnetic nanoparticles: Application to ferritin", *Phys. Rev. B*, vol. 71, no. 18, pp. 184408, 2005.

Chapter 6

Work in Progress

In this Chapter we present several research works that are currently under study. In section 6.1 we introduce the use of ferromagnetic resonance (FMR) for the characterization of magnetic nanowire (NW) and nanotube (NT) arrays. For the Ni NT arrays, a broad spectrum with lower value of H_{eff} when compared to the NW array was observed in the whole range of angles. While for the Co NT arrays, the intensity of the main FMR peak was found to drastically increase when the external field was oriented in the vicinity of the sample plane, exhibiting a higher H_{eff} value than the Co NWs. Section 6.2 describes the fabrication of NiO NWs in nanoporous alumina templates (NpATs), using a sol-gel template filling method. Morphological, structural and magnetic characterizations were performed, confirming the formation of NiO NWs with a face centered cubic crystallographic structure and weak ferromagnetic-like behavior at room temperature. In section 6.3 two different methods to establish electric contact to a single NT are introduced. In the first method (sub-section 6.3.1), the NTs are removed from the template and dispersed in a substrate, where four nanocontacts are deposited on top of a single NT by focused ion-beam and/or electron-beam lithography. The second method (sub-section 6.3.2) requires the monitorization of the current transients during the NTs deposition. By sputtering a thin metallic contact on top of the NpAT, a drastic increase in the deposition current is observed (when the first NT reaches the top of the membrane). Stopping the deposition at that exact time allows one to access a single NT while still inside the NpAT.

6.1 Comparative Study on Arrays of Magnetic Nanowires and Nanotubes by Ferromagnetic Resonance

Ferromagnetic resonance (FMR) is a powerful experimental technique to probe the magnetic parameters (different types of magnetic anisotropy fields, exchange interactions, etc.) of continuous thin films [1], multilayers [2], and patterned structures [3]. Recently it was successfully applied to probe Ni nanowire (NW) arrays in nanoporous alumina templates (NpATs) [4–6]. It was demonstrated in Ref. [7] that FMR is very efficient in the evaluation of magnetization, magnetic anisotropy and

dipolar interactions, and also of the structural quality and magnetic (in)homogeneity of the NWs.

In this section we introduce a comparative study on Ni and Co NW and NT arrays, prepared in similar NpATs (with pore diameter of $d \sim 50$ nm and interpore distance of $D_{int} \sim 105$ nm) by continuous wave FMR techniques. Comparative study of similar NT and NW arrays has proved to be effective in extracting additional information regarding internal structure and magnetic anisotropies of the studied samples.

FMR spectra were recorded using continuous wave electron spin resonance spectrometer BRUKER ESP-300 operating at 9.8 GHz. Measurements were performed at room temperature in the full range of angles θ_H between the external magnetic field and the normal to the sample plane ($0° - 90°$, as schematically represented in Fig. 6.1).

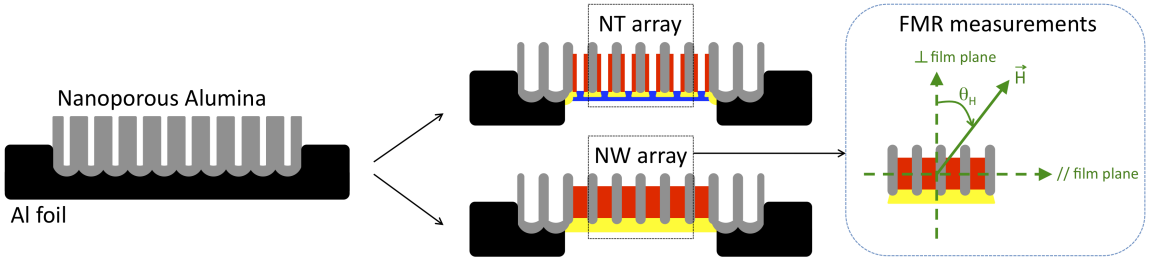


Figure 6.1: Schematic representation of a nanoporous alumina template filled with NTs and NWs, and the geometry used for the angular dependent FMR measurements.

The ferromagnetic resonance field H_R of the flat magnetic sample without in-plane anisotropy at a given frequency depends on the dc magnetic field orientation θ and is given by the well known Kittel's equation:

$$\left(\frac{\omega}{\gamma}\right)^2 = [H_R \cos(\theta_0 - \theta) - H_{eff} \cos^2 \theta_0] \times [H_R \cos(\theta_0 - \theta) - H_{eff} \cos 2\theta_0], \tag{6.1}$$

where H_{eff} represents the magnitude of the total anisotropy field of uniaxial perpendicular symmetry, ω is the microwave field frequency and γ is the gyromagnetic ratio. For the given value of applied external field H, the equilibrium magnetization angle θ_0 can be derived from the equation

$$H \sin(\theta_0 - \theta) = H_{eff} \sin \theta_0 \cos \theta_0. \tag{6.2}$$

In the general case, the effective anisotropy field can be written as $H_{eff} = (N_z - N_x)M_{Sat} - H^{\perp}$, where N_z and N_x are demagnetizing factors along the normal to the sample and in the sample plane, respectively, M_{Sat} is the saturation magnetization, and $H^{\perp}$ is the sum of all the possible perpendicular anisotropy fields having non-magnetostatic nature, including magnetostrictive, magnetocrystalline and surface anisotropy.

For the case of an array of magnetic NWs, the effective demagnetizing factor depends on the dipolar interactions between NWs. A rather simple formula $N_z - N_x = 2\pi(3f - 1)$ for the case when

the NW length is much larger than its diameter was proposed in Ref. [8]. Here f is the volumetric filling factor of nanopores in the insulating matrix. For a hexagonal array, $f = \pi d^2/(2\sqrt{3}D_{int}^2)$.

For the case of an array of magnetic NTs the formula for the demagnetizing factor becomes more complicated, since now it is necessary to take into account the wall thickness of the nanotube t_w. The exact formula:

$$N_z = \frac{2R}{L(1-\beta^2)} \int_0^\infty \frac{1 - e^{-qL/R}}{q^2} [J_1(q) - \beta J_1(\beta q)]^2 dq, \tag{6.3}$$

was proposed in Ref. [9] where R and L are the NT radii and length, respectively, $\beta = 1 - t_w/R$ and J_1 is the Bessel function of the first kind and order one. In all our experiments L was much higher than d, significantly simplifying the analysis. Also, we found that in the range of thicknesses $t_w < R/2$ the much simpler formula $N_z = (2/3) \times (t_w/R)^{3/2}$ can be used.

6.1.1 Ni Samples

For the array of Ni NWs a single resonance peak was observed in the whole range of angles from in-plane ($\theta_H = 90°$) to out of plane ($\theta_H = 0°$) orientation (Fig. 6.2). The resonance linewidth ΔH_R was found to be around 1 kOe for all orientations of external field, the typical value for arrays of Ni NWs [4, 7]. The angular dependence of the resonance field H_R was fitted using Kittel's equation [Eq. (6.1)]. The best fit was obtained for $H_{eff} = 2.45$ kOe and $\gamma/2\pi = 3.11$ MHz Oe^{-1}. It is worth mentioning that the reference value of $\gamma/2\pi$ for bulk Ni is 3.12 MHz Oe^{-1} [2], revealing that our fit is quite reasonable. However, if we consider only shape anisotropy (including dipolar interactions between wires) and perfect filling of all pores with Ni, one obtains a nanowire diameter of ~ 30 nm to match the obtained H_{eff}. For 50 nm NWs in the hexagonal matrix with $D_{int} = 105$ nm the expected H_{eff} is only 1.2 kOe. The difference between estimated and obtained values of effective anisotropy field ($\sim$ 1.2 kOe) can be explained either by the existence of an additional uniaxial anisotropy along the NW axis or by an inhomogeneous pore filling. Among possible anisotropies, we can consider magnetostrictive or magnetocrystalline. In fact, magnetostrictive anisotropy can generate an additional perpendicular anisotropy field of 2 kOe in nanocrystalline Ni films [10], but its appearance in NW arrays is not very probable due to the absence of high temperatures during sample preparation [11]. On the other hand, the effective field of cubic anisotropy of bulk Ni is ~ 200 Oe, which is not enough to explain the observed difference. Therefore the inhomogeneous filling of pores seems to be the most probable reason. To compensate the observed difference in H_{eff}, one should only have $\sim 40\%$ of the pores filled with Ni, including pores that are only partially filled. However, these values are in disagreement with previous results (Chapter 2), thus further works are still needed to better understand our results.

In the case of the Ni NT arrays again a single resonance signal was observed in the whole range of angles of external magnetic field (Fig. 6.3). It is important to note that the resonance linewidth behaves quite differently when compared to the Ni NWs – it increased significantly when the external field approached the in-plane orientation, reaching 2.2 kOe. This can be explained by the fact that

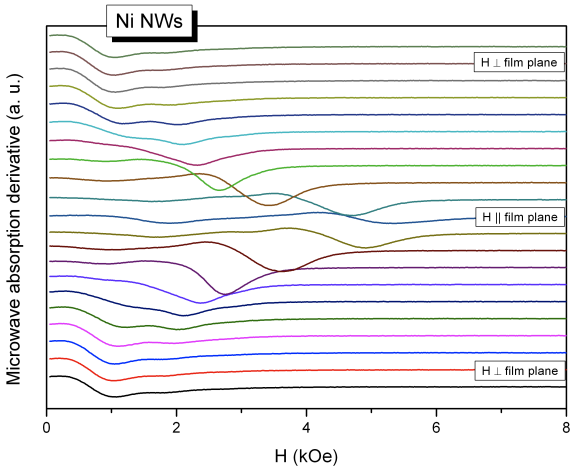


Figure 6.2: Angular dependencies of the FMR spectra for the Ni NW array. The angle θ_H changes from -10° to 190° with a step of 10°.

in this orientation the resonance field is lower than the magnetization saturation field of the sample and we are therefore observing resonance in the not completely saturated state. These results were additionally confirmed with magnetic hysteresis loops along the hard direction (external field applied in the sample plane) measured by vibrating sample magnetometry. The saturation field of the array of NTs was found to be smaller than that of the array of NWs, which should lead to a larger H_R in the case of NWs. The angular dependence of the resonance field for Ni NTs was fitted using the same procedure. The best fit was obtained for $H_{eff} = 0.75$ kOe and $\gamma/2\pi = 3.12$ MHz Oe^{-1}. This value of H_{eff} is in a good agreement with the theoretically predicted by magnetostatic interactions for arrays of NTs.

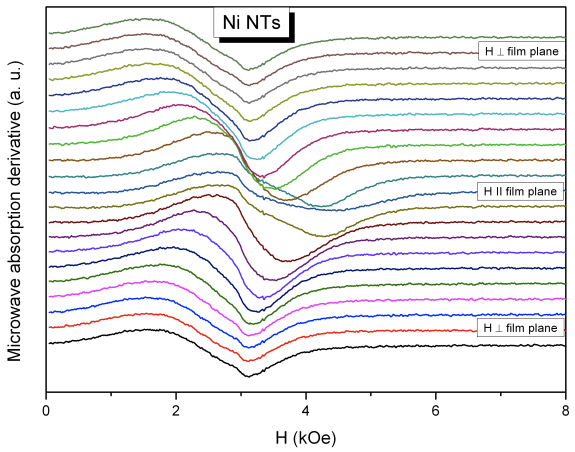


Figure 6.3: Angular dependencies of the FMR spectra for the Ni NT array. The angle θ_H changes from -10° to 190° with a step of 10°.

6.1.2 Co Samples

In the case of Co NWs and NTs the obtained results were quite different. Due to the much higher saturation magnetization of Co (1420 vs. 484 emu cm^{-3} for Ni), it was impossible to observe the FMR spectra in the whole range of angles of external field – for the perpendicular orientation ($\theta_H = 0°$) the resonance field moves to negative values of magnetic fields (Fig. 6.4) and unfortunately our spectrometer is not equipped with a bipolar magnet. Therefore H_{eff} was extracted from the in-plane value of H_R using the Kittel equation for the particular case of $\theta = 90°$:

$$\frac{\omega}{\gamma} = \sqrt{H_R(H_R + H_{eff})}\ . \tag{6.4}$$

For simplicity, the $\gamma/2\pi$ factor was fixed at the bulk value of Co, 3.09 MHz Oe^{-1} [2] (having in mind that the bulk value was retrieved from the fittings in the case of Ni NWs and NTs). For the Co NWs the H_{eff} value was found to be 5.4 kOe. If one considers only magnetostatic interactions, one would expect an effective field of 3.3 kOe for the used NW diameter and interwire distance. Therefore, we need again to consider some extra contribution to H_{eff} ($\sim$ 2 kOe) and following the same logic as for Ni, inhomogeneous pore filling is one possibility.

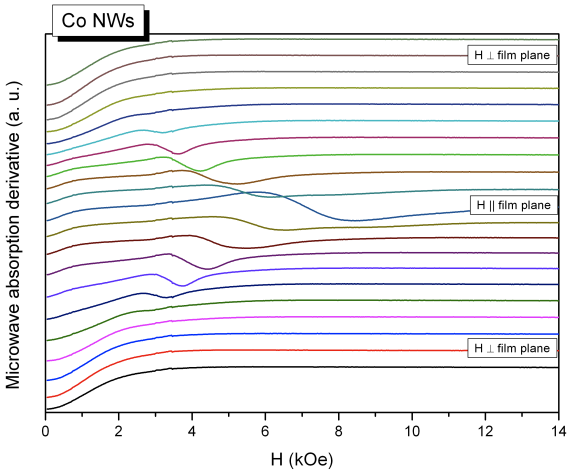


Figure 6.4: Angular dependencies of the FMR spectra for the Co NW array. The angle θ_H changes from -10° to 190° with a step of 10°.

Perhaps the most interesting results were obtained for the studied Co NT array. First of all, it was possible to observe FMR signal only in the vicinity of $\theta_H = 90°$. As one can see from Fig. 6.5, its integral intensity increases several dozen times when θ_H changes from 75 to 90°. This remarkable behavior (having in mind that for Co NWs it was possible to observe the FMR signal in a broader range of angles) can be associated with the complete alignment of magnetic moments at resonance field only for particular orientations of external magnetic fields. Also, the shape of the observed FMR signal is rather symmetric when compared to the Ni NTs case.

Another quite unexpected peculiarity of the FMR signal in Co NTs is that the resonance field at $\theta_H = 90°$ is higher than for the Co NWs with the same parameters. Moreover, this resonance

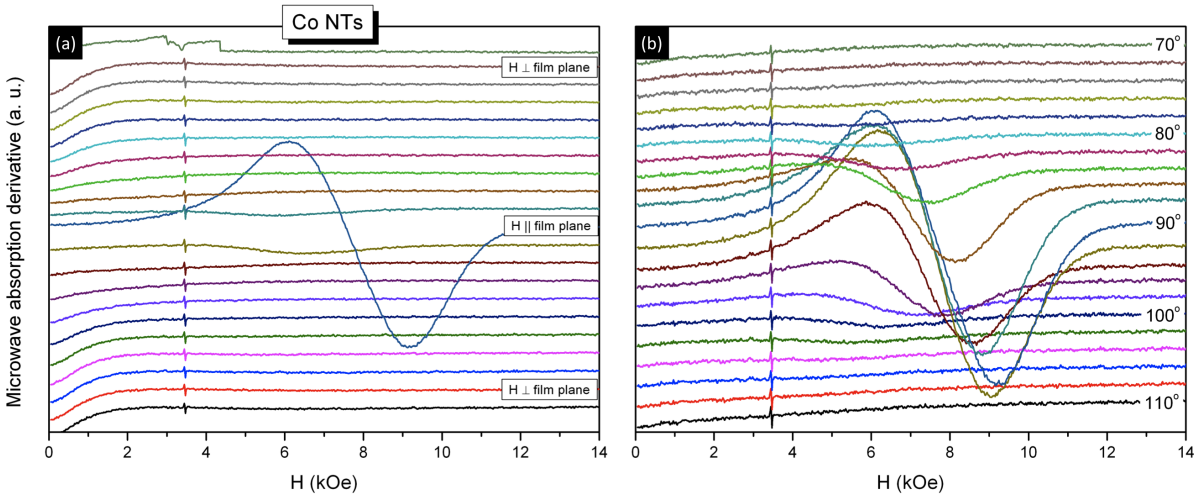


Figure 6.5: Angular dependencies of the FMR spectra for the Co NT array. (a) The angle θ_H changes from -10° to 190° with a step of 10°. (b) The angle θ_H changes from 70° to 110° with a step of 2°.

field is higher than the theoretically calculated one for the case of non-interacting NTs with the given values of R and t_w, i.e. it cannot be explained by the reduction of the filling factor f. The additional perpendicular contribution to the effective anisotropy field is estimated to be 3.2 kOe. Since H_{eff} depends significantly on the wall thickness t_w, it is reasonable to consider that part of our NT wall was oxidized. Even a small wall thickness change can increase the in-plane resonance field by several kOe. Another possible mechanism of perpendicular anisotropy for Co-based systems is magnetocrystalline anisotropy, that can reach several kOe. Of course, in our case it would mean that the Co NTs were better ordered structurally than the corresponding NWs. Additional structural studies are thus necessary to confirm this possibility.

The FMR results for Co NTs and NWs were also confirmed with magnetic hysteresis loops measured along the hard direction. In the case of Co it is easier to saturate the array of NWs than the array of NTs. Therefore the value of the in-plane H_R is expected to be larger in the case of NTs.

6.2 NiO Nanowires by Sol-gel Template Filling

As introduced in sub-section 1.3.2, the combination of different pore filling methods, such as electrodeposition and sol-gel, give the possibility to fabricate concentric nanowires (NWs) presenting a core-shell bilayer structure. New interesting physical phenomena then emerge due to the exchange coupling behavior between the inner wire core and the outer tubular shell. In Chapter 4, exchange bias was found in Co/CoO nanotubes (NTs), presenting inner antiferromagnetic (AFM) tubular walls of CoO and outer ferromagnetic (FM) walls of Co. Aiming the fabrication of concentric NWs presenting a core-shell bilayer structure composed of a NiO (AFM) wire core and a Ni (FM) tubular shell, we present in this section preliminary results on the fabrication of NiO NW arrays by a sol-gel template filling method.

Two different sol-gel methods were used for the fabrication of NiO NW arrays inside nanoporous alumina templates (NpATs), based on previously reported sol-gel procedures used in the preparation of NiO nanocomposites [12–19]. Prior to the sol-gel template filling, the pore diameters were adjusted to $\sim 50-70$ nm and the nanopores opened from both sides by chemically etching the Al and alumina at the bottom of the template.

In the first sol-gel method [15, 16], an aqueous solution composed of citric acid and $Ni(NO_3)_2{\cdot}6H_2O$ was prepared, with a molar ratio of citric acid to nickel nitrate of 1:1, and a pH of 1.9 at room temperature. The final solution was stirred and heated at 70°C overnight for the aging of the gel. The NpAT was then submerged in the sol-gel solution for 2 h, and then dried at 110°C for 25 h and calcined at 500°C for 4 h at a heating rate of 1°C min^{-1}. Figure 6.6 shows SEM images of the NiO NWs formed inside the NpAT, after partial etching of the alumina membrane in NaOH. Due to the low pore filling factor found using this method, a new sol-gel approach was then tested.

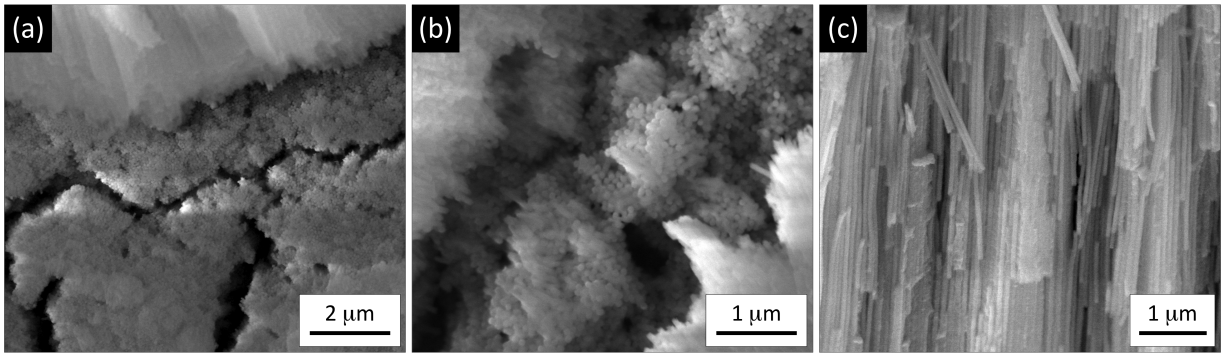


Figure 6.6: SEM images of NiO NWs grown by the first sol-gel method in NpATs.

In the second method [18], the sol-gel precursor solution was prepared by dissolving $Ni(NO_3)_2{\cdot}6H_2O$ in a methanol/ethylene glycol mixed solution, with a volume ratio of 3:7. The concentration of Ni^{2+} ions was adjusted to 0.5 M. After aging the gel at room temperature for 24 h, the NpAT was submerged in the sol-gel solution and the whole set-up dried at 100°C for 24 h and calcined at 500°C for 4 h at a heating rate of 1°C min^{-1}. For a better SEM visualization of the NiO NWs, the template was again partially etched in NaOH. Figure 6.7 shows SEM images of the NiO NWs, evidencing the high pore filling obtained. Previous works on ordered nanoporous alumina surfaces have reported different wettability states depending on the pore diameter and liquid viscosity [20, 21]. We therefore believe that the use of a methanol/ethylene glycol solution allows one to improve the infiltration of the sol-gel inside the nanopores due to a better wetting state of the nanoporous alumina surface.

Structural characterization of the NiO NWs inside the NpAT was performed by X-ray diffraction (XRD; Panalytical X'Pert Pro) using Cu $K_{\alpha 1}$ radiation ($\lambda = 0.15406$ nm) and the Bragg-Brentano $\theta/2\theta$ geometry. Figure 6.8 illustrates the obtained results, showing that the NiO NWs formed inside the NpAT grow in a face-centered cubic crystallographic structure.

The magnetic properties of the NiO NWs embedded in the NpAT were also studied, by measuring

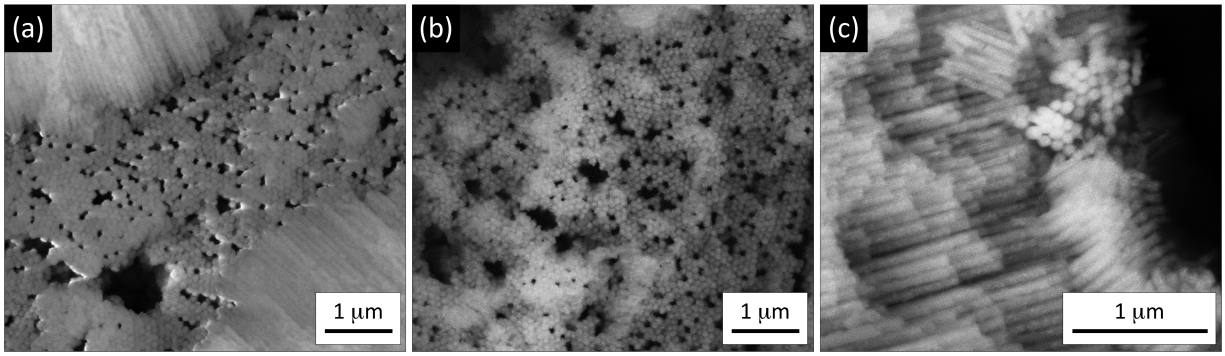


Figure 6.7: SEM images of NiO NWs grown by the second sol-gel method in NpATs.

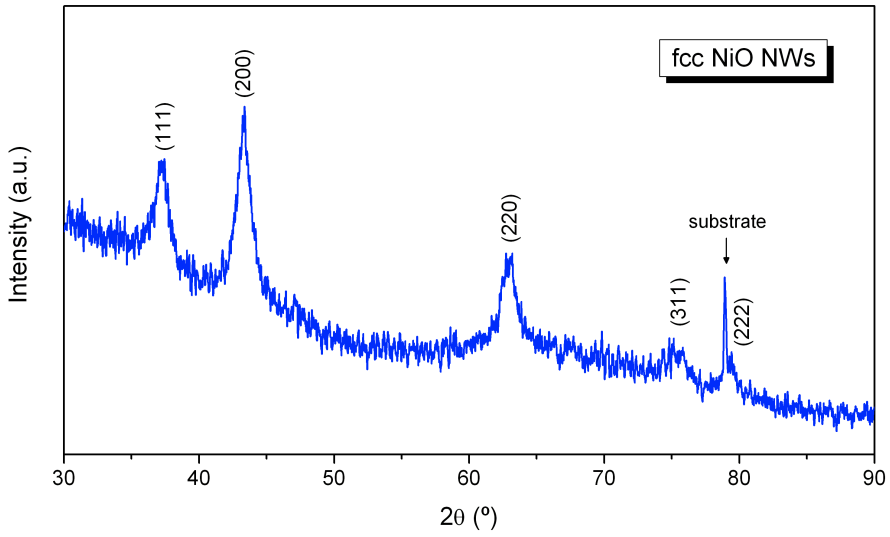


Figure 6.8: XRD pattern of the NiO NWs grown in a NpAT.

magnetic hysteresis cycles [$M(H)$] at room temperature and at 6 K, after zero-field-cooling (ZFC) and field-cooling (FC) in 10 kOe. The magnetic characterizations were performed using a vibrating sample magnetometer (VSM; LOT-Oriel EV7), and a superconducting quantum interference device (SQUID) magnetometer from Quantum Design, by applying the magnetic field parallel ($H^{\parallel}$) and perpendicular ($H^{\perp}$) to the NW axis. Figure 6.9 illustrates a weak ferromagnetic-like behavior at room temperature, exhibiting low coercivities of $H_c^{\parallel} \sim 80$ Oe and $H_c^{\perp} \sim 40$ Oe. At 6 K, a coercivity enhancement of around one order of magnitude was found, which can be attributed to the presence of uncompensated spins at the NWs surface, as previously observed for NiO NPs (Chapter 5). Additionally, after FC in 10 kOe from 350 to 6 K, the $M(H)$ exhibits an exchange-bias shift ($H_{ex}^{\parallel} \sim$ -2.0 kOe and $H_{ex}^{\perp} \sim$ -1.8 kOe) along the negative direction of the applied field axis. This can also be ascribed to the coupling between the AFM NW core and uncompensated spins at the tubular shell.

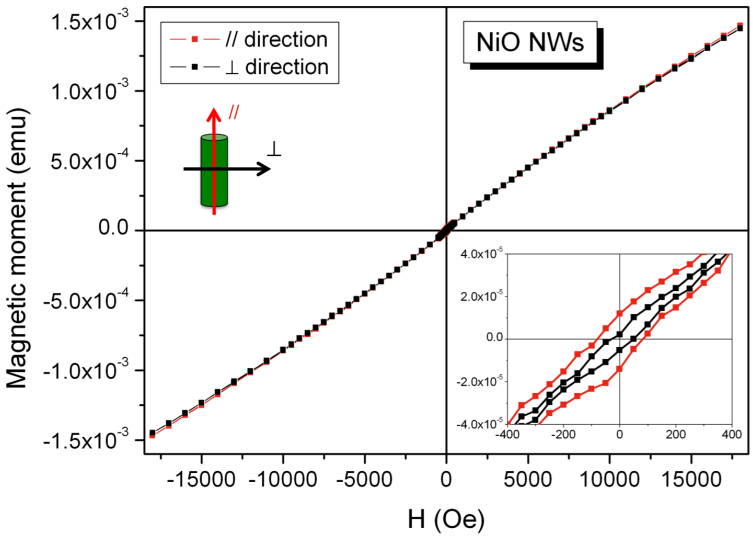


Figure 6.9: Magnetic hysteresis loops of NiO NWs inside a NpAT, measured at room temperature by applying the magnetic field parallel (∥) and perpendicular (⊥) to the NW axis. Inset shows a detail of the hysteresis loops around zero field.

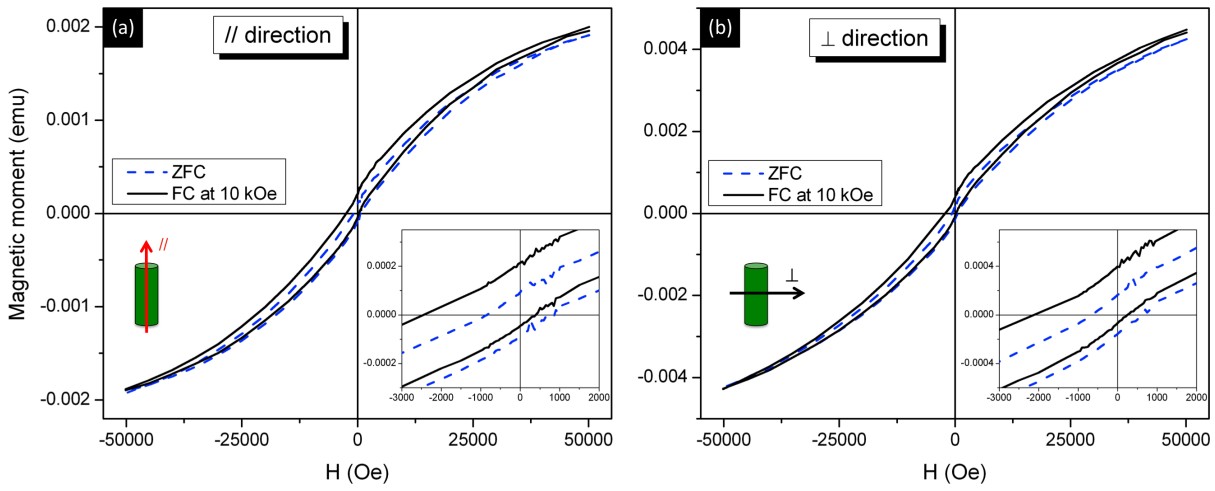


Figure 6.10: Magnetic hysteresis loops of NiO NWs inside a NpAT, measured at 6 K after zero-field-cooling (ZFC) and field-cooling (FC) in 10 kOe, by applying the magnetic field (a) parallel and (b) perpendicular to the NW axis. Insets show a detail of the hysteresis loops around zero field, evidencing the exchange bias found after FC.

6.3 Accessing a Single Nanotube

As observed throughout this thesis, an array of NWs/NTs has a different magnetic response than a single NW/NT, due to the magnetic interactions found between neighboring nanostructures. The possibility to electrically access a single NW/NT and study its transport and magneto-transport behaviors would give further insights into the physical properties of individual nanoelements, including a better understanding of their interwire coupling when ordered in an array.

Several methods have been reported in the literature to access a single NW/NT [22–26]. At IFIMUP–IN in Porto (Portugal), and ICMM in Madrid (Spain), novel methodologies are being developed. In the next sub-sections two different approaches to electrically contact a single NT will be presented.

6.3.1 Nanocontacts by Focused Ion- and Electron-beam Lithography

In this sub-section we present an experimental method for positioning four electrical contacts on top of an isolated NT by a direct writing/deposition method. These nanocontacts were made using focused ion- and electron-beam lithographic techniques, in collaboration with Prof. J. M. de Teresa from the *Instituto de Ciencia de Materiales de Aragón* in Zaragoza (Spain).

Two sets of Ni NT arrays with lengths higher than 10 μm and outer diameters of $\sim$ 50 and $\sim$ 300 nm each, were electrodeposited inside nanoporous alumina templates using a potentiostatic method, as previously described in Chapter 2. The NTs were then removed from the template by chemically etching the alumina in 0.2 M H_2CrO_4 + 0.4 M H_3PO_4 at 60°C. The resulting NTs dispersed in the solution were then cleaned several times in ethanol (99.99% purity) assisted by magnetic separation. Afterwards, one small drop of the suspension containing the NTs was placed over a Si/SiO_2 substrate (7×7 mm^2), and the ethanol evaporated with a small flux of N_2 on top, and an auxiliary magnet at the substrate's bottom, to better fix the NTs. Au cross marks had previously been deposited on top of the Si/SiO_2 substrate, forming a 100×100 μm^2 grid. These marks are only used to locate the dispersed NTs and adjust coordinates between the scanning electron microscope (SEM), for visualization, and the focused ion-beam induced deposition (FIBID) for the deposition of the nanocontacts.

To access a single NT and deposit the nanocontacts we used a commercial Nova 200 NanoLab Dual Beam equipment, which incorporates different tools, such as SEM, in-situ growth of different materials, and focused ion-beam etching. First, we selected several dispersed NTs by SEM, and registered their positions in the substrate using the reference Au cross marks. Then, a 400 nm thick positive photoresist was deposited on top of the substrate with the dispersed NTs, using spin coating (50 s at 2000 rpm). The sample was then placed again in the Dual Beam equipment where a focused electron-beam (FEB) was scanned over the place where one wants to define the nanocontacts. After the development of the photoresist, metallic nanocontacts of Cr ($5-10$ nm) and Au ($60-70$ nm) were evaporated on top of the sample. Finally, the photoresist was lifted-off, revealing the nanocontacts of Cr-Au on top of the selected single NTs in the respective areas previously exposed by the electron-beam (Fig. 6.11).

In recent experiments of electrically accessing a single NW, the nanocontacts had been deposited directly on top of the NW using FIBID, instead of following the procedure described above with a FEBID [27, 28]. However, the use of a focused ion-beam on top of the NW was found to partially etch its walls. Since in our case the NTs are known to have very thin walls ($\sim$ 10 nm), the use of FIBID for the deposition of nanocontacts would undesirably damage the NTs. Nonetheless, for the NTs

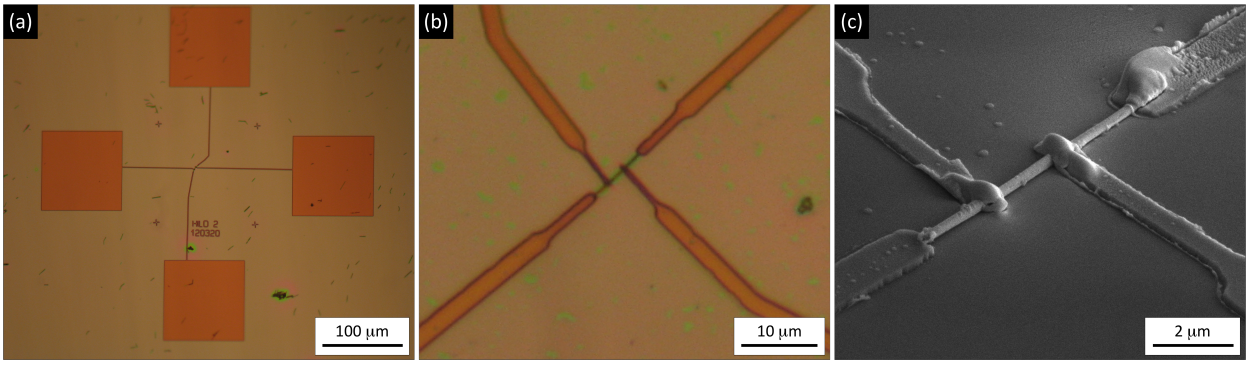


Figure 6.11: Optical [(a) and (b)] and SEM (c) images of the pads and nanocontacts deposited on top of a single dispersed NT.

with outer diameters of ~ 300 nm, a combination of the two procedures had to be used due to their large diameters. In this new method, the initial nanocontacts were evaporated using the procedure described above with a FEBID, and then reinforced by depositing Pt on top of the nanocontacts using FIBID.

6.3.2 Monitoring the Electrodeposition Current

In the previous sub-section, the electrical access of a single NW/NT was made using nanolithography, which has the disadvantage of being a highly expensive technique. Additionally, contacting single dispersed NWs/NTs implies removing them from the nanoporous template where they were grown. This step will not only speed up the oxidation of the NWs/NTs, but will also change their magnetostatic interactions and magnetoelastic properties, as they are no longer ordered in an array of wires/tubes neither subjected to mechanical stresses arising from the porous membrane. To avoid these issues, a new method has been proposed, where a single NW/NT can be electrically contacted while still inside the porous membrane, by monitoring the electrodeposition current [22].

To this end, Ni and Co NT arrays were electrodeposited inside NpATs with their pores opened from both ends (as described in Chapters 2 and 3). In particular, the study on the electrodeposition of Ni NTs inside the nanopores and the overfilling process by monitoring the deposition current transients, presented in section 2.2, showed that while the NTs are being formed inside the nanopores the deposition current remains constant. However, when the first NTs reach the top of the membrane, the current is found to progressively rise due the increase of the deposition area.

To electrically contact a single NT inside the NpAT, an extra Au layer, thin enough (~ 10 nm) not to cover the pores, was sputtered on top of the membrane prior to the electrodeposition process. Ni or Co NTs were then electrodeposited inside the nanopores, growing upwards from the metallic contact previously sputtered at the bottom of the membrane, towards the upper thinner Au layer. The emergence of the first NT coming into contact with the top Au layer can be detected by a sharp increase of the deposition current, as evidenced in Fig. 6.12. By stopping the electrodeposition

immediately after the sharp current increase, we can avoid the emergence of other NTs, and therefore ensure that only a small limited number of NTs are electrically contacted by both upper and bottom Au layers.

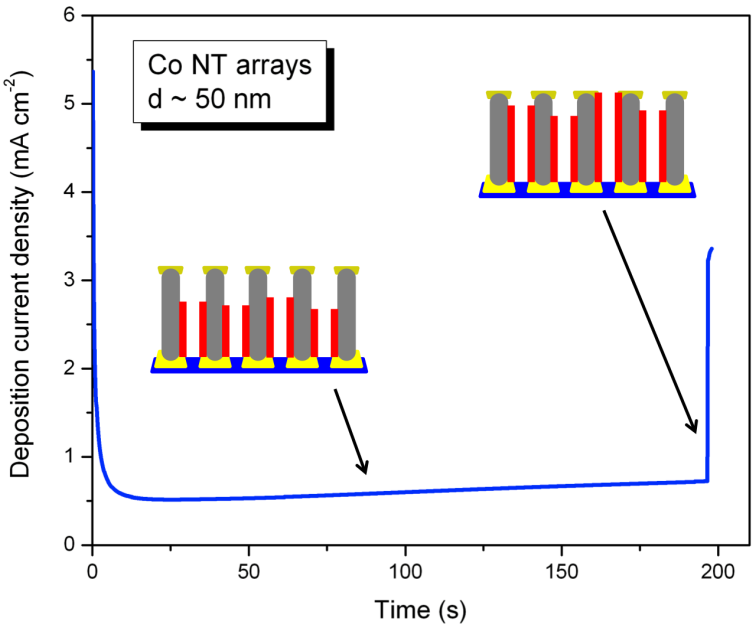


Figure 6.12: Deposition current density transient during the electrodeposition of Co NTs inside a NpAT, illustrating the sharp increase in current when the first NT reaches the Au layer on top.

Bibliography

[1] B. Heinrich, Z. Celinski, J. F. Cochran, A. S. Arrott, and K. Myrtle, "Magnetic anisotropies in single and multilayered structures", *J. Appl. Phys.*, vol. 70, no. 10, pp. 5769–5774, 1991.

[2] M. Farle, "Ferromagnetic resonance of ultrathin metallic layers", *Rep. Prog. Phys.*, vol. 61, no. 7, pp. 755–826, 1998.

[3] G. N. Kakazei, P. E. Wigen, K. Yu. Guslienko, R. W. Chantrell, N. A. Lesnik, V. Metlushko, H. Shima, K. Fukamichi, Y. Otani, and V. Novosad, "In-plane and out-of-plane uniaxial anisotropies in rectangular arrays of circular dots studied by ferromagnetic resonance", *J. Appl. Phys.*, vol. 93, no. 10, pp. 8418–8420, 2003.

[4] U. Ebels, J.-L. Duvail, P. E. Wigen, L. Piraux, L. D. Buda, and K. Ounadjela, "Ferromagnetic resonance studies of Ni nanowire arrays", *Phys. Rev. B*, vol. 64, no. 14, pp. 144421, 2001.

[5] C. A. Ramos, E. Vasallo Brigneti, and M. Vazquez, "Self-organized nanowires: Evidence of dipolar interactions from ferromagnetic resonance measurements", *Physica B*, vol. 354, no. 1-4, pp. 195–197, 2004.

[6] G. Kartopu, O. Yalcin, S. Kazan, and B. Aktas, "Preparation and FMR analysis of Co nanowires in alumina templates", *J. Magn. Magn. Mater.*, vol. 321, no. 9, pp. 1142–1147, 2009.

[7] C. T. Sousa, D. C. Leitao, M. P. Proenca, A. Apolinario, A. M. Azevedo, N. A. Sobolev, S. A. Bunyaev, Yu. G. Pogorelov, J. Ventura, J. P. Araujo, and G. N. Kakazei, "Probing the quality of Ni filled nanoporous alumina templates by magnetic techniques", *J. Nanosci. Nanotechnol.*, vol. 12, pp. 7486–7490, 2012.

[8] G. N. Kakazei, A. F. Kravets, N. A. Lesnik, M. M. Pereira de Azevedo, Yu. G. Pogorelov, and J. B. Sousa, "Ferromagnetic resonance in granular thin films", *J. Appl. Phys.*, vol. 85, no. 8, pp. 5654, 1999.

[9] J. Escrig, M. Daub, P. Landeros, K. Nielsch, and D. Altbir, "Angular dependence of coercivity in magnetic nanotubes", *Nanotechnology*, vol. 18, no. 44, pp. 445706, 2007.

[10] G. N. Kakazei and N. A. Lesnik, "The study of the perpendicular anisotropy in the nanocrystalline Ni and Co films", *J. Magn. Magn. Mater.*, vol. 155, pp. 57–59, 1996.

[11] D. C. Leitao, J. Ventura, C. T. Sousa, A. M. Pereira, J. B. Sousa, M. Vazquez, and J. P. Araujo, "Insights into the role of magnetoelastic anisotropy in the magnetization reorientation of magnetic nanowires", *Phys. Rev. B.*, vol. 84, pp. 014410, 2011.

[12] Q. Yang, J. Sha, X. Ma, and D. Yang, "Synthesis of NiO nanowires by a sol-gel process", *Mater. Lett.*, vol. 59, no. 14-15, pp. 1967–1970, 2005.

[13] C. Parada and E. Moran, "Microwave-assisted synthesis and magnetic study of nanosized Ni/NiO materials", *Chem. Mater.*, vol. 18, no. 11, pp. 2719–2725, 2006.

[14] M. Yu, J. Liu, and S. Li, "Preparation and characterization of highly ordered NiO nanowire arrays by sol-gel template method", *J. Univ. Sci. Technol. Beijing*, vol. 13, no. 2, pp. 169–173, 2006.

[15] Y. Wu, Y. He, T. Wu, W. Weng, and H. Wan, "Effect of synthesis method on the physical and catalytic property of nanosized NiO", *Mater. Lett.*, vol. 61, pp. 2679–2682, 2007.

[16] Y. Wu, Y. He, T. Wu, T. Chen, W. Weng, and H. Wan, "Influence of some parameters on the synthesis of nanosized NiO material by modified sol-gel method", *Mater. Lett.*, vol. 61, no. 14-15, pp. 3174–3178, 2007.

[17] S. Thota and J. Kumar, "Sol-gel synthesis and anomalous magnetic behaviour of NiO nanoparticles", *J. Phys. Chem. Sol.*, vol. 68, no. 10, pp. 1951–1964, 2007.

[18] M. Panapoy, S. Supattanapalapol, and B. Ksapabutr, "Preparation and electrical conductivity of Ni/NiO composites using microwave radiation", in *2nd IEEE International Nanoelectronics Conference*, 2008, pp. 452–457.

[19] H. Gao, D. Gao, J. Zhang, Z. Zhang, G. Yang, Z. Shi, J. Zhang, Z. Zhu, and D. Xue, "Synthesis and anomalous magnetic behaviour of NiO nanotubes and nanoparticles", *Micro Nano Lett.*, vol. 7, no. 1, pp. 5–8, 2012.

[20] H. Haidara, B. Lebeau, C. Grzelakowski, L. Vonna, F. Biguenet, and L. Vidal, "Competitive spreading versus imbibition of polymer liquid drops in nanoporous membranes: Scaling behavior with viscosity", *Langmuir*, vol. 24, no. 8, pp. 4209–4214, 2008.

[21] C. Ran, G. Ding, W. Liu, Y. Deng, and W. Hou, "Wetting on nanoporous alumina surface: Transition between Wenzel and Cassie states controlled by surface structure", *Langmuir*, vol. 24, no. 18, pp. 9952–9955, 2008.

[22] S. Pignard, G. Goglio, A. Radulescu, L. Piraux, S. Dubois, A. Declemy, and J. L. Duvail, "Study of the magnetization reversal in individual nickel nanowires", *J. Appl. Phys.*, vol. 87, no. 2, pp. 824–829, 2000.

[23] Y. Rheem, B.-Y. Yoo, W. P. Beyermann, and N. V. Myung, "Magnetotransport studies of a single nickel nanowire", *Nanotechnology*, vol. 18, no. 1, pp. 015202, 2007.

[24] M. N. Ou, T. J. Yang, S. R. Harutyunyan, Y. Y. Chen, C. D. Chen, and S. J. Lai, "Electrical and thermal transport in single nickel nanowire", *Appl. Phys. Lett.*, vol. 92, no. 6, pp. 063101, 2008.

[25] B. Varghese, Y. Zhang, L. Dai, V. B. C. Tan, C. T. Lim, and C.-H. Sow, "Structure-mechanical property of individual cobalt oxide nanowires", *Nano Lett.*, vol. 8, no. 10, pp. 3226–3232, 2008.

[26] Y.-Z. Long, M.-M. Li, C. Gu, M. Wan, J.-L. Duvail, Z. Liu, and Z. Fan, "Recent advances in synthesis, physical properties and applications of conducting polymer nanotubes and nanofibers", *Prog. Polym. Sci.*, vol. 36, no. 10, pp. 1415–1442, 2011.

[27] D. C. Leitao, *Micro and nano patterned magnetic structures*, PhD thesis, University of Porto, 2010.

[28] L. G. Vivas, *On the magnetic and structural properties of Co and Co-based nanowire arrays*, PhD thesis, Universidad Autonoma de Madrid, 2012.

Chapter 7

Conclusions and Perspectives

In this Chapter we summarize the main conclusions and achievements accomplished throughout this thesis, ending by giving an outlook on the future perspectives.

The work presented in this thesis began by implementing and optimizing new experimental set-ups, both at the IFIMUP-IN and ICMM-CSIC laboratories. These allowed us to fabricate metal oxide nanoparticles (NPs) using sol-gel methods, and to grow ordered arrays of metallic nanowires (NWs) and nanotubes (NTs), with diameters from 25 to 300 nm, in nanoporous alumina templates (NpATs), by sol-gel and potentiostatic electrodeposition methods. In particular, NPs and ordered metallic NT arrays were fabricated, for the first time, at the MMMN (IFIMUP-IN) and GNMP (ICMM-CSIC) groups. The accurate control of the sol-gel and electrodeposition conditions, allowed us to tune the sizes of the NPs/NWs/NTs obtained. In this thesis we fabricated Ni and Co NW/NT arrays using the template filling potentiostatic electrodeposition technique. This optimized method can be used in the future to fabricate other metallic NWs/NTs, such as Fe, NiFe, Cu, Ag or Au.

A systematic study on the potentiostatic electrodeposition of Ni NWs inside NpATs was performed by tuning the applied potential. This allowed us to enhance the deposition rate to around 10 μm min^{-1} (ten times larger than the usual reported values), without affecting the crystallographic and magnetic properties of the deposited NWs. We also optimized the fabrication of NT ordered arrays with small diameters (< 60 nm), by introducing a new fabrication step in the membranes' preparation procedure, prior to the electrodeposition process. The monitorization of the deposition current transients during the potentiostatic electrodeposition of Ni NW and NT arrays allowed us to distinguish between NW and NT formation. The depositions were performed for long times, allowing the deposited metal to reach the top of the template and form a continuous Ni film. The Ni overfilling process was then found to occur in two steps when depositing NWs and in a single step in the case of NTs.

The magnetic properties of ordered Ni and Co NW and NT arrays were subsequently measured using a vibrating sample magnetometer and a superconducting quantum interference device. Experimental and theoretical (by analytical calculations) results on the angular dependence of the coercivity gave us a better understanding on the magnetization reversal processes that occur in NW

and NT ordered arrays. For NW arrays with diameters in the range of $26-65$ nm, the magnetization reversal was found to occur by the nucleation and propagation of a transverse domain wall. The same reversal mode was also observed for Ni and Co NT arrays with outer diameters smaller than 50 nm, while for diameters of $\sim 50-65$ nm, a non-monotonic behavior occurred, revealing a transition between the vortex and transverse reversal modes. The magnetic interactions between individual NWs and NTs in the array were also studied using first-order reversal curves. Increasing the diameter from 40 to 65 nm, at a lattice constant of 105 nm, the magnetic interactions were found to increase with the diameter of the NWs/NTs, exhibiting higher values for the NW arrays.

Exchange-bias (EB) coupling was reported, for the first time, in Co/CoO NT arrays, along both parallel and perpendicular directions of applied magnetic field. Co NT arrays electrodeposited inside the NpATs with pore diameter of $\sim$ 40 nm were left in air for natural oxidation of their inner walls, forming ferromagnetic/antiferromagnetic (FM/AFM) core-shell nanotubular structures. Temperature and field-cooling dependence of EB allowed us to estimate a maximum blocking temperature (T_B) of $\sim$ 220 K, which is very close to the bulk Néel temperature of CoO (293 K). Training effect of the EB was also observed at 6 K after field-cooling, and fitted using a recursive formula proposed by Binek. The small values obtained for the characteristic decay rate of the training behavior were interpreted as the existence of a stronger coupling between the FM/AFM layer when shaped into a core-shell nanotubular structure. A bimodal T_B-distribution was obtained when measuring along both parallel and perpendicular directions. The low-temperature peak was ascribed to interfacial spin-glass phases, while the high-temperature peak was attributed to thermal reversal of AFM grains.

Crystalline NiO NPs with diameters ranging from $\sim 13-100$ nm were synthesized using a sol-gel procedure. Temperature dependent magnetization measurements of NiO NPs illustrated a superparamagnetic behavior at room temperature, an increase of T_B with the NPs' size, and an increase of the effective anisotropy as the particle size decreases. From the magnetic susceptibility and particle size measurements we estimated the number of uncompensated spins (q) per NP. This was found to be proportional to $n_S^{1/3}$ ($n_S \equiv$ total number of spins), indicating that they are randomly distributed on the NP surface. The effective anisotropy constant (K_{eff}) extracted from the T_B values showed a tendency to increase as the particle size decreases. For small diameters (< 30 nm) the surface anisotropy constant was estimated, using a recent model describing the evolution of K_{eff} with particle size. Considering a shell of uncompensated spins with a thickness of the order of the NiO lattice parameter, we obtained a surface anisotropy constant value which was in close agreement with the values reported elsewhere for NiO thin films. Coercivity enhancement, EB and training effects were also obtained at 6 K after field-cooling. These results demonstrated the existence of uncompensated spins with FM correlations at the surface of the NP coupled to the AFM core, therefore exhibiting an EB behavior similar to the one observed in FM/AFM bilayers.

In this thesis we also presented several ongoing research works. A comparative study of Ni and Co NW and NT arrays was performed by means of continuous wave ferromagnetic resonance. NiO NW arrays were fabricated using sol-gel template assisted methods. Their magnetic measurements

illustrated the existence of EB coupling at 6 K after field-cooling, along both parallel and perpendicular directions of applied magnetic field. To electrically access a single NT, two different methods were implemented, either by nanolithography of four electrical contacts on top of a dispersed NT, or by sputtering an extra Au layer on the upper side of the NpAT and monitor the deposition current transient until the first NT reached the top.

From all the results obtained throughout these four years, we can now summarize some of the most interesting future works that can be developed following this thesis:

- Measuring the magnetotransport properties of a single NT, already electrically contacted by two different methods: four nanocontacts by lithography on top of a dispersed NT; two Au contacts at the NT's ends, while still inside the NpAT.
- Fabricate concentric and multisegmented NW and NT arrays, by combining sol-gel, electrodeposition, oxidation and atomic layer deposition techniques inside nanoporous membranes; and study their magnetic and magnetotransport properties.
- Study domain wall propagation in single dispersed NTs, using, for example, Lorentz microscopy.

List of Publications

Several contributions were made to the scientific community, directly related to the work developed in the present thesis, including 15 oral communications, 12 poster presentations, and the following publications:

1. M. P. Proenca, C. T. Sousa, A. M. Pereira, P. B. Tavares, J. Ventura, M. Vazquez, and J. P. Araujo, "Size and surface effects on the magnetic properties of NiO nanoparticles", *Phys. Chem. Chem. Phys.*, vol. 13, no. 20, pp. 9561–9567, 2011.

2. M. P. Proenca, C. T. Sousa, J. Ventura, M. Vazquez, and J. P. Araujo, "Ni growth inside ordered arrays of alumina nanopores: Enhancing the deposition rate", *Electrochim. Acta*, vol. 72, pp. 215–221, 2012.

3. M. P. Proenca, C. T. Sousa, J. Ventura, M. Vazquez, and J. P. Araujo, "Distinguishing nanowires and nanotubes formation by the deposition current transients", *Nanoscale Res. Lett.*, vol. 7, pp. 280, 2012.

4. M. P. Proenca, C. T. Sousa, J. Ventura, J. P. Araujo, J. Escrig, and M. Vazquez, "Crossover between magnetic reversal modes in ordered Ni and Co nanotube arrays", *SPIN*, accepted, DOI: 10.1142/S2010324712500142.

5. M. P. Proenca, C. T. Sousa, J. Escrig, J. Ventura, M. Vazquez, and J. P. Araujo, "Magnetic interactions and reversal mechanisms in Co nanowire and nanotube arrays", submitted to *J. Appl. Phys.*.

6. M. P. Proenca, J. Ventura, C. T. Sousa, M. Vazquez, and J. P. Araujo, "Exchange bias, training effect and bimodal distribution of blocking temperatures in electrodeposited core-shell nanotubes", submitted to *Phys. Rev. B*.

7. M. P. Proenca, C. T. Sousa, J. Ventura, Yu. G. Pogorelov, M. Vazquez, A. Timopheev, N. A. Sobolev, J. P. Araujo, and G. N. Kakazei, "Comparative study on arrays of magnetic nanowires and nanotubes by ferromagnetic resonance", submitted to *J. Appl. Phys.*.

Nevertheless, several collaborations also took place, resulting in 12 oral communications, 11 poster presentations, and the following publications:

8. C. T. Sousa, A. M. L. Lopes, M. P. Proenca, D. C. Leitao, J. G. Correia, and J. P. Araujo, "Rapid synthesis of ordered manganite nanotubes by microwave irradiation in alumina templates", *J. Nanosci. Nanotechnol.*, vol. 9, no. 10, pp. 6084–6088, 2009.

9. J. G. Barbosa, M. R. Pereira, J. A. Mendes, M. P. Proenca, J. P. Araujo, and B. G. Almeida, "Cobalt ferrite thin films deposited by electrophoresis on p-doped Si substrates", *J. Phys.: Conf. Ser.*, vol. 200, pp. 072009, 2010.

10. M. P. Fernandez-Garcia, P. Gorria, M. Sevilla, M. P. Proenca, R. Boada, J. Chaboy, A. B. Fuertes, and J. A. Blanco, "Enhanced protection of carbon-encapsulated magnetic nickel nanoparticles through a sucrose-based synthetic strategy", *J. Phys. Chem. C*, vol. 115, no. 13, pp. 5294–5300, 2011.

11. C. T. Sousa, D. C. Leitao, M. P. Proenca, A. Apolinario, J. G. Correia, J. Ventura, and J. P. Araujo, "Tunning pore filling of anodic alumina templates by accurate control of the bottom barrier layer thickness", *Nanotechology*, vol. 22, pp. 315602, 2011.

12. C. T. Sousa, C. Nunes, M. P. Proenca, D. C. Leitao, J. L. F. C. Lima, S. Reis, J. P. Araujo, and M. Lucio, "pH sensitive silica nanotubes as rationally designed vehicles for NSAIDs delivery", *Coll. Surf. B*, vol. 94, pp. 288–295, 2012.

13. C. T. Sousa, D. C. Leitao, M. P. Proenca, A. Apolinario, A. M. Azevedo, N. A. Sobolev, S. A. Bunyaev, Yu. G. Pogorelov, J. Ventura, J. P. Araujo, and G. N. Kakazei, "Probing the quality of Ni filled nanoporous alumina templates by magnetic techniques", *J. Nanosci. Nanotechnol.*, vol. 12, pp. 7486–7490, 2012.

14. C. T. Sousa, C. Nunes, M. P. Proenca, A. Apolinario, J. L. F. C. Lima, S. Reis, J. P. Araujo, and M. Lucio, "Synchrotron small angle X-ray scattering for the evaluation of silica nanotubes interaction with lipid membranes", submitted to *Nanoscale*.

15. L. G. Vivas, Yu. P. Ivanov, D. G. Trabada, M. P. Proenca, O. Chubykalo-Fesenko, and M. Vazquez, "Reversal modes in Co nanopillar arrays", submitted to *Nanotechnology*.

16. C. T. Sousa, D. C. Leitao, M. P. Proenca, A. M. Pereira, J. Ventura, and J. P. Araujo, "Nanoporous alumina as templates for multifunctional applications", chapter submitted for publication in the book *Nanotechnology Techniques*, Ed. American Nano Society, USA.

List of Abbreviations

- A, Magnetic stiffness constant
- AFM, Antiferromagnetic
- d, Outer diameter
- d_i, Inner diameter
- D_{int}, Interpore Distance
- DW, Domain wall
- EA, Easy axis
- EB, Exchange bias
- FC, Field cooling
- FM, Ferromagnetic
- FORC, First order reversal curve
- H, Applied magnetic field
- HA, Hard axis
- H_c, Coercive field
- H_c^{FORC}, Coercive field extracted from FORC diagrams
- H_{ex}, Exchange bias field
- $H_{int,sat}$, Interaction field at saturation
- H_{eff}, Effective anisotropy field
- H_r, Reversal field
- H_R, Ferromagnetic resonance field
- H_{sat}, Magnetic saturation field
- H_u, Interaction field
- $H^{\parallel}$ Parallel applied magnetic field
- $H^{\perp}$ Perpendicular applied magnetic field
- IBD, Ion beam deposition
- j, Current density
- k_B, Boltzmann constant
- K_{eff}, Effective magnetic anisotropy
- K_{mc}, Magnetocrystalline anisotropy
- K_S, Surface anisotropy
- K_{sh}, Shape anisotropy
- K_V, Volume anisotropy
- L_{ex}, Exchange length
- M, Magnetization
- M_R, Remanent magnetization
- M_{Sat}, Saturation magnetization
- NP, Nanoparticle
- NpAT, Nanoporous alumina template
- NT, Nanotube
- NW, Nanowire
- r, Radius
- S, Squareness
- SAED, Selected area electron diffraction
- SEM, Scanning electron microscopy
- SG, Spin-glass
- SPM, Superparamagnetic
- SQUID, Superconducting quantum interference device
- STEM, Scanning transmission electron microscopy
- T, Temperature
- T_C, Curie temperature
- T_N, Néel temperature
- T_B, Blocking temperature
- TEM, Transmission electron microscopy

- VSM, Vibrating sample magnetometer
- XRD, X-ray diffraction
- ZFC, Zero field cooling
- δ_b, Alumina barrier layer thickness
- δ_{film}, Film thickness
- ΔH_u, Mean interaction field extracted from FORC diagrams
- δ_w, Domain wall width
- μ_0, Vacuum magnetic permeability
- μ_B, Bohr magneton
- ρ_{FORC}, FORC distribution
- σ_{int}, Local interaction field
- χ, Magnetic susceptibility

List of Tables

1.1 Anodization parameters and pore characteristics. 31

5.1 Preparation conditions used for each sample during a sol-gel process and respective particle size and lattice strain estimated by XRD and TEM 126

List of Figures

1.1 (a) The first transistor, developed in 1947, which is a point-contact device roughly one centimeter across [10]. (b) IBM logo written using 35 Xenon atoms arranged in a Ni surface by a scanning tunneling microscope [6]. Schematic representations of (c) 'dip-pen' nanolithography [7] and (d) nanocar with turning buckyball wheels [11]. . . . 10
1.2 Schematic representation of the increased surface area in nanoscaled materials [12]. . . 11
1.3 Illustrations of the various types of materials by size of their structural elements: 0D (zero-dimensional) nanoparticles; 1D nanowires/nanotubes; 2D thin films; 3D polycrystals. Adapted from [22]. . . . 12
1.4 Characteristic length scales in magnetism (adapted from [41]). . . . 13
1.5 Exchange bias effect on the magnetic hysteresis loop of a FM layer coupled to an AFM layer, where H_c, H_{ex}, T_N and T_C, are the coercive and exchange bias fields, and the Néel and Curie temperatures, respectively (adapted from [44]). . . . 14
1.6 (*Left*) Schematic representation of a magnetic tunnel junction read-head in a hard disk drive [34]. (*Right*) Illustration of a conventional memory element design, where the relative orientation of the two magnetic layers will define two different states [47]. . . . 15
1.7 Representative diagram of a racetrack memory, evidencing the operating principles of (a) selecting, (b) writing and (c) reading a memory bit. By applying a positive (negative) current pulse to the NW, the magnetic domain walls move to the right (left) in the diagram, controlling in this way the access to the data stored along the wire (adapted from [49, 50]). . . . 16
1.8 Magnetic force microscopy images of an hexagonal ordered array of Ni NWs ($d \sim$ 180 nm) inside a nanoporous alumina template. The white (black) contrast corresponds to NWs with magnetization oriented opposite (equal) to the tip field direction. In (b) and (c) a magnetic field of 350 and 700 Oe, respectively, was applied along the axial direction of the NWs. The increment of the number of black NWs from image (a) to (c) evidences the magnetization reversal of individual NWs by the applied external magnetic field. (Adapted from [54]). . . . 16
1.9 Magnetization reversal modes: coherent (C), transverse (T) and vortex (V) modes [38]. w_V and w_T represent the domain wall widths of a vortex and a transverse DW, respectively. . . . 17
1.10 Results of the analytical calculations of the angular dependence of coercivity considering a coherent, transverse and vortex mode of magnetization reversal. The calculations were performed for (a) Ni NWs with $d = 50$ nm and $L = 12$ μm; and (b) infinite Ni NWs and NTs with $d = 100$ nm. (c) Geometrical parameters of a nanotube. [(a) and (b) were adapted from [15] and [9], respectively]. . . . 19
1.11 Representation of the mathematical hysteron from the classical Preisach model [12]. . 20
1.12 Set of first-order reversal curves measured for an array of CoFe NWs with the applied field parallel to the wires' axis [12]. . . . 20

1.13 Set of FORCs, corresponding FORC 3D distribution (top horizontal panel), and FORC diagram (bottom horizontal panel), measured for an array of Ni NWs with the applied field parallel to the wires' axis [30]. 21
1.14 FORC diagram illustrating the extraction of H_c^{FORC} and ΔH_u. (a), (b) and (c) are three representations of mathematical hysterons: (a) fundamental hysteron (vertical reversible), (b) and (c) easy hysteron (vertical irreversible). (Adapted from [11]). . . . 22
1.15 Theoretical FORC diagram made with the moving Preisach model, illustrating the effects of the k value for $\sigma_{int} = 100$ Oe: (a) $k = +100$, (b) $k = 0$, (c) $k = -100$ Oe. μ_c and σ_c correspond to theoretical parameter values assumed for the center and width of the coercivity normal distribution, respectively. (Adapted from [37]). 22
1.16 (*Left*) Illustration of the influence of nanoparticles' size and shape on the optical properties of the respective suspensions [85]. Colloidal suspensions of CdSe nanoparticles with increasing sizes from left to right, exposed to ultraviolet (top) and ambient (bottom) illumination [86]. 23
1.17 Schematic representation of the different magnetic effects occurring in magnetic nanomaterials, where (a) and (b) illustrate the spin arrangements in a ferromagnetic (FM) and an antiferromagnetic (AFM) material, respectively [87]. 25
1.18 Scheme of top-down and bottom-up nanofabrication approaches. 25
1.19 Schematic representations of (*left*) an hexagonal closed-pack array of pore cells in an anodic alumina membrane and (*right*) respective cross-sectional view [91]. 27
1.20 (*Left*) Representation of an electrochemical set-up with two electrodes. (*Right*) Electrochemical cell and experimental set-up used for the anodization process. 28
1.21 Illustration of the four major stages of pore formation in a nanoporous alumina membrane: a) an oxide barrier layer is formed; b) small irregularities are formed at the *o/e* interface due to mechanical stress; c) pores start to nucleate and begin to grow; d) continuous growth of a porous-type alumina film. 29
1.22 Illustration of the fabrication process of a nanoporous alumina template by anodization of an Al foil. For each step of the fabrication process, atomic force microscopy {(a) and (b), taken from [26]} and scanning electron microscopy [(c), (d), (e) and (f)] images of the corresponding top surfaces are shown. 32
1.23 Scheme of the barrier thinning process in a NpAT, and subsequent pore filling by the PED or AC deposition methods. SEM cross-sectional image of a NpAT filled with Ni NWs by the PED method, evidencing the filling of the hollow dendrites previously formed at the pores' bottom [7]. 33
1.24 Scheme of the template preparation for NW and NT growth by DC electrodeposition. SEM cross-sectional images of Ni (a) NWs with $d \sim 50$ nm and (b) NTs with $d \sim 300$ nm, fabricated by the DC electrodeposition method. 34
1.25 Illustration of the DC electrodeposition set-up using a three-electrode cell. 35
1.26 Scheme of the fabrication of concentric NW arrays by combining the template-assisted sol-gel and DC electrodeposition methods. 36

2.1 Linear potential sweep curves during Ni deposition on an Au substrate (Ni film 01) and in a NpAT (Ni NWs 01 and 02). The scattered points correspond to the current density values after 60 s of Ni potentiostatic deposition. 52
2.2 Linear potential sweep curves during Ni deposition on an Au substrate (Ni film at 50 mV s^{-1}) and in NpATs at different scan rates (1^{st} to 4^{th} scans). Inset plots the cathodic peak current vs. the square root of sweep rate. 52

2.3 Selected current density transients during Ni electrodeposition in NpATs performed at different constant potentials for 1 min. Inset evidences the H_2 gas bubble formation and release during an anomalous Ni deposition at -3.5 V. 53
2.4 Percentage of normal samples obtained at different applied potentials during Ni deposition inside nanopores. 54
2.5 XRD pattern of the Ni NWs electrodeposited in a NpAT at -2.5 V. Inset shows a detail of the (220) Ni peak for selected samples. 55
2.6 FESEM cross-sectional images of Ni NWs deposited in NpATs for 1 min at a constant potential of: (a) -1.0 V ($L \sim 830$ nm); (b) -1.5 V ($L \sim 2.5$ μm); (c) -2.0 V ($L \sim 4.5$ μm); (d) -2.5 V ($L \sim 7.5$ μm); (e) -2.8 V ($L \sim 12$ μm); (f) -3.0 V ($L \sim 11.5$ μm); (g) -3.2 V ($L \sim 8.5$ μm); (h) -3.5 V ($L \sim 11.8$ μm); (i) -2.5 V (anomalous sample); (j) -4.0 V (anomalous sample). 56
2.7 Ni deposition rate η after 1 min of deposition at different applied potentials. The error bars were estimated considering several samples fabricated at each potential. 57
2.8 (a) Selected hysteretic cycles of Ni NWs measured by VSM, with the magnetic field applied parallel (solid line) and perpendicular (dashed line) to the nanowires axis. Influence of deposition potential on: (b) the coercive field parallel (squares) and perpendicular (triangles) to the wire axis; (c) the squareness parallel (diamonds) and perpendicular (triangles) to the wire axis; and (d) the magnetic texture (circles); for normal (filled symbols) and anomalous (open symbols) samples. 58
2.9 Saturation magnetic moment at a field of 15,000 Oe vs. the Ni estimated mass (considering a deposition current efficiency of 95% [30]). The linear fit allows extracting the saturation magnetization value of around 49.5 emu g^{-1} for Ni NWs. 59
2.10 Stages in the fabrication of NW and NT arrays in NpATs by potentiostatic deposition. 67
2.11 SEM images of Ni NWs (a, b, c) and NTs (d, e, f) in NpATs. Cross-sectional (a, d), bottom (b, e, after 1 μm milling), and top (c, f, after 5 μm milling) views. 69
2.12 XRD patterns of the Ni NWs, NTs and films overgrown on top after electrodeposition in NpAT. 70
2.13 Schematic representations of the preferential growth directions of the deposited material. Growth directions on top of a nanotube (left) and nanowire (right). 70
2.14 Current transients during Ni NW (a) and NT (b) deposition in NpATs. 71
2.15 Cross-sectional (a) and top (b) SEM images of polygonal caps. These are formed at the NpAT surface when Ni NWs start to overfill, forming a continuous Ni film on top (c). 72
2.16 Cross-sectional (a, b) and top (c, d) SEM images of spherical polycrystalline caps. These are formed at the NpAT surface when Ni NTs start to overfill (d), creating a continuous Ni film on top (c). 73
2.17 SEM images of the Ni film formed on top of the NpAT. Cross-sectional view of respective lift off after NWs deposition (a), and Ni film's bottom view after NWs (b) and NTs (c) deposition. 73
2.18 Magnetic hysteresis loops of Ni NW (a) and NT (b) arrays in NpATs. The hysteresis loops were measured in the parallel ($\parallel$, red) and perpendicular ($\perp$, black) directions. . 74

3.1 SEM bottom (after $\sim$ 200 nm of ion-milling) images of (a) Co NW and (b) Ni NT arrays in NpATs with $d \sim 50$ and 60 nm, respectively. (c) STEM image of Ni NTs. . . 84
3.2 Magnetic hysteresis loops of ordered Ni NT arrays with $d \sim 60$ nm and $d_i \sim 36$ nm, measured at different angles of applied magnetic field, with a 10° step. 85

3.3 Angular dependence of the coercive field measured experimentally (squares) and calculated analytically (C mode: blue solid; T mode: red dashed; and V mode: green dotted) for Co NW [(a) and (b)] and NT [(c) and (d)] arrays in NpATs with different outer diameters. 87
3.4 Angular dependence of the coercive field measured experimentally (squares) and calculated analytically (C mode: blue solid; T mode: red dashed; and V mode: green dotted) for Ni NW [(a) and (b)] and NT [(c) and (d)] arrays in NpATs with different outer diameters. 87
3.5 SEM [(a), (b) and (d)] bottom (after 200 nm milling) and (c) cross-sectional images of Co [(a), (b) and (c)] NW and (d) NT arrays in NpATs with (a) $d \sim 50$ nm and [(b), (c) and (d)] $d \sim 40$ nm and $D_{int} \sim 102$ nm. 95
3.6 FORCs (insets) and FORC diagrams of Co NW and NT ordered hexagonal arrays with different diameters and lattice parameter of ~ 102 nm, when applying the magnetic field parallel to the wire/tube long axis. 97
3.7 Magnetic interactions, extracted from the FORC diagrams in Fig. 3.6, as a function of the wire/tube diameter. Inset shows the cross-section of the FORC diagram along the H_u axis for NW and NT arrays with $d \sim 50$ nm. 98
3.8 Coercive field along the parallel direction, extracted from the maximum value of the FORC diagrams (H_c^{FORC}) in Fig. 3.6, and from the major magnetic hysteresis loops (H_c^{Hyst}), as a function of the NWs/NTs diameter. 99
3.9 Magnetic hysteresis loops of ordered Co NW (left) and NT (right) arrays with $d \sim 50$ nm and $d_i \sim 30$ nm, measured at different angles of H, in 10° steps. Inset shows the angular dependence of squareness (dots - experimental data; line - theoretical calculations). 100
3.10 Angular dependence of the coercive field measured experimentally (dots) and calculated analytically (C mode: black solid; T mode: green dashed; and V mode: orange dotted) for Co NW and NT arrays in NpATs with different outer diameters. 101

4.1 SEM bottom image of a NpAT (a) empty and (b) filled with Co NTs, after ~ 200 nm of etching by ion-milling. (c) Schematic representation of a Co/CoO NT. 111
4.2 Magnetic hysteresis loops of Co/CoO NT arrays measured at 6 K after field cooling in 50 kOe, by applying the magnetic field parallel (filled symbols) and perpendicular (opened symbols) to the NT axis, evidencing the exchange-bias effect (loop shift along the field axis). Inset shows a comparison between the magnetic hysteresis loop of Co/CoO NT (filled symbols) and Co NW (opened symbols) arrays, measured at 6 K after field cooling in 50 kOe, by applying the magnetic field parallel to the wire/tube axis, evidencing the inexistence of loop shift in the NW arrays. 111
4.3 Magnetic hysteresis loops of Co/CoO NT arrays measured at different temperatures after field cooling in 50 kOe, by applying the magnetic field (a) parallel and (b) perpendicular to the NT axis. Inset shows the temperature dependence of the exchange-bias field, measured by applying the magnetic field parallel (filled symbols) and perpendicular (opened symbols) to the tube long axis. 112
4.4 Dependence of H_{ex} on the field-cooling field (H_{FC}), measured at 6 K by applying the magnetic field parallel (filled symbols) and perpendicular (opened symbols) to the tube long axis. 114
4.5 Dependence of $|H_{ex}|$ on the number of magnetic hysteresis cycles, measured at 6 K after field cooling in 50 kOe, by applying the magnetic field parallel ($\parallel$) and perpendicular ($\perp$) to the tube axis, and respective fits using Eq. (4.3). Inset illustrates the corresponding training effect (TE). 115

4.6 Representation of the T_B-distribution of the CoO AFM grains formed at the inner Co NT walls, by illustrating the dependence on T_0 of the derivative of normalized H_{ex}, $\mathrm{d}H_{ex}^{norm}/\mathrm{d}T_0$, along both parallel (filled symbols) and perpendicular (opened symbols) directions. Inset shows the magnetic hysteresis loops measured at 6 K along the perpendicular direction for T_0 = 6, 50 and 100 K. 117

5.1 TEM images of samples S1 (a), S2 (b) and S3 (c). Lower inset on (a) shows the respective histogram of the particles' size distribution and a log-normal fit. Upper insets on all images show the corresponding SAED where the usual rings of polycrystalline NiO can be identified. 127
5.2 (a) XRD pattern of the NiO NPs synthesized and (b) linear fit using the Williamson-Hall correlation (the different slopes represent different mean strains and the line interception gives the inverse particle size). 127
5.3 ZFC and FC magnetization measurements of samples S1 (a), S2 (b) and S3 (c). Inset shows the relation between the number of uncompensated spins q and the total number of spins n_S in a small particle, showing that $q \propto n_S^{1/3}$. 128
5.4 Variation of magnetic susceptibility with temperature for all samples. Inset shows the linear variation of magnetic susceptibility with the inverse of the NPs' size at 298 K. . 129
5.5 Variation of the effective magnetic anisotropy with the inverse diameter of small NiO NPs. Samples 3, 5 and 7 IDC are taken from Ref. [45]. Inset scheme illustrates the NiO NP formed by a shell of uncompensated spins with FM correlations and an AFM core. 131
5.6 Magnetic hysteresis loop of sample S1 at 300 K (dash-dotted line) and at 6 K after ZFC (dashed line) and after FC with an applied field of 10 kOe (continuous line - 1^{st} cycle and dotted line - 2^{nd} cycle). Inset shows a detail of the hysteresis loop around zero field, evidencing the exchange bias and training effect found after FC. 132

6.1 Schematic representation of a nanoporous alumina template filled with NTs and NWs, and the geometry used for the angular dependent FMR measurements. 140
6.2 Angular dependencies of the FMR spectra for the Ni NW array. The angle θ_H changes from -10° to 190° with a step of 10°. 142
6.3 Angular dependencies of the FMR spectra for the Ni NT array. The angle θ_H changes from -10° to 190° with a step of 10°. 142
6.4 Angular dependencies of the FMR spectra for the Co NW array. The angle θ_H changes from -10° to 190° with a step of 10°. 143
6.5 Angular dependencies of the FMR spectra for the Co NT array. (a) The angle θ_H changes from -10° to 190° with a step of 10°. (b) The angle θ_H changes from 70° to 110° with a step of 2°. 144
6.6 SEM images of NiO NWs grown by the first sol-gel method in NpATs. 145
6.7 SEM images of NiO NWs grown by the second sol-gel method in NpATs. 146
6.8 XRD pattern of the NiO NWs grown in a NpAT. 146
6.9 Magnetic hysteresis loops of NiO NWs inside a NpAT, measured at room temperature by applying the magnetic field parallel ($\parallel$) and perpendicular ($\perp$) to the NW axis. Inset shows a detail of the hysteresis loops around zero field. 147
6.10 Magnetic hysteresis loops of NiO NWs inside a NpAT, measured at 6 K after zero-field-cooling (ZFC) and field-cooling (FC) in 10 kOe, by applying the magnetic field (a) parallel and (b) perpendicular to the NW axis. Insets show a detail of the hysteresis loops around zero field, evidencing the exchange bias found after FC. 147

6.11 Optical [(a) and (b)] and SEM (c) images of the pads and nanocontacts deposited on top of a single dispersed NT. 149
6.12 Deposition current density transient during the electrodeposition of Co NTs inside a NpAT, illustrating the sharp increase in current when the first NT reaches the Au layer on top. 150